

ABSTRACT

Title of Dissertation: RETRIEVAL OF TROPOSPHERIC AEROSOL PROPERTIES OVER LAND FROM INVERSION OF VISIBLE AND NEAR-INFRARED SPECTRAL REFLECTANCE: APPLICATION OVER MARYLAND

Robert Carroll Levy, Doctor of Philosophy, 2007

Directed By: Professor Russell R. Dickerson, Department of Atmospheric and Ocean Sciences, and Dr. Lorraine A. Remer, NASA-Goddard Space Flight Center

Aerosols are major components of the Earth's global climate system, affecting the radiation budget and cloud processes of the atmosphere. When located near the surface, high concentrations lead to lowered visibility, increased health problems and generally reduced quality of life for the human population. Over the United States mid-Atlantic region, aerosol pollution is a problem mainly during the summer. Satellites, such as the MODerate Imaging Spectrometer (MODIS), from their vantage point above the atmosphere, provide unprecedented coverage of global and regional aerosols over land. During MODIS' eight-year operation, exhaustive data validation and analyses have shown how the algorithm should be improved. This dissertation describes the development of the 'second-generation' operational algorithm for retrieval of global tropospheric aerosol properties over dark land surfaces, from

MODIS -observed spectral reflectance. New understanding about global aerosol properties, land surface reflectance characteristics, and radiative transfer properties were learned in the process. This new operational algorithm performs a simultaneous inversion of reflectance in two visible channels (0.47 and 0.66 μm) and one shortwave infrared channel (2.12 μm), thereby having increased sensitivity to coarse aerosol. Inversion of the three channels retrieves the aerosol optical depth (τ) at 0.55 μm , the percentage of non-dust (fine model) aerosol (η) and the surface reflectance. This algorithm is applied globally, and retrieves τ that is highly correlated ($y = 0.02 + 1.0x$, $R=0.9$) with ground-based sunphotometer measurements. The new algorithm estimates the global, over-land, long-term averaged $\tau \sim 0.21$, a 25% reduction from previous MODIS estimates. This leads to reducing estimates of global, non-desert, over-land aerosol direct radiative effect (all aerosols) by $1.7 \text{ W}\cdot\text{m}^{-2}$ ($0.5 \text{ W}\cdot\text{m}^{-2}$ over the entire globe), which significantly impacts assessment of aerosol direct radiative forcing (contribution from anthropogenic aerosols only). Over the U.S. mid-Atlantic region, validated retrievals of τ (an integrated column property) can help to estimate surface $\text{PM}_{2.5}$ concentration, a monitored criteria air quality property. The 3-dimensional aerosol loading in the region is characterized using aircraft measurements and the Community Multi-scale Air Quality Model (CMAQ) model, leading to some convergence of observed quantities and modeled processes.

RETRIEVAL OF TROPOSPHERIC AEROSOL PROPERTIES OVER LAND
FROM VISIBLE AND NEAR-INFRARED SPECTRAL REFLECTANCE:
APPLICATION OVER MARYLAND

By

Robert Carroll Levy

Dissertation submitted to the Faculty of the Graduate School of the
University of Maryland, College Park, in partial fulfillment
of the requirements for the degree of
Doctor of Philosophy,
2007

Advisory Committee:
Professor Russell Dickerson, Chair
Dr. Lorraine Remer
Professor Zhanqing Li
Professor Rachel Pinker
Professor Raymond Hoff
Professor Shunlin Liang

© Copyright by
Robert Carroll Levy
2007

Dedication

To Deborah, Samantha and Jordan for your love, support, and above all, your patience.



me with the kids pursuing who knows what

To Yoram Kaufman (1948-2006) for your scientific genius and optimism.



Yoram pursuing first class scientific research

Acknowledgements

First of all, none of this would have been possible without my family. Thank you Deborah, Samantha and Jordan for your patience, support and love. I was not happy when Samantha, then age 3, mouse-dragged dissertation into the ‘trash’, but I forgive her. Thank you, Ronald and Rosalind (my parents), for being such ‘great’ grandparents and taking the kids over my stress-filled weekends. I love you all!

I am grateful that my committee, led by Professor Dickerson, tackled ‘the beast’ (this 260 page document) and made it much, much better. As for continual guidance, direction and motivation, as well as time management, I thank my guru and mentor, Lorraine Remer. I thank my company, SSAI, for supporting me financially and allowing me the flexibility to complete this work within reasonable time. This work was mostly funded by the ‘MODIS-aerosols’ NASA contract.

I thank Pete Colarco and Mian Chin for help with modeling, aerosol theory, and coding. Similar thanks goes to Jennifer Hains, for putting up with all my questions, and handing me perfectly working codes, (not to mention that she let me hang out in the Chem. Lab). In addition, I note Charles Ichoku, Rich Kleidman, Santiago Gasso, Shana Mattoo, Eric Vermote, Oleg Dubovik, Brett Taubman and the many others who have given me scientific advice, and have made work fun.

Finally I thank those that inspired me. Since judging my barometer building (for 7th grade science fair), Dr. Alan Weinstein has pushed me toward that three letter word (Ph.D.). Yoram Kaufman provided the suggestion and optimism for me to successfully work AND go back to school.

Table of Contents

Dedication.....	ii
Acknowledgements.....	iii
Table of Contents.....	iv
List of Tables.....	vii
List of Figures.....	viii
Chapter 1: Background and Scope of the Dissertation	1
1.1: Why this research?	1
1.2: Objectives of this research.....	8
1.3: Organization of the dissertation	9
1.4: Statement of originality	10
Chapter 2: Properties of aerosols.....	11
2.1: Physical properties of aerosols.....	11
2.2: Properties of aerosol size distributions.....	14
2.3: Aerosol optical properties.....	15
2.4: Dependence of relative humidity on aerosol mass and optical properties	20
2.5: Linking aerosol physical and optical properties: closure	22
2.6: Global and US mid-Atlantic aerosol properties.....	24
2.6.1 Global aerosol properties	24
2.6.2 U.S. mid-Atlantic aerosol properties	29
Chapter 3: Aerosol measurement techniques	36
3.1: Aerosol measurement overview.....	36
3.2: Passive aerosol remote sensing.....	41
3.3: Aerosol remote sensing from AERONET	45
3.3.1 AERONET retrievals of spectral τ from direct sun.....	45
3.3.2 AERONET retrievals of aerosol properties from sky radiance.....	46
3.4: Aerosol remote sensing from MODIS.....	49
3.4.1 Characteristics of the MODIS instrument.....	49
3.4.2 Introduction to the MODIS aerosol algorithm	54
3.4.3 MODIS aerosol retrieval: Collection 4 algorithms.....	56
3.5: Summary.....	61
Chapter 4: Evaluation of MODIS c004 products.....	63
4.1: Global validation of c004 products; comparison to AERONET	65
4.2: Evaluation of c004 over the U.S. East Coast during CLAMS.....	67
4.2.1 Comparison of MODIS-derived τ with sunphotometer.....	69
4.2.2 Comparison of MODIS-derived η with sunphotometer	71
4.3: Summary.....	75
Chapter 5: Strategies for improving aerosol retrieval over land.....	76
5.1: New aerosol models for improving the slope	76
5.2: Surface reflectance correction for improving the y-offset.....	81
5.2.1 Atmospheric correction of CLAMS data.....	82
5.2.2 Application of CLAMS-derived surface reflectance relationship.....	85
5.3: Use of vector RT code for simulating polarization effects.....	87

5.3.1	Errors in TOA spectral reflectance	90
5.3.2	Errors in τ retrieval	93
5.4:	Additional strategies for improving MODIS aerosol retrieval over land	97
5.5:	A new paradigm for MODIS aerosol retrieval.....	98
Chapter 6:	Global aerosol models for the second-generation algorithm.....	100
6.1:	Motivation.....	100
6.2:	Cluster analysis of AERONET data.....	102
6.3:	Regional assignment of aerosol type.....	107
6.4:	Physical and optical properties of the aerosol models.....	112
6.5:	Simulation of spectral τ with model optical properties.....	119
Chapter 7:	The second-generation MODIS aerosol algorithm over land.....	123
7.1:	Motivation.....	123
7.2:	MODIS and AERONET datasets.....	124
7.3:	Creating the new LUT	125
7.3.1	Choice of radiative transfer code, assumed wavelengths and Rayleigh optical depths	126
7.3.2	Structure of the LUT.....	128
7.4:	VISvs2.12 surface reflectance.....	129
7.4.1	Atmospheric correction of c004 MODIS/AERONET co-located products 130	
7.4.2	Mean values of VISvs2.12 surface reflectance relationships.....	132
7.4.3	Variability of VISvs2.12 surface reflectance relationships: Angle	134
7.4.4	Variability of VISvs2.12 surface reflectance relationships: Surface type and NDVI _{SWIR}	137
7.4.5	Final parameterization of VISvs2.12 surface reflectance relationships	139
7.4.6	Notes on VISvs2.12 surface reflectance relationship errors	141
7.5:	Inversion of spectral reflectance, including 2.12 μm	142
7.5.1	Selection of “dark pixels”	147
7.5.2	Correcting the LUT for elevation	149
7.5.3	Procedure A: Inversion for dark surfaces.....	151
7.5.4	Procedure B: Alternative Retrieval for Brighter surfaces.....	153
7.5.5	Low and negative optical depth retrievals	154
7.5.6	Sensitivity study	155
7.6:	Preliminary validation	162
7.6.1	Direct comparison of V5.2 and V5.1	164
7.6.2	Statistics of V5.2 versus V5.1	165
7.6.3	Comparison of V5.2 to V5.1 and with AERONET	168
7.7:	Summary and future c005 evaluation.....	172
Chapter 8:	Using MODIS for evaluating modeled relationship between τ and surface {PM _{2.5} } over the U.S. mid-Atlantic	174
8.1:	Historical perspective of estimating surface {PM _{2.5} } from MODIS.....	175
8.2:	Observed aerosol properties over the mid-Atlantic during July-August 2002	178
8.2.1	Datasets	179
8.2.2	Summary of events	180
8.2.3	Comparisons of datasets.....	182

8.3: Introduction to CMAQ	186
8.4: CMAQ estimates of surface {PM _{2.5} }	189
8.5: Evaluation of τ /PM relationship in CMAQ	190
8.5.1 Computation of τ from CMAQ output.....	190
8.5.2 Calculating τ with the Malm reconstructed mass extinction	193
8.5.3 Calculating τ using GOCART models for reconstructed mass extinction 195	
8.5.4 Calculating τ using c005 LUT models for reconstructed mass extinction 197	
8.6: Spatial comparison between MODIS and CMAQ derived τ	198
8.7: CMAQ τ and vertical profiles compared to UMD Aircraft.....	200
8.8: Summary.....	203
Chapter 9: Conclusion: Summary and Further Study	205
9.1: Summary.....	205
9.2: Aerosol Direct Radiative Effect.....	209
9.3: Further study	210
Glossary (of symbols and acronyms).....	212
Bibliography	214

This Table of Contents is automatically generated by MS Word, linked to the Heading formats used within the Chapter text.

List of Tables

TABLE 3.1: Characteristics of MODIS Channels used in Aerosol Retrieval	52
TABLE 5.1 Solar/Surface/Satellite Geometry for eight examples.....	91
TABLE 6.1: Optical Properties of the Aerosol Models used for the over-land Lookup Table.....	114
TABLE 6.2: Extinction/Mass Properties of the Aerosol Models	116
TABLE 7.1: List of Prescribed Errors for V5.2 Sensitivity Study.....	161
TABLE 7.2: Results of Sensitivity Study using Prescribed Errors	161

List of Figures

Fig. 1.1: Global evaluation of MODIS c004	6
Fig. 1.2: Regional evaluation of MODIS during CLAMS	7
Fig. 2.1: Properties of some global aerosol types, from physical and optical perspectives.....	13
Fig. 2.2: Spectral dependence of selected aerosol types viewed from the top of the atmosphere.....	18
Fig. 2.3: Relative humidity dependence of the scattering coefficient used in the regional haze rule (IMPROVE).	21
Fig. 2.4: Global aerosol distribution. Monthly averaged τ (AOT), under all sky conditions, simulated by GOCART for July 2002.....	28
Fig. 2.5: Photograph of mid-Atlantic haze taken aboard the UMD Piper Aztec.....	31
Fig. 2.6: Climatology of aerosol property vertical profiles measured by UMD aircraft over the mid-Atlantic.....	32
Fig. 2.7: Daily average τ (at 0.55 μm) observed by AERONET sunphotometer (red), compared with daily $\{\text{PM}_{2.5}\}$ from the EPA-FRM monitor (black), in Baltimore, between June 2002 and June 2003.	34
Fig. 3.1: Schematic of a sunphotometer direct measurement of extinction of solar radiation through the atmosphere.....	38
Fig. 3.2: Schematic of sun/surface/satellite remote sensing geometry, defining the angles as viewed from the surface target.....	43
Fig. 3.3: Schematic of satellite remote sensing of the Earth, using Terra as an example.....	50
Fig. 3.4: Example of a composite MODIS ‘RGB’ image for a whole day, April 1, 2001.	51
Fig. 4.1: Illustration of Ichoku <i>et al.</i> , [2002a] spatial/temporal validation technique over a coastal AERONET site	66
Fig. 4.2: Illustration (and blowup) of discontinuity between MODIS over-land and over-ocean $\tau_{0.55}$ retrievals for 1 August 2001 (CLAMS).	70
Fig. 4.3: Comparison of MODIS over-land and over-ocean retrieved τ (at 0.66 μm) with AERONET (only) during CLAMS.	71
Fig. 4.4: CLAMS-averaged ‘equal total volume’ aerosol volume distribution (a) and ‘equal total area’ aerosol area distribution (b) from MODIS over ocean and land separately, and from AERONET inversions during CLAMS	73
Fig. 5.1: Volume size distributions for the dynamic urban/industrial models of Remer and Kaufman [1998] (‘RK-model’) and Dubovik <i>et al.</i> , [2002a] (‘D-model). ..	78
Fig. 5.2: Conversion from the RK-model to the D-model.	79
Fig. 5.3: Empirically corrected τ (AOD) over land.	81
Fig. 5.4: Atmospherically corrected surface reflectance a) at 0.47 μm ; b) at 0.66 μm ; and c) at 2.1 μm , for a small portion of the August 1, 2001 granule shown in the RGB image.	85

Fig. 5.5: τ at 0.55 μm for the August 1 case retrieved a) using the c004 assumed VISvs2.12 surface reflectance ratios and b) using the CLAMS-derived VISvs2.12 ratios.....	86
Fig. 5.6: Comparison of τ (at 0.47 and 0.66 μm) retrieved by MODIS-land and by AERONET.....	87
Fig. 5.6: Difference between vector and scalar derived reflectance at the TOA, for eight example sun/surface/satellite geometries, as a function of τ	91
Fig. 5.7: Contour plots of the reflectance difference (vector – scalar) between RT3 calculations of TOA 0.466 μm reflectance, as a function of view and solar zenith angles for two relative azimuths, for $\phi = 30^\circ$ (left) and $\phi = 150^\circ$ (right).	93
Fig. 5.8: Errors in retrieved τ (AOT), as a function of input τ , due to the neglect of polarization in the RT formulation,.....	94
Fig. 5.9: Maximum, minimum, median and quartile values of the difference between vector and scalar TOA reflectance, plotted as a function of τ	95
Fig. 5.10: Histograms of scattering angles simulated by our set of geometry compared to scattering angles observed by MODIS throughout the course of 2003.	97
Fig. 6.1: Percentage (pie charts) of spherical aerosol model type (from cluster analysis) observed at each AERONET site per season.	106
Fig 6.2: Final spherical aerosol model type designated at each AERONET site per season.	109
Fig 6.3: Final spherical aerosol model type designated at $1^\circ \times 1^\circ$ gridbox per season.	111
Fig 6.4: Aerosol size distribution as a function of τ (AOD) bin for the three spherical (moderately absorbing, absorbing and weakly-absorbing) and spheroid (dust) models identified by clustering of AERONET.....	113
Fig 6.5: Optical properties of the AERONET-derived models, compared with the Continental model for $\tau_{0.55} = 0.5$	117
Fig 6.6: Comparison of phase function (at 0.55 μm) between new (solid curves) and analogous MODIS (dotted curves) aerosol models.....	118
Fig 6.7: Comparison of spectral τ between new models (filled shapes) and averages of AERONET ‘sun’ measurements (dotted curves) at selected sites and seasons, for $\tau_{0.55} = 0.5$	121
Figure 7.1: Atmospherically corrected surface reflectance in the visible (0.47 and 0.66 μm channels) compared with that in the 2.12 μm SWIR channel (top), and the 0.47 μm compared with that in the 0.66 μm channel (bottom).....	133
Figure 7.2: VISvs2.12 surface reflectance relationships as a function of scattering angle.	136
Figure 7.3: 0.66 μm versus 2.12 μm surface reflectance as a function of bins of $NDVI_{SWIR}$ values.	139
Fig 7.4: Cartoon of inversion technique.....	144
Fig. 7.6: Flowchart illustrating the derivation of aerosol over land for the new algorithm.....	148

Fig. 7.7: Retrieved MODIS products as a function of Air Mass (a-c) and Scattering Angle (d-f) for inputted atmospheric conditions ($\tau=0.5$, $\eta=0.5$ and $\rho^s_{2.12}=0.15$) and 720 LUT geometrical combinations.	158
Fig. 7.8: Retrieved MODIS products as a function of Air Mass for inputted atmospheric conditions ($\tau=0.5$, $\eta=0.25$ and $\rho^s_{2.12}=0.15$) and 720 LUT geometrical combinations.	159
Fig. 7.9: Retrieved aerosol and surface properties over the Eastern U.S. on May 4, 2001.	163
Fig. 7.10: Retrieved τ (AOT) at 0.55 μm for Old V5.1 (a) and New V5.2 (b) over California for 30 September 2003.	165
Fig. 7.9: Histogram of retrieved τ (AOD) over land, from V5.2 (c005) in green, compared to V5.1 (c004) in orange.	167
Fig. 7.12: Preliminary validation of c005 products.	169
Fig. 7.13: MODIS aerosol size retrievals compared with AERONET derived products.	171
Fig. 8.1: Daily average τ (at 0.55 μm) observed by AERONET sunphotometer (red), compared with daily $\{\text{PM}_{2.5}\}$ from the EPA-FRM monitor (black), in Baltimore, between July and August 2002.	181
Fig. 8.2: Comparison of MODIS-land and AERONET derived τ (A) and η (B) over the mid-Atlantic region during July-August 2002.	182
Fig. 8.3: Comparison of two-hourly averaged measured surface $\{\text{PM}_{2.5}\}$ with 5x5 box averaged MODIS over land –derived τ for July and August 2002 in the mid Atlantic.	184
Fig. 8.4: Comparison (and regression) of MODIS derived τ (either Terra or Aqua) if observed within two hours of aircraft measured profile.	185
Fig. 8.5: Comparison of CMAQ 5x5 box averages (60 km) of surface $\{\text{PM}_{2.5}\}$ with observed two-hourly averaged $\{\text{PM}_{2.5}\}$ from continuous monitors.	189
Fig. 8.6: A) CMAQ 5x5 (60 x 60 km) box averaged τ derived with the Malm (IMPROVE) LUT compared with MODIS 5x5 box averages (between 50-80 km depending on view angle). B) CMAQ 5x5 box averages (60 km) of surface $\{\text{PM}_{2.5}\}$ compared with CMAQ-derived τ (Malm LUT).	194
Fig. 8.7: A) CMAQ 5x5 (60 x 60 km) box averaged τ derived with the GOCART LUT compared with MODIS 5x5 box averages (between 50-80 km depending on view angle).	196
Fig. 8.9: Comparison of CMAQ (GOCART LUT) to MODIS retrievals of τ at 0.55 μm . The top panel (A) is for a day of typical sulfate pollution (July 16, 2001) where the model matches the satellite. The bottom panel (B) is from an unusually heavy infusion of Canadian smoke at high altitudes (July 7, 2001), where the model does captures very little of satellite measured τ	199
Fig. 8.10: A) Comparison of CMAQ derived τ (GOCART LUT) to derived τ from aircraft profiles.	201
Fig. 8.11: Comparison of CMAQ extinction (GOCART LUT) to specific UMD aircraft profiles of scattering over airports (both at 0.55 μm).	202

Chapter 1: Background and Scope of the Dissertation

1.1: Why this research?

Tropospheric aerosols significantly influence global climate, by changing the radiative energy balance [Kaufman and Chou, 1993; Hansen et al., 1997; Haywood and Boucher, 2002; Hignett et al., 2002; Jacobson et al., 2001; Ghan et al., 2002; Yu et al., 2006] and clouds as well as the hydrological cycle [IPCC, 2007; Ramanathan et al., 2001; Rosenfeld, 2000; Kaufman and Koren, 2005]. Spanning from nanometers to tens of micrometers (μm) in radius, aerosols are efficient at scattering solar radiation back to space. Their hygroscopic properties enable them to act as cloud condensation nuclei (CCN), which in turn influence cloud/precipitation processes [Toon, 2000; Rosenfeld, 2000] and global albedo [Twomey, 1977]. Also known as suspended airborne particles, or particulate matter (PM), aerosols are a component of smog and air pollution [USEPA, 2003; Chen et al., 2002; Dickerson et al. 1997] and on the list of the EPA's (recently revised) regulated criteria air pollutants (e.g., <http://www.epa.gov/oar/particlepollution/naaqsrev2006.html>). Aerosols reduce aesthetic visibility [Malm, 1994; Watson, 2002; Hand et al., 2000] and those less than about 2.5 micrometers (μm) in diameter (known as $\text{PM}_{2.5}$) can adversely affect human health by being ingested into lungs [Samet et al., 2000; Prospero, 1999b] or accompany disease [Mims et al., 1997].

Unlike greenhouse gases, aerosols are not well mixed in the atmosphere. They are spatially and temporally inhomogeneous, and usually concentrated near Earth's surface. The scale height for aerosol mass is on the order of 2-3 km,

compared to 8 km for the molecular atmosphere. Depending on their source, their size, and their ability to react within the atmosphere, aerosols can be found near or far from their sources. Dust arising from the Saharan desert is commonly observed in the Caribbean Sea [*Prospero*, 1996; *Levy et al.*, 2003], and urban aerosols from the U.S. East Coast are observed far out into the Atlantic Ocean [*Dickerson et al.*, 1995; *Fraser et al.*, 1972].

Although aerosols are inhomogenous, studies have attempted to measure their global radiative effect (on climate) as compared to those from greenhouse gases (specifically, CO₂). In its series of assessments, the Intergovernmental Panel on Climate Change (IPCC) aims to estimate the radiative forcing (effects due to anthropogenic processes) at the top-of-atmosphere (TOA) and their respective uncertainties. The recently released IPCC summary [*IPCC*, 2007] assigned values and uncertainties to global CO₂ forcing and aerosol direct radiative forcing (DRF) of $+1.66 \pm 0.15 \text{ W} \cdot \text{m}^{-2}$ and $-0.5 \pm 0.4 \text{ W} \cdot \text{m}^{-2}$, respectively. Thus, aerosol DRF compensates for about 30% of the CO₂ forcing. *Yu et al.*, [2006] compiled a summary of observationally based estimates of aerosol direct radiative effect (DRE, which represents the sum of natural and anthropogenic aerosols). Over the global ocean, the measurement consensus was $\text{DRE}_{\text{ocean}} \sim -5.5 \pm 0.2 \text{ W} \cdot \text{m}^{-2}$. Estimates of DRE over land had larger uncertainty, e.g., $\text{DRE}_{\text{land}} \sim -4.9 \pm 0.7 \text{ W} \cdot \text{m}^{-2}$, derived from limited observational data [*Yu et al.*, 2006]. Globally, the DRF is approximately 30% of the total DRE, but may be as much as 47% over land surface.

Over the Washington/Baltimore corridor and the rest of the U.S. mid-Atlantic region, poor surface air quality (for particulate matter) is prevalent during the summer

[*Kaufman and Fraser*, 1981; *USEPA*, 2003]. These heavy aerosol events often are associated with high surface temperatures, high humidity and poor surface ozone air quality. Numerous counties in the region have annual average surface $PM_{2.5}$ concentration greater than $15 \mu\text{g}\cdot\text{m}^{-3}$, meaning that they are considered in ‘non-attainment’ of National Ambient Air Quality Standards (NAAQS) required by the U.S. Environmental Protection Agency’s (USEPA). These same areas may exceed $35 \mu\text{g}\cdot\text{m}^{-3}$ for 24-hour periods, also exceeding USEPA requirements (revised as of September 2006). As part of the USEPA’s State Implementation Program (SIP), states in non-attainment (including Maryland) are required to develop plans for reducing pollution and coming into compliance with the NAAQS. The Maryland Department of the Environment (MDE; <http://www.mde.state.md.us>) is responsible for the effort in Maryland.

Due to their ability to scatter and absorb solar radiation, high concentrations of aerosols near the surface reduce visibility. The Interagency Monitoring of Protected Visual Environments (IMPROVE; <http://vista.cira.colostate.edu/improve/>) program aims at evaluating the aesthetic impacts of pollution in our national parks. In addition, aerosols lend themselves to be studied by passive and active remote sensing techniques. The AErosol Robotic NETwork (AERONET, [*Holben et al.*, 1998]) is a federated network of global ground-based sunphotometers, that when properly calibrated, use a simple application of the Beer-Bouguer-Lambert law to measure spectral (multiple wavelengths) aerosol extinction, directly retrieving spectral aerosol optical depth (AOD or τ) to expected accuracies of ± 0.02 . Passive satellite sensors, from their vantage point above the atmosphere, provide the means

for the assessment of global τ distribution [Kaufman *et al.*, 1997a], by analyzing scattered radiation. Remotely sensed measurements of τ during these heavy aerosol events are on the order of 1.0 or higher (at 0.55 μm) in the mid-Atlantic region. During these events, observed visibilities may be reduced to a few kilometers or less.

Combining sensors and information helps to characterize aerosols on all scales, from the global radiative budget (e.g., Yu *et al.*, [2006]), aerosol interactions with clouds and the hydrologic cycle (e.g., Kaufman and Koren, [2005]), and with air quality and visibility at the surface. Given recent success of passive sensors to characterize global aerosols, satellite products may be able to monitor aerosols related to poor surface air quality, both globally and over the U.S. mid-Atlantic. In fact, products from both GEOstationary Satellites (GOES, [Knapp *et al.*, 2005]) sensors and polar-orbiting (e.g., Advanced Very High Resolution Radiometer (AVHRR, [Higurashi *et al.*, 2000; Mischenko *et al.*, 1997; Stowe *et al.*, 1997]) sensors can be applied to characterize aerosol pollution events in the mid-Atlantic region [e.g., Al-Saadi *et al.*, 2005].

It was not until the launch of the MODerate Imaging Spectroradiometer (MODIS, [Salomonson *et al.*, 1989; King *et al.*, 1993]) sensors aboard NASA's *Terra* (in 1999; [Kaufman *et al.* 1998]) and *Aqua* (in 2002; [Parkinson *et al.*, 2003]) satellites, that the uncertainties of the retrievals over land were quantified [Kaufman *et al.*, 1997b]. In particular, the spectral and spatial resolution of the MODIS instrument provided significant potential for assessing both global and regional columnar aerosol properties over land. The over-land algorithm described by Kaufman *et al.*, [1997b], in combination with an over-ocean algorithm [Tanré *et al.*,

1996; Tanré *et al.*, 1997] became the basis for an *operational* algorithm (near real time processing) for retrieving global aerosol properties. The products are free and available to any investigator. Not only have MODIS aerosol products been used to answer scientific questions about radiation and climate [IPCC, 2001; Yu *et al.*, 2006], they are being used for all kinds of applications, including surface air quality monitoring. From operational products, studies such as Chu *et al.*, [2003], Al-Saadi *et al.*, [2005], Engel-Cox *et al.*, [2004; 2006] and Wang and Christopher, [2003], demonstrated that MODIS –derived aerosol optical depth (τ) product has the potential to monitor air quality, by estimating surface PM_{2.5} concentration ($\{PM_{2.5}\}$), globally and in the mid-Atlantic region.

By 2004, enough MODIS data had been collected to enable extensive statistical evaluation of the aerosol products, both globally and regionally [Remer *et al.*, 2005]. One facet of this analysis was comparison of MODIS-derived τ over land (from Collection 4, τ_{MODIS}) to ‘ground-truth’ measured by AERONET (τ_{true}). Regression of this comparison (shown in Fig. 1.1) showed correlation coefficient $R=0.80$, and that 68% (about one standard deviation) of the MODIS-derived values were retrieved to within expected uncertainty (τ_ϵ), defined by Remer *et al.*, [2005] as

$$\tau_\epsilon = \pm 0.05 \pm 0.15 \tau_{true}. \quad (1.1)$$

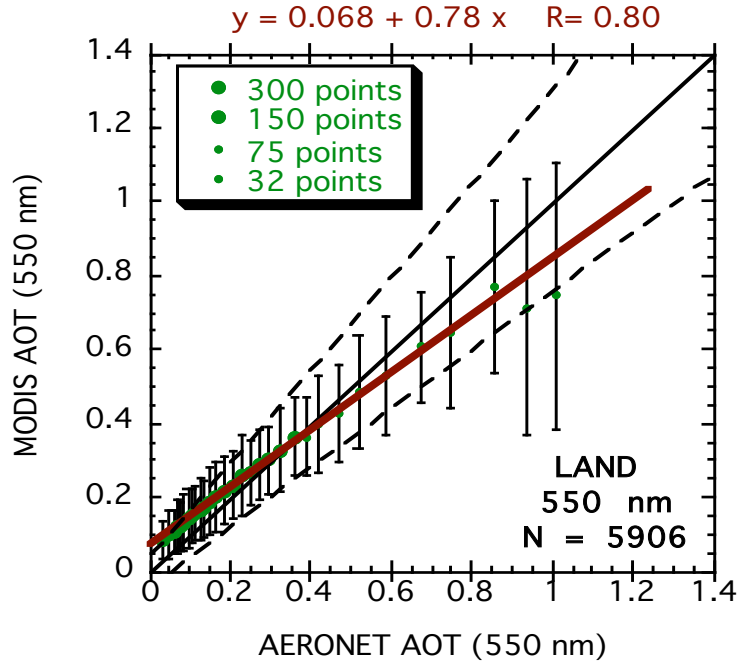


Fig. 1.1: Global evaluation of MODIS c004. MODIS τ (AOT) retrievals over land at 0.55 μm (550 nm) as a function of AERONET observations co-located in space and time. The data were sorted according to AERONET aerosol optical thickness and averaged for every 100 points. At higher optical thickness where the data become sparser, fewer points are used in the average (as indicated). The standard deviation of the MODIS –derived τ each bin is shown by the error bars. The regression (red line) equation given at the top of the plot was calculated from the full scatter plots before binning. The solid black line is the 1:1 line and the dashed lines denote the expected uncertainty calculated pre-launch. Figure adapted from *Remer et al.*, [2005].

The high quality of the comparison was said to have *validated* the MODIS-derived τ product. However, the same analysis showed that MODIS tended to be biased high in low τ conditions, and biased low for high τ , such that

$$\tau_{MODIS} = 0.07 + 0.78\tau_{true} \quad (1.2)$$

at 0.55 μm wavelength. The regression equation was poorer for the eastern United States, such that only about 64% of MODIS τ fell within the expected error, with y-offset more than 0.1. For *Levy et al.*, [2005], I found a similar poor regression

equation as compared to a (nearly) independent set of sunphotometer data, collected during the summer of 2001 over the region (Fig. 1.2).

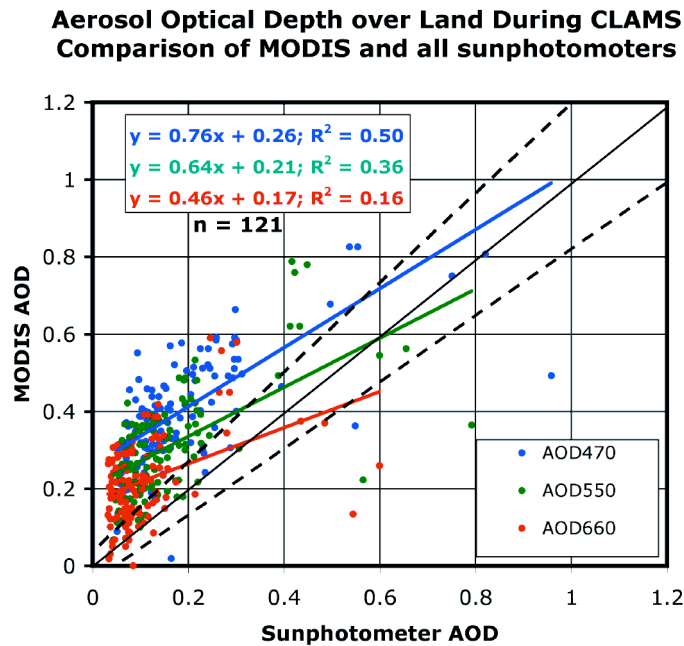


Fig. 1.2: Regional evaluation of MODIS during CLAMS. Scatterplot of MODIS (Terra) versus sun-photometer –derived τ (AOD) over the land during the CLAMS experiment (July-August 2001 over the mid-Atlantic) for three MODIS land wavelengths (0.47, 0.55 and 0.66 μm). MODIS data are averages for 5x5 boxes, centered on the sunphotometer site. Sunphotometer data are within ± 0.5 hour of MODIS overpass. The black dashed lines denote the MODIS expected uncertainty with the 1:1 line in solid black. (Figure from Levy *et al.*, [2005]).

These results indicate that the MODIS algorithm needs improvement, globally and regionally. As a first step in studying regional aerosols and their link to regional and urban-scale quality over the U.S. mid-Atlantic, it is necessary to use MODIS products that are unbiased, showing better comparison to ground truth (sunphotometer) data. Only after the MODIS products are defined properly, should they be applied to problems such as climate forcing or regional air quality. In the

case of regional air quality in the mid-Atlantic, the MODIS retrievals and surface measurements may be linked through use of a chemical transport or air quality model.

1.2: Objectives of this research

My original intent for this Ph.D. was to correct (likely by tuning) the biases in the MODIS algorithm for specific retrieval over the mid-Atlantic, and then to use the products to help characterize aerosols in the region. However, during the process of evaluating the algorithm over the mid-Atlantic, it became clear how one could improve the *global* operational algorithm. Therefore, the first task was to develop an algorithm that would retrieve global aerosol properties over all dark land surfaces, with low bias, and to the accuracy suggested by Eq. 1.1 [Remer *et al.*, 2005]. It is required that the similar accuracy be achieved over the U.S. mid-Atlantic region, specifically.

Assuming the MODIS algorithm can perform to the required accuracy globally and regionally, the products can be applied in other applications. In this thesis, I relate the products of the new algorithm with surface measurements at selected sites in Maryland. For some understanding of the vertical properties of the aerosol, I use aircraft measurements made by the University of Maryland-College Park's (UMCP) Piper Aztec [Taubman *et al.*, 2004; 2006]. Finally, the measurements are compared with those calculated from results from the Community Multi-scale Air Quality Model (CMAQ) [Byun and Ching, 1999] air quality forecast model, for July and August 2002.

1.3: Organization of the dissertation

This dissertation is organized as follows. Chapter 2 introduces the fundamental physical and optical properties of aerosols, provides an overview of *in situ* and remote sensing aerosol methods, and summarizes current knowledge about global aerosol and aerosol over the U.S. mid-Atlantic. MODIS, AERONET, and the physics of aerosol remote sensing are introduced in Chapter 3. Chapter 4 describes the previous operational version of the aerosol algorithm, discussing global and regional biases of the products. Chapter 5 suggests some steps that would improve the MODIS retrieval, which are developed in Chapters 6 and 7. Chapter 6 concentrates on global aerosol optical models, whereas Chapter 7 introduces the assumptions of surface reflectance and inversion of spectral reflectance. Preliminary global validation of the new algorithm is also presented in Chapter 7. Chapter 8 evaluates MODIS in the context of PM_{2.5} in the U.S. mid-Atlantic, combining remotely sensed and *in situ* measurements, from surface, aircraft and satellite, all in the context of developing a 3-dimensional aerosol climatology in the region. For a specific two-month period (July and August 2002), known to have many interesting aerosol events, the CMAQ model results are analyzed in the context of the measurements. The last chapter is dedicated to conclusions and suggestions of future work.

1.4: Statement of originality

During the course of my doctoral studies, I performed the following:

- Evaluated previous versions of the MODIS algorithm (c004 products), globally and regionally, and found biases and inconsistencies that could be fixed.
- Determined possible causes of retrieval bias, including assumptions of: global aerosol properties, surface reflectance relationships, radiative transfer, MODIS instrument characteristics, and retrieval technique.
- Evaluated each potential source of error, leading to new characterization of the inherent physical properties of aerosol, radiative transfer and earth's surface.
- Combined the new physical understanding to create a new algorithm that would produce better aerosol retrievals, with properly characterized internal consistency using valid physical assumptions.
- Performed preliminary evaluation of the products, globally and regionally, to show that the new algorithm provides better estimates of aerosol optical depth.
- Discovered that the over-land, globally averaged τ product (from MODIS) was significantly reduced from 0.28 (old) to 0.21 (new), greatly affecting estimates of aerosol direct radiative effect (DRE).
- Related MODIS products to surface and aircraft measured aerosol properties to characterize the 3-dimensional properties of the aerosol over the U.S. mid-Atlantic region during the summer of 2002.
- Evaluated the CMAQ air quality model for aerosol events in the region during the summer of 2002, and showed that CMAQ underestimated aerosol near the surface and throughout the column.

While I worked as part of a team, this document highlights my contribution to the aerosol community. This work has resulted in two published and two accepted first-authored papers [*Levy et al.*, 2004, 2005, 2007a and 2007b], as well as the on-line technical document known as the Algorithm Theoretical Basis Document (ATBD, [*MAST*, 2006]). In addition, I have contributed to other work, including: *Remer et al.*, [2005], *Chin et al.*, [2004], *Vant-Hull et al.*, [2005] and *Mi et al.*, [2007]. Any data work provided by others is noted within this dissertation.

Chapter 2: Properties of aerosols

2.1: Physical properties of aerosols

An aerosol is a system of particles, solid or liquid, in gaseous suspension. Unlike ozone or other atmospheric gases, aerosols are a mixture of particles of different sizes, shapes, compositions, and chemical, physical, and thermodynamic properties. They range in size from a few nanometers to nearly 100 μm , spanning from molecular aggregates to cloud droplets. Aerosols between about 0.1 μm and 2.5 μm in radius are of main interest to climate, precipitation, visibility, and human health studies. Most aerosols of interest are found in the troposphere and concentrated toward the Earth's surface (having a scale height about 2-3 km).

Aerosols are normally either defined by their source or their size. In its third assessment of climate report, the IPCC identified a number of major aerosol types, including: soil dust, sea salt, carbonaceous (both organic and black/elemental carbon), sulfate and nitrate [IPCC, 2001]. Much of the carbonaceous, sulfate and nitrate aerosols are produced directly from human activities (e.g., biomass burning, heating/cooking, agriculture, electricity generation and transportation). Others, such as soil dust, may be in part related to human activities as well (e.g., agriculture, land use change). Aerosol physical and chemical properties are determined by their sources and production processes. *Very fine* aerosols (radius < 0.1 μm) are also known as *Aitken* particles or *ultrafine* aerosols, and are primarily formed by gas to particle conversion (*nucleation*) in oxidizing environments. The concentration of

these very fine aerosols depends on numerous factors, including the proximity of emissions, presence of reactive/oxidizing species, and atmospheric conditions (humidity, temperature, solar radiation). Very fine aerosols coagulate and combine to form *fine* aerosols between 0.1 and 1.0 μm . Fine-sized aerosols are also produced directly during incomplete burning of biomass or coal. Finally, aerosols larger than about 1.0 μm are known as *coarse* particles. These aerosols are mainly produced by mechanical erosion of the Earth's surface, including sea salt and soil dust lifted by winds. Because of their larger size (and mass), coarse particles are usually quickly settled out of the atmosphere by gravity and are concentrated close to their sources. However, if they have been lifted by convection into the prevailing winds, they may be transported far from their sources.

Ambient aerosol distributions contain all three size ranges [*Whitby*, 1978]. Particles in the coarse mode are small in number but can contain the largest portion of aerosol mass (or volume). In contrast, the nuclei (very fine) mode encompasses the largest number, but the smallest volume (e.g., *Hegg and Kaufman*, [1998]). The fine mode contains the largest portion of aerosol surface area. Also known as the *accumulation* mode, the fine mode has the longest residence time (days to weeks) because it neither efficiently settles nor coagulates on its own. In terms of health, fine aerosols are the most efficient at penetrating deep into the lung.

Many aerosols are *hygroscopic*, meaning that they have the ability to attract and absorb water vapor [*Day and Malm*, 2001; *Hand et al.*, 2000; *Malm et al.*, 1994; *Kotchenruther et al.*, 1999; *Gassó et al.*, 2003]. As water vapor is added to the aerosol, they grow until they become activated. It turns out that the size change is not

a linear function of relative humidity (RH), and that the functional dependence differs whether the RH is increasing or decreasing. Because of this hygroscopicity, the residence time for aerosols is on the same order as water vapor in the atmosphere, usually about four to fourteen days.

Generally, more hygroscopic aerosols (known as hydrophilic, e.g., sulfate or sea salt) are spherical in shape, whereas those less hygroscopic (e.g., hydrophobic, e.g., soot or dust) may be non-spherical. Non-spherical aerosols may be clumplike (soot) or crystalline (certain dusts). Fig. 2.1 displays some size and shape properties of commonly observed aerosols.

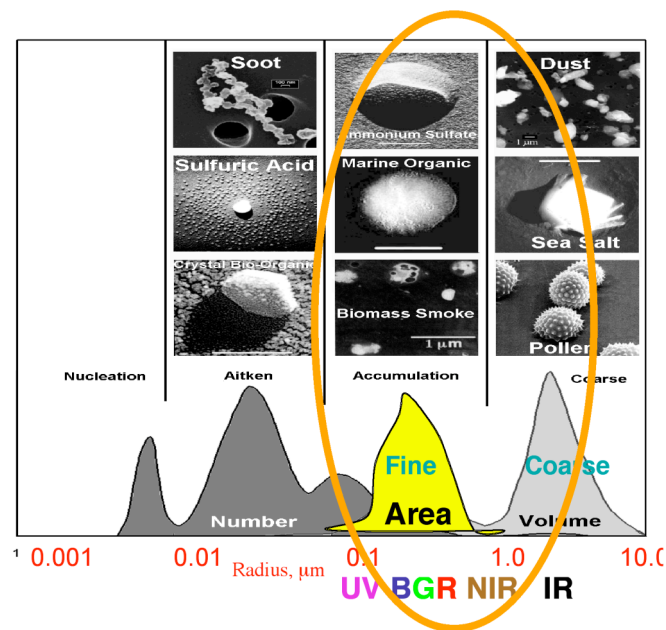


Fig. 2.1: Properties of some global aerosol types, from physical and optical perspectives. Electron microscope pictures of aerosol shape binned by their approximate radius. The orange oval encompasses the aerosol types that interact with solar radiation with wavelengths listed below the x-axis. The moments of ‘number’, ‘area’ and ‘volume’ represent which particle size dominates in that distribution; the ‘area’ distribution dominates the shortwave signal. Within the remote sensing community, ‘fine’ and ‘coarse’ aerosol are roughly analogous to the ‘accumulation’ and ‘coarse’ modes known within the *in situ* community. This figure is modified from Heintzenberg *et al.*, [2000].

2.2: Properties of aerosol size distributions

For any size distribution of spherical particles, the number distribution as a function of radius, $N(r)$, (or more simply N) is related to the volume V and area A distributions by:

$$\frac{dN}{d \ln r} = \frac{3}{4\pi r^3} \frac{dV}{d \ln r} = \frac{1}{\pi r^2} \frac{dA}{d \ln r}, \quad (2.1)$$

such that N_0 , V_0 , and A_0 are the amplitudes of the corresponding distributions, i.e.,

$$V_0 = \int_0^\infty \frac{dV}{d \ln r} d \ln r \quad N_0 = \int_0^\infty \frac{dN}{d \ln r} d \ln r \quad A_0 = \int_0^\infty \frac{dA}{d \ln r} d \ln r \quad (2.2)$$

and $dN/d \ln r$ is the number size distribution with r denoting radius (in μm). Note that whereas the *in situ* community defines in terms of diameter (for example, *Seinfeld and Pandis*, [1998]), the remote sensing community defines as function of radius.

For a single lognormal mode (e.g., *Remer and Kaufman*, [1998]), the median radius of the number distribution (r_g) is related to the median radius of the volume (or mass) distribution (r_v), and the radial standard deviation (σ) by

$$r_g = r_v \exp(-3\sigma^2), \quad (2.3)$$

such that the number size distribution is

$$\frac{dN}{d \ln r} = \frac{N_0}{\sigma\sqrt{2\pi}} \exp\left(-\frac{\ln(r/r_g)^2}{2\sigma^2}\right) \quad \text{and} \quad (2.4)$$

$$N_0 = V_0 \frac{3}{4\pi r_g^3} \exp\left(-\frac{9}{2}\sigma^2\right)$$

Within the remote sensing community, the width of the size distribution (σ) is the natural log of the quantity defined within the *in situ* community. Note that σ has the

same value whether describing number or volume distributions. The moments of order k , M^k are defined as

$$M^k = \int_0^\infty r^k \frac{dN}{d \ln r} d \ln r = (r_g)^k \exp(0.5k^2 \sigma^2). \quad (2.5)$$

The effective radius r_{eff} in [μm] of a lognormal mode is

$$r_{eff} = \frac{M^3}{M^2} = \frac{\int_0^\infty r^3 \frac{dN}{d \ln r} d \ln r}{\int_0^\infty r^2 \frac{dN}{d \ln r} d \ln r} = \frac{3}{4} \frac{V_0}{A_0} = r_g \exp\left(\frac{5}{2} \sigma^2\right). \quad (2.6)$$

For aerosols composed of two or more modes, integration must be over both size bin and mode. For example, if there are two modes, (i.e., modes 1 and 2), r_{eff} is

$$r_{eff} = \frac{\int_0^\infty r^3 \frac{(dN_1 + dN_2)}{d \ln r} d \ln r}{\int_0^\infty r^2 \frac{(dN_1 + dN_2)}{d \ln r} d \ln r}. \quad (2.7)$$

2.3: Aerosol optical properties

Aerosols are important to Earth's climate and radiation because of their size. Mie theory (more properly Lorenz-Mie-Debye theory: e.g., *Mie*, [1908]; *Chandrasekhar*, [1950]) states that particles most strongly affect the radiation field when their size is most similar to the wavelength of the radiation. Aerosols in the fine mode (0.1 to 1.0 μm) are similar in size to the wavelengths of solar radiation within the atmosphere, and are also the largest contributors to aerosol surface area (Fig. 2.1). Radiation incident on aerosols may be absorbed, reflected or transmitted, depending on the chemical composition (complex refractive index, m) and orientation (if non-spherical) of the aerosol particles. Scattering and absorption quantities [*Thomas and Stamnes*, 1999] may be represented as functions of path distance (the

scattering/absorption *coefficients*, β_{sca}/β_{abs} , each in units of [per length]), column number (the scattering/absorption *cross sections*, $\sigma_{sca}/\sigma_{abs}$, each in units of [area]) or mass (the scattering/absorption *mass coefficients*, B_{sca}/B_{abs} , each in units of [area per mass]). The use of symbols is inconsistent within the literature, so symbols are defined for this dissertation like that of *Liou*, [2002]. *Extinction* (coefficient/cross section/mass coefficient) is the sum of the appropriate absorption and scattering (coefficients/cross sections/mass coefficients), e.g.,

$$\sigma_{ext}(\lambda) = \sigma_{sca}(\lambda) + \sigma_{abs}(\lambda). \quad (2.8)$$

for the cross sections. These properties define the amount of radiation ‘lost’ from the radiation field, per unit of material loading, in the beam direction. Note all of the parameters are dependent on the wavelength λ . The ratio of scattering to extinction (e.g., β_{sca}/β_{ext}) is known as the single scattering albedo (SSA or ω_0). As most aerosols are weakly absorbing in mid-visible wavelengths (except for those with large concentrations of organic/black carbon), extinction is primarily by scattering ($\omega_0 > 0.90$ at $0.55 \mu\text{m}$). Black or elemental carbon (soot) can have $\omega_0 < 0.5$ [*Bond and Bergstrom*, 2006] especially near sources. Mineral dusts are unique in that they have a spectral dependence of absorption, such that they absorb more strongly in short visible and UV wavelengths ($\lambda < 0.47 \mu\text{m}$) than at longer wavelengths.

Properties of extinction (scattering and absorption) are related to the ambient size number distribution ($N(r)$), chemical composition, and physical shape of the aerosols, as well as the wavelength of radiation. For a single spherical aerosol particle with radius (r), interacting with radiation of wavelength (λ), the *Mie size parameter*, X , describes the ratio of size to wavelength, $X = 2\pi r/\lambda$. Values of the complex refractive

index $(m+ki)$ are required for Mie formulae to yield expressions for the scattering and extinction cross sections (e.g., σ_{sca} and σ_{ext}). These cross sections represent the interaction of a photon with the cross-sectional area (or ‘face’) of the aerosol. The scattering/extinction *efficiencies* (Q) are defined per unit aerosol as:

$$Q_{sca} = \sigma_{sca} / \pi r^2 \text{ and } Q_{ext} = \sigma_{ext} / \pi r^2. \quad (2.9)$$

The scattered photons have an angular pattern, known as the *scattering phase* ($P_\lambda(\Theta)$), which is a function of the scattering angle (Θ) and wavelength. In other words, the Mie quantities describe whether an incoming photon is displaced by an aerosol, whether it is scattered, and towards which direction relative to the incoming path.

For a distribution of aerosol particles, one is concerned with the scattering by all particles within a space. In general, since the average separation distance between aerosols is so much greater than particle radius, particles are considered independent of each other. This means that if the unit volume contains N particles of varying r , the integrated cross sections are

$$\sigma_{ext} = \int \sigma_{ext}(r)N(r)dr \text{ and } \sigma_{sca} = \int \sigma_{sca}(r)N(r)dr. \quad (2.10)$$

The scattering/extinction efficiencies for a representative single aerosol are calculated by dividing by the total integrated cross section ($\int \pi r^2 N(r)dr$) of the distribution (Q_{sca} and Q_{ext}).

Light scattering by aerosols is a function of the wavelength, the aerosol size distribution, and the aerosol composition [Fraser, 1975]. Fig. 2.2 demonstrates the spectral response of aerosol scattering for a number of idealized aerosol types.

Calculating the scattering properties at two or more wavelengths provides information

about the aerosols' size. The Ångstrom exponent (α) relates the spectral dependence of the scattering at two wavelengths, λ_1 and λ_2 :

$$\alpha_{\lambda_1, \lambda_2} = \frac{-\log(\sigma_{sca,p,\lambda_1} / \sigma_{sca,p,\lambda_2})}{\log(\lambda_1 / \lambda_2)}, \quad (2.11)$$

[Ångstrom, 1929; Eck *et al.*, 1999]. Often the two wavelengths are defined in the visible or infrared (e.g., 0.47 and either 0.66 or 0.87 μm). Aerosol size is inversely proportional to α , such that aerosol distributions dominated by fine aerosols have $\alpha \geq 1.6$, whereas those dominated by coarse aerosols have $\alpha \leq 0.6$. Quadratic fits to more than two wavelengths, known as modified Ångstrom exponents, can provide additional size information including the relative weighting of fine mode aerosol to the total (known as Fine Weighting, FW, or η) [O'Neill *et al.*, 2001].

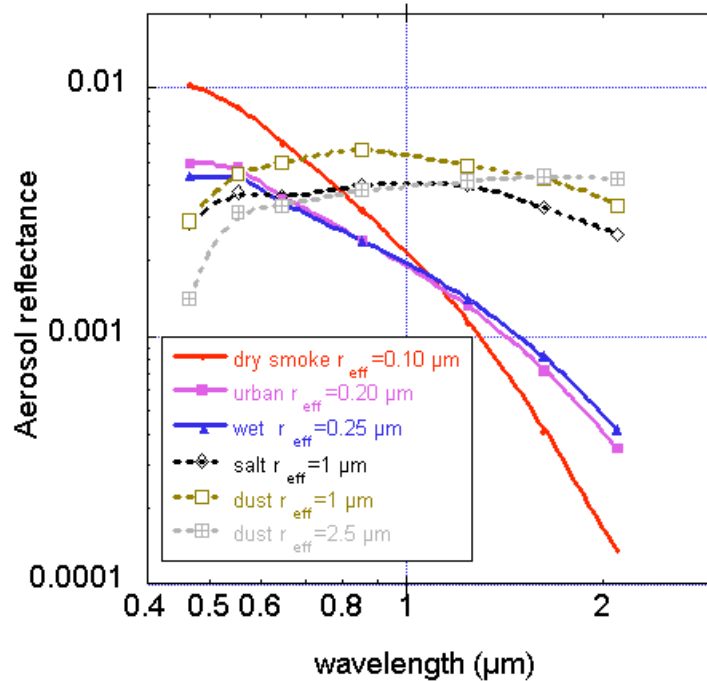


Fig. 2.2: Spectral dependence of selected aerosol types viewed from the top of the atmosphere. (Figure provided by Yoram Kaufman)

The asymmetry parameter, g , represents the degree of asymmetry of the angular scattering, and is defined as:

$$g_{\lambda} = \frac{1}{2} \int_0^{\pi} P_{\lambda}(\Theta) \cos \Theta \sin \Theta d\Theta \quad (2.12)$$

Values of g range from -1 for entirely backscattered light to +1 for entirely forward scattering. Due to the phase function's dependence on aerosol size, the asymmetry parameter also is related to aerosol size. *Andrews et al.*, [2006] showed that aerosols at a site in Oklahoma typically have values of g (at $0.55\mu\text{m}$) ranging between 0.6 and 0.7, the lower values in dry (low relative humidity) conditions. They also found a strong relationship between the accumulation mode size distribution and g . These values of g signify that aerosols produce mostly forward scattering, in contrast to the symmetry ($g = 0$) of molecular (Rayleigh) scattering.

The aerosol (scattering) optical depth (AOD or τ) is the integral of the aerosol scattering or extinction coefficients over vertical path through the atmosphere, i.e.

$$\tau(\lambda) = \int_0^{TOA} \beta_{ext,p}(\lambda, z) dz \quad (2.13)$$

where the subscript p is the contribution from the particles (to be separated from molecular or Rayleigh optical depth). Typically, aerosol optical depths (at $0.55 \mu\text{m}$) range from 0.05 over the remote ocean to 1.0, 2.0 or even 5.0, during episodes of heavy pollution, smoke or dust. The sun is obscured to a ground observer when τ is greater than about 3.0. The optical depth is the fundamental aerosol quantity retrieved by passive remote sensing.

An additional effect of aerosol scattering is on photochemistry and ozone production in the atmosphere. *Dickerson et al.*, [1997] demonstrated how increased

optical depth can lead to increased photolysis, suggesting that multiple scattering due to the presence of many aerosols (with ω_0 near 1.0, like sulfate) increases the chance of photolysis. However, absorbing aerosols (with low ω_0) will inhibit photolysis.

2.4: Dependence of relative humidity on aerosol mass and optical properties

As discussed in the previous section, the *mass extinction coefficient*, B_{ext} , represents the area extinction for a unit mass of the aerosol (literature usually reports units of $[m^2/g]$). It is related to the extinction efficiency Q_{ext} , effective radius, r_{eff} , and aerosol density ρ . For a distribution of aerosols, the mass extinction coefficient can be defined as

$$B_{ext} = \frac{3Q_{ext}}{4\rho r_{eff}}. \quad (2.14)$$

[Chin *et al.*, 2002]. Therefore, τ can be calculated by multiplying B_{ext} by the columnar aerosol mass per unit area, M .

Many aerosols are hygroscopic, however, so that the extinction properties of aerosols are modified by the addition of water. Observational studies show that aerosols grow with humidity (e.g., *Malm*, [1994]), thus increasing r_{eff} . The increase is minimal at low relative humidity (i.e., $< \sim 30\%$), slow and linear between 30% and 80%, and nearly exponential at $RH > 80\%$. At $RH \sim 98\%$, the size ratio $r_{eff}/r_{eff,dry} \sim 2.0$, but depends of aerosol type. Corresponding ratios of light scattering, (f_{RH}) at $0.55 \mu m$, in humid versus dry conditions ($RH \sim 30\%$), range from $f_{RH} \sim 2$ for $RH \sim 80\%$ to $f_{RH} \sim 15$ or more for $RH \sim 98\%$ [*Malm et al.*, 1994; *Kotchenruther et al.*, 1999; *Gassó et al.*, 2003]. Fig. 2.3 plots the f_{RH} curve assumed for sulfate aerosol within the

IMPROVE program [Malm *et al.*, 1994; IMPROVE, 2006]. Empirical fits to the f_{RH} curve suggest

$$f_{RH} = \left(\frac{1 - RH_{amb}}{1 - RH_{dry}} \right)^{-\gamma} \quad (2.15)$$

where γ is a fitting exponent (on the order of 0.2-0.7, depending on aerosol type). For example, Remer *et al.*, [1997] suggested values of 0.35-0.50, which were adapted by Taubman, [2004] to estimate dry mass from aircraft scattering measurements.

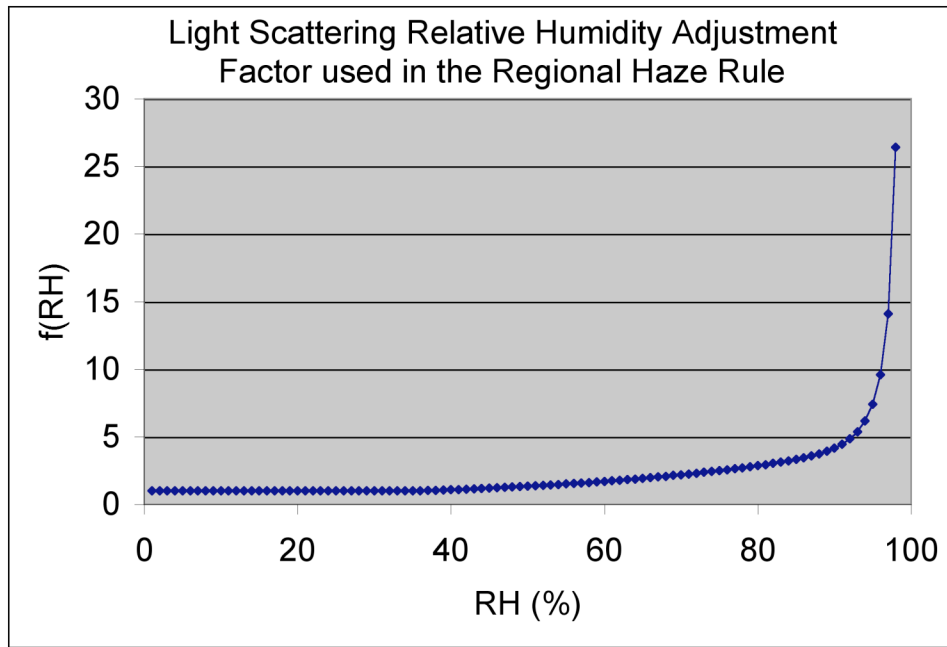


Fig. 2.3: Relative humidity dependence of the scattering coefficient used in the regional haze rule (IMPROVE). Figure adapted from the IMPROVE web site.

Köpke *et al.*, [1997] describe how one might parameterize observed f_{RH} in a chemical transport or general circulation model. Eq. 2.15 requires additional terms (relating to aerosol growth as a function of humidity) if B_{ext} should represent ambient aerosol mass extinction. For example, the aerosol mass, M contains both dry aerosol mass, M_{dry} , and water mass. The particle density is a linear combination of dry

aerosol density and water, assuming that the volume of the water and the dry particle are additive in the solution droplets [Köpke *et al.*, 1997], i.e.

$$\rho = \rho_{water} + (\rho_{dry} - \rho_{water}) \frac{r_{g,dry}^3}{r_g^3}. \quad (2.16)$$

Complex refractive indices used for calculating Q can be combined the same way [Köpke *et al.*, 1997; Chin *et al.*, 2002]. This means that ambient B_{ext} may also be represented by

$$B_{ext} = \frac{3Q_{ext}M}{4\rho r_{eff}M_{dry}}. \quad (2.17)$$

[Chin *et al.*, 2002]. Q_{ext} , r_{eff} , and ρ are properties of the ambient aerosol. Optical depth (τ) can be calculated by simply multiplying by the dry aerosol mass, M_{dry} , i.e [Chin *et al.*, 2002],

$$\tau = B_{ext}M_{dry}. \quad (2.18)$$

Note that also,

$$B_{ext} = f_{RH}B_{ext,dry}. \quad (2.19)$$

2.5: Linking aerosol physical and optical properties: closure

An aerosol ‘closure’ study is where one attempts to characterize ambient conditions with internal consistency, using multiple independent measurements of different aerosol properties. Some may be optical measurements (e.g., aerosol extinction or optical depth), whereas others may be physical measurements (e.g., aerosol mass or concentration). In theory, combining results from enough different types of aerosol measurements could completely characterize the ambient aerosol field. *Yet all* current instrument platforms have strengths and limitations. Therefore,

appropriate models must be used to link measurement from multiple vantage points, and customized to the intended application. Applications for climate, visibility, and human health each require knowledge of different aerosol properties.

As an example, satellite retrievals of ambient (relative humidity) column τ (intended as a ‘climate’ product) have been shown to relate to measurements of dried (to low relative humidity) surface particulate matter (PM) concentrations (‘air quality’ products). Under normal (for the U.S. mid-Atlantic during the summertime) conditions where the bulk of aerosol is found within the boundary layer, τ correlates with surface $PM_{2.5}$ concentration (dry aerosol less than 2.5 μm in diameter). In fact numerous papers have empirically calculated formulas to relate the two quantities (e.g., *Chu et al.*, [2003], *Al-Saadi et al.*, [2005], and *Engel-Cox et al.*, [2006]), and use as a basis for developing algorithms for monitoring and forecasting surface air quality from satellite.

While it is beneficial to note empirical correlations, it is more scientifically interesting to develop appropriate models to link optical and physical aerosol properties. For example, physically converting τ to surface $PM_{2.5}$ concentration $\{PM_{2.5}\}$ begins with understanding the mass extinction coefficient described in Eq. 2.17. One must also know the effect of measurement size cutoff compared to the theoretical (Mie) size distribution. Thus, if the aerosols are well mixed in the boundary layer, the full relationship is

$$[PM_{2.5}] = \frac{\tau}{\Delta Z_{PBL} B'_{ext}} \quad (2.20)$$

where B'_{ext} is mass extinction coefficient appropriate for a measured (truncated) size distribution (ambient RH), which in case of $PM_{2.5}$ means aerosols less than 2.5 μm in

diameter ($r < 1.25 \mu\text{m}$). ΔZ_{PBL} is the thickness of the surface aerosol layer (usually taken to be the boundary layer). Note the necessity of performing correct unit conversion to get $\{\text{PM}_{2.5}\}$ in units of $[\mu\text{g}/\text{m}^3]$. In Chapter 8, this calculation will be performed explicitly, linking satellite-derived τ and $\{\text{PM}_{2.5}\}$ over the U.S. mid-Atlantic.

2.6: Global and US mid-Atlantic aerosol properties

A quick search of the ISI's Science Citation Index (Thomson Scientific; <http://www.thomsonisi.com/>) yields thousands of articles relating to 'aerosol', suggesting an exhaustive survey of all aerosol-related literature is impossible. This section provides a brief review of global and U.S. mid-Atlantic aerosol properties in the literature.

2.6.1 Global aerosol properties

The IPCC determined that aerosols that interact with climate and radiation include sulfate, nitrate, carbonaceous (both organic carbon and elemental/black carbon), sea salt and dust [IPCC, 2001]. Globally, the largest 'emitter' of aerosols is the ocean's surface, emitting on the order of 5000 Tg ($\text{Tg} = 10^{12}$ grams) per year [Chin *et al.*, 2002]. However, these are primarily coarse sized aerosols, such that they are immediately returned to the ocean. Therefore, their number concentration ($< 500\text{m}^{-3}$) and total optical depth (< 0.15) are much smaller in magnitude than values over continents. From the continents, dust aerosol emitted mass is a distant second to sea salt, on the order of 1600 Tg/year [Chin *et al.*, 2002]. However, as dust arises from much more concentrated sources (primarily topographic depressions in deserts),

its concentrations and optical depths can be much, much higher. Values of $\tau > 2.0$ are not uncommon over areas near and downwind of major dust sources (e.g., Cape Verde Islands off the coast of the Sahara desert in Africa). Like sea-salt, dust aerosols are primarily coarse in size ($r > 1.0 \mu\text{m}$). Sea salt is hydrophilic, while most dusts are generally hydrophobic. Single scattering albedos for sea-salt are generally agreed to be nearly unity, whereas there is debate among the values for dust. Most dust shows ω_0 spectral dependence, from $\omega_0 < 0.90$ in the ultraviolet and deep blue ($\lambda < 0.47 \mu\text{m}$), to $\omega_0 > 0.95$ in visible and near-infrared wavelengths, although it depends on the specific source and aging of the dust. Visually, some dust is yellow, where others are orange, or brown in color, suggesting variability of its optical properties.

Among the aerosol types considered to be clearly influenced or dominated by anthropogenic processes, organic aerosols are next on the list for global emitted mass, about 100-120 Tg/year [Chin *et al.* 2002]. Organic aerosols are emitted by biomass burning (forest clearing for agriculture) in the tropics, and local and regional emissions from transportation and industry. These are often separated into *organic* carbon (OC) and *elemental (black)* carbon (EC or BC), as they represent aerosols with very different refractive indices, densities and hygroscopic properties. OC aerosols generally have $\omega_0 \sim 0.95$ or more, are hydrophilic, and result from complete combustion processes. BC, often found in soot, arise from incomplete fuel combustion processes (e.g., wood or oil heating, cooking, diesel combustion, flaming combustion). BC may have $\omega_0 < 0.5$ or even $\omega_0 \ll 0.5$, depending on the measurement [Bond *et al.*, 2006], and are usually hydrophobic. Most of the OC and BC mass is contained as fine-sized aerosols. Biomass burning aerosols close to the source can be

very dense, having $\tau > 2.0$ or even more. In special cases, due to the extreme heating within a burning area, these aerosols may be lofted high enough into the atmosphere to be transported long distances.

Finally, also dominated by fine mode, are the sulfate and nitrate aerosols. Primarily formed by oxidation of SO_2 and NO_2 , respectively, sulfate and nitrate are primarily the result of manmade activities. Except for emissions from biological processes in the ocean, and emissions from low altitude volcanoes, most tropospheric sulfate and nitrate are related to electrical generation (coal fired power plants), industry, and agriculture (fertilizing processes). These aerosols are emitted globally at the rate of ~ 40 Tg/year [Chin *et al.*, 2002]. Easily combined with ammonium, as ammonium sulfate or ammonium nitrate, these hydrophilic aerosols ($f_{\text{RH}} > 2$ in $\text{RH} > 80\%$ conditions) have similar scattering properties ($\omega_0 > 0.95$). As these aerosols age, it is not uncommon to observe $\tau > 1.0$ in polluted conditions. In fact, much of the particle pollution in the Eastern U.S. and Western Europe are compounds of sulfate and nitrate.

Of course, aerosols representative of a region may be transported into other regions. Fraser *et al.*, [1984] attempted to measure aerosol mass transported from the U.S. into the Atlantic, using Geostationary Satellite (GOES) satellites. Saharan dust is found in the Caribbean [Prospero, 1996; Levy *et al.*, 2003; Colarco *et al.*, 2003], whereas Asian dust and pollution is found over the United States (e.g., Chin *et al.*, [2003]; Heald *et al.*, [2006]). Also, depending on meteorology, aerosol types may be mixed with each other, thus eliminating most distinguishing optical and physical features. For example, eastern Asia can be a soup of dust, pollution and smoke.

Choudhary et al., [submitted 2007] found that fine aerosols over Xianghe (southeast of Beijing, China) during the early spring were characteristic of pollution mixed with soot, whereas coarse aerosols indicated dust mixed with soot. They measured bulk $\omega_0 \sim 0.80$, but varied widely on a daily basis.

Global simulations of aerosol in climate transport models suggest that the largest optical depth values ($\tau > 0.5$ on a monthly basis) are persistent over Saharan Northern Africa and directly downwind into the eastern Atlantic Ocean. These high values are dominated by dust. Other ‘hotspots’ of elevated τ include: over and downwind of the Eastern U.S. and Europe (primarily sulfate), Southern Africa and South America (OC and BC), eastern Asia (a mix of everything: dust, sulfate and carbon), and the Indian Ocean [*Ramanathan et al.*, 2003]. Fig. 2.4 displays a simulation of monthly averaged τ for July 2002, provided by the Georgia Tech-Goddard Global Ozone Chemistry Aerosol Radiation and Transport model (GOCART, [*Chin et al.*, 2002]). Shown are the optical depths contributed by each major aerosol type (dust, seasalt, OC, BC, sulfate and the grand total).

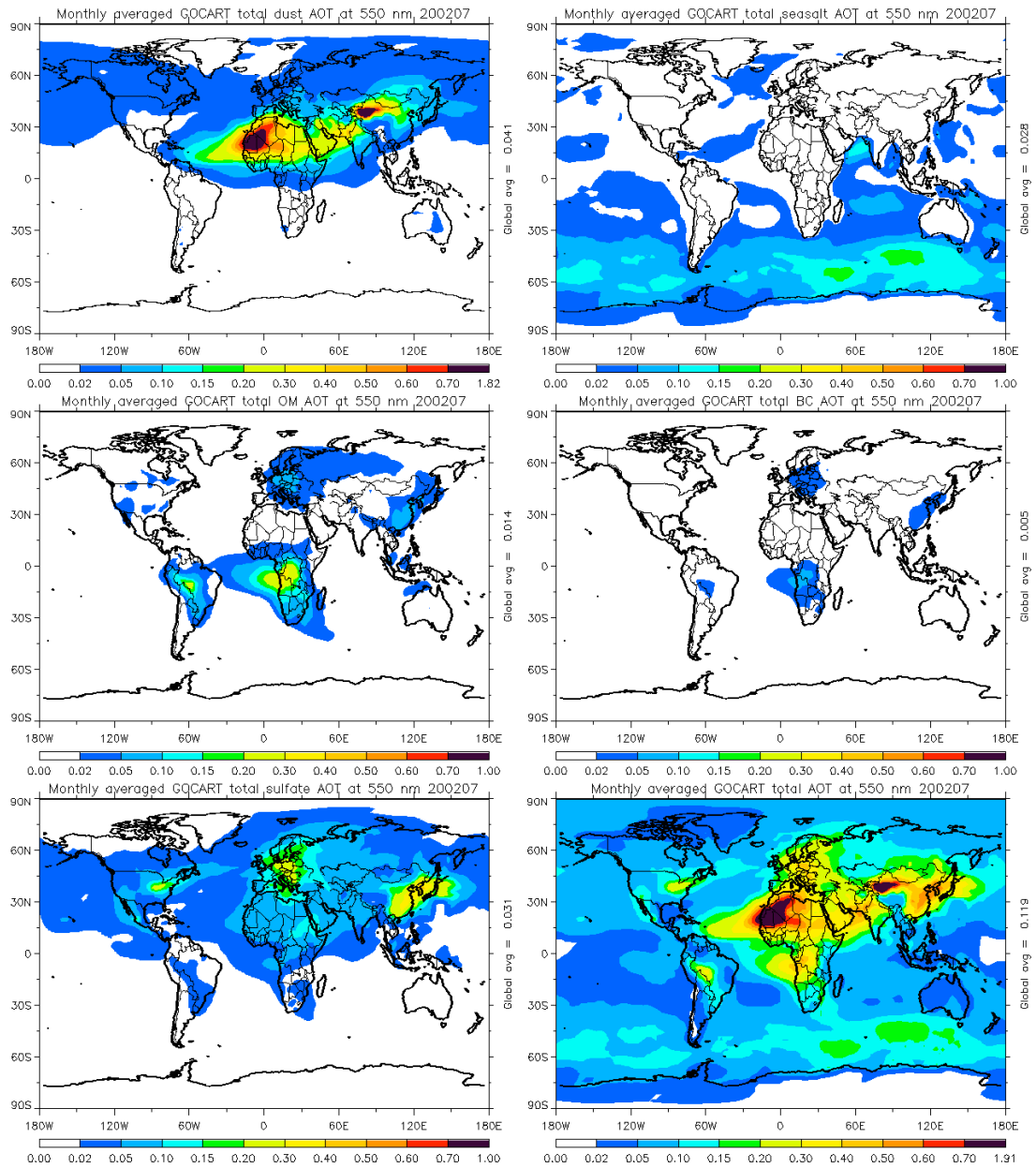


Fig. 2.4: Global aerosol distribution. Monthly averaged τ (AOT) under ‘all sky’ conditions, simulated by GOCART for July 2002. Simulated are τ for dust, seasalt, organic matter (OM), black carbon (BC), sulfate and total.

2.6.2 U.S. mid-Atlantic aerosol properties

In the eastern U.S., aerosols are dominated by hydrophilic sulfate (~50%; e.g., [Russell *et al.*, 1999]), with f_{RH} (80% vs 30%) on the order of two or more (e.g., Kotchenruther, [1999]; Malm *et al.*, [1994]; Gassó *et al.*, [2003]). Deviations from this growth factor are due to the history of the aerosol field, owing to the interaction between sulfate with clouds as well as other aerosols. Carbonaceous (BC and OC) represents most of the remaining aerosol fraction (e.g., Novakov *et al.*, [1999]; Chen *et al.*, [2002]), with relatively small contributions from dust and seasalt. Total annually averaged $PM_{2.5}$ concentrations are on the order of 13-15 $\mu\text{g m}^{-3}$, depending mainly on urban density near the monitoring site. There is some indication that total PM loadings in the region may be dropping [USEPA, 2003].

The USEPA has designated areas in the mid-Atlantic as *PM supersites*, including Baltimore, Maryland. This is an ambient monitoring research program intended to address the scientific uncertainties associated with fine particulate matter. Most of the research concentrates on highly time resolved surface filter measurements for mass and chemical apportionment for source determination (e.g., Ondov *et al.*, [2006], Frank, [2006] and Lake *et al.*, [2003]).

Chen *et al.*, [2002; 2003] performed analysis and speciation of fine aerosol ($PM_{2.5}$) mass at Fort Meade, Maryland (FME, about halfway between Baltimore, MD and Washington, D.C.) during 2000, and found that sulfate dominates in summer (>50%), but drops to 30% in the winter and spring. Carbonaceous aerosols (both OC

and BC) accounted for 30-45% of the aerosol mass, whereas seasalt and dust accounted for less than 5%. Through back-trajectory and chemical analyses, *Chen et al.*, [2002] determined that most of the sulfate is aged and regional, arising from upwind sources, whereas the carbonaceous aerosols are locally produced, the result of wood burning and transportation. During heavy haze episodes, PM_{2.5} concentrations can reach 45 µg m⁻³ or greater, such that water within the aerosol contributes >40% to the total extinction [*Chen et al.*, 2003]. *Hains et al.*, [submitted, 2007] continued analysis of speciated and total PM_{2.5} at FME. Another set of measurements at Wallops Island, Virginia during the summer of 2001 [*Castanho et al.*, 2005] suggested that out of total measured fine particle mass at the ground, on average ~55% was sulfate, ~3% was BC, ~6% was dust, and the most of the rest was likely composed of OC. However, sulfate can contribute nearly 70% of fine aerosol mass during heavy regional pollution, like that observed on July 17, 2001 at Wallops Island.

Coordinated regional intensive experiments, such as the Tropospheric Aerosol Radiative Forcing Operational Experiment (TARFOX, [*Russell et al.*, 1997]), the Chesapeake Lighthouse and Aircraft Measurements for Satellites (CLAMS, [*Smith et al.*, 2005]) have shown that the bulk of aerosol is found in the planetary boundary layer (PBL). The thickness of the PBL is governed by the strength of convection, and it varies diurnally. During the peak of afternoon heating in the summer time, the bulk of aerosol over mid-Atlantic is found in a PBL that is on the order of 2-3km (e.g., [*Redemann et al.*, 2000; *Gasso et al.*, 2003]). In most cases, there is some variability of the aerosol size and aerosol complex refractive index in the aerosol layer

[Redemann *et al.*, 2000], suggesting that the composition of the aerosol changes with altitude. Regular aircraft measurements, as part of the Regional Atmospheric Measurement Modeling and Prediction Program (RAMMPP, [http://www.atmos.umd.edu/~RAMMPP]), have been made over many years, further characterizing the vertical structure of aerosol physical and optical properties [e.g., Taubman *et al.*, 2006]. Fig. 2.5 displays a photo of a haze layer, taken aboard the University of Maryland's (UMD) Piper Aztec. Fig. 2.6 is adapted from Taubman's dissertation [2004], displaying the statistics of the vertical structure of ω_0 and α measured in the mid-Atlantic (biased toward polluted conditions).



Fig. 2.5: Photograph of mid-Atlantic haze taken aboard the UMD Piper Aztec. Picture taken by Brett Taubman.

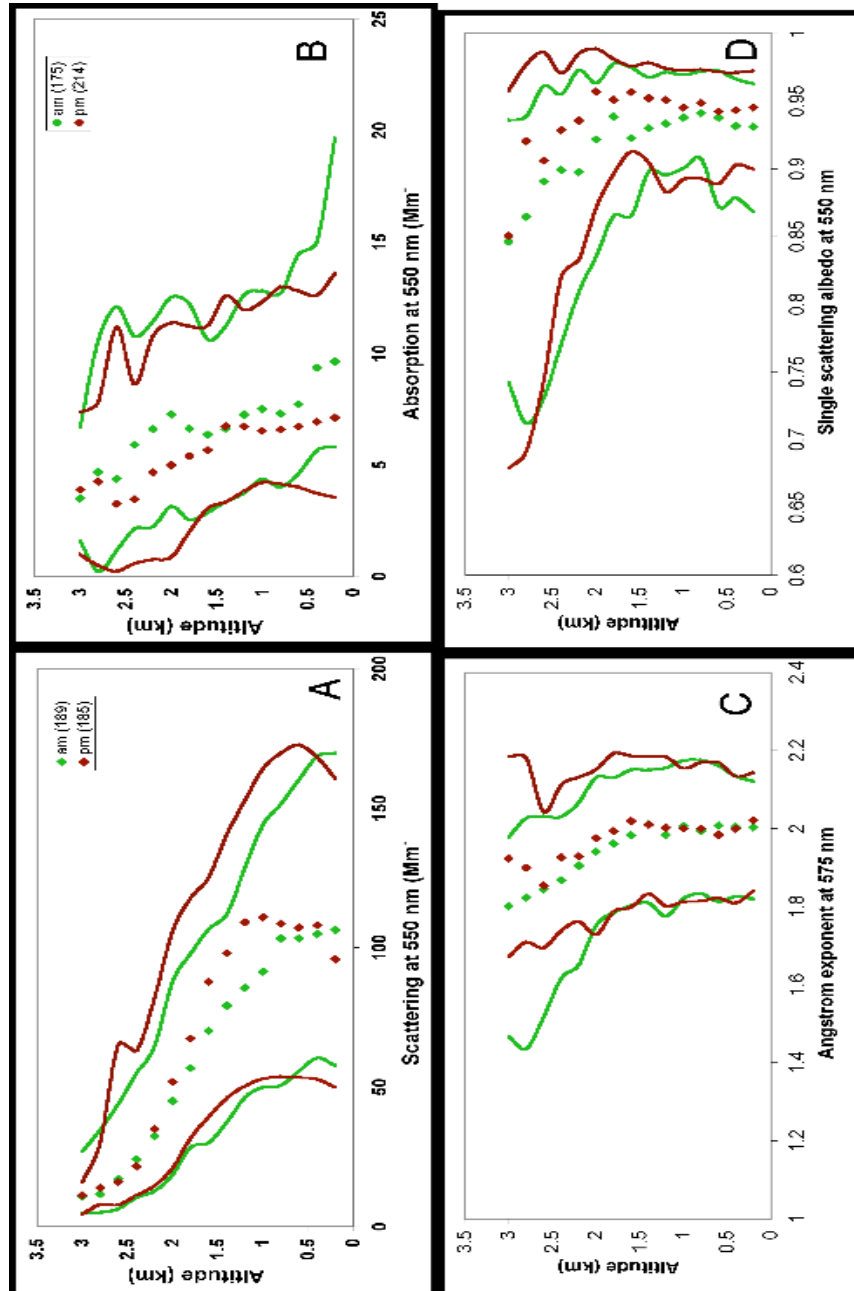


Fig. 2.6: Climatology of aerosol property vertical profiles measured by UMD aircraft over the mid-Atlantic. Median values calculated every 250 m from all morning (green, before Noon Local Standard Time, LST) and afternoon (red, after Noon LST) profiles for A) scattering, B) absorption, C) single scattering albedo at 0.55 μm and D) Angstrom exponent at 0.575 μm . The solid lines indicate the 1st and 3rd quartiles of AM and PM profiles. Figure parts prepared by Jennifer Hains and Brett Taubman.

In heavily polluted (sulfate dominated) conditions, aerosol optical depths may be $\tau > 1.0$. Fig. 2.7 shows a time series (June 2002-June 2003) of daily averaged τ (at $0.55 \mu\text{m}$) from (Level 2; quality controlled) data collected from AERONET sunphotometers at the Maryland Science Center (MD_Science_Center) in Baltimore, compared with daily averaged surface $\{\text{PM}_{2.5}\}$ measured by an EPA Federal Reference Monitor (FRM) also in Baltimore (Old_Town). There is a strong seasonal dependence of τ , with maximum τ during the summer time. These values are also associated with highest values of columnar water vapor ($>4.0 \text{ cm}$) as derived by AERONET [Holben *et al.*, 2001]. Derived $440 \mu\text{m} - 870 \mu\text{m}$ Ångstrom exponents show large spectral dependence on average ($\alpha \sim 1.55$) indicating dominance of fine sized aerosols. There is a seasonal dependence of α , ranging from $\alpha \sim 1.8$ in the summertime to $\alpha \sim 1.2$ in the spring. The springtime minimums may be associated with the presence of transported Asian coarse dust aerosols [Chin *et al.*, 2003]. Derived fine aerosol fractions (also from AERONET) also indicate seasonal dependence, ranging from $\sim 90\%$ in the summertime to $\sim 70\%$ in the spring. The seasonal dependence of surface $\{\text{PM}_{2.5}\}$ is also present, although it is much noisier. Annual averaged values of τ and $\{\text{PM}_{2.5}\}$ (for one year; June 2002-May 2003) are 0.24 and $16.7 \mu\text{m} \cdot \text{m}^{-3}$ (above NAAQS), respectively.

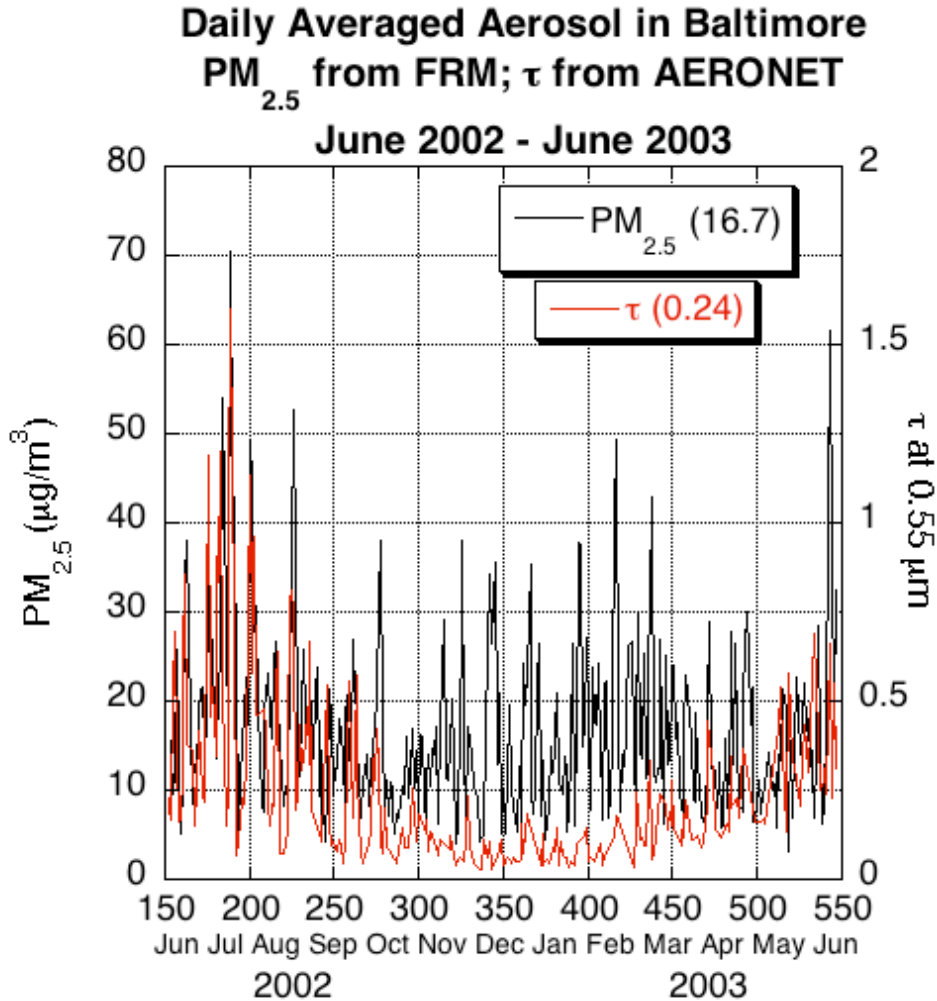


Fig. 2.7: Daily average τ (at 0.55 μm) observed by AERONET sunphotometer (red), compared with daily $\{\text{PM}_{2.5}\}$ from the EPA-FRM monitor (black), in Baltimore, between June 2002 and June 2003. The yearly mean (June-May) of each dataset are given in parentheses in the legend. The AERONET data are Level 2 (quality controlled).

While the average and normal variability of aerosol properties is well characterized in the region, there are cases with unexpected aerosol properties. During CLAMS, *Castanho et al.*, [2005] observed that dust contributed 40% of the total fine aerosol mass at Wallops Island during an incursion of Saharan dust between July 24 and 26, 2001. At other times, smoke from biomass burning in Canada can flow into the region by strong northwesterly winds. For example, during July 6 and

9, 2002, extremely dense smoke was transported at high altitudes ($> 3\text{km}$) from northern Quebec [Taubman *et al.*, 2004; Vant-Hull *et al.*, 2005; Colarco *et al.*, 2005]. This episode was marked by extremely high optical depth ($\tau > 5.0$), slightly lower than normal ω_0 (~ 0.90) and except for one day, very little evidence for it at surface PM monitors. As part of RAMMPP, the UMD aircraft flew during the episode, and demonstrated that this heavy aerosol event was not a result of a stagnant summertime air mass, the usual environment for buildup of the mid-Atlantic's soup of sulfate and organic carbon.

In contrast to heavy aerosol events, the UMD aircraft also has flown through unusually light aerosol events. On August 15, 2003, much of the Eastern United States was affected by a near total blackout of the electrical grid. This 2003 electrical blackout event later became known as the 'accidental experiment in atmospheric chemistry' [Marafu *et al.*, 2004], providing a unique opportunity to evaluate the contribution of power plant emissions to regional haze. With the UMD aircraft, they measured vertical profiles of the aerosol at two locations. Marafu *et al.*, [2004] found that without the normal burden of power plant emissions, the relative scattering and extinction properties of the aerosol column were substantially lower than would be expected in similar meteorological conditions. Yet absorption remained normal. This suggested that since local source contributions to PM (transportation and the like) were unaffected by the blackout, carbonaceous aerosol, not sulfate, was dominating the measured aerosol signal.

Chapter 3: Aerosol measurement techniques

3.1: Aerosol measurement overview

Numerous techniques are used to observe and quantify aerosol physical and chemical properties (e.g., *Seinfeld and Pandis*, [1998]), either *in situ* or by remote sensing. Each of these techniques may be passive (operating under ambient conditions) or active (perturbed conditions). Combined surface and airborne measurements provide profiles of aerosol properties such as loading, size distribution, and chemistry. For example, aerosol mass concentrations at the surface may be measured *in situ* by weighing filters before and after aerosol collection. In fact, the EPA calls for the use of the Federal Reference Method (Code of Federal Regulations (CFR), [1997]) for the measurement of filter based, gravimetric PM_{2.5} mass to determine compliance to NAAQS. Aerosol size distributions may be determined by setting filter sizes to selectively collect aerosols of certain diameters (e.g., <2.5 μm). These are active techniques that perturb the aerosols during collection. Subsequent laboratory analyses can be used to determine chemical properties. Different protocols have been used extensively in other non-NAAQS air quality monitoring projects, such as the Speciation Trends Network (STN), [*USEPA*, 1999], and the Interagency Monitoring and Protective Visual Environment network (IMPROVE), [*Ames and Malm*, 2001; *Malm et al.*, 2004]).

Other *in situ* techniques measure extinction of radiation, by measuring the optical properties to infer aerosol properties. These active instruments emit radiation into a container or filter of aerosols, collected by pumping (usually warmed and

dried) air (containing aerosols) through an inlet. In fact, both types of instruments were present aboard the UMD research aircraft. A nephelometer [e.g., Anderson *et al.*, 1996] attempts to retrieve part of the aerosol scattering phase function at one or more wavelengths (nominally 0.45, 0.55 and 0.70 μm), by shining light into a cavity, and measuring the signal at specific angles. The Particle/Soot Absorption Photometer (PSAP, Radiance Research, Seattle, WA) attempts to retrieve aerosol absorption properties by measuring the absorption of an emitted 0.565 μm light beam as it passes through a filter subjected to ambient aerosol deposition. In either case, the aerosols must be brought into the instrument and may be dried, de-iced, or otherwise modified before measurement. While these *in situ* instruments are appropriate for measuring properties of dry aerosols, they may not represent the properties of ambient aerosol.

Remote sensing techniques measure the ambient (undisturbed) aerosol field. Like *in situ* techniques, remote sensing also includes ground based and airborne measurements. Radiometers of various types measure different components of the solar radiation field. The simplest technique is sunphotometry [Volz, 1959], where the solar disc is observed through a collimator. When calibrated and pointed properly, the sunphotometer applies the Beer-Bouguer-Lambert law to accurately measure extinction at one or more wavelengths. Water vapor, ozone and Rayleigh effects can be removed to yield the aerosol optical depth (to within expected error of ± 0.02). Fig. 3.1 displays a schematic of the sunphotometer measurement, using a Cimel Electronique (Cimel) instrument. Spectral dependence of τ (or α) can then be related to aerosol size distribution. Examples include the global automated Cimel instruments of the AERosol Robotic Network (AERONET) [Holben *et al.*, 1998;

Holben et al., 2001], the accurate portable handheld Microtops instruments [*Morys et al.*, 2001; *Ichoku et al.*, 2002b], and the Automated Airborne Tracking Sunphotometer (AATS) [*Ehasani et al.*, 1988; *Redemann et al.*, 2005]. Scattered sky radiance measurements from AERONET have been used to determine aerosol size distributions [*Kaufman et al.*, 1994; *Nakajima et al.*, 1996; *Dubovik and King*, 2000; *Dubovik et al.*, 2003]. Yet, like the *in situ* techniques, most sunphotometer measurements lack spatial and temporal representation. They do not operate at night. Sunphotometer –derived τ is not necessarily representative of surface concentrations or profiles (except when measured directly by the AATS). Also, sunphotometers cannot determine aerosol properties in between sites.

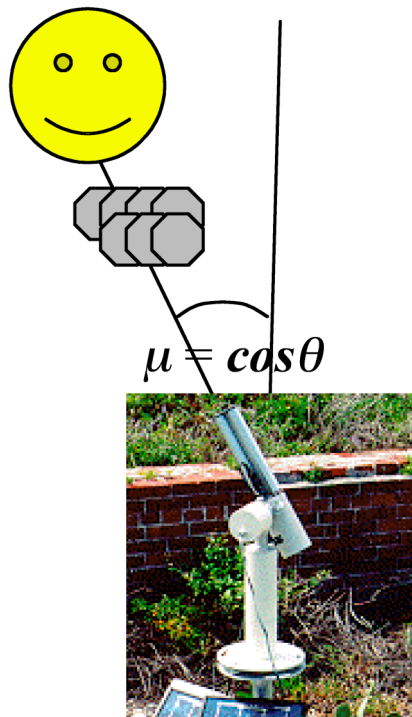


Fig. 3.1: Schematic of a sunphotometer direct measurement of extinction of solar radiation through the atmosphere. The instrument illustrated is the Cimel instrument used for AERONET.

Passive satellite sensors are uniquely able to retrieve aerosol information on a regional and global scale [Kaufman *et al.*, 1997a; King *et al.*, 1999; Kaufman *et al.*, 2002]. Using measurements of the spectral radiance exiting the Earth system, properties of atmospheric aerosols can be inferred, especially at certain wavelengths, where the surface contribution or other atmospheric contributions can be neglected or assumed. Aerosol properties are retrieved by comparing the observed radiance with a lookup table (LUT) of radiance values simulated by radiative transfer (RT) codes. Whitby [1978] showed that *in situ* aerosol size distributions are accurately modeled by three *log-normal* distributions with appropriate parameters. O'Neill *et al.* [2001] showed that remote sensed aerosol distributions also are log-normal. This provides a convenient method for modeling aerosol properties in radiative transfer applications (such as satellite remote sensing). Tropospheric aerosol properties have been operationally retrieved from passive (non-emitting), nadir-viewing, polar-orbiting satellite sensors, such as the Advanced Very High Resolution Radiometer (AVHRR) [Stowe *et al.*, 1997; Husar *et al.*, 1997; Higurashi *et al.*, 2000], and the Total Ozone Mapping Sensor (TOMS) [Herman *et al.*, 1997; Torres *et al.*, 1998; Torres *et al.*, 2002], both of which have been flown on a variety of satellites over the past two decades. Other passive sensors that are or have been used to retrieve aerosol properties, operationally, include the family of polarization sensing instruments (e.g., the POLarization and Directionality of the Earth's Reflectance – POLDER, [Deuze *et al.*, 1997]), the family of geostationary sensors [e.g., Global Aerosol and Smoke Product – GASP, Knapp *et al.*, [2005]], and multi-angle instruments such as MISR [Diner *et al.*, 1998]. These sensors are not ideal, however, because they lack the

temporal, spatial and/or spectral resolution necessary for deriving global and regional scale aerosol properties.

LIght Detection And Ranging (LIDAR or lidar) is an example of ‘active’ remote sensing capable of detecting aerosol properties. Instead of using ambient radiation, a lidar transmits light out to a target. The light that is reflected / scattered back to the instrument includes aerosol signal. Lidars are usually ground-based (e.g., Micro-Pulse Lidar – MPL [Welton *et al.*, 2001] or Raman Lidar, <http://ramanlidar.gsfc.nasa.gov/>), but may be deployed on aircraft or in space (like the Cloud-Aerosol Lidar and Infrared Pathfinder Satellite Observation (CALIPSO); <http://www-calipso.larc.nasa.gov/>). Lidars present a unique view of the vertical structure of the aerosol, but their measurements are usually limited to a single thin horizontal column and can miss plumes. For example, the resolution of CALIPSO is only ~350 m along track.

Measurements from all instruments should all be considered for understanding the 4-dimensional (including time) properties of aerosol, globally, regionally and locally (e.g., Kim *et al.*, [2006]). Ideally, these measurements should be evaluated and compared within a modeling framework to understand the physical and chemical processes that occur with aerosols. This thesis, however, focuses on passive remote sensing as the central to the aerosol characterization effort.

3.2: Passive aerosol remote sensing

Passive remote sensing of ambient tropospheric aerosol properties operates on the concept that solar radiation is modified as it interacts with the atmosphere (by gases and aerosols) and the surface [Kaufman *et al.*, 1997b]. The simplest conceptual measurement is derivation of the optical depth via observation of the direct beam of solar radiation through a collimated radiometer (known as a sunphotometer) in clear skies (e.g., Volz, [1957]). This measurement assumes that the radiation has had little or no interaction with the surface or clouds, and that there is minimal (or known) gas absorption in the chosen wavelength, λ . In other words, sunphotometry is a basic application of the Beer-Bouguer-Lambert law, in the form of:

$$L_{\lambda}(\theta_0) = F_{0,\lambda}(\theta_0, d) \exp[-\tau_{\lambda}^t m^t(\theta_0)] \quad (3.1)$$

where L , F_0 , d , θ_0 , τ , and m are the measured solar radiance, extra-terrestrial solar irradiance (irradiance outside the atmosphere), ratio of the actual and average Earth/Sun distance, solar zenith angle, total atmospheric optical depth, and total relative optical air mass, respectively. The factor $\tau^t m^t$ is the only unknown (the other parameters can be calculated), and it can be further broken down as:

$$\tau_{\lambda}^t m^t = \tau_{\lambda}^R m^R + \tau_{\lambda}^a m^a + \tau_{\lambda}^g m^g \quad (3.2)$$

where the superscripts t , R , a and g refer to total, molecular (Rayleigh scattering), aerosol and gas absorption (variably distributed gases such as H₂O, O₃, NO₂, etc). The relative optical air masses of each component differ due to differing vertical distributions. The molecular portions of Eq. 3.2 are dependent only on the altitude of the surface target, and can be accurately calculated (e.g., Bodhaine *et al.*, [2003]) and

the gas absorption portion, while less spatially homogenous can be reasonably estimated. Therefore, since errors are well defined, estimation of aerosol optical depth (τ^a , or hereby simplified as τ) is straightforward from a sunphotometer. Except for instrument calibration and uncertainties due to cloud screening, estimates of τ from sunphotometer should be within ± 0.02 (e.g., *Holben et al.*, 1998]). When made at more than one wavelength, sunphotometers retrieve spectral (wavelength dependent) τ , which in turn can be used to characterize the relative size of the ambient aerosol [*Eck et al.*, 1999; *O'Neill et al.*, 2003].

Instead of pointing directly at the sun, collimated radiometers can be pointed at discrete points in the sky to observe scattered sky radiance. Requiring additional assumptions as to aerosol shape, interaction with the surface and multiple scattering processes, properties of aerosol size distribution and scattering/extinction properties can be retrieved from these sky radiance measurements (e.g., *Nakajima et al.*, [1996], *Dubovik et al.*, [2000] and *Dubovik et al.*, [2002b]). In essence, this technique boils down to retrieval of the spectral aerosol scattering phase function, $P_\lambda(\Theta)$, from measurements of the scattering angle dependence of the sky radiance. The scattering angle, Θ , is defined as:

$$\Theta = \cos^{-1}(-\cos\theta_0 \cos\theta + \sin\theta_0 \sin\theta \cos\phi), \quad (3.3)$$

where θ_0 , θ and ϕ are the solar zenith, target view zenith and relative solar/target relative azimuth angles, respectively (illustrated in Fig. 3.2).

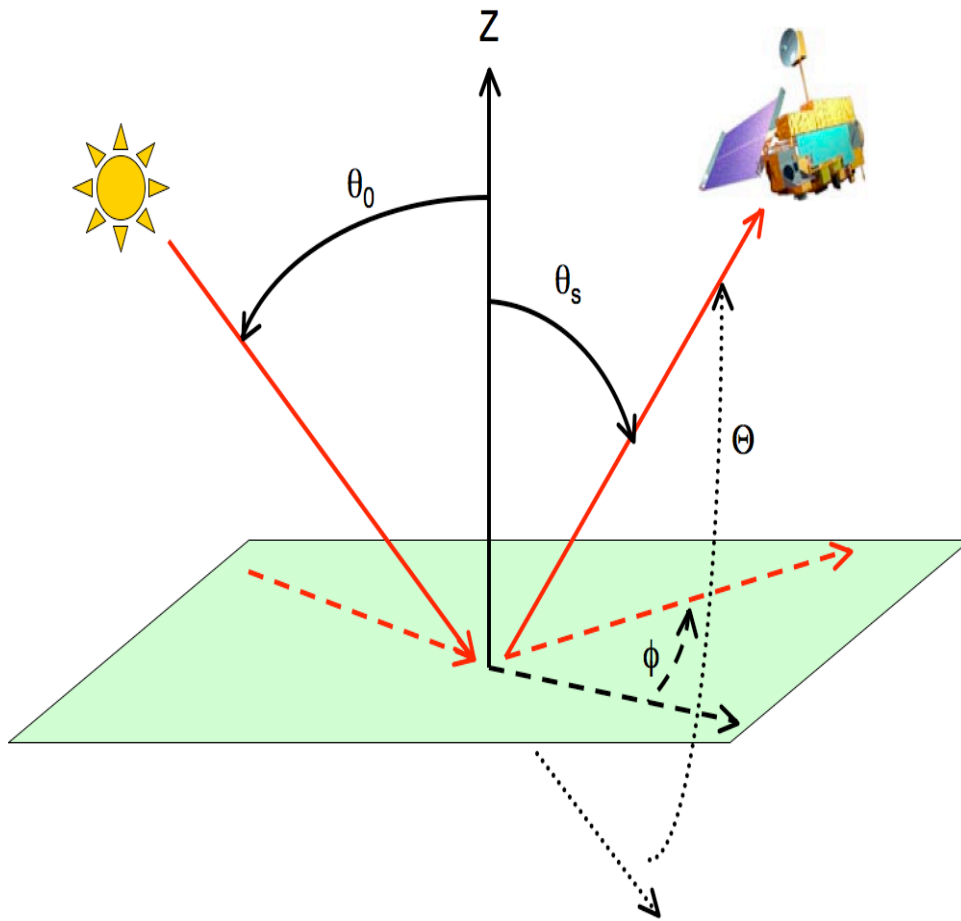


Fig. 3.2: Schematic of sun/surface/satellite remote sensing geometry, defining the angles as viewed from the surface target. The solid lines (and curves) represent solar zenith θ_0 and satellite view zenith θ angles (measured from the zenith, Z). The dashed lines (and curves) represent the relative azimuth angle ϕ (measured from the extension of the solar azimuth), whereas the dotted lines (and curves) represent the scattering angle Θ (measured from the extension of the direct beam). The Terra satellite icon is from the Earth Observatory (<http://earthobservatory.nasa.gov>).

Tropospheric aerosol properties may also be retrieved from satellite measurements of backscattered radiation [Kaufman *et al.*, 1997a]. Instead of

radiance, satellite algorithms make use of normalized spectral solar radiance, or *reflectance*, ρ_λ , defined by

$$\rho_\lambda = L_\lambda \frac{\pi}{F_{0,\lambda} \cos(\theta_0)}, \quad (3.4)$$

assuming the atmosphere is nearly a Lambertian reflector. Because the backscattered radiation includes multiple contributions from the atmosphere and surface, reasonable assumptions must be made to separate them. The upward spectral reflectance observed by a satellite at the top of the atmosphere (TOA) is a function of successive orders of radiation interactions within the coupled surface-atmosphere system. The observed spectral reflectance results in a combination of processes, including: scattering of radiation within the atmosphere without interaction with the surface (known as the ‘atmospheric path reflectance’), the reflection of radiation off the surface that is directly transmitted to the TOA (the ‘surface function’), and the reflection of radiation from outside the sensor’s field of view (the ‘environment function’). The environment function is neglected so that to a good approximation, the angle dependent TOA reflectance at a wavelength λ is described by:

$$\rho_\lambda^*(\theta_0, \theta, \phi) = \rho_\lambda^a(\theta_0, \theta, \phi) + \frac{F_{d,\lambda}(\theta_0) T_\lambda(\theta) \rho_\lambda^s(\theta_0, \theta, \phi)}{1 - s_\lambda \rho_\lambda^s(\theta_0, \theta, \phi)} \quad (3.5),$$

where ρ_λ^a represents the atmospheric path reflectance, including aerosol and molecular contributions, $F_{d,\lambda}$ is the ‘normalized downward flux’ for zero surface reflectance, T_λ represents ‘upward total transmission’ into the satellite field of view, s_λ is the ‘atmospheric backscattering ratio’ (reflectance of the atmosphere for isotropic light leaving the surface), and ρ_λ^s is the angular ‘surface reflectance’ [Kaufman *et al.*, 1997a]. Except for the surface reflectance, each term on the right

hand side of Eq. 3.5 is a function of the aerosol type (chemical composition, size distribution) and its columnar loading τ . Assuming dark and well-defined spectral surface reflectance, accurate measurements of TOA spectral reflectance can lead to retrievals of spectral τ and reasonable estimates of one or more aerosol size parameters [Tanré *et al.*, 1996]. Note that in the context of satellite observations, the ‘target’ angles (defined in Eq. 3.5) are referred to as ‘sensor’ angles or ‘view’ angles. In any case, the Earth’s surface is considered the vantage point. As the surface becomes brighter, the term in the denominator approaches zero, leading to poorly defined atmosphere-surface interactions.

In order to reduce the computational cost of difficult radiative transfer calculations at every satellite observed pixel, most, if not all operational aerosol retrievals from satellite make use of a lookup table (LUT). The LUT is a simulation of the atmospheric contribution to the TOA reflectance, namely the non-surface terms in Eq. 3.5. The LUT must be sufficiently representative of all reasonably likely atmospheric scenarios and satellite observations. Not only must the LUT span the real parameter space, it must have sufficient sensitivity to information contained in the measurements.

3.3: Aerosol remote sensing from AERONET

3.3.1 AERONET retrievals of spectral τ from direct sun

Although sunphotometers have been used for decades, the products provided by AERONET [Holben *et al.*, 1998] are considered the state-of-the-art for consistent, calibrated and useful spectral aerosol depth data. Operating at hundreds of sites

globally, the AERONET sunphotometers (produced by Cimel Electronique in France) have been reporting at some sites since 1993 (e.g., <http://climate.gsfc.nasa.gov>). ‘Sun’ products are retrievals of spectral τ at several wavelengths (0.34, 0.38, 0.44, 0.67, 0.87 and 1.02 μm , and possibly others depending on instrument), resulting from application of Eq. 3.1 to the observations of spectral extinction of the direct sunbeam. In addition to spectral τ , AERONET provides retrievals of columnar water vapor (PW) from a water vapor absorbing channel. Approximately every 15 minutes during the daytime, the sunphotometer points directly at the sun, taking spectral measurements in triplicate during a 1.5 minute span. Transmitted to GSFC in real time, averages and standard deviations of these triplets are calculated. Cloud screening [Smirnov *et al.*, 2001] is performed by limiting the variability within each triplet and compared to prior and subsequent triplets.

Level 1 (raw data averages) and Level 1.5 (cloud screened data) are provided in near real time to the user community. Level 2 data is considered calibrated, quality assured data, meaning that the instrument has been corrected for optical drift and the products meet certain requirements. Since the upgrade to Level 2 requires the instrument to be taken from the field and re-calibrated, it may not be available for months or years after Level 1.5 is available. Currently, AERONET is going through a re-processing of its products that will be collectively known as ‘Version 2’, but my analyses employed the completed set of ‘Version 1’ data. For sun-derived measurements of τ , the use of the older data should not lead to significant errors.

3.3.2 AERONET retrievals of aerosol properties from sky radiance

In addition to the direct ‘sun’ measurements, the AERONET instruments are programmed to observe angular distribution of sky radiance, approximately every hour during the daytime. These ‘sky’ measurements are made in the almucantur (a circle made with constant zenith angle equal to solar zenith angle), and the principal plane (line of constant azimuth angle) in at least at four wavelengths (0.44, 0.67, 0.87 and 1.02 μm), in order to observe aerosol spectral scattering. These observations are controlled for quality, through rigorous cloud screening and requirements of angularly symmetric radiance. Like the sun-derived AERONET products, the sky radiance products are undergoing reprocessing to Version 2, the main difference being improved characterization of the surface albedo around the site. This reprocessing may lead to significant changes from Version 1 products at some sites, however this work required the entire AERONET time series, completed as Version 1 products. Thus, this section introduces the sky-derived products of Version 1.

Sky radiance measurements are used to retrieve size distribution and scattering/extinction properties of the ambient aerosol field using spherical aerosol assumptions [Nakajima and King, 1990; Kaufman *et al.*, 1994; Dubovik and King, 2000a], and more recently, non-spherical assumptions [Dubovik *et al.*, 2002b]. By assuming the ambient aerosol to be a homogenous ensemble of poly-disperse spheres and randomly oriented spheroids [Dubovik *et al.*, 2006], the algorithm retrieves the volume distribution ($dV/d\ln R$) for 22 radius size bins and spectral complex refractive index (at wavelengths of sky radiances observations) that correspond to the best fit of both sun-measured τ and almucantur sky radiances. The non-spherical fraction is modeled with distribution of aspect ratios retrieved [Dubovik *et al.*, 2006] that fit

scattering matrices of mineral dust measured in the laboratory [Volten *et al.* 2001]. In either case, the modeling is performed using kernel lookup tables of quadrature coefficients employed in the numerical integration of spheroid optical properties over size and shape. These kernel look-up tables were generated using exact T-Matrix code [Mishchenko and Travis, 1994] and approximated geometric-optics-integral method of Yang and Liou [1996], that was used for size or shape parameters exceeded convergence limits of T-Matrix code. As a result the kernels cover wide range of sizes ($\sim 0.12 \leq 2\pi R/\lambda \leq \sim 625$) and axis ratios ε ($0.3 \leq \varepsilon \leq 3$). The usage of kernel look-up table allows quick and accurate simulations of optical properties of spheroids and therefore it allows using model of randomly oriented spheroids (introduced by Mishchenko *et al.* [1997] for desert dust) in AERONET operational retrievals.

The retrieved size distribution and complex refractive index uniquely determine the aerosol radiative properties of phase function (P) and single scattering albedo (ω_0), also provided as retrieved products. In addition, AERONET derives optical properties (τ , P and ω_0) and integral parameters of size distributions (volume concentration C_v , volume median radius r_v and σ - standard deviation from r_v), separately for fine mode ($r \leq 0.6 \mu\text{m}$) and coarse mode ($r > 0.6 \mu\text{m}$) of the retrieved aerosol. Such representation of AERONET retrievals is based on the convenient observation that the majority aerosol is bi-modal. Although the parameters C_v , r_v , σ are simulated for each mode without assuming any particular shape of size distribution (see formulation in [Dubovik *et al.*, 2002a]), they are analogous to corresponding parameters of log-normal size distributions described in Section 2.1 (V_0 , r_v , σ). In fact, the assumption of log-normality allows accurate reproduction of

aerosol optical properties in many cases (especially those dominated by fine mode), suggesting that these parameters represent log-normal properties of AERONET climatology [Dubovik *et al.*, 2002a]. To ensure large enough signal, retrievals of optical properties from sky radiance require sun-observed ambient optical depth to be at least 0.4 at 0.44 μm .

Retrievals from both sun and sky AERONET measurements are controlled by rigorous calibration and cloud screening processes. The results are also constrained by the criteria identified in sensitivity studies [Dubovik *et al.*, 2000]. As discussed by Dubovik *et al.*, [2002a] these selections yield more accurate retrieval results that can be used as ground-truth estimates (for certain aerosol properties). These products are known as Level 2 AERONET products, and within this dissertation are designated as ‘L2A’ products. Again, it is noted the AERONET team is performing a re-processing the entire dataset, known as ‘Version 2’ (<http://aeronet.gsfc.nasa.gov>) and may lead to conclusions different from those in my thesis.

3.4: Aerosol remote sensing from MODIS

3.4.1 Characteristics of the MODIS instrument

The MODerate resolution Imaging Spectro-radiometer (MODIS) is one of the first passive satellite radiometers to be designed with aerosols in mind [King *et al.*, 1993]. From polar-orbit, approximately 700 km above the surface and a $\pm 55^\circ$ view scan, MODIS views the earth with a swath about 2330 km (schematic in Fig 3.3), thereby observing nearly the entire globe on a daily basis (Fig. 3.4), and repeating orbits every 16 days. MODIS measures radiance in 36 wavelength bands, ranging from 0.41 to 14.235 μm [Salomonson *et al.*, 1989], with on-ground spatial resolutions

between 250 meters and 1 km. Its measurements are organized into 5 minute sections, known as *granules*, each ~2300 km long. MODIS actually flies on two NASA satellites, *Terra* and *Aqua*. *Terra* has a *descending* orbit (southward), passing over the equator about 10:30 local sun time, whereas *Aqua* is in *ascending* orbit (northward), so that it passes over the equator about 13:30 local sun time.

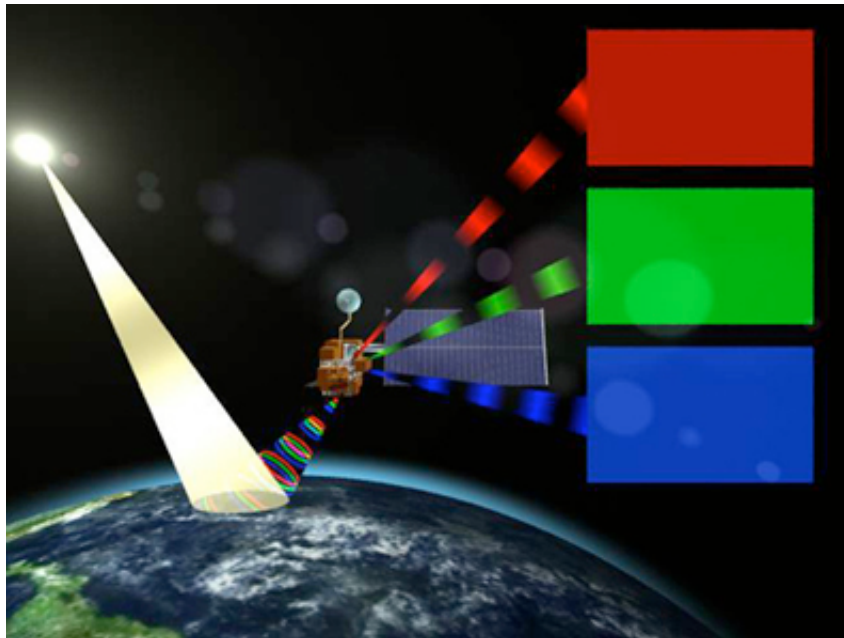


Fig. 3.3: Schematic of satellite remote sensing of the Earth, using *Terra* as an example. (Figure from Earth Observatory, <http://earthobservatory.nasa.gov>)

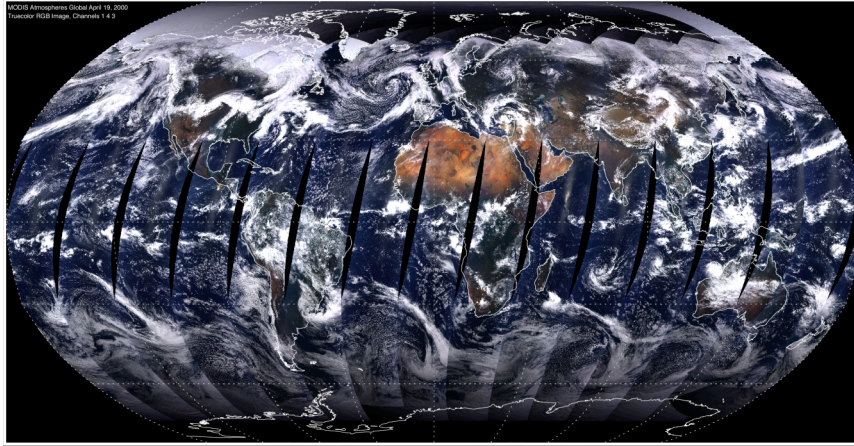


Fig. 3.4: Example of a composite MODIS ‘RGB’ image for a whole day, April 1, 2001. Images are known as ‘RGB’ or ‘True-Color’, created by merging MODIS observations in 0.47, 0.55 and 0.66 μm .

The over-land algorithm described by *Kaufman et al.*, [1997a], in combination with an over-ocean algorithm [*Tanré et al.*, 1996; *Tanré et al.*, 1997] became the basis for an *operational* algorithm for retrieving global aerosol properties from MODIS observations. The operational algorithms are maintained by the MODIS Data Processing System (MODAPS) at NASA Goddard Space Flight Center (GSFC) in Greenbelt, Maryland. The MODIS Aerosol Science Team (MAST; also at NASA-GSFC) is responsible for *validation* of the aerosol products and for updating the ‘science’ of the algorithm when necessary. The products are free and available to any investigator.

The aerosol retrieval uses the seven wavelength bands (listed in Table 1.1), which are all in atmospheric ‘windows’ (little or no absorption by gases). Included in Table 3.1 are estimates of the central wavelength in each band (obtained by integration of the channel-averaged response functions). To keep in line with common references in the literature, MODIS channels 1, 2, 3, 4, 5, 6 and 7 are known

in this document as the 0.66, 0.86, 0.47, 0.55, 1.24, 1.64 and 2.12 μm channels, respectively. In addition, the aerosol algorithms make use of radiance in other MODIS bands to help with cloud and surface screening.

TABLE 3.1: CHARACTERISTICS OF MODIS CHANNELS USED IN THE AEROSOL RETRIEVAL

Band #	Bandwidth (μm)	Weighted Central Wavelength (μm)	Resolution (m)	$\text{Ne}\Delta\rho$ ($\times 10^{-4}$)	Max ρ	Required SNR	Rayleigh optical depth
1	0.620 - 0.670	0.646	250	3.39	1.38	128	0.0520
2	0.841 - 0.876	0.855	250	3.99	0.92	201	0.0165
3	0.459 - 0.479	0.466	500	2.35	0.96	243	0.1948
4	0.545 - 0.565	0.553	500	2.11	0.86	228	0.0963
5	1.230 – 1.250	1.243	500	3.12	0.47	74	0.0037
6	1.628 – 1.652	1.632	500	3.63	0.94	275	0.0012
7	2.105 – 2.155	2.119	500	3.06	0.75	110	0.0004

Note: $\text{Ne}\Delta\rho$ corresponds to the sun at zenith ($\theta = 0^\circ$)

The MODIS instrument is spectrally stable and is sufficiently sensitive to changes in aerosol properties (e.g., *Guenther et al.*, [2002]; *Xiong et al.*, [2003]). The spectral stability for each instrument is better than 2 nm (0.002 μm). The *Noise equivalent Differential Spectral Reflectance* ($\text{Ne}\Delta\rho$) represents the sensitivity to changes in the signal, and is an inherent property of the instrument. *Signal to Noise Ratio* (SNR) is defined as the ratio of the *typical scene reflectance* (ρ^{ts}) and $\text{Ne}\Delta\rho$. The $\text{Ne}\Delta\rho$ and the SNR specifications are given in Table 3.1. To be understood in the framework of aerosol remote sensing, the definition of SNR should be based on the expected

aerosol signal. Therefore, the *Noise Equivalent Differential optical depth* ($Ne\Delta\tau$) can be defined as

$$Ne\Delta\tau = \pi Ne\Delta\rho \frac{4 \cos(\theta_0) \cos(\theta_v)}{\omega_0 P(\Theta)} \quad (3.6)$$

where ω_0 is the aerosol single scattering albedo. The least sensitivity to aerosol scattering optical depth (largest noise) is expected when both sun and satellite are at nadir views ($\theta_0 = \theta_v = 0.0$), the aerosol and Rayleigh phase functions are minimum ($\Theta \sim 120^\circ$) and the channel used is the least sensitive (channel 7, at 2.12 μm). With a typical phase function value of 0.08 at 120° , a typical aerosol scene requires $Ne\Delta\tau \sim 1.5 \times 10^{-2}$. The 2.12 μm channel's 'typical scene optical depth' (τ^s) is on the order of 0.01 or less, suggesting that the SNR defined by the ratio $\tau^s/Ne\Delta\tau$ is $\text{SNR} \sim 0.66$. If one requires that the $\text{SNR} > 10$ for sufficient sensitivity to aerosol variability, then a single 500 m pixel is insufficient.

However, if individual pixels are aggregated to larger areas, say to a grid of $10 \times 10 \text{ km}^2$ (20 x 20 of 500 m pixels), then the noise is reduced by a factor of 400. Instead of 0.66, the SNR becomes 266. However, since clouds and surface inhomogenities affect aerosol retrievals, not all pixels in the aggregate box may be suitable for aerosol retrieval. If only 5% of the 500 m pixels are suitable for retrieval, the SNR is reduced to 13. Thus, to require $\text{SNR} > 10$, $10 \times 10 \text{ km}^2$ boxes can be safely used as the default retrieval size [Tanré *et al.*, 1996]. Of course if either the aerosol signal is larger or the noise is lower, than the retrieval requires fewer pixels.

3.4.2 Introduction to the MODIS aerosol algorithm

Since MODIS' launch aboard *Terra* (in late 1999) and aboard *Aqua* (in early 2002), MODIS spectral reflectance observations have led to retrievals of spectral τ and a measure of aerosol size, known as the fine weighting (FW or η), each with 10 km resolution (at nadir). Separate algorithms derive aerosol properties over ocean and land [Remer *et al.*, 2005], necessitated by different surface optical properties. While this dissertation focuses on over-land aerosol retrievals, MODIS also retrieves aerosol products over water. Because of better-constrained ocean-surface optical properties, the algorithm used over ocean [Tanré *et al.*, 1997; Levy *et al.*, 2003; Remer *et al.*, 2005] has more sensitivity to aerosol. Later sections of this dissertation discuss concepts of the over-ocean inversion technique that are applied to the retrieval over land.

For either over-land or over-water retrieval, the algorithm must ensure that the target is free of clouds, snow, ice and extreme surface variability. A number of tests are performed to separate water bodies and land surfaces and to select appropriate pixels for retrieval [Remer *et al.*, 2005; MAST, 2006]. Over either surface, some of the brightest and darkest pixels (within the 10 km box) are removed, in order to reduce residual cloud and surface contamination effects (such as shadowing or adjacency effects).

For both over-land and over-water, the MODIS algorithm uses a lookup table (LUT). The LUT is derived by a radiative transfer (RT) code, to simulate the radiative effects of a small set of aerosol types, loadings, and geometry that presumably span the range of global aerosol conditions [Kaufman *et al.*, 1997b]. The

goal of the algorithm is to select which of the LUT's simulated scenarios best matches the MODIS-observed spectral reflectance. To retrieve realistic aerosol properties, it is essential that the LUT represent realistic scenarios.

The original MODIS retrieval algorithms were formulated for over dark land by *Kaufman et al.* [1997a] and for over water by *Tanre et al.*, [1997]. By MODIS launch aboard *Terra* (in December, 1999), the algorithm had been already revised in order to align with actual MODIS specifications and operational needs. The operational algorithms and products have been continuously evaluated for self-consistency and comparability to other datasets, including AERONET [*Remer et al.*, 2005]. MODIS algorithms are organized by 'versions' (e.g., vX.Y.Z, where X represents major 'science' update, Y represents minor updates, and Z represents bug fixes or otherwise presumably small updates; see <http://modis-atmos.gsfc.nasa.gov/MOD04/history>), whereas products are arranged as 'collections' (e.g., c00X, where X represents major science updates or reprocessing). After initial review by the MODIS science team, the products were released to the public as Collection 003. *Chu et al.*, [2002] and *Remer et al.*, [2002] evaluated c003 products over land and ocean, respectively. Soon after *Aqua* was launched (in June 2002), the algorithm was applied to both MODIS instruments, beginning the product dataset known as Collection 004. In theory, the entire c004 dataset should have been derived with a static algorithm. However, while the fundamental science assumptions remained in place, the c004 algorithm continued to evolve. Updates were necessary due to changes in MODIS instrument calibration, operational processing environments, and new science (for example improved cloud masking). *Remer et al.*,

[2005] describe v4.2.2 of the algorithm, (c004), which are used in this dissertation to provide baselines for the algorithm and products.

3.4.3 MODIS aerosol retrieval: Collection 4 algorithms

As explained in the previous section, *Kaufman et al.*, [1997b] introduced the MODIS aerosol retrieval algorithm from MODIS. Its major assumptions and methodology were unchanged through v4.2.2 [*Remer et al.*, 2005] and the processing of c004. This section summarizes the major assumptions of the c004 family of algorithms, highlighting the assumptions that were revised during c005 algorithm development and for this dissertation. While the focus of this dissertation is on over-land aerosol retrieval of aerosol properties, I also include a short section outlining the basic assumptions of the algorithm over ocean.

Processing of the MODIS data begins with collecting raw data (known as *Level 0*), and cutting them into 5-minute chunks (known as *granules*) as *Level 1A*. Each granule is converted into calibrated radiance/reflectance and geo-location data (known as *Level 1B* or *LIB*). The aerosol retrieval uses calibrated reflectance data from the seven MODIS bands listed in Table 1. These reflectance data are first corrected (by about 1-2%) for trace gas and water vapor columns, using ‘ancillary’ data from NCEP (National Centers for Environmental Prediction) analysis [*MAST*, 2006]. They are organized into 10 km x 10 km boxes (e.g., 40x40 of 250 m data, 20x20 of 500m data and 10x10 of 1 km data), and separated into land and ocean pixels. Depending on the relative dominance of either surface, the appropriate

algorithm is assigned. Near coastlines, if any of the observed pixels are considered land, then the over-land algorithm is followed.

Primary products for each algorithm include the total optical depth (τ) at 0.55 μm and an estimate of the fine aerosol weighting (η) to the total optical depth. At the conclusion of either algorithm, these primary products are evaluated and given Quality Assurance (QA) values, ranging from 0 (not to be trusted) to 3 (trustworthy). The MODIS products include trusted and non-trusted products, it is up to the user to determine which QA level, he or she should use. It is also noted here, that whereas the definitions of τ are the same, the definitions of η are different for land and ocean. This difference is explained more in detail as it relates within the dissertation.

3.4.3.1 MODIS c004 over ocean

The main premise of the over-ocean algorithm is that the ocean reflectance is generally close to zero at red (0.66 μm) and longer wavelengths, providing a dark background to view aerosol. If all pixels in the 10km x 10km box are identified as water pixels, the ocean algorithm is chosen. First, obstructed pixels (cloudy-or otherwise unsuitable for retrieval) are removed, including: those within the glint mask (within 40° of the specular reflection angle), those flagged as cloudy [*Platnick et al.*, 2003; *Martins et al.*, 2002; *Gao et al.*, 2003], and those that contain suspended river or other sediments [*Li et al.*, 2003]. The remaining good pixels are sorted by their 0.86 μm brightness. Of these, the darkest and brightest 25% are removed, thereby eliminating residual cloud and or surface contamination. If at least 10 pixels remain in the 10km x 10km box, then reflectance statistics for all seven channels are calculated and used for the inversion.

As introduced by *Tanré et al.* [1997], updated by *Levy et al.* [2003] and again by *Remer et al.* [2005], the c004 over-ocean inversion attempts to minimize the difference between the observed spectral radiance in six MODIS channels and radiance pre-computed in a LUT. The ocean LUT models the total reflectance observed by satellite, which includes not only aerosol contributions, but also spatially and temporally constant atmospheric (Rayleigh) and ocean surface (chlorophyll, foam, whitecaps and sunglint) contributions. The c004 LUT is computed by vector RT (to include polarization effects on the radiance) for 2304 sun/surface/satellite geometries and five total aerosol loadings, for four fine modes and five coarse modes [*Remer et al.*, 2005]. The inversion first interpolates the LUT to match the sun/surface/satellite geometry of the observation. The major assumption is that the total aerosol contribution is composed of a single fine and single coarse mode. For each combination of fine and coarse modes (20 combinations) the inversion determines the total spectral τ and the *fine mode weighting* (η) to the total τ that minimizes the least squares difference error (ϵ) between the modeled and observed spectral reflectance. The fine/coarse mode combination providing the smallest ϵ is the final solution. A variety of other aerosol parameters are inferred, including the effective radius of the aerosol size distribution.

3.4.3.2 MODIS c004 over land

Land surfaces do not provide the same uniform surface signal as the ocean. Land surfaces are much more variable in their reflectance properties and therefore the algorithm must include additional steps to estimate the land surface contribution to

the satellite -observed signal. If the surface is well behaved (i.e., it is either completely dark or its reflectance can be accurately modeled or assumed), the atmospheric signal may be sufficiently decoupled from the combined surface/atmosphere signal.

The aerosol retrieval over land uses spectral reflectance in four of the channels listed in Table 3.1, specifically the 0.66, 0.86, 0.47 and 2.12 μm channels. In cloud-free regions, these bands are sensitive primarily to molecular, aerosol and surface scattering. Preliminary steps of the retrieval include testing the spectral observations to screen the 10 km box for clouds [*Martins et al.*, 2002; *Gao et al.*, 2002], snow and ice [*Li et al.*, 2005], and sub-pixel water bodies such as ponds or swamps [*Remer et al.*, 2005]. The pixels that remain are sorted by their relative reflectance (at 0.66 μm), such that the 20% of the darkest pixels and 50% of the brightest pixels are removed. The remaining pixels are expected to represent dark surface targets with the least amount of contamination from clouds (including cloud shadowing) as well as surface inhomogenities. This means that at most, 120 pixels remain from the original 400.

The retrieval can proceed if least 12 pixels (10%; 5% of original 400 for sufficient SNR) remain. These remaining pixels are averaged, yielding one set of spectral (0.47, 0.66 and 2.12 μm) reflectance values that are used to the retrieve 10 km products. The first key assumption is that surface reflectance in the visible channels (0.47 and 0.66 μm) are each fixed ratios of the surface reflectance at 2.12 μm [*Kaufman et al.*, 1997a; *Remer et al.*, 2005], which are denoted here as the ‘VISvs2.12’ ratios. Specifically, the c004 VISvs2.12 ratios are assumed as 0.25 for 0.47vs2.12 and 0.50 for 0.66vs2.12. These empirically derived relationships

[Kaufman and Remer, 1994] represent the relationship of liquid water absorption and chlorophyll reflectance in healthy vegetation [Kaufman *et al.*, 2002], meaning that they are expected to be valid only in vegetated and semi-vegetated regions.

Even in conditions of large numbers of coarse aerosols (such as in dust-dominated regions), aerosols are assumed to be transparent to radiation at 2.12 μm [Kaufman *et al.*, 1997a]. This means that the surface reflectance in the visible channels can be calculated from the observed reflectance at 2.12 μm , via the VISvs2.12 ratios. Therefore, any difference between the satellite reflectance (observed) and visible surface reflectance (estimated via the ratios) is due to the radiative impacts of the impeding atmosphere (including the aerosol).

According to Remer *et al.* [2005], the c004 LUT contains simulations for five aerosol types (known as ‘Continental’, ‘Urban/Industrial’, ‘Moderate Smoke/Developing World’, ‘Absorbing Smoke’, and ‘Dust’) at 2304 angle combinations, six τ loadings (plus $\tau = 0$; molecular conditions), and for two channels (the 0.47 and 0.66 μm channels). The c004 LUT was simulated with scalar radiative transfer (RT) code, meaning that any polarization effects on the reflectance were neglected.

The procedure begins by performing linear interpolation upon the LUT, so that the LUT represents the exact geometry of the MODIS observation. The algorithm selects the ‘Continental’ model [Lenoble and Brogniez, 1984] to derive an initial estimate of the spectral τ . τ is retrieved in the two visible channels (0.47 and 0.66 μm) independently, such that the difference to the observed reflectance (the fitting error, ϵ) is minimized. From the spectral dependence of τ , the two channel

Ångstrom exponent (α) is calculated, which in turn is used to derive the relative contribution of fine aerosol to the total τ (η) [Chu *et al.* 2002].

The algorithm then modifies its initial estimate of spectral τ . It selects the appropriate fine-dominated aerosol type (choice of the ‘Urban/Industrial’, ‘Moderate Smoke/Developing World’ or ‘Absorbing Smoke’) characteristic of the region and season being observed [Remer *et al.*, 2005]. The choice of aerosol type is mixed with ‘Dust’ using the previously derived fraction η . Again τ is retrieved independently for the two visible channels (based on minimum ϵ). This revised retrieval of spectral τ is known as the ‘Corrected Optical Depth.’ If the surface is elevated (e.g., a mountain), the ‘Corrected Optical Depth’ is further corrected by adding (in the 0.47 μm channel only), the difference in Rayleigh optical depth between the elevated surface and a sea level surface. The final products of the over land algorithm include the spectral τ (at 0.47, 0.66 and interpolated to 0.55 μm), as well as the Fine Weighting (the fine fraction), η . Again, it is noted the difference in land and ocean η definitions; while over ocean η refers to *fine mode* weighting, over land it refers to *fine model* weighting or non-dust weighting.

There are additional details of pixel selection and dark target criteria not described here, but the reader is referred to Remer *et al.*, [2005] and MAST, [2006] for more discussion.

3.5: Summary

Aerosols are complicated and require a variety of measurement techniques from different platforms (surface, airborne and satellite) to fully characterize them.

Measurements of mass and optical properties can be made *in situ* with high temporal resolution, but are only representative of aerosol properties at that site. In addition, many *in situ* measurements must collect the aerosol onto a filter or into a cavity, thus modifying the aerosol characteristics. Since the USEPA regulates dry aerosol concentrations, the aerosols must be dried, thus further distancing from ambient aerosol conditions. Remote sensing techniques do not modify the physical characteristics of the aerosol, thus they have the advantage that they observe ambient aerosol conditions. However, passive remote sensing products represent aerosol properties integrated over a distance (e.g., the atmospheric column), so that they may not represent the portion of aerosol (say near the surface) that effects human health and is regulated by the USEPA.

Passive remote sensing techniques, however, should and do make use of *in situ* measurements and active remote sensing (e.g., Lidars) to constrain their algorithms and understand their results. Retrieval algorithms from measurements of reflected sky radiance (sunphotometer) and reflected light to space (satellites) use the physical understanding brought by other datasets to relate the aerosol's optical properties with the physical characteristics that affect our lives on earth's surface.

Chapter 4: Evaluation of MODIS c004 products

Evaluation of a satellite (or any) dataset refers to the exercise of understanding the quality of the data under all measurement conditions. Validation implies quantitative assessment of the measurement uncertainty. The validation process asks questions about the precision, accuracy and consistency of the derived data products. This dissertation focuses on consistency (Do the products represent physical quantities with no artificial boundaries?), precision (Do the products represent small enough increments of physical quantities?) and accuracy (Can the products be matched with reference standards?).

The total aerosol optical depth (τ) is a physical quantity, resulting from the interaction of a particular wavelength of radiation with a particular composition and amount of aerosol within the atmospheric column. All remote sensing techniques are essentially attempting to measure the same defined physical quantity. If one assumes that sunphotometry provides the most simple and direct measurement of this quantity, then satellite derivations of τ should be directly compared to them.

The fine weighting (FW or η) is defined differently by AERONET and by each MODIS algorithm. By the technique of AERONET *almucantur* (Version 1) inversions [Dubovik and King, 2000], η is a ‘volume fine weighting’ or fraction of the total volume (size) distribution contributed by fine aerosol (defined as all aerosol of radius, $r < 0.6 \mu\text{m}$). By the technique of spectral deconvolution of AERONET sun measurements [O’Neill *et al.*, 2003], η is the ‘ τ fine weighting’, or the fraction of total τ resulting from the fine mode (assuming one fine mode and one coarse mode,

both log-normal). This η can be defined at any visible wavelength, but $0.55 \mu\text{m}$ is chosen to be consistent with MODIS. MODIS over land defines η to be a ‘ τ fine model weighting’, or the fraction of τ contributed by fine-dominated *model*, where the model is comprised of multiple lognormal modes (for example, fraction of urban/industrial aerosol to the total aerosol, or non-dust fraction). Finally, the MODIS over ocean algorithm defines η to be a true ‘ τ fine mode weighting’, the fraction of the total optical depth contributed by the fine (lognormal) *mode*. While the definitions of η vary across products, the physical meaning of η is similar enough that it is reasonable to compare them directly.

Unlike comparisons of MODIS and AERONET -derived τ (which is the same physical quantity) and η , (different definitions but should be correlated), comparisons of remotely sensed products with most other aerosol measurements are not usually as straightforward. For example, much recent research has focused on using MODIS - derived τ products to monitor surface concentrations of dry $\text{PM}_{2.5}$ mass concentration $\{\text{PM}_{2.5}\}$, which are two completely different physical quantities. Yet, since there are situations in which they should be comparable (when the bulk of the aerosol column is located in the boundary layer near the surface), and much can be gained by exploiting this relationship, regulatory agencies (e.g., the USEPA) are developing the tools to use satellite -derived τ (including MODIS) for $\text{PM}_{2.5}$ monitoring and forecasting.

4.1: Global validation of c004 products; comparison to AERONET

Remer et al. [2005] attempted to validate the c004 spectral τ products on global and regional scales, over both ocean and land. They showed that the MODIS yielded physically reasonable values in a variety of conditions, and that there was sufficient sensitivity to differentiate relative aerosol load. The bulk of their validation study was comparison with reference ground based sunphotometers (AERONET) at over a hundred global sites. Specifically, they applied the spatial-temporal technique of *Ichoku et al.* [2002a], such that the average of a 50 km x 50 km area of MODIS products centered at the AERONET site (a 5 x 5 box = 25 retrievals at 10 km) was compared to the average of the AERONET direct-sun measurements within one hour of satellite overpass (normally four or five measurements). Fig. 4.1 illustrates the validation process. Requiring cloud-free conditions (MODIS must retrieve at least 5 pixels out of 25 and AERONET must retrieve at least twice during the hour) and quality assured data (MODIS QA=3, cloud screened AERONET L15), *Remer et al.* [2005] demonstrated that MODIS retrieves τ to within the expected uncertainty over land (Eq. 1.1). Over ocean, they found that MODIS performed to within more stringent expected errors, except in dust regions (as shown by *Levy et al.*, [2003]).

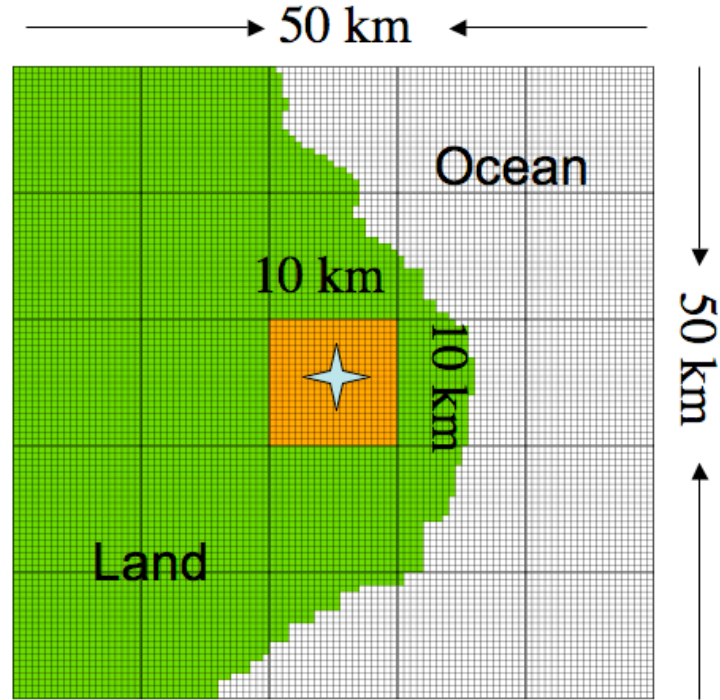


Fig. 4.1: Illustration of Ichoku *et al.*, [2002a] spatial/temporal validation technique over a coastal AERONET site (star). The orange box is the 10 km x 10 km MODIS retrieval containing the site. Since both MODIS over-land and over-ocean retrievals are performed in this case, both are averaged over the 50 km x 50 km domain, and will be compared with the AERONET measurements. Any 10 km MODIS retrieval containing land is derived as land, whereas 100% water is necessary for deriving as ocean. The tiny boxes represent the 20 x 20 original 500 m MODIS pixels within each 10 km. The time domain for AERONET is one hour (± 30 minutes of overpass)

While MODIS over-land retrievals generally compared to AERONET within pre-launch expectations, *Remer et al.*, [2005] found that MODIS tended to overestimate τ for low aerosol loadings, and underestimate for high loadings (that is, Eq. 1.2). Over ocean, they found no such consistent bias (except in conditions of dust aerosol).

Global, long term scatterplots are informative, but they may hide systematic errors pertaining to certain regions. *Remer et al.*, [2005] separated the global

scatterplot into a number of large regions, presumably each region representing a given aerosol regime. The algorithm performed in similar fashion in most regions, some better, some worse. Some of the poorest MODIS/AERONET comparisons were over the land along the East Coast of the United States, where less than 60% of the retrievals fell within expected error bars over land (between 2000 and 2002). Retrievals over the nearby ocean were much closer, falling within the more stringent over ocean error bars.

Kleidman et al. [2005] evaluated the MODIS fine weighting (η) products (over ocean) in context of those retrieved from AERONET data. Generally, they found that aerosol product over ocean has higher values (by about 0.2) than those estimated by AERONET. *Anderson et al.*, [2006] evaluated the retrievals of η over land and ocean separately, in the vicinity of Japan, by comparing to *in situ* profiles (from nephelometers, PSAPs and AATS) of spectral dependence (e.g., Ångström exponent, α) and sub-micrometer fraction (SMF) of τ . The MODIS ocean retrievals were systematically higher than SMF by about 0.2, suggesting that *in situ* measurements indicate a systematically different relationship between fine fraction and α than what is assumed from satellite. Over land, *Anderson et al.*, [2006] found very little significance to MODIS reported η values.

4.2: Evaluation of c004 over the U.S. East Coast during CLAMS

Based on *Remer et al.* [2005], the MODIS -derived τ products over land were not as accurate as expected, globally, and over the eastern United States. The Chesapeake Lighthouse Aircraft Measurements for Satellites (CLAMS) field

experiment offered an opportunity to evaluate some of the uncertainties of the MODIS retrievals.

CLAMS took place from July 10 to August 2, 2001, in a combined ocean/land region that included the Chesapeake Lighthouse (COVE) and the Wallops Flight Facility (WFF), both along coastal Virginia [*Smith Jr. et al.*, 2005]. This experiment was designed mainly for validating instruments and algorithms aboard Terra, including MODIS. Held in July and August 2001, it was expected that CLAMS would showcase the heavy aerosol loadings common to the U.S. East Coast during the summer.

I was deployed at CLAMS, along with other members of the MAST. One of our objectives was to set up a network of handheld Microtops [*Morys et al.*, 2001; *Ichoku et al.*, 2002b] sunphotometers, that measure spectral τ in conjunction with baseline AERONET instruments located at Wallops and COVE, two independent robotic instruments [*Ehsani et al.*, 1998] at NASA's Langley Research Center (LaRC), and the Ames Airborne Tracking 14 Channel Sunphotometer (AATS-14; [*Redemann et al.*, 2005]). This network was designed primarily to test spatial variability of aerosol properties, but also to evaluate the performance of longer wavelength (1.6 and 2.1 μm) sunphotometers (AATS-14 and Microtops) over ocean. All sun-photometers used in this study were pre- and/or post- calibrated, and were expected to measure optical depths with accuracy of ± 0.03 or better [*Holben et al.*, 1998; *Ichoku et al.*, 2002b; *Russell et al.*, 1993; *Ehsani et al.*, 1998]. Thus, I chose to consider all sunphotometer measurements as one large dataset.

Over the ocean, MODIS retrieved τ at seven wavelengths and an estimate of the aerosol size. Over the land, MODIS retrieved τ at three wavelengths, plus very qualitative estimates of the aerosol size. As most CLAMS sunphotometer data were obtained near the coastline, in many cases there were both ocean and land retrievals from MODIS that could be separately compared with sunphotometer. This experiment was productive for the MAST, resulting in numerous papers within the CLAMS ‘special section’ published in the *Journal of Atmospheric Sciences*, including my paper [Levy *et al.*, 2005].

4.2.1 Comparison of MODIS-derived τ with sunphotometer

As most CLAMS sunphotometer data were obtained near the coastline, in many cases there were both ocean and land retrievals from MODIS to be compared with sunphotometer measurements. Over the nearby ocean, MODIS -derived τ (at 0.55 μm) correlated well with sun-photometer measurements, such that nearly 86% of the ocean points lay within ocean expected error bars, with correlation coefficients $R > 0.9$ and nearly one-to-one fit. Over land, however, the correlation is weak, and a majority of MODIS retrievals are outside the expected error (Eq. 1.1). Like the global results seen by Remer *et al.*, [2005], MODIS over-estimates τ for low aerosol loadings and under-estimates for higher τ . At 0.55 μm , the linear least square regression was $y=0.64x + 0.21$, with correlation coefficient, $R=0.6$ (e.g., Fig. 1.2).

Fig. (4.2) shows a case where there is pronounced discontinuity of the MODIS-derived τ . Even though MODIS algorithm does not require or even expect τ to match at the coastline, the extreme discontinuity suggests a problem with either over-land or over-ocean algorithms. Fig. 4.3 shows τ comparisons for AERONET sites during

CLAMS, both over ocean and over land. The black symbols represent ocean and land separately, whereas the red shapes display τ in cases that MODIS retrieved both ocean and land. AERONET sites along the coastline were better represented by the ocean retrieval. In all cases, the retrieved land values were much larger (often more than double) the ocean values. I focused on determining the cause of the poor over-land retrievals.

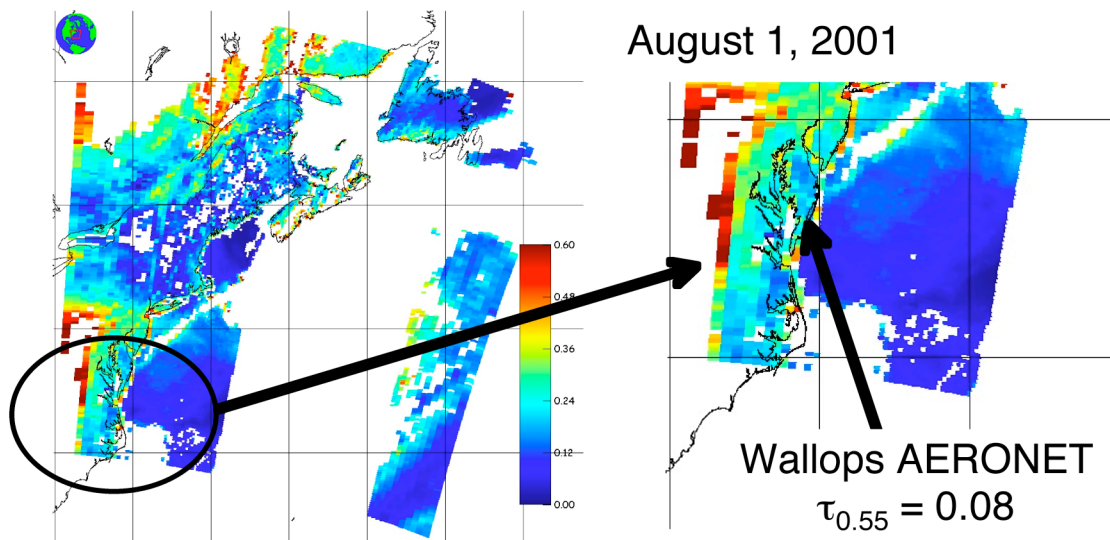


Fig. 4.2: Illustration (and blowup) of discontinuity between MODIS over-land and over-ocean $\tau_{0.55}$ retrievals for 1 August 2001 (CLAMS). The AERONET value at Wallops ($\tau_{0.55} = 0.08$) is placed for comparison. Figure adapted from Levy *et al.*, [2005].

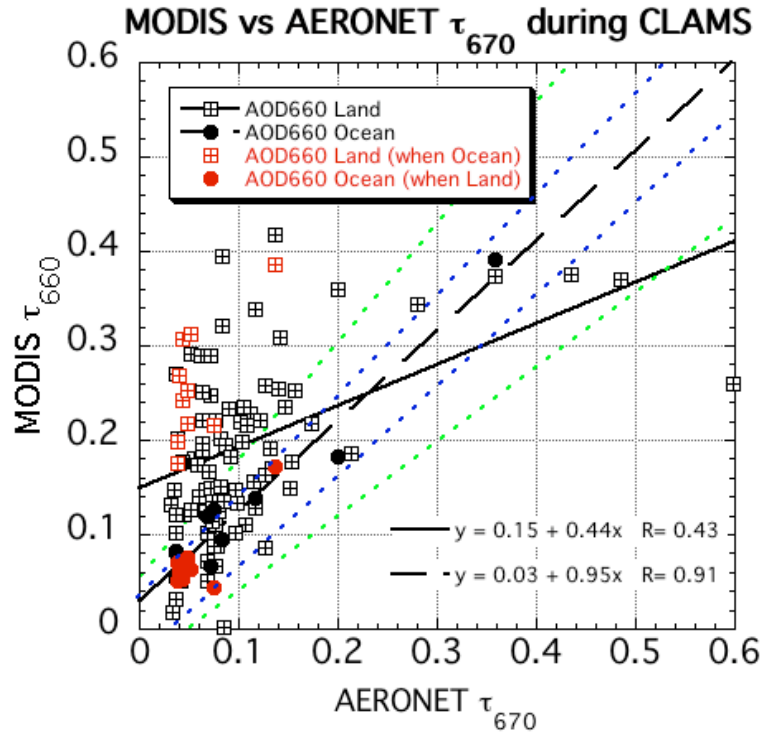


Fig. 4.3: Comparison of MODIS over-land and over-ocean retrieved τ (at 0.66 μm) with AERONET (only). The open squares are for over-land, where the closed dots are for over-ocean. Black shapes denote land and ocean retrievals independent of whether the other is performed. Their regression lines are given. Red shapes represent cases when both land and ocean retrievals were performed for a site. Land and ocean expected errors are the green and blue dashed lines, respectively. (Figure adapted from *Levy et al.* [2005].

4.2.2 Comparison of MODIS-derived η with sunphotometer

As noted above, the fine weighting (FW or η) is defined differently for different retrieval techniques. Nonetheless, I evaluated the retrievals by comparing the size distributions implied by η and the choice of aerosol models (or modes) from MODIS to those retrieved by AERONET. These results were included in *Levy et al.*, [2005].

The MODIS over ocean algorithm retrieves between two and three pieces of information [*Tanré et al.*, 1996]. This information includes the total τ , the choice of

fine and coarse modes, and the relative weighting of the two modes η . Of the three products, only τ is expected to be accurate. In combination, the other two products should correctly portray the observed reflectance, but may not each be individually accurate. However, one can infer a relative aerosol size distribution that created these products and simulates the spectral reflectance. While these ‘optically equivalent’ modes have no direct conversion to size distribution units (such as $\mu\text{m}^3/\mu\text{m}^2$), they can be normalized to yield understanding of the relative maxima and standard deviations of the bi-modal size distribution.

The MODIS over land algorithm retrieves τ and the relative weighting η of dust and non-dust (urban/industrial in the U.S. mid-Atlantic). While each multi-modal aerosol model has physical size distribution units, the total retrieved size distribution can also be normalized to understand the relative maxima and standard deviations.

Finally, for this experiment, I chose to compare the normalized ocean size distributions against the size distributions retrieved by inverted AERONET *almucanturs*. Again, even though the AERONET size distributions represent physical (with units) size distributions, they can be normalized as well. By assuming that all three techniques observed similar aerosol conditions, I compared relative mean radius and radius standard deviations from all three techniques.

Using results from spatio-temporal MODIS/AERONET matches [*Ichoku et al.*, 2002a], I derived a relative aerosol size distribution that represented 50 km x 50 km boxes over AERONET sites. Averaging across all matches, I obtained the MODIS-derived unitless aerosol size distribution from CLAMS. Fig 4.4a visually shows CLAMS averaged aerosol size distributions independently retrieved by the over-

ocean (blue curve) and over-land (green curve) algorithms from MODIS, and from AERONET almucantur radiance inversions (red curve). The size distributions show significant differences. Although all three have fine mode peaks at approximately $0.15 \mu\text{m}$, the AERONET fine mode peak has much smaller width or standard deviation. The contribution to the total volume is larger for ocean than for land near the inflection point (fine/coarse mode split at $0.6 \mu\text{m}$), but smaller as the radius increases over $1 \mu\text{m}$. Because the AERONET retrievals are split into fine and coarse mode at a radius of $0.6 \mu\text{m}$, radii bins near $0.6 \mu\text{m}$ are not well represented.

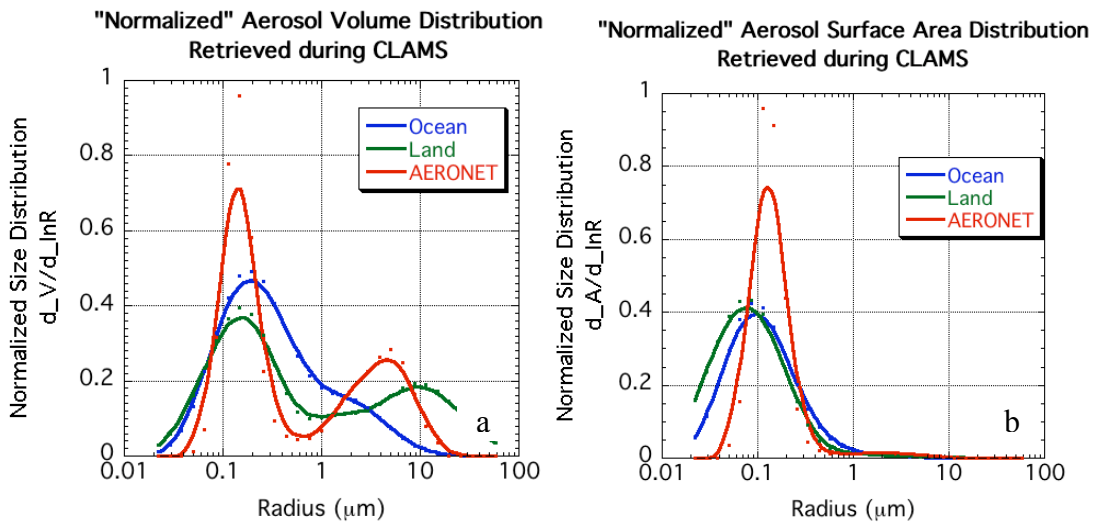


Fig. 4.4: CLAMS-averaged ‘equal total volume’ aerosol volume distribution (a) and ‘equal total area’ aerosol area distribution (b) from MODIS over ocean and land separately, and from AERONET inversions. Figure from *Levy et al.*, [2005].

The scattering effects of aerosols are best explained by estimating surface area distributions. Fig. 4.4b is analogous to Fig. 4.4a, but plots surface area distribution, such that each area distribution curve encloses the same total aerosol unitless surface area. For CLAMS, the aerosol fine mode clearly dominated the area size distribution,

presumably dominating aerosol scattering. There is, however, a small contribution from the coarse mode (just above 0.6 μm), especially as retrieved by the ocean retrieval.

One way to compare the size distributions is to compute the modal radius r_v , standard deviation of the modal radius σ , and the effective radius r_{eff} . We used the strategy prescribed by AERONET (splitting at 0.6 μm) to define fine and coarse mode. Table 4.1 shows the results of calculating average CLAMS effective radii, modal radii and standard deviation. The AERONET and the MODIS over-ocean algorithm's fine mode effective radii are similar, while the MODIS over-land algorithm represents smaller values. On the other hand, the over land's coarse mode effective radius agrees better with AERONET. For the total effective radius, all three values are close, with the land and ocean retrievals are nearly identical. AERONET retrieves slightly larger total effective radius. The largest differences are in the fine mode standard deviation, σ_f .

Table 4.1: CLAMS-averaged total, coarse mode and fine mode modal radius, standard deviation σ , and effective radius r_{eff} calculated from MODIS over ocean, over land and by AERONET.

PARAMETER / MODE	$r_v(\mu\text{m})$	σ	r_{eff}
Ocean algorithm			
Fine	0.178	0.718	0.136
Coarse	1.870	0.724	1.498
Total	0.327	1.258	0.178
Land algorithm			
Fine	0.143	0.746	0.108
Coarse	6.166	1.137	3.334
Total	0.708	2.081	0.183
AERONET			
Fine	0.149	0.410	0.138
Coarse	3.657	0.696	2.849
Total	0.493	1.638	0.214

4.3: Summary

The MODIS aerosol algorithm was formulated well before the launch of the first MODIS sensor (aboard Terra) in December of 1999. It is actually composed of two separate algorithms (over land and over ocean) that have been updated since launch. The c004 land algorithm has deficiencies globally and regionally that were noted within this chapter.

Chapter 5: Strategies for improving aerosol retrieval over land

Globally, regionally, and specifically for CLAMS, the MODIS c004 / sun-photometer τ regression equations over land showed significant positive offsets and slopes less than one. The y-offset (MODIS retrieves τ when in fact there is none) implies errors induced by assuming inappropriate surface reflectance. On the other hand, the less than one slope implies errors in the aerosol models. For Levy *et al.*, [2005], I used CLAMS data to address each of these problems and introduced possible solutions. In a previous work [Levy *et al.*, 2004], I had shown that the simplified scalar RT code used to derive the c004 LUT neglected effects of atmospheric polarization and could lead to retrieval errors. This Chapter summarizes some of the main reasons that the over-land algorithm may be performing poorly, and strategies for correcting the problems.

5.1: New aerosol models for improving the slope

Ichoku et al., [2003] showed that c003 MODIS retrieval errors for smoke over Southern Africa could be significantly reduced by decreasing the assumed single scattering albedo (ω_0) from ~ 0.90 to ~ 0.85 . This ‘absorbing’ model was added for c004 and improved MODIS retrievals in Africa. However, fixing single scattering albedo is not the correct strategy in all parts of the world. For example, the assumed ω_0 (~ 0.96) for the c004 urban/industrial model of *Remer and Kaufman* [1998] is

appropriate over the U.S. mid-Atlantic [*Vant-Hull et al.*, 2005; *Taubman et al.*, 2004]. Therefore, for this region (and others), a different strategy must be prescribed.

The c004 dynamical urban/industrial aerosol model [RK-model; *Remer and Kaufman*, 1998] was derived from data collected from 5 AERONET sites along the U.S. East Coast, during the Sulfates Clouds and Radiation – Atlantic (SCAR-A) experiment of summer 1993. After cloud screening and almucantur symmetry determination, the method of *Nakajima et al.*, [1996] was used to retrieve aerosol size volume distributions from 125 sky radiance measurements. *Remer and Kaufman* [1998] noted that aerosol size depended on τ , such that τ explained 60% of the variance in the shift (growth) of the aerosol modes and the total volume distribution. This τ dependence was denoted as a ‘dynamic’ property of urban/industrial aerosol.

Using eight years of AERONET data obtained at the GSFC site, *Dubovik et al.*, [2002a] developed a similar dynamic urban/industrial aerosol model based on *Dubovik and King’s* [2000] almucantur inversion technique. Like the RK-model, this so-called ‘D-model’ [*Levy et al.*, 2005], describes a size distribution that depends on τ . Unlike the RK-model, a tri-modal distribution, the D-model is modeled as a combination of two lognormal distributions. Particles with radius less than 0.6 μm belong to the fine mode and larger than 0.6 μm belong to the coarse mode.

Figs. 5.1a and 5.1b show size distributions (plotted as a function of τ at 0.44 μm , [*Dubovik et al.*, 2002a]) of the RK-model and D-model, respectively. There are substantial differences between the two models. The fine mode for the D-model has a peak at a slightly smaller radius, with narrower curvature (smaller σ). The RK-model’s coarse mode (centered around 9 μm) lack of τ dependence looks unphysical

compared to direct observations, but the D-model seems more realistic and better defined. The refractive indices (m) differ as well. The RK-model uses $m = 1.43 + 0.0035i$ for the accumulation modes, $1.43 + 0.0i$ for the marine (salt) mode, and $1.53 + 0.008i$ for the coarse (dust) mode. For both fine and coarse modes, the D-model's refractive index is a function of τ , i.e., $m = 1.41 - 0.03\tau_{0.44} + 0.003i$, where $\tau_{0.44}$ is the τ at $0.44 \mu\text{m}$. For the τ ranges displayed in Fig. 5.1, this means the real part m_r ranges between about 1.41 and 1.38, which is closer to that of water ($m_r=1.33$) than used for the RK-model.

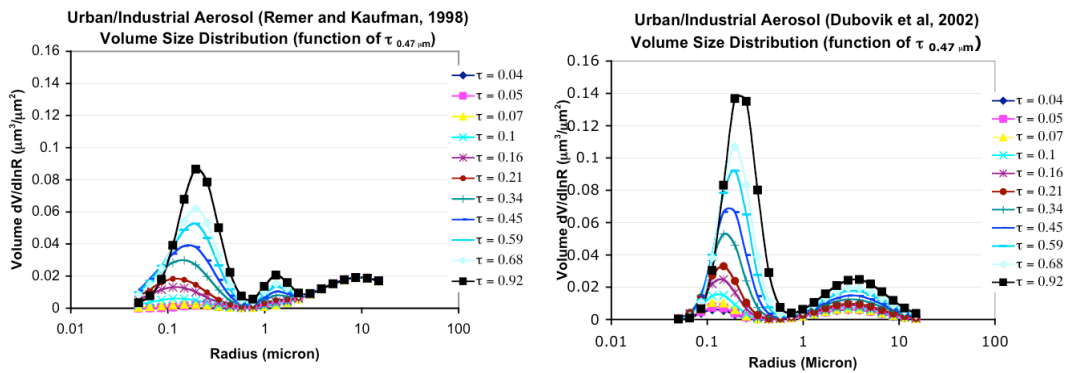


Fig. 5.1: Volume size distributions for the dynamic urban/industrial models of Remer and Kaufman [1998] ('RK-model') and Dubovik *et al.*, [2002a] ('D-model'). Curves are monotonically increasing functions of τ at $0.44 \mu\text{m}$. The $0.44 \mu\text{m}$ channel was selected to be consistent with the AERONET derivations. Figure reproduced from Levy *et al.*, [2005].

For Levy *et al.*, [2005], I attempted to correct the less-than-one slope, by replacing the RK-model by the D-model. I created two lookup tables, one for each aerosol model. Using a single value of solar/surface/satellite geometry and spectral surface reflectance for both tables, I used the Second Simulation of the Satellite Signal in the Solar Spectrum (6S) radiative transfer code [Vermote *et al.*, 1997b] to

simulate apparent (satellite) reflectance as a function of τ . Fig. 5.2 (from *Levy et al.*, [2005]) plots apparent reflectance in three MODIS wavelengths (0.47, 0.66 and 2.1 μm) for an example of solar/surface/satellite geometry, observed during CLAMS. Empirical conversion from one aerosol model to another is also illustrated in Fig. 5.2. A line of constant apparent reflectance ($\rho = 0.16$ in the example), describes different values of τ for the two models. In this example, τ of 0.5 for the RK-model is equivalent to 0.7 for the D-model. In essence, updating the assumed aerosol model increases the MODIS-derived τ .

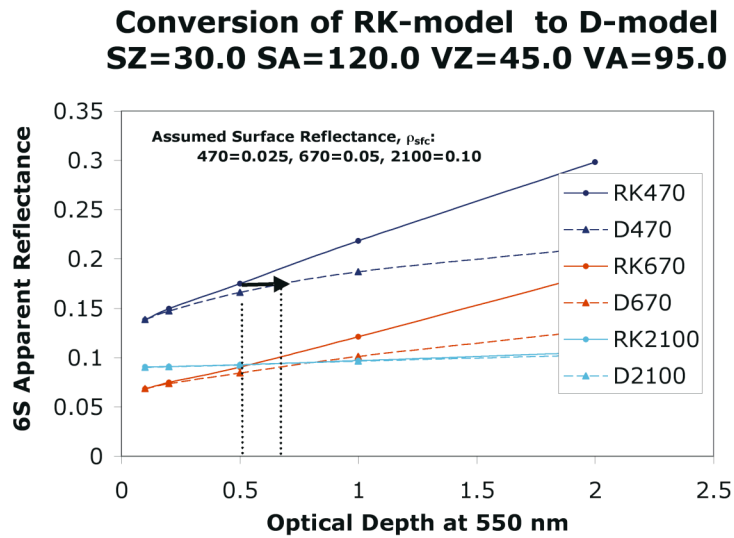


Fig. 5.2: Conversion from the RK-model to the D-model. Apparent (satellite) reflectance has been calculated using 6S code. Black arrow shows conversion for a given apparent reflectance. SZ is the solar zenith angle, SA is the solar azimuth angle, VZ is the satellite view zenith angle and VA is the satellite view azimuth angle, all in degrees. Figure reproduced from *Levy et al.*, [2005].

Fig. 5.3 demonstrates how updating to the D-model could apply to the entire CLAMS dataset. The red (at 0.66 μm) and blue (0.47 μm) solid lines are of the regression fitted by CLAMS c004 data. Assuming that all geometry behaves like the

example of Fig. 5.2, conversion from the RK-model to the D-model results in the red and blue dashed lines. The slopes for the dashed lines are increased (from 0.76 to 1.23 in the blue and from 0.46 to 0.58 in the red). While not plotted, the slope of 0.55 μm would increase from 0.64 to something much closer to one. Note that the offsets are unchanged, due to the same reflectance for both models at zero τ . This suggests that the D-model is better than the RK-model for CLAMS. Note however, that the assumption of a single set of geometrical conditions to represent all CLAMS' geometries is questionable, and inclusion of angle dependence would have changed the plot. This exercise, nonetheless, demonstrated that the retrieval technique is sensitive to the assumed aerosol models, and that updating the aerosol models (in other regions) may improve the MODIS products. It also suggested that AERONET derived products could be used to better constrain the MODIS retrieval algorithm. Other efforts (e.g [Jeong *et al.*, 2005]) performed similar types of empirical model 'correction', but primarily over ocean.

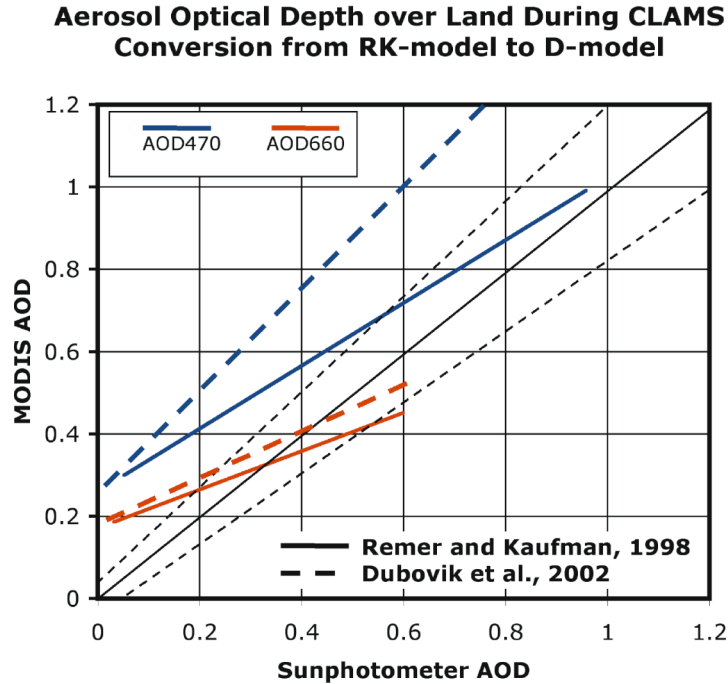


Fig. 5.3: Empirically corrected τ (AOD) over land. Solid red and blue lines are the regression lines from Fig. 1.2. The red and blue dashed lines are the corrected optical depths. The black lines are the expected errors plotted in Fig. 1.2. Figure reproduced from *Levy et al.*, [2005].

5.2: Surface reflectance correction for improving the y-offset

Both measurements [*Kaufman and Remer*, 1994; *Kaufman et al.*, 1997c] and theoretical studies [*Kaufman et al.*, 2002]) demonstrated a relationship between visible and IR surface reflectance ρ_λ , for certain vegetated surfaces throughout the globe. These are known as the c004 VISvs2.12 surface ratios, and were assumed to be 0.25 for 0.47 μm vs 2.12 μm (0.47vs2.12) and 0.5 for 0.66 μm vs 2.12 μm (0.66vs2.12), and assumed globally for the operational MODIS retrieval over land [*Kaufman et al.*, 1997a].

Yet it is known that these ratios vary over vegetation types and exact viewing geometry. Remer *et al.* [2001] measured surface reflectance aboard a low flying aircraft, and found that the VISvs2.12 relationship depends on geometry. Generally, the 0.66vs2.12 ratio was less than 0.5 for backscattering view angles, and greater than 0.5 for forward scattering. They also found seasonal differences that were weakly correlated with changes in the degree of vegetation ('greenness') of the surface (such as might be associated with the Normalized Differential Vegetation Index (NDVI; e.g., Tucker, [1979])). The blue channel (0.47 μm) exhibited even greater deviations from assumed ratios when viewed from the aircraft. Also from aircraft, Gatebe *et al.*, [2001] demonstrated a bi-directional reflectance function (BRF) to the surface reflectance relationships.

The landscape along the U.S. East Coast is heterogeneous, containing urban areas, forests, and grassy/agricultural fields. Due to ample rainfall and proximity to the ocean, small land water bodies (such as puddles or swamps) are also ubiquitous and may be underneath the tree canopy. While the MODIS over land algorithm attempts to mask even the most shallow water bodies, puddles and swamps are not always completely masked out. Because water is nearly black (near zero reflectance) at 2.12 μm , assuming the standard VISvs2.12 ratios would result in over-estimating the aerosol path reflectance, contributing to the y-offsets. Indeed, some of the very high VIS/IR points (outliers) displayed in Remer *et al.* [2001] were measured over swamps or puddles in forests.

5.2.1 Atmospheric correction of CLAMS data

What was the actual spectral surface reflectance relationship over the U.S. mid-Atlantic during CLAMS or over another region at a different time period? One strategy is to assume that clean aerosol conditions lead to surface reflectance retrievals with small atmospheric contamination. Operational algorithms for determining MODIS surface albedo properties employ this strategy - by searching for the cleanest cases in eight or sixteen-day periods, and assuming appropriately low τ . However, instead of using assumptions of spectral τ , co-located sunphotometers can provide exact values.

Atmospheric correction [Kaufman and Sendra, 1998; Kaufman, 1999] is the process of determining the surface reflectance that would be measured if there were no atmosphere [Kaufman et al., 1997b]. Vermote et al., [1997a] describes how the atmospheric correction could be applied to estimate land surface properties from a satellite. Using the MODIS spectral reflectance data as the primary input, the satellite reflectance can be corrected for Rayleigh scattering, aerosol scattering, and coupling between the atmospheric and surface reflectance functions. The 6S RT code includes a module for performing atmospheric correction with MODIS data [Vermote et al., 1997b], which includes trace gas and ozone assumptions.

I performed atmospheric correction on some CLAMS data to determine whether the global c004 VISvs2.12 ratios were appropriate [Levy et al., 2005]. On August 1, the AERONET instruments at both Wallops and Oyster reported very clean ($\tau \sim 0.08$ at $0.55 \mu\text{m}$) and dry ($\text{PW} \sim 2.4 \text{ cm}$) conditions. Assuming the U.S. standard mid-latitude profile [1976] for temperature, ozone gas climatology, and near zero τ at $2.1 \mu\text{m}$, 6S was used to perform atmospheric correction on Level 1B (reflectance)

MODIS reflectance data over the CLAMS area (small box in Fig. 5.4a). Figs. 5.4b,c and d show the resulting atmospherically corrected surface reflectance at 0.47, 0.66 and 2.12 μm respectively, on a 500 m resolution. Figs 5.4e and 5.4f show the resulting 0.47vs2.12 and 0.66vs2.12 reflectance ratios over the same region. Note the bright clouds (that would be masked by the MODIS algorithm) in Fig. 5.4a that carry over to Fig. 5.4b-d as high reflectance and to Figs. 5.4e and 5.4f as high ratios. Over much of the grassy and open agricultural regions (central peninsula), the VISvs2.12 ratios are generally lower than assumed, about 0.13 and 0.45, for 0.47vs2.12 and 0.66vs2.12, respectively. Toward the coastline, however, sandy beach shores (bright in the visible) alternate with swampy forests (very dark at 2.12 μm), both would greatly increase the VISvs2.12 ratios, to 0.7 and 0.8, respectively. These ratios, much higher than the assumed values, would introduce significant offsets into retrieved τ .

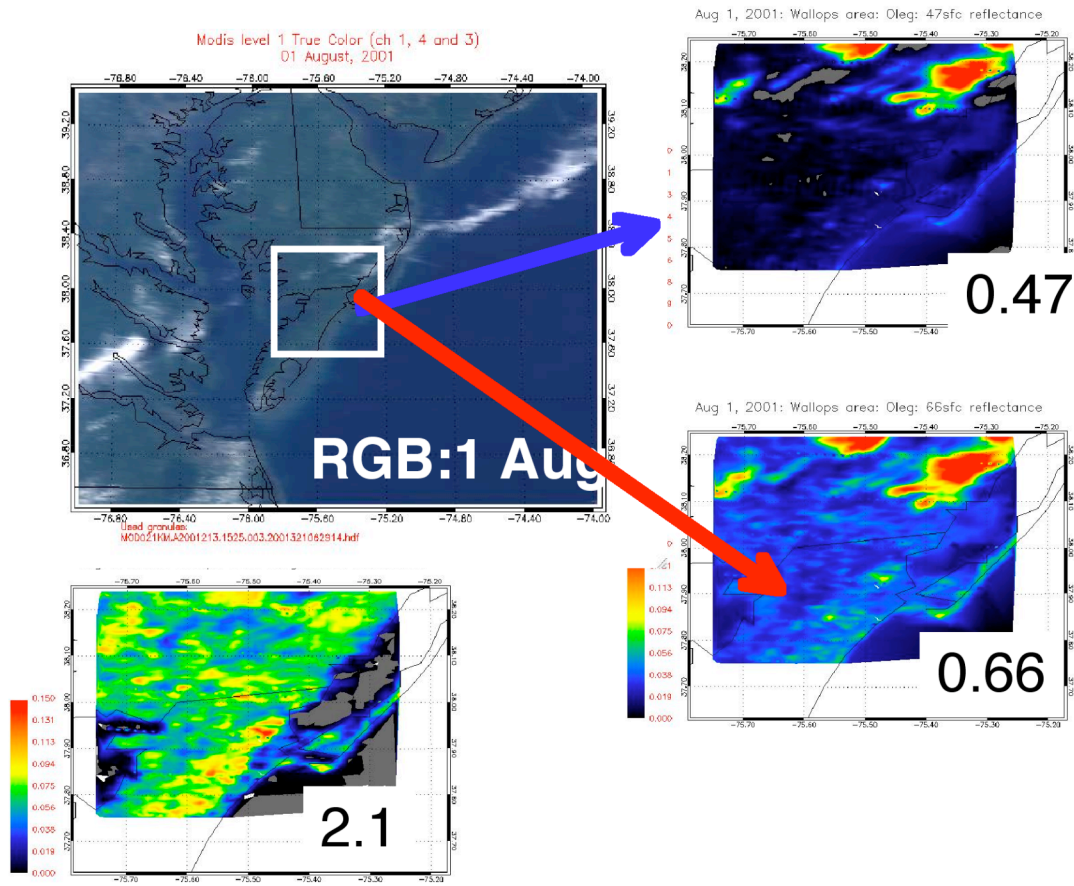


Fig. 5.4: Atmosphericly corrected surface reflectance a) at $0.47\ \mu\text{m}$; b) at $0.66\ \mu\text{m}$; and c) at $2.1\ \mu\text{m}$, for a small portion of the August 1, 2001 granule shown in the RGB image. The clouds have high reflectance in the visible wavelengths, but are not as distinct at $2.12\ \mu\text{m}$. Figure reproduced from *Levy et al., 2005*].

I also performed atmospheric correction on the lower resolution co-located $50 \times 50\ \text{km}$ [*Ichoku et al., 2002a*] MODIS/AERONET data from the clean August 1 case. Even on this much larger scale, the VISvs2.12 ratios were higher than assumed by the retrieval algorithm, about 0.45 and 0.63 for 0.47vs2.12 and 0.66vs2.12 respectively.

5.2.2 Application of CLAMS-derived surface reflectance relationship

Fig. 5.5 displays images of both the operational (c004) retrieval (a) and that retrieved by simply increasing the assumed VISvs2.12 ratios to 0.45 and 0.63, respectively (b). The use of the derived CLAMS ratios removes much of the τ discontinuity over the coastline. Applying the CLAMS ratios to all CLAMS MODIS/AERONET comparisons (where the bulk of the AERONET sites are located near the coastline) cuts the regression y-offset in half. However, Fig. 5.5 also shows that some of the pixels far from the coastline are not retrieved when the CLAMS ratios are applied. Presumably, these increased ratios caused the algorithm to over-correct for the surface and retrieve $\tau < 0.0$ (which is screened as an unphysical value). Thus, from this exercise, it was clear that while a new VISvs2.12 surface reflectance assumption improves the regression of MODIS and AERONET during CLAMS (Fig. 5.6), the CLAMS -derived ratios are not applicable everywhere.

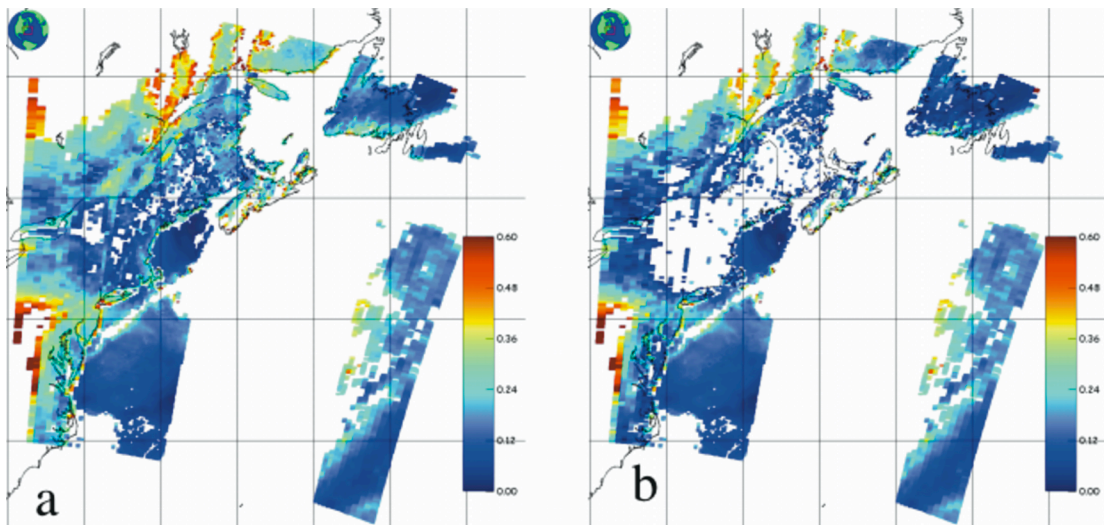


Fig. 5.5: τ at 0.55 μm for the August 1 case retrieved a) using the c004 assumed VISvs2.12 surface reflectance ratios and b) using the CLAMS-derived VISvs2.12 ratios. The discontinuities along the coastline in a) that were mostly removed in b). Note that some of the τ retrievals in New England are now missing.

New Surface Reflectance vs Operational Compared to AERONET

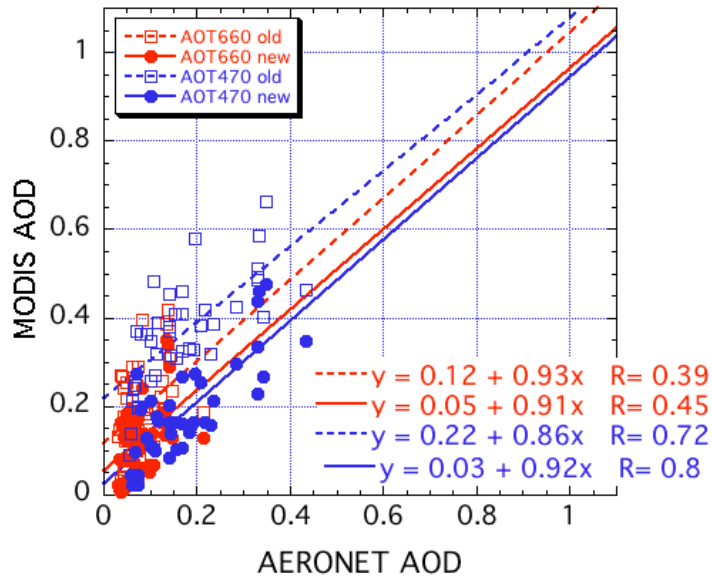


Fig. 5.6: Comparison of τ (at 0.47 and 0.66 μm) retrieved by MODIS-land and by AERONET. The open symbols and dashed lines represent retrievals using the c004 VISvs2.12 surface reflectance ratios, whereas the filled symbols and solid lines represent retrievals using the CLAMS-derived surface reflectance ratios. Figure reproduced from *Levy et al., 2005*].

5.3: Use of vector RT code for simulating polarization effects

As described previously, MODIS uses two separate algorithms to retrieve clear sky (non-cloudy) τ over ocean and land. Both algorithms make use of lookup tables (LUT), wherein TOA spectral reflectance (in %) is simulated by RT calculations. Included within the RT are assumptions about the surface reflectance, molecular scattering and aerosol scattering/absorption (functions of assumed aerosol chemical and size parameters). I suspected that one reason for differences in the performance of retrievals over land versus over ocean had to do with the treatment of atmospheric

polarization within the RT codes used for the LUTs. The over-ocean algorithm employs a vector radiative transfer code [Ahmad *et al.*, 1982] that includes polarization within the atmosphere, whereas the over-land algorithm assumes a scalar RT [Dave, 1970] that neglects this effect. Under conditions of Rayleigh (molecular) optical depth (ROD) greater than 0.1, (characteristic of wavelengths < 0.55 μm) polarization within the atmosphere modifies the TOA radiance by 2% or more [Mishchenko *et al.*, 1994]. At 0.47 μm , the sea-level ROD is nearly 0.2, introducing errors of 4% or more [Fraser *et al.*, 1989]. The addition of at least moderate τ (say 0.2) induces multiple scattering of the Rayleigh induced polarization. While aerosols tend to depolarize radiation (reducing the relative error from neglecting polarization), however, the increased AOT increases the TOA radiance, resulting in larger *absolute* errors in scalar assumed radiance. It is the absolute error in reflectance, not the relative error that introduces error into the retrieval of τ .

To fully describe electromagnetic radiation at the TOA, one must use the Stokes vector, \mathbf{I} , composed of four Stokes parameters,

$$\mathbf{I} = \{I, Q, U, V\}, \quad (5.1)$$

where the scalar I represents the intensity (radiance in units of W/m^2), or reflectance (normalized radiance), and Q , U and V describe the polarization state of the radiation. Incoming sunlight at the TOA is unpolarized, such that $\mathbf{I} = \{I, 0, 0, 0\}$. However, due to interaction with the surface and the atmosphere, reflected light at the TOA generally becomes polarized (Q , U , and/or V are nonzero). The degree of polarization, P , is defined as

$$P = (Q^2 + U^2 + V^2)^{1/2} / I \quad (5.2)$$

This means that radiation with polarization P , can be decomposed into unpolarized and polarized components such that [Liou, 2002; Van de Hulst, 1984]:

$$\mathbf{I} = \mathbf{I}_{\text{Unpol}} + \mathbf{I}_{\text{Pol}} = [I(1-P), 0, 0, 0] + [IP, Q, U, V], \quad (5.3)$$

and that intensity itself is

$$I = I_{\text{Unpol}} + I_{\text{Pol}} = I(1-P) + IP. \quad (5.4)$$

If P is assumed equal to zero, this is known as the *scalar approximation* of RT transfer, and results in estimating I by I_{Unpol} . In many applications of remote sensing, the scalar approximation is considered to be sufficient. If P is large, however, substantial errors will be introduced by equating I with I_{Unpol} . It was first shown by Chandrasekhar [1950] that radiance errors introduced by the scalar approximation can exceed 10% for Rayleigh scattering. Mishchenko *et al.* [1994] provided expanded discussion and formal analysis of Rayleigh scattering errors in a plane-parallel atmosphere above a Lambertian surface. Their study showed that the relative error of the TOA intensity decreased with increasing depolarization (arising from multiple scattering for example), and/or increasing surface albedo. For Rayleigh single scattering albedo of 1.0 (conservative scattering), maximum relative errors were observed at (Rayleigh) optical depth near one and at scattering angles near 0° and 90° . These findings were attributed to the unique qualities of Rayleigh scattering. The Mishchenko *et al.* [1994] study did not include aerosols, nor did they address how errors of the estimated intensity would lead to errors in remote sensing applications, such as retrieval of τ .

For Levy *et al.*, [2004] I employed the polarized atmospheric radiative transfer model (RT3) of Evans and Stephens [1991]. This plane-parallel, adding/doubling

code allows for polarization to be turned on or off by changing only one line within an input file. Thus, it was easy to determine differences in reflectance due only to polarization. The other inputs, including the wavelength, aerosol parameters, surface reflectance and atmospheric profiles, were kept constant in both representations. Like *Colarco et al.* [2002], I used the Mie Vector (MIEV) code [*Wiscombe et al.*, 1980] to compute aerosol optical properties, to be used as input to RT3. Results are presented in the following subsections.

5.3.1 Errors in TOA spectral reflectance

For *Levy et al.* [2004], I simulated the ‘Continental’ aerosol model [*Lenoble and Brogniez*, 1984; *Kaufman et al.*, 1997a], composed of three lognormal modes. Mie outputs (from MIEV), included the extinction and scattering coefficients, and coefficients of the scattering phase matrix (calculated for 750 moments). For the atmospheric profile (temperature, pressure, humidity), I assumed the U.S. Mid-latitude summer profile [1976], at 36 levels between the surface and TOA. Aerosols were placed within this model atmosphere as an exponential distribution, having a scale height of 2km. I assumed the land surface to be Lambertian and very dark vegetation (as may be found around Washington, D.C), with spectral reflectance of 0.04 and 0.08 for 0.47 μm 0.66 μm , respectively. The RODs (at sea level) are about 0.194 and 0.051 for the two wavelengths, respectively (Table 3.1). Within each layer of the atmosphere, aerosol and molecular extinction was combined to derive spectral τ and phase matrices, for seven discrete values of τ (at 0.55 μm) between 0.0 and 5.0.

The TOA spectral reflectance was calculated by both the scalar and the vector implementations of the RT3 code, for a set of 3069 sun/surface/satellite geometrical conditions. Plotted in Fig. 5.6 are the 0.47 μm and 0.66 μm differences (vector – scalar) in TOA reflectance, for eight geometries representative of MODIS geometry in the tropics and midlatitudes (Table 5.1).

TABLE 5.1 SOLAR/SURFACE/SATELLITE GEOMETRY FOR EIGHT EXAMPLES

Angle / Reference	Solar Zenith	View Zenith	Relative Azimuth	Scattering
A	12.00	6.97	60.00	163.40
B	12.00	52.84	60.00	120.53
C	12.00	6.97	120.00	169.59
D	12.00	52.84	120.00	132.35
E	36.00	6.97	60.00	140.12
F	36.00	52.84	60.00	104.74
G	36.00	6.97	120.00	147.00
H	36.00	52.84	120.00	136.29

All units are degrees

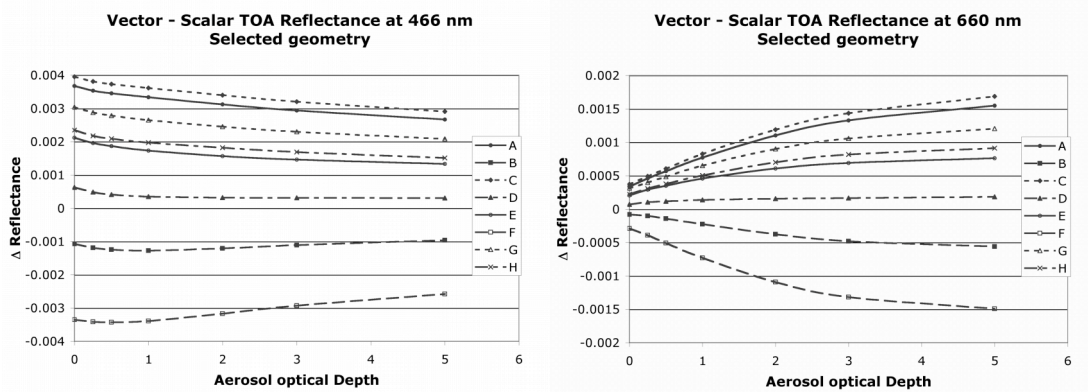


Fig. 5.6: Difference between vector and scalar derived reflectance at the TOA, for eight example sun/surface/satellite geometries, as a function of τ . At 0.466 μm , where the ROD = 0.194 (left). At 0.66 μm , where the ROD = 0.051 (right). Details of the eight geometries are given in Table 5.1. Figure reproduced from *Levy et al., [2004]*.

At large optical depths, the magnitude of the vector-scalar reflectance at $0.47\ \mu\text{m}$ (~ 0.003) is about double that at $0.66\ \mu\text{m}$ (~ 0.0015). However, in more normal aerosol loadings ($\tau = 0.25$), the differences at $0.47\ \mu\text{m}$ (~ 0.004) may be more than eight times than that at $0.66\ \mu\text{m}$ (~ 0.0008).

Fig. 5.6 also demonstrates that the sign of the vector/scalar reflectance difference can be either positive or negative. This is mainly a result of the scattering angle Θ , a result of the relative positions of the sun, surface and satellite (Eq. 2.5). Fig. 5.7 displays contour plots of the vector/scalar difference as a function of solar and view zenith geometry, for two separate relative azimuth angles ($\phi = 30^\circ$ and 150°). Scattering angles are also plotted as contours. Generally, vector-scalar reflectance is positive when $\Theta > 135^\circ$ and negative when $\Theta < 135^\circ$. Magnitudes of the differences increase toward 180° and 90° , similar as would be expected from simulating a purely Rayleigh atmosphere (e.g., *Lacis et al.*, [1998]). However, the contours are not necessarily parallel. Because upward and downward radiation paths are asymmetric, all angles must be considered, not just the scattering angle. Due to the orbit of a polar orbiting satellite such as MODIS, passing the equator close to noon, scattering angles less than 90° are rare.

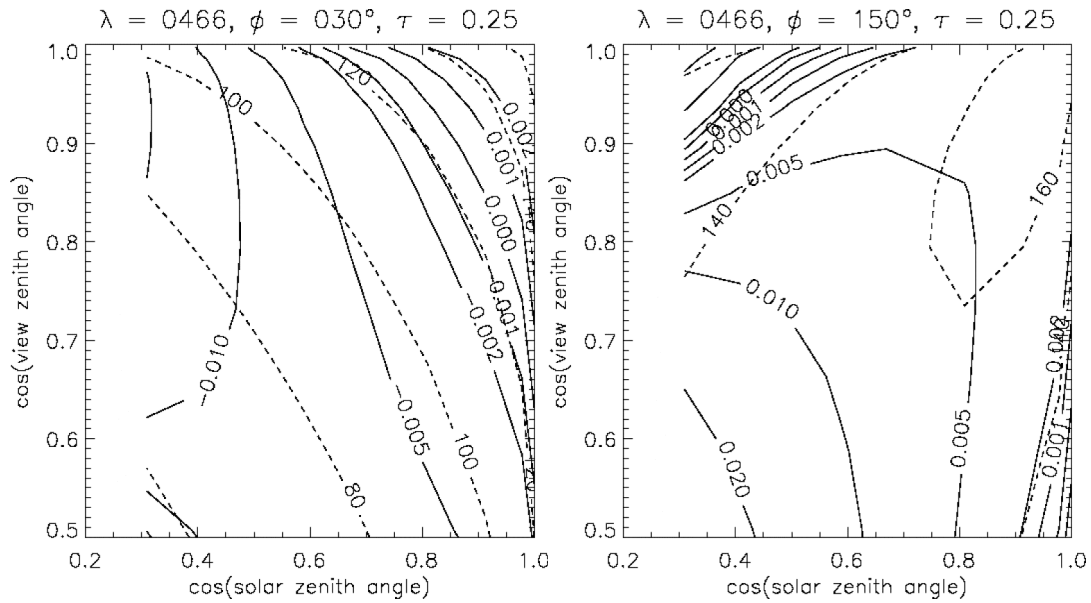


Fig. 5.7: Contour plots of the reflectance difference (vector – scalar) between RT3 calculations of TOA 0.466 μm reflectance, as a function of view and solar zenith angles for two different relative azimuths, for $\phi = 30^\circ$ (left) and $\phi = 150^\circ$ (right). Contours of scattering angle are also plotted. In both plots, $\tau = 0.25$ and ROD = 0.194. Note the signs of the contours. Figure reproduced from *Levy et al.*, [2004].

5.3.2 Errors in τ retrieval

For the above examples of solar and satellite geometry, absolute vector-scalar reflectance differences at 0.47 μm are often greater than 0.01, and may be as high as 0.03 for very large solar zenith angles. For the eight selected geometrical conditions described in Table 5.1, I integrated the vector-scalar reflectance differences into the MODIS algorithm. Fig. 5.8 plots the change in retrieved τ as a function of input τ , at 0.47 μm (a) and 0.66 μm (b). Positive differences in reflectance lead to negative errors in the retrieved τ . In other words, if at a particular input τ , the new (polarized) reflectance value is larger than the old (scalar) value, the retrieved τ must be lower.

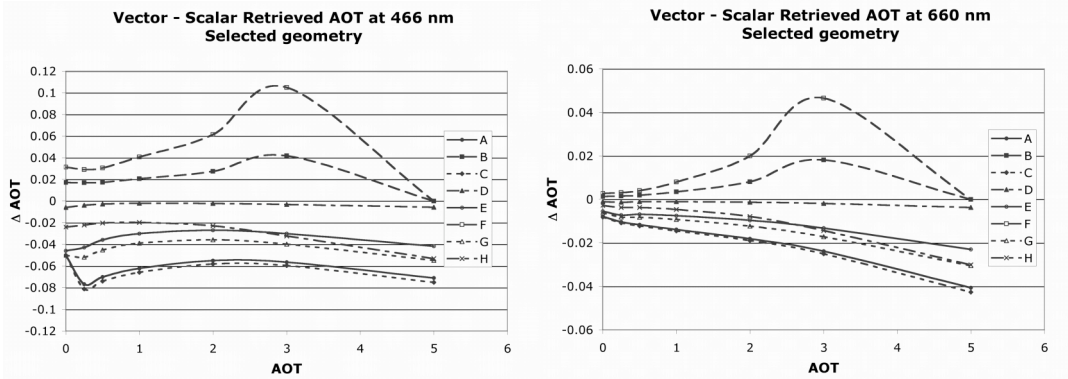


Fig. 5.8: Errors in retrieved τ (AOT), as a function of input τ , due to the neglect of polarization in the RT formulation, for each of the sample geometries listed in Table 5.1. Plotted are at $0.466 \mu\text{m}$ (left) and $0.660 \mu\text{m}$ (right). Figure reproduced from *Levy et al.*, [2004].

In most cases, the magnitude of the τ error is about ten times the magnitude of the reflectance error. However, at some geometries and optical depths, the ratio can be even larger. Some examples include geometries ‘F’ and ‘B’ at $0.47 \mu\text{m}$, where the τ error is thirty times the reflectance difference at input $\tau = 3.0$, and for geometries ‘G’ and ‘A’, where the error is more than twenty times the difference at $\tau = 0.25$. The “kinks” in Fig. 5.8 are a result of numerical instability in the MODIS algorithm’s interpolation.

Whereas the neglect of polarization can induce large errors (either positive or negative) upon individual aerosol retrievals, it is not clear how neglecting polarization will affect retrievals of aerosol climatology. Fig. 5.9 displays the extreme, median and quartile values of vector-scalar differences of TOA reflectance, for the entire set of simulated τ and geometrical conditions. Whereas the magnitude of vector-scalar differences can be greater than 0.03 at $0.47 \mu\text{m}$, more than half of our simulations result in differences of 0.004 or less at this wavelength. This translates into errors of approximately 0.04 in retrieved τ (assuming a ratio of ten to one), which is not so

extreme. At 0.66 μm , maximum vector-scalar differences are 0.01, but most are less than 0.002. Also plotted in Fig. 5.9 are the maximum (magnitude) reflectance differences that would still yield τ within expected MODIS uncertainty over land, defined here as $\tau_e = \pm 0.05 \pm 0.2\tau_{\text{true}}$ [Chu *et al.*, 2002], assuming that a 0.01 error in reflectance leads to 0.1 error in derived τ . In more than half the simulations, the neglect of polarization does not lead to extreme errors in retrieved τ , even at 0.47 μm .

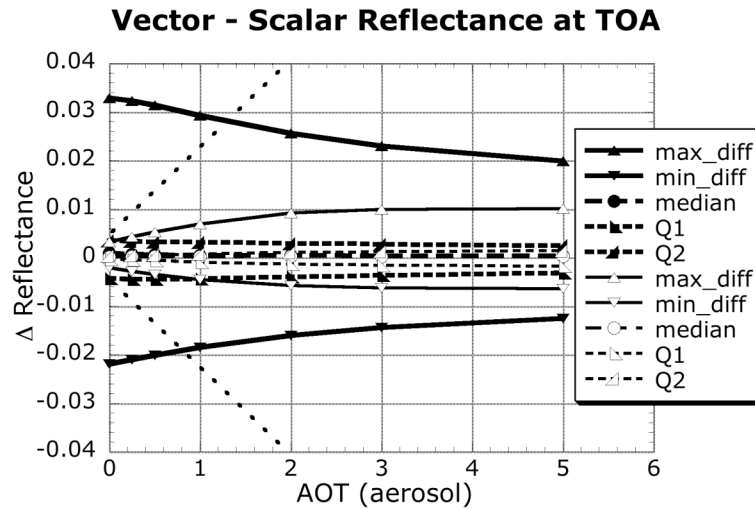


Fig. 5.9: Maximum, minimum, median and quartile values of the difference between vector and scalar TOA reflectance, plotted as a function of τ . Thick curves and closed symbols represent 0.47 μm whereas thin curves and open symbols depict 0.66 μm MODIS channels. The black dotted lines approximate the maximum difference in reflectance that would yield τ retrieved within the expected τ error ($\Delta\rho \sim ((0.05 + 0.2\tau) / 10)$). Figure reproduced from Levy *et al.*, 2004].

Finally, Fig. 5.9 also plots the median vector-scalar reflectance difference for the set of simulated geometry, -0.0008 for 0.47 μm and -0.0002 for 0.66 μm . These errors would introduce approximately $+0.008$ and $+0.002$ errors upon the retrieved

τ in the two wavelengths, respectively. These are small relative to typical $\tau \sim 0.2$ (over the continents).

Next, I compared the simulated geometry to the statistics of MODIS observation geometry over long-term and global scales. MODIS-atmosphere global data (Level 3 Daily) includes scattering angle histogram data, that can be aggregated into a year-long histogram. [<http://modis-atmos.gsfc.nasa.gov>] that includes over two billion observations (Fig. 5.10). MODIS from Terra and MODIS from Aqua are plotted separately as well as together. The Figure shows that the simulated geometry is similar to the observed geometry, and may even over represent extreme angles, suggesting that TOA reflectance errors from neglecting polarization would introduce only a small error (~ 0.008) into a global, long term value of MODIS derived τ over land. This means that whereas a vector code is not required for deriving aerosol climatology, including polarization is necessary for characterizing individual aerosol events for air quality applications.

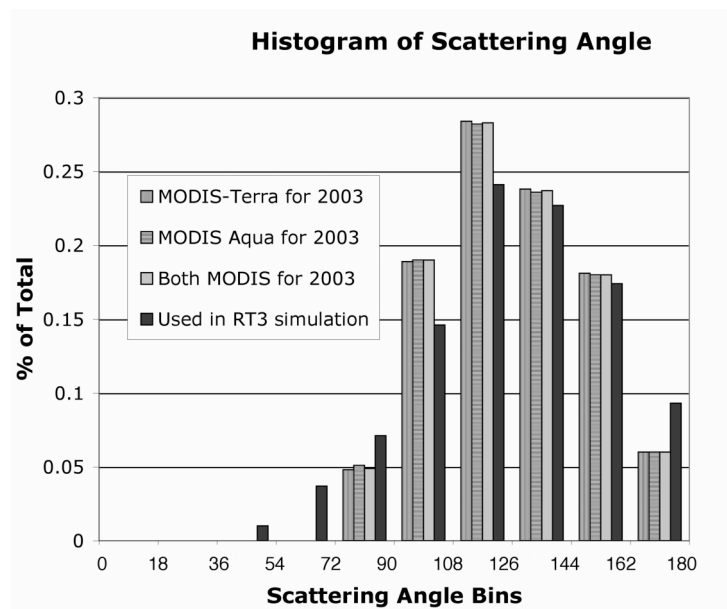


Fig. 5.10: Histograms of scattering angles simulated by our set of geometry compared to scattering angles observed by MODIS throughout the course of 2003. Terra and Aqua are plotted separately and together. Figure reproduced from Levy *et al.*, 2004].

5.4: Additional strategies for improving MODIS aerosol retrieval over land

The first three subsections in this chapter describe several approaches for improving aerosol retrieval from MODIS. These were all investigated based on my original intent to improve the algorithm for specific application over the U.S. mid-Atlantic. These approaches should be generally and universally applicable regionally and globally. However, there are a number of other concepts that should be addressed, including:

- Consistency of the assumed wavelengths compared to response function of the MODIS channels. The assumed wavelengths for the MODIS c004 over-land algorithm differ from those assumed over ocean, in some channels, by up to 10 nm.

- Assumption of sea-level Rayleigh optical depth (ROD) as a function of the ‘correct’ MODIS channel wavelength. For the 0.47 μm channel, the over-ocean algorithm assumes 0.466 μm , whereas the over-land algorithm assumes 0.470 μm . This amounts to differences in assumed ROD of ~ 0.008 .
- Correction for (lower) Rayleigh optical depth in elevated terrain. The MODIS over-land algorithm makes a correction for elevated terrain, by simply adding the difference from assumed sea-level ROD, and in the 0.47 μm channel only. Differences in Rayleigh versus aerosol phase functions may introduce errors.
- Cloud masking and selection of statistically appropriate pixels to be used in a 10 x 10 km framework.
- Implementation of a MODIS aerosol retrieval on a finer (urban?) scale.

The last two points were not considered for this dissertation.

5.5: A new paradigm for MODIS aerosol retrieval.

Yoram Kaufman challenged me to find a way to estimate the land surface reflectance with higher accuracy, such that one could separate aerosol and land surface signals based on the observed spectral dependence including that in the 2.12 μm channel. One major theoretical flaw of the c004 algorithm is that aerosol is assumed to have no interaction with the 2.12 μm radiation. In other words, τ at 2.12 μm is assumed zero for all aerosols. For a fine-dominated aerosol such as urban/industrial aerosol (either the *Remer and Kaufman*, [1998] or *Dubovik et al.* [2002a] models), $\tau = 0.50$ at 0.55 μm translates into $\tau \sim 0.05$ at 2.12 μm . Assuming surface reflectance VISvs2.1 ratios of 0.25 for the 0.47 μm channel and 0.5 for the

0.66 μm channel results in retrieval errors (τ_ϵ) of 0.0125 and 0.025 for τ in the two channels. By neglecting the information in 2.12 μm , we introduce errors in translating surface reflectance from 2.12 μm to visible, and therefore errors in retrieving τ in the visible. With (coarse dominated) dust, having much lower spectral dependence, the potential errors are much larger. In the dust case ($\tau_{2.12} \sim 0.3$, Fig. 2.2), neglecting 2.12 μm aerosol signal would lead to $\tau_\epsilon \sim 0.15$ at 0.66 μm . However, this bias is correctable, providing the major incentive for development of the second-generation operational algorithm.

Chapter 6: Global aerosol models for the second-generation algorithm

Chapter 5 examined some of the sources of error in the global MODIS aerosol retrieval (c004). The next two chapters summarize the development of the second-generation algorithm, expanding the concepts introduced in Chapter 5. This chapter summarizes the derivation of new global aerosol models and optical properties [Levy *et al.*, 2007a]. Chapter 7 details the implementation of the new algorithm, including parameterization of surface reflectance [Levy *et al.*, 2007b].

6.1: Motivation

The limited wavelengths used in the MODIS algorithm over land provide rough information about aerosol size, and can be used to estimate η (non-dust fraction). However, since the MODIS over-land retrieval suffers from surface and other contaminations, it is not sufficiently sensitive to aerosol ω_0 or details of the size distribution within each size range (fine or coarse). Therefore, the algorithm must select the aerosol model *a priori* of the retrieval.

As described by Remer *et al.*, [2005], the c004 over-land aerosol algorithm selects the aerosol type (model) appropriate for a given region and season. For many regions around the world, there was little or no information prior to launch and algorithm development. In other words, some of the model assignments were essentially guesses. The assumed optical properties (size and refractive index) used for creating the LUTs were also based on very limited information. For example, the ‘Urban/Industrial’ model, derived by Remer and Kaufman [1998], was derived from fewer than 150 AERONET almucantur measurements at six sites along the East Coast

of the U.S, during the summertime only. The model's optical properties were calculated using early versions of the almucantur retrieval algorithm [*Nakajima and King, 1990; Kaufman et al., 1994*]. Even though aerosol properties are different in the winter (less water), in Europe (more absorbing) and the U.S. Midwest (larger particles), the *Remer and Kaufman [1998]* East Coast summertime aerosol model was assumed not only for the U.S. Eastern seaboard during all seasons, but to the entire Eastern half of the U.S. and Europe.

Since the original development of the MODIS aerosol algorithm, and even since the advent of c004 products, much has been learned about global and regional aerosols' physical and optical properties. *Dubovik et al. [2002]* analyzed AERONET almucantur inversions at selected sites around the globe, where each site presumably represented a different aerosol regime. Their study resulted in derivation of bi-lognormal aerosol models for each of these sites, which included descriptions of their size and optical properties. For *Levy et al. [2005]*, I applied the *Dubovik et al. [2002]* version of the Urban/Industrial aerosol model derived at GSFC, and found that the model improved retrievals of U.S. mid-Atlantic aerosol during the summer of 2001. While these studies found unique aerosol types at each site, they did not account for seasonal variation, nor were they necessarily representative of all AERONET sites.

Omar et al. [2005] attempted to interpret all almucantur retrievals from all AERONET sites to determine global aerosol climatology. They performed a cluster analysis of AERONET data and found that six aerosol models (listed as desert dust, biomass burning, background/rural, polluted continental, marine, and dirty pollution) represented the global AERONET dataset. These models varied mainly by their ω_0

and size parameters. Two models were representative of clean conditions (marine and background/rural $\tau < 0.1$). One of the remaining models (dust) was dominated by coarse mode, whereas three were dominated by fine mode. The three fine-dominated models varied mainly by their ω_0 (biomass burning, polluted continental, and dirty pollution). While their study determined which models were observed over each AERONET site, it did not try to assign unique aerosol type to each site. Because of the similarity (in physics) of remotely sensed measurements from AERONET and satellite, the following section uses the AERONET data to distinguish regional aerosol types.

6.2: Cluster analysis of AERONET data

Cluster analysis encompasses a number of different algorithms and methods for grouping objects of similar kind into respective categories. A general question facing researchers in many areas of inquiry is how to organize observed data into meaningful structures. In other words cluster analysis is an exploratory data analysis tool which aims at sorting different objects into groups in a way that the degree of association between two objects is maximal if they belong to the same group and minimal otherwise. Therefore, cluster analysis can be used to discover structures in data without providing an explanation for why they exist at all. It is up to the investigator to provide this explanation based on his or her theoretical understanding of the matter. For air quality studies, clustering has been used to organize wind backtrajectories for understanding the interaction of sources and meteorology that contributes to polluted conditions along the U.S. mid-Atlantic [Taubman *et al.*, 2006; Hains *et al.*, submitted 2007].

The goal here is to discover patterns in AERONET data in order to determine the properties of aerosol at a given site. For the purpose of a constrained satellite algorithm, where the aerosol type must be known *a priori* to the retrieval, the final goal is to assign an aerosol model that is appropriate in a given region. Thus, the Omar *et al.* [2005] study, while it provides meaningful interpretation to aerosol *optical* models, does not assign a particular model at a particular site. Therefore, I performed a sort of ‘forced’ cluster analysis, thereby limiting the number of potential clusters. I used the cluster analysis routines provided with the IDL (Interactive Display Language) software version 6.1.

There were about 136,000 AERONET almucantur retrievals that were processed as of February 2005. At that time, the AERONET retrievals did not determine non-spherical fraction (e.g., *Dubovik et al.*, [2006]), instead assuming that either aerosol is 100% spherical or 100% spheroid mixture. About 13,496 spherical and 5128 spheroid retrievals (~14%) met the minimum quality parameters suggested by the AERONET team, including: $\tau_{0.44} > 0.4$, $\theta_0 > 45^\circ$, 21 symmetric left/right azimuth angles, and radiance retrieval error less than 4%. Quadratic fit to the spectral τ [*Eck et al.*, [1999]], yielded τ at 0.55 μm ($\tau_{0.55}$) associated with each almucantur retrieval. In order to extract expected (dynamic) dependence of τ , (e.g., *Remer and Kaufman*, [1998]), the retrievals were separated into ten equal bins of τ (having $\tau_{0.55}$ medians ranging between 0.28 and 1.33). Although AERONET requires $\tau_{0.44} > 0.40$, because of the strong spectral dependence of most aerosol types (except for dust), the minimum bin for $\tau_{0.55}$ is around $\tau_{0.55} = 0.28$. This is only slightly higher than the lowest τ index within the operational c004 MODIS LUT ($\tau = 0.25$), so no significant

aerosol information is lost. I clustered each τ bin separately to keep track of dynamic (dependence on τ) properties.

Knowing that MODIS is incapable of separating similar sized aerosol types over land, I chose to limit the number of possible aerosol types, to represent ‘low’, ‘medium’ and ‘high’ in some parameter space. Thus, the cluster analysis is allowed to find only three clusters. It is assumed that clusters from separate τ bins can be recombined in some way, to collectively describe the dynamical (τ dependent) properties of a particular aerosol type.

Omar et al., [2005] showed that other than τ , unique aerosol types are identified by parameters that represent aerosol size and absorption. Therefore, I chose to cluster with respect to only two optical parameters: SSA (ω_0) at 0.67 μm and the asymmetry parameter (ASYM or g) at 0.44 μm , assuming that one absorption parameter (ω_0) and one size parameter (g) is sufficient to represent the entire aerosol parameter space. Separate wavelengths were chosen to reduce the chance for finding an artificial dust cluster due to its near-ultraviolet 0.44 μm absorption (ω_0), while noting that larger-sized aerosols are better separated by phase function asymmetry at the shortest wavelength (0.44 μm).

Since I ‘forced’ the cluster analysis to retrieve three distinct aerosol clusters, I imagined that each cluster would comprise about a third (plus or minus) of the entire AERONET population. However, the results displayed quite different characteristics, there were two clusters with significant fraction and a third with only 11 points. This eleven-point cluster included points with unusually low $\omega_0 < 0.6$, and/or $g < 0.5$, indicating either retrieval errors or true (physically unlikely) outliers. Upon removing

these points and re-clustering, there are now three clusters each having reasonably similar number of points. Averaging the optical parameters within each cluster yields three distinct spherical fine-dominated aerosol optical models.

At each AERONET site, and for each season, Fig. 6.1 (a-d) displays pie-plots showing the percentage of the retrievals attributed to each cluster. To remove poor statistics, only shown are pie plots at sites having at least 10 observations (per season) during the history of AERONET, excluding the many sites that have few retrievals of $\tau_{0.44} > 0.4$ ($\tau_{0.55} > \sim 0.28$). Green pie segments represent the weakly absorbing $\omega_0 \sim 0.95$ model (presumably urban/industrial aerosol, dominated by sulfate and OC), blue segments are the moderately absorbing $\omega_0 \sim 0.90$ model (presumably aerosol from forest burning and developing world processes), and red segments designate the highly absorbing $\omega_0 \sim 0.85$ model (presumably savanna/grassland burning aerosol). At most sites and most seasons, the aerosol type is as expected. Weakly absorbing aerosol (green) dominates the U.S. East Coast and far western Europe, whereas highly absorbing aerosol (red) dominates the savannas of South America and Africa. Most other sites are either dominated by moderately absorbing aerosol (blue) or are a mix of all clusters.

There are some surprises, however. Southeast Asia seems to be primarily weakly absorbing aerosols, as opposed to more absorbing type assumed by *Remer et al.*, [2005]. Recent studies (e.g., *Eck et al.*, [2005]) confirm that aerosol in urban areas in far Southeast Asia are primarily weakly absorbing ($\omega_0 \sim 0.95$). A few sites in Western Europe have large fractions of absorbing aerosol, possibly a result of heavy diesel use.

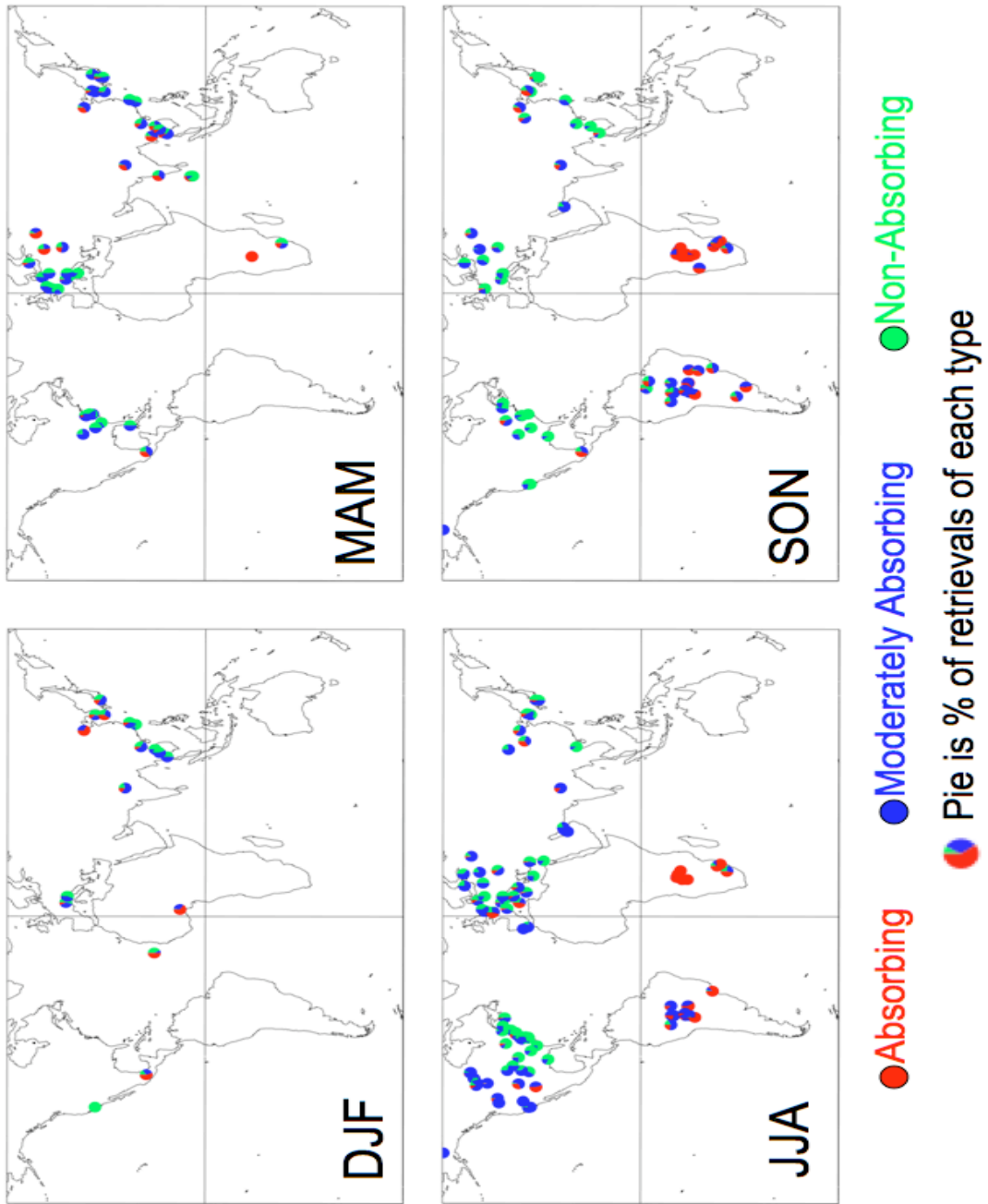


Fig. 6.1: Percentage (pie charts) of spherical aerosol model type (from cluster analysis) observed at each AERONET site per season. Colors represent absorbing ($\omega_0 \sim 0.85$), moderately absorbing ($\omega_0 \sim 0.90$) and weakly absorbing ($\omega_0 \sim 0.95$), respectively. Figure from *Levy et al.*, [2007a].

A similar cluster analysis was performed for the spheroid retrievals, resulting in a single cluster sufficient for describing the spheroid-based almucantur inversions [Dubovik *et al.*, 2006]. Since the sites contributing to spheroid data are primarily those known to be in dust regions, the spheroid model presumably represents coarse-dominated (dust) aerosol.

6.3: Regional assignment of aerosol type

Since the MODIS aerosol retrieval over land is not sufficiently sensitive to ω_0 , the expected aerosol type must be assigned *a priori* to the retrieval. Remer *et al.*, [2005] described how assumed aerosol type was assigned to region and season for the c004 algorithm, even where little was known about the prevailing aerosol type. For example, MODIS assigned the same moderately absorbing smoke properties in regions of forest fire burning (both tropical and high latitude forest) and developing industrial regions in Eastern Europe and most of Asia. Whether the c004 boundaries are appropriate can be evaluated by determining the dominant aerosol type represented at each AERONET site (Fig. 6.1), and within regions.

Keeping in mind our goal of dividing the world into plausible aerosol types, a MODIS algorithm requires that each site should have an assumed aerosol type attached to it. The moderately absorbing aerosol type is set as the default, overwritten only if clear dominance of one of the other two aerosol types is observed. If either the weakly-absorbing or the absorbing aerosol occupies more than 40% of the pie, while the other occupies less than 20%, the site is assigned to the dominant aerosol type. For example, GSFC (39°N, 77°W) during the summer months (JJA), is 87%

weakly-absorbing and 13% moderately absorbing, meaning the weakly-absorbing type is assigned.

Fig. 6.2 (a-d) displays the aerosol types assigned at each site. As in Fig. 6.2, green represents weakly absorbing, blue represents moderately absorbing and red designates absorbing aerosol types. Most site designations seem reasonable and expected. North America during the summer (JJA) is split between weakly absorbing and moderately absorbing aerosol types at approximately 100°W longitude, similar to that assumed in *Remer et al.*, [2005]. Southern Africa during the winter season (DJF) is solidly designated as absorbing aerosol (like was found by *Ichoku et al.*, [2003]). Even though Western Europe is evenly split between weakly absorbing and moderately absorbing (except for two absorbing sites), the entire region was assigned to ‘weakly absorbing’, deferring to that assumed by the MODIS c004 algorithm.

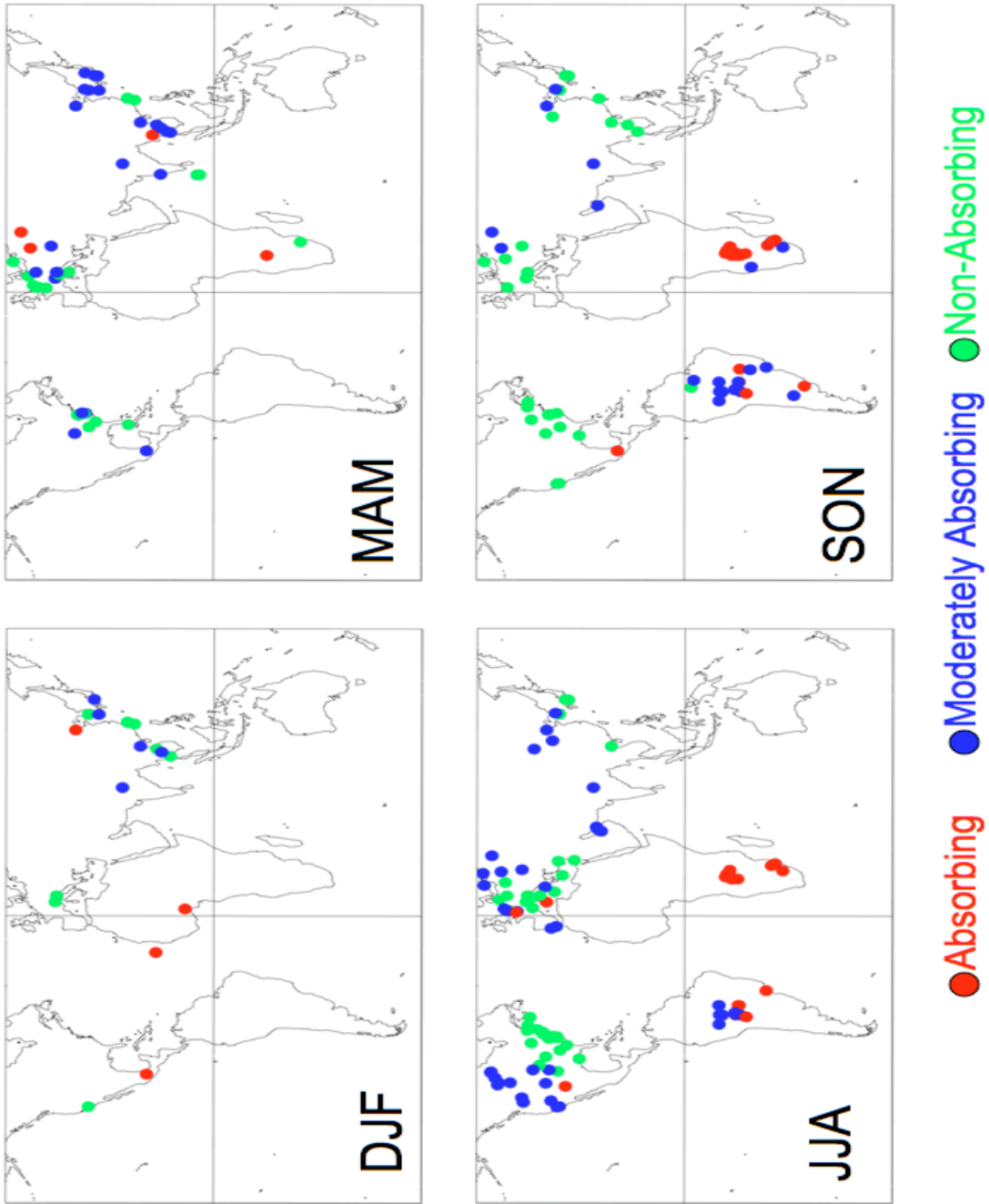


Fig 6.2: Final spherical aerosol model type designated at each AERONET site per season. Colors represent absorbing ($\omega_0 \sim 0.85$), moderately absorbing ($\omega_0 \sim 0.90$) and weakly absorbing ($\omega_0 \sim 0.95$), respectively. Figure from *Levy et al., [2007a]*.

Fig. 6.3 plots the final assignment of aerosol types around the globe, as a function of season. Note that where possible the shapes correspond with the clustering of AERONET sites over land. At some regions, however, some subjectivity was needed to connect areas and draw lines. Over southeastern Asia, high mountains are boundaries between two aerosol regimes. Over Brazil, the boundary is near the border of Amazon forest and grasslands. Even though insufficient data exists for Africa north of the equator, the known surface types and seasonal cycles suggest that heavy absorbing aerosol would be produced during the biomass-burning season. Red designates regions where the absorbing aerosol is chosen, whereas green represents weakly absorbing aerosol. The moderately absorbing ($\omega_0 \sim 0.90$) model is assumed everywhere else. These images were mapped onto a 1° longitude x 1° latitude grid, such that a fine aerosol type is assumed for each grid point, and each season. As new information becomes available (e.g., [Mi *et al.*, submitted 2007]), these maps can be easily updated.

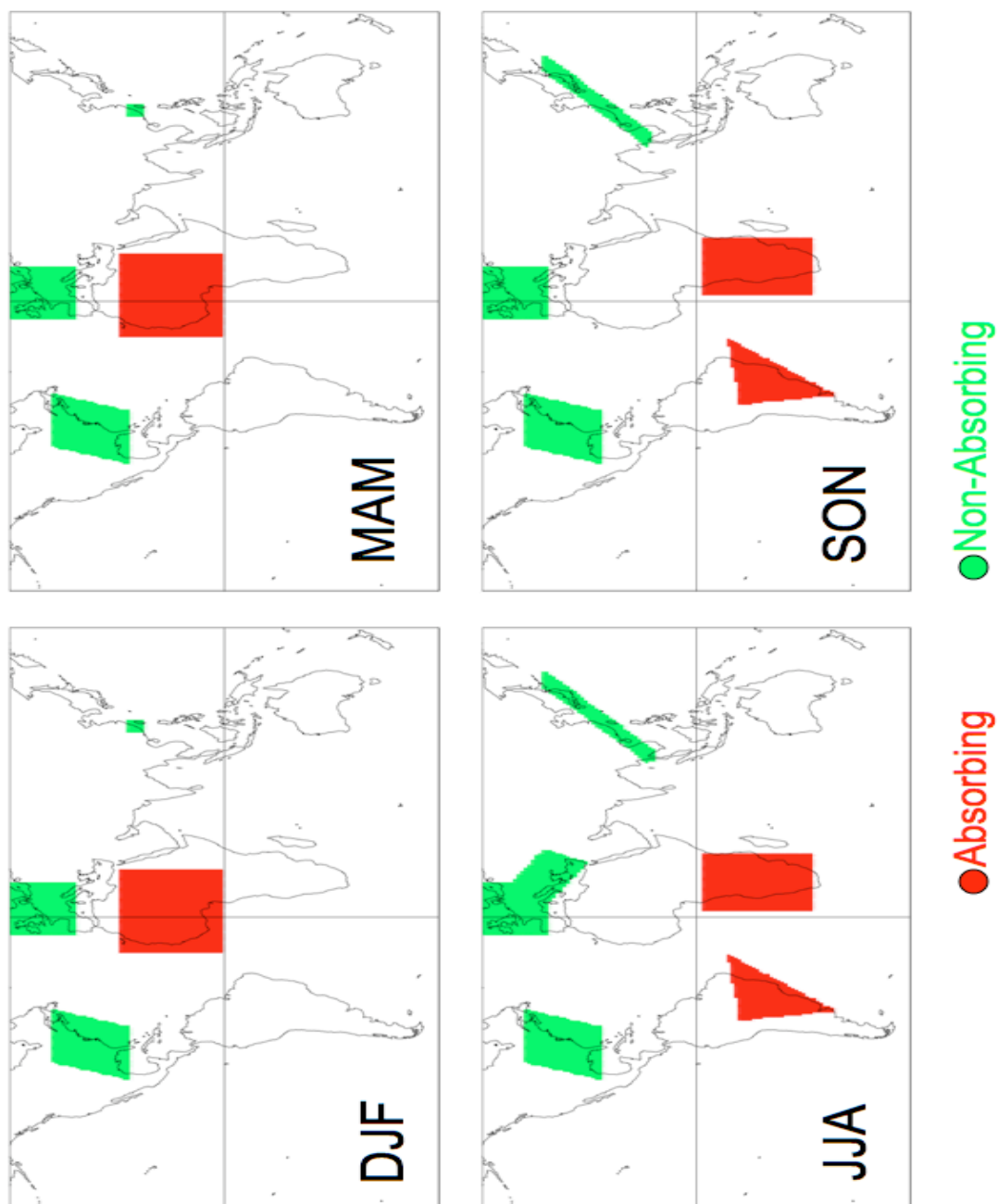


Fig 6.3: Final spherical aerosol model type designated at $1^\circ \times 1^\circ$ gridbox per season. Red and green represent absorbing ($\omega_0 \sim 0.85$) or weakly-absorbing ($\omega_0 \sim 0.95$) models, respectively. Moderately absorbing ($\omega_0 \sim 0.90$) is assumed everywhere else (as a default). Figure from *Levy et al., [2007a]*.

6.4: Physical and optical properties of the aerosol models

As indicated in section 6.2, the ‘forced’ AERONET clustering produced three spherical, fine-dominated models (moderately absorbing, absorbing and weakly-absorbing), and one spheroid, coarse-dominated type (dust). I considered these to represent the range of expected global aerosol. By averaging the properties within each aerosol type cluster, the physical properties of each aerosol ‘model’ are determined. These models can be compared with the well-known ‘Continental’ model [*Lenoble and Brogniez, 1984*] that is used in many satellite applications, including over-land applications of MODIS (e.g., [*MAST, 2006*] for aerosol and <http://modis-land.gsfc.nasa.gov> for MODIS land surface products).

Fig. 6.4 shows the size distributions for the four AERONET-derived models as a function of τ . Note the strong dynamic nature of the size properties of the weaklyabsorbing model, consistent with urban/industrial aerosol models [*Dubovik et al., 2002; Remer and Kaufman, 1998*]. While the primary product of the AERONET almucantur inversion is the complex refractive index and the volume size distribution $dV(r)/d\ln(r)$ in 22 bins of equal log size ($d\ln r$), the AERONET retrieval reports the set of two lognormal modes that represent the size distribution.

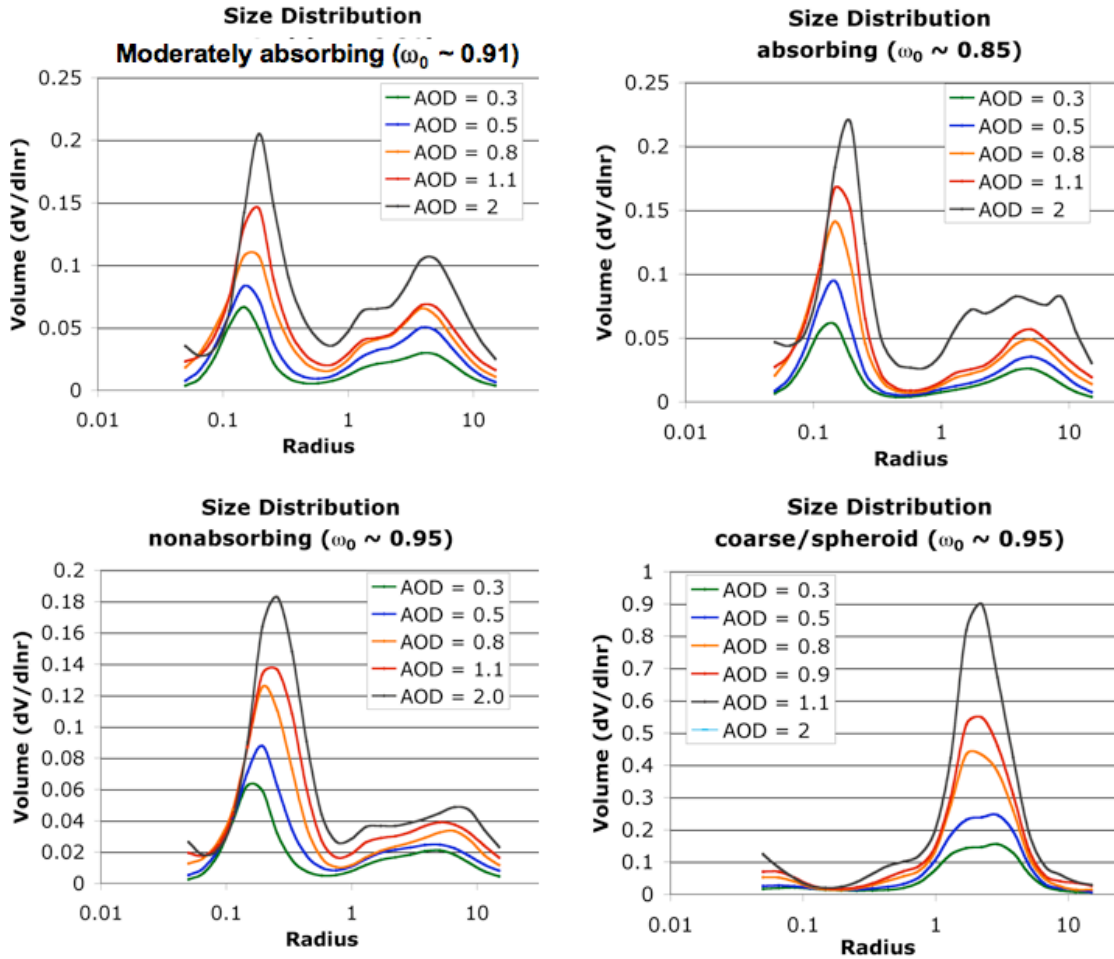


Fig 6.4: Aerosol size distribution as a function of τ (AOD) bin for the three spherical (moderately absorbing, absorbing and weakly absorbing) and spheroid (dust) models identified by clustering of AERONET. Figure from *Levy et al., [2007a]*

Table 6.1a displays the lognormal size parameters and refractive indices for the four AERONET-derived models, as well as the ‘Continental’ model. For each lognormal mode, r_v is the median radius of the volume size distribution, σ is the standard deviation of the radius, and V_0 is the volume of particles per cross section of the atmospheric column (i.e., the amplitude of the lognormal size distribution).

TABLE 6.1: OPTICAL PROPERTIES OF THE AEROSOL MODELS USED FOR THE OVER-LAND LOOKUP TABLE

Model	Mode	r_v (μm)	σ	V_0 ($\mu\text{m}^3/\mu\text{m}^2$)	Refractive Index: k
Continental					
	Water Solub	0.176	1.09	3.05	1.53 - 0.005i; 1 1.53 - 0.006i; 2 1.53 - 0.006i; 3 1.42 - 0.01i; 4
	Dust	17.6	1.09	7.364	1.53 - 0.008i; 1 1.53 - 0.008i; 2 1.53 - 0.008i; 3 1.22 - 0.009i; 4
	Soot	0.050	0.693	0.105	1.75 - 0.45i; 1 1.75 - 0.44i; 2 1.75 - 0.43i; 3 1.81 - 0.50i; 4
Moderate-absorbing					
	Accum	$0.0203\tau + 0.145$	$0.1365\tau + 0.374$	$0.1642 \tau^{0.775}$	$1.43 - (-0.002\tau + 0.008)i$
	Coarse	$0.3364\tau + 3.101$	$0.098\tau + 0.729$	$0.1482 \tau^{0.684}$	$1.43 - (-0.002\tau + 0.008)i$
Absorbing					
	Accum	$0.0096\tau + 0.134$	$0.0794\tau + 0.383$	$0.1748 \tau^{0.891}$	$1.51 - 0.02i$
	Coarse	$0.9489\tau + 3.448$	$0.0409\tau + 0.743$	$0.1043 \tau^{0.682}$	$1.51 - 0.02i$
Weak-absorbing					
	Accum	$0.0434\tau + 0.160$	$0.1529\tau + 0.364$	$0.1718 \tau^{0.821}$	$1.42 - (-0.0015\tau + 0.007)i$
	Coarse	$0.1411\tau + 3.325$	$0.1638\tau + 0.759$	$0.0934 \tau^{0.639}$	$1.42 - (-0.0015\tau + 0.007)i$
Spheroid/Dust					
	Accum	$0.1416 \tau^{-0.052}$	$0.7561 \tau^{0.148}$	$0.0871 \tau^{1.026}$	$1.48\tau^{-0.021} - (0.0025\tau^{0.132})i$; 1 $1.48\tau^{-0.021} - 0.002i$; 2 $1.48\tau^{-0.021} - (0.0018\tau^{-0.08})i$; 3 $1.46\tau^{-0.040} - (0.0018\tau^{-0.30})i$; 4
	Coarse	2.2	$0.554 \tau^{-0.052}$	$0.6786 \tau^{1.057}$	$1.48\tau^{-0.021} - (0.0025\tau^{0.132})i$; 1 $1.48\tau^{-0.021} - 0.002i$; 2 $1.48\tau^{-0.021} - (0.0018\tau^{-0.08})i$; 3 $1.46\tau^{-0.040} - (0.0018\tau^{-0.30})i$; 4

Listed for each model are the individual lognormal modes, and the final SSA at different wavelengths. Listed for each mode are the volume modal radius r_v , standard deviation σ of the volume distribution, and total volume of the mode, V_0 . The complex refractive index is assumed for all wavelengths (1,2,3 and 4 for 0.47, 0.55, 0.66 and 2.1 μm , respectively), unless otherwise noted. The Absorbing and Moderately absorbing model parameters (r_v , σ and k) are defined for $\tau \leq 2.0$; for $\tau > 2.0$, we assume $\tau = 2.0$. Likewise, the Weakly-absorbing and Spheroid model parameters are defined for $\tau \leq 1.0$. V_0 (for all models) is defined for all τ .

Theoretical scattering and absorption properties of aerosols were explained in Chapter 2, and are defined as a function of wavelength, aerosol size and composition (which establishes the complex refractive index). Calculation of extinction and scattering efficiencies are accomplished by using a Mie computer program (MIEV, [Wiscombe, 1980]). Assuming the size distribution is normalized ($N_0=1$), Q_{ext} , Q_{sca} and $P(\Theta)$ for the particle population are defined by integrating the single particle properties over the size distribution. This requires a sufficient number of Mie size parameter ($X=2\pi r/\lambda$) bins (such as 300 or more that cover $0.02 < X < 2000$). The actual number of bins depends on how many are needed to represent a given accuracy (say 99.99%) of the area distribution described by the theoretical distribution. For non-spherical aerosol particles, a code (such as a complete or approximate T-matrix code; [Mischenko *et al.*, 1994, Dubovik *et al.*, 2006] is required.

Mass and extinction properties are related through the mass extinction coefficient, B_{ext} . For the purpose of columnar mass M estimation, the *mass concentration coefficient* (M_c) can be defined as:

$$M_c = \frac{1}{B_{ext}} \quad (6.1)$$

so that

$$M = \tau M_c. \quad (6.2)$$

In reality, since the aerosol lognormal properties are dependent on τ , the extinction parameters and thus M_c is also a weak function of τ . Table 6.2 lists the extinction, scattering and mass conversion factors for the four AERONET-derived aerosol models, along with the Continental model for comparison. In each case, $\tau_{0.55}=0.5$.

TABLE 6.2: EXTINCTION/MASS PROPERTIES OF THE AEROSOL MODELS

Model	ω_0	Q_{ext} []	r_{eff} [μm]	B_{ext} [m^2/g]	M_c [$\mu\text{g}/\text{cm}^2$]
Continental	0.886	0.621	0.293	1.5910	62.8600
Moderately Absorbing / Developing World	0.920	1.018	0.261	2.9220	34.2230
Absorbing / Smoke	0.869	0.977	0.256	3.5330	28.3070
Weakly-absorbing / Urban-Industrial	0.947	1.172	0.207	3.4310	29.1460
Spheroid / Dust	0.953	1.339	0.680	1.4770	67.6960

Listed for each model are the single scattering albedo, extinction efficiency, effective radius, mass extinction coefficient and mass concentration conversion factor. These parameters are calculated at $0.55 \mu\text{m}$, for $\tau_{0.55} = 0.5$. The particle density is assumed to be $1 \text{ g}/\text{cm}^3$.

Fig. 6.5 plots properties of the four AERONET-derived aerosol models, along with the Continental model for comparison. Figs. 6.5-d are plotted for $\tau_{0.55} = 0.5$, where Fig. 6.5b plots the spectral dependence of τ , 6.5a plots phase function at $0.55 \mu\text{m}$, 6.5c plots the spectral dependence of ω_0 , and 6.5d plots the spectral dependence of g . Note that even though the three fine-dominated models have similar τ spectral dependence, they differ in other properties. The coarse model (spheroid-dust) has much smaller spectral dependence than any of the fine-dominated models, and nearly flat phase function in the 90° - 180° scattering angle range observable by MODIS.

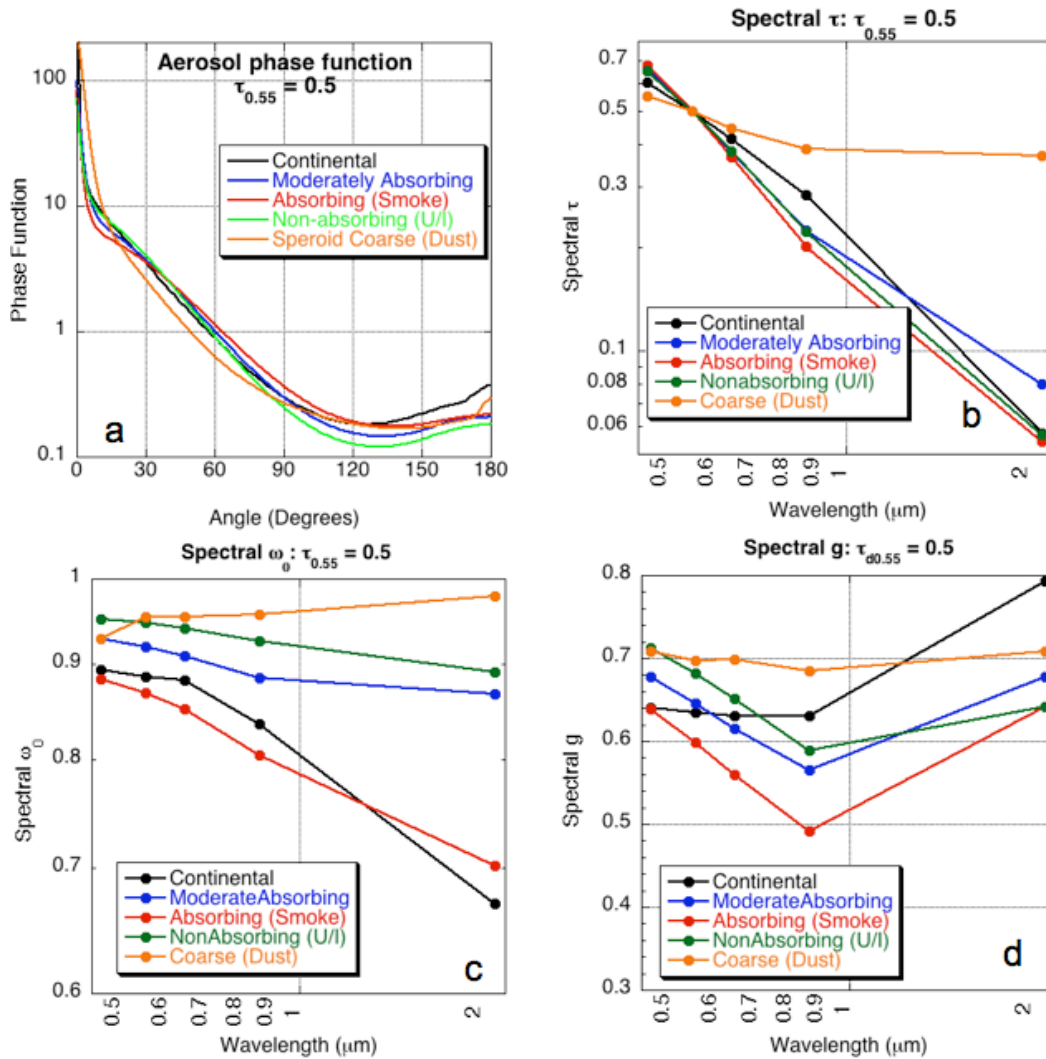


Fig 6.5: Optical properties of the AERONET-derived models, compared with the Continental model for $\tau_{0.55} = 0.5$. The phase function at 0.55 μm is plotted in (a), whereas the spectral dependence of the optical depth, single scattering albedo and asymmetry parameter are plotted in (b-d), respectively. Figure from *Levy et al., [2007a]*.

Fig. 6.6 compares the phase function of each of the models (also for $\tau_{0.55}=0.5$) as compared to the analogous models from the MODIS c004 algorithm. Differences are minimal (especially for the 90°-180° scattering angle range) for the weakly-absorbing (urban/industrial) and absorbing (heavy smoke) aerosol types. A possibly significant change is seen in the moderately absorbing (developing world/moderate

smoke) phase function. The largest change is for the ‘dust’ model, due to assuming spheroids instead of spheres. The differences are primarily in the MODIS-observable scattering angle ranges, which will have a significant effect within the aerosol retrieval. The quality of these aerosol models is evaluated in the next section.

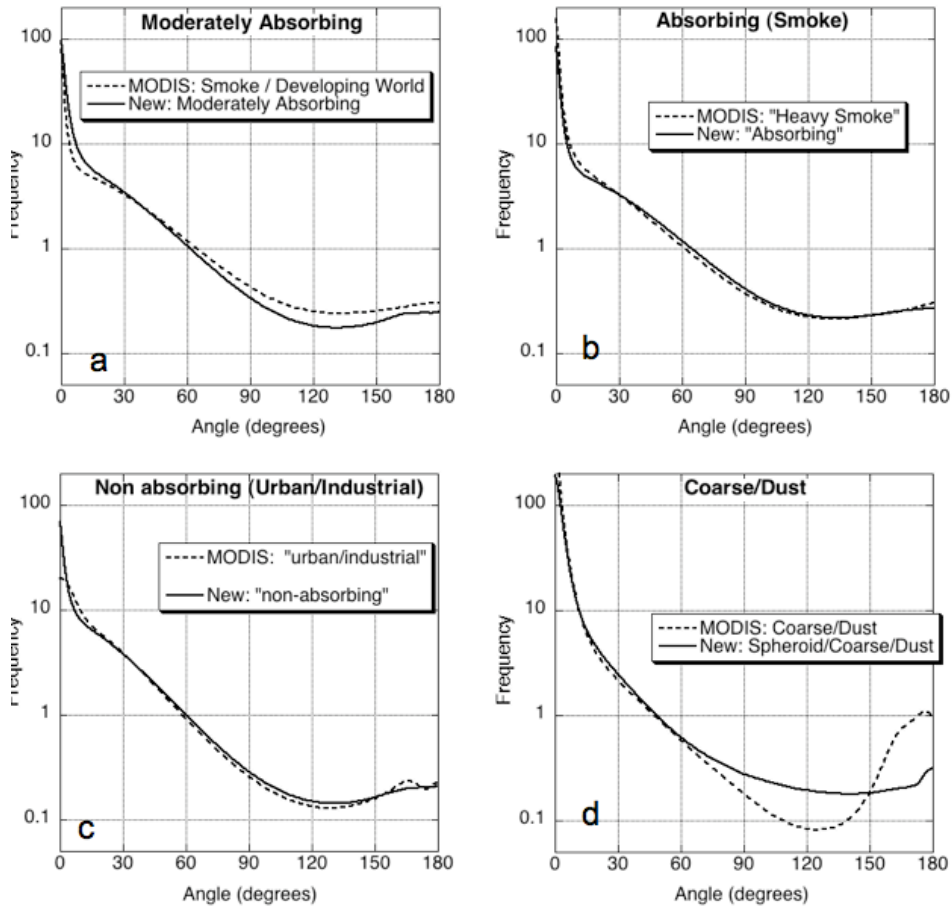


Fig 6.6: Comparison of phase function (at 0.55 μm) between new (solid curves) and analogous MODIS (dotted curves) aerosol models. Models are moderately absorbing (a), absorbing (b), weakly absorbing (c), and dust (d). For all plots, $\tau_{0.55} = 0.5$. Figure from Levy *et al.*, [2007a].

6.5: Optical properties and spectral τ

How well do the assigned aerosol models represent ambient aerosol at specific AERONET sites? The time series of Level 2 ‘sun’ (extinction of direct solar radiation) retrieved products from AERONET are independent of the ‘sky’ retrieved products. The sun measurements cannot evaluate the assumed absorption properties, but can validate the resulting spectral dependence of the aerosol optical depth.

Fig. 6.5b showed the spectral τ dependence of each model for $\tau_{0.55}=0.5$. Similar plots could be made from the spectral dependence indexed by other $\tau_{0.55}$ values. For each AERONET site, the sun-retrievals were divided into three-month seasons (winter = DJF, spring = MAM, summer = JJA, fall = SON). The N (number of) observations within each season were sorted according to $\tau_{0.55}$, where $\tau_{0.55}$ was calculated by fitting a quadratic to the observed spectral τ . For given indexed value of $\tau_{0.55}$ ($\tau = 0.25, 0.5, 1.0, 2.0$), I determined which AERONET observation contained $\tau_{0.55}$ closest in magnitude to the indexed value. This location was considered the ‘central’ (C) index of the bin and all observations indexed between $C-N/20$ and $C+N/20$ determined all observations considered ‘close’ to the indexed $\tau_{0.55}$ value. The spectral optical thickness for each bin was calculated by averaging the spectral optical thickness for the set of observations within the bin.

Fig. 6.7 compares spectral dependence of the aerosol models with spectral dependence at selected AERONET sites, for indexed $\tau_{0.55} = 0.5$. Since MODIS observes at many wavelengths (including 0.47, 0.55, 0.66, 0.86 and 2.12 μm bands), the AERONET spectral τ observations (4 to 8 bands between 0.34 and 1.02 μm ,

depending on site) were interpolated to the same wavelengths. Extrapolation of AERONET to 2.12 μm was not performed because of the great distance from 1.02 μm . Different seasons (for AERONET) are represented by different line styles. At least one fine-dominated model, plus dust, are plotted for each site.

At Alta Floresta (9°S, 56°W), the spectral dependence in the visible wavelengths agrees well with either the moderately absorbing or absorbing models. The AERONET spectral dependence varies with season, and is seen most clearly at 0.86 μm . During the summer and fall, the AERONET dependence is slightly closer to the absorbing model than the moderately absorbing, and during the winter and spring, the moderately absorbing model provides a slightly better match to sun-derived spectral τ . Therefore, the distribution of models includes this seasonal dependence at this location.

At Cape Verde (16°N, 22°W), although the moderately absorbing fine-dominated model is assumed all year, coarse (dust) is expected to dominate. Plotted for Cape Verde is the AERONET spectral τ compared with the modeled dust. Even though the dust model is improved from that assumed by MODIS c004, my modeled spectral dependence is still too large to properly represent dust over Cape Verde. This means that my global dust properties may not be specifically appropriate for Cape Verde and that separate dust models may be required at different sites. Yet, errors between modeled and observed spectral dependence are smaller than for c004.

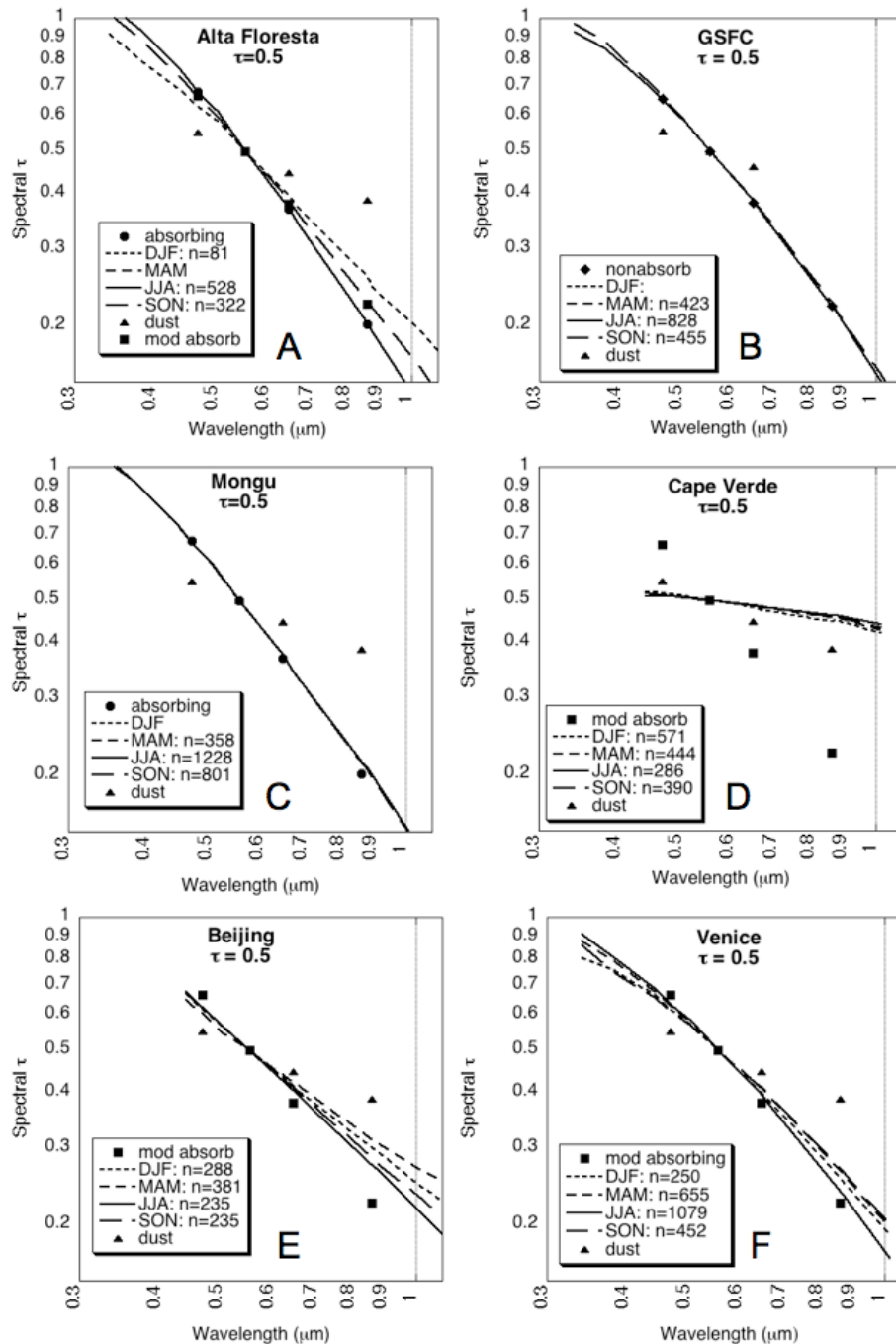


Fig 6.7: Comparison of spectral τ between new models (filled shapes) and averages of AERONET ‘sun’ measurements (dotted curves) at selected sites and seasons, for $\tau_{0.55} = 0.5$. Different curves represent AERONET data during different seasons. The number of observations (n) used to create each curve is displayed in the legend. Note that there are at least two aerosol types displayed (at least one fine-dominated type plus dust). Sites plotted are Alta Floresta (A), GSFC (B), Mongu (C), Cape Verde (D), Beijing (E) and Venice (F). Figure from *Levy et al., [2007a]*.

The weakly absorbing model ($\omega_0 \sim 0.95$) shows remarkable match to observations at GSFC (39°N, 77°W). The only difference is seen during the winter and spring for the lowest τ value (0.25), where the particles are known to be larger (have less spectral dependence) than the rest of the year. Mongu (15°S, 23°E) is another site that is well represented by its assumed aerosol type (absorbing).

Beijing (39°N, 116°E) and Venice (45°N, 12°E) are interesting because dominant aerosol type is known to vary. Both sites are influenced by dust transport, so that the averaged AERONET spectral dependence should lie somewhere between the fine-dominated and coarse-dominated (dust) models. It is clear that Beijing is mixed, and is more coarse-dominated during the winter and spring. Venice is less often in the path of dust (from Africa) but its averaged spectral dependence shows the addition of coarse aerosol not represented by a fine-dominated model.

The derivation of the new set of aerosol models provides important information on characterizing the global aerosol system. Details about their derivation are important for comparison with measurements from other sensors and with models. These models have been implemented within the new aerosol algorithm, and have improved the aerosol retrieval over land (Chapter 7).

Chapter 7: The second-generation MODIS aerosol algorithm over land.

The work described in this Chapter has been accepted as *Levy et al.*, [2007b].

7.1: Motivation

Kaufman et al., [1997a] introduced the strategy for retrieving aerosol over land from MODIS, based on Eq. 3.5. Except for the surface reflectance, each term on the right hand side is a function of the Rayleigh scattering, aerosol type and aerosol loading (τ). While Eq. 3.5 is technically valid only for a dark, uniform, Lambertian surface, the bi-directional properties of the surface reflectance can be approximated by the value of the surface reflectance for the relevant solar and satellite viewing geometry [*Kaufman et al.*, 1997a]. Assuming that a small set of aerosol types and loadings can describe the range of global aerosol, the algorithm relies on a LUT to determine the conditions that best mimic the MODIS-observed spectral reflectance ρ_{λ}^m , and retrieve the associated aerosol properties (including τ and η). The key to maximal accuracy lies in making the most appropriate assumptions about both the surface and atmospheric contributions.

Since launch, the aerosol products have been continuously monitored and the algorithm improved and updated as required. Some of the improvements included bug fixes, cloud masking subroutines and pixel selection. However, comparisons with ground truth sunphotometer observations still indicated deficiencies in the algorithm that were correctable (discussed in Chapter 5). Chapter 6 derived a set of

new global aerosol models that are applicable to a MODIS-type retrieval algorithm. This chapter describes the essential components of the second-generation algorithm, performs sensitivity tests, and performs some preliminary evaluation.

7.2: MODIS and AERONET datasets

This work made extensive use of both MODIS (collection 4) and AERONET (Version 1, Level 2) data products. For MODIS, this dataset included about $\sim 10^8$ MODIS retrievals (from both Terra and Aqua) over-land obtained during 2000-2005. Of these measurements, there were about 15,000 co-locations with AERONET sun-data, at over 200 global sites, co-located in time via the technique of Ichoku *et al.*, [2002a]. A valid MODIS/AERONET match was noted when there at least five (out of a possible 25) MODIS retrievals (10 km x 10 km resolution) within the box, and at least two (out of a possible five) AERONET observations within the hour. MODIS products included the statistics (mean, standard deviation and pixel containing AERONET sites), spectral optical depth (τ_λ), the fine aerosol weighting (η), and the gas-corrected spectral reflectances used to drive the retrieval. Co-located AERONET products included the statistics (mean, standard deviation and closest in time to overpass) spectral optical depths.

Although the actual products provided by MODIS and AERONET are not necessarily physically identical, in many cases they are comparable. For example, by fitting a quadratic equation through the logarithms of τ and wavelength, AERONET τ can be interpolated to $0.55 \mu\text{m}$ [Eck *et al.*, 1999] to match directly with the MODIS retrieval. Comparison of η is trickier. Over land, MODIS considers η to be the contribution of the fine-dominated model (the non-dust model) to the total τ , the

AERONET sky retrievals designate η to be the volume contribution from aerosol below a radius of $0.6 \mu\text{m}$, whereas the O'Neill method [O'Neill *et al.*, 2005] separates fine and coarse aerosol by spectral behavior. Practically, however, the definitions of η are similar enough so that they should be correlated [Kleidman *et al.*, 2005; Anderson *et al.*, 2005; Chu *et al.*, 2005].

7.3: Creating the new LUT

The derivation of new aerosol models was discussed in Chapter 6. Cluster analysis yielded three fine-dominated, spherical, models including: a 'weakly absorbing' aerosol model ($\omega_0 \sim 0.95$), presumably corresponding to urban/industrial aerosol in the industrialized Northern Hemisphere, an 'absorbing' ($\omega_0 \sim 0.85$) aerosol model found in the known sooty and/or savanna-burning regions of South America and Africa, and a 'moderately absorbing' aerosol model representative of biomass burning and incomplete fossil fuel burning in the developing world. Similar cluster analysis of spheroid assumed retrievals yielded only one model, a coarse-dominated model that presumably represented global dust aerosol. Each aerosol 'model' is comprised of two lognormal modes, either dominated by the fine mode (the three spherical models) or the coarse mode (the spheroid model). For each model, the spectral dependence of τ and optical properties (scattering and extinction) were calculated via Mie code or T-matrix code (depending on spherical or spheroid assumptions). Based on the dominant aerosol type found during clustering, an aerosol type was 'assigned' to each AERONET site (as a function of season) and then extrapolated to include the surrounding region. These regions were mapped onto a 1°

longitude x 1° latitude grid, such that a fine aerosol type is assigned for each grid point, globally. As more information becomes available (for example, studies like [Mi *et al.*, submitted 2007]), it should be easy to update this map.

7.3.1 Choice of radiative transfer code, assumed wavelengths and Rayleigh optical depths

The c004 (and previous MODIS over-land) LUTs were calculated using ‘SPD’, the scalar version of the RT code written by *Dave et al.*, [1970], a code that is standard in the remote sensing community. However, as discussed in Chapter 5, *Fraser et al.* [1989] suggested and I confirmed [*Levy et al.*, 2004] that under some geometries, neglecting polarization would lead to significant errors in top of atmosphere reflectance, further leading to significant errors ($> 10\%$ or > 0.1) in τ retrieval. Dave also provided a vector (polarized) option to the code (VPD), although the code had not been kept up to date, and was unusable. Therefore, the choice of vector code should be well understood and suitable for creating the LUT. In scalar mode, the RT code should be consistent with the Dave benchmark. Also, it should reasonably match the *Ahmad et al.*, [1982] calculations used for the over ocean aerosol retrieval [*Remer et al.*, 2005]. Since I had used RT3 [*Evans and Stephens* [1991] for my polarization study [*Levy et al.*, 2004], I was familiar with compiling and executing the code, as well as analyzing its products. This plane-parallel adding/doubling code allows for polarization to be turned on or off, by changing only one line within an input file. Thus, it was easy to compare the results to the Dave code’s scalar mode, and then upgrade to vector mode to include polarization effects.

Under most geometries and optical depths, differences between the two RT codes are less than 0.001 (~1%).

As noted in Chapter 6, the aerosol scattering phase function elements and extinction efficiencies (that are inputs to RT3) are calculated by integrating (over size distribution) the results of Mie code (MIEV, [Wiscombe *et al.*, 1980]) or T-matrix kernel code [Dubovik *et al.*, 2002b; Dubovik *et al.*, 2006] depending on spherical or spheroid assumptions. Assuming a Rayleigh atmosphere and realistic layering of the aerosol, I computed the Legendre moments of the combined Rayleigh and aerosol, for each layer of a US Standard Atmosphere [U.S. Government, 1976]. These moments were fed into RT3 to calculate TOA reflectance and total fluxes.

While Table 3.1 represents best estimates of MODIS central wavelengths and expected Rayleigh optical depth (ROD) for each channel, the c004 algorithm over land used different values. For example, the MODIS 0.47 μm band (channel 3) stretches between 0.459 and 0.479 μm (<http://modis.gsfc.nasa.gov>). The sea-level Rayleigh optical depth (*ROD* or τ_R) drops drastically over this channel, from about 0.203 at 0.459 μm to 0.170 at 0.479 μm [Bodhaine *et al.*, 1999]. Therefore, the choice of ‘center’ wavelength to model and its associated ROD is crucial to obtaining unbiased aerosol retrieval. This is also an issue for the 0.66 μm channel (channel 1: 0.620 - 0.670 μm), but since the RODs are only about one-quarter of those at 0.47 μm , any error is much less crucial. In c004, the assumed ROD was 0.186 for channel 3 and 0.048 for channel 1. The 6S RT code [Vermote *et al.*, 1997] models the MODIS channel filter functions, and suggests that the ROD values should be more like 0.193 and 0.051, respectively for the two channels. The MODIS aerosol over

ocean algorithm [Tanré *et al.*, 1997, Ahmad *et al.*, 1982] assumes the RODs for the channels as 0.195 and 0.052, respectively. The assumptions for other channels (Table 3.1) are also consistent with those assumed over ocean.

7.3.2 Structure of the LUT

As introduced in Chapter 5, it is desirable that a new aerosol algorithm should include aerosol information in the longer wavelengths (e.g., 2.12 μm). Therefore the LUT is computed at the four weighted central wavelengths (λ of 0.466, 0.553, 0.644 and 2.119 μm) representing the MODIS channels 3, 4, 1 and 7, respectively. The aerosol model-dependent parameters of Eq. 3.5 are calculated for several values of aerosol total loadings (indexed by τ at 0.55 μm), and for a variety of geometry. Each of the spherical aerosol models (Continental, moderately absorbing, absorbing and weakly-absorbing) and the one spheroid model (dust) are represented within the LUT.

The scattering and reflectance parameters are calculated for seven aerosol loadings ($\tau_{0.55} = 0.0, 0.25, 0.5, 1.0, 2.0, 3.0,$ and 5.0). TOA reflectance is calculated for 9 solar zenith angles ($\theta_0 = 0.0, 6.0, 12.0, 24.0, 36.0, 48.0, 54.0, 60.0$ and 66.0), 16 sensor zenith angles ($\theta = 0.0$ to 65.8 , approximate increments of 6.0 , based on Lobatto quadrature with 8 abscissa points (e.g., <http://mathworld.wolfram.com/LobattoQuadrature.html>)), and 16 relative azimuth angles ($\phi = 0.0$ to 180.0 increments of 12.0). All of these parameters are calculated assuming a surface reflectance of zero. These are similar to the indices and geometry calculated for c004 LUT.

When surface reflectance is present, the second term in Eq. 3.5 is nonzero. The flux is a function only of the atmosphere, however, the atmospheric

backscattering term, s , and the transmission term, T , are functions of both the atmosphere and the surface. Therefore, RT3 was run two additional times with distinct positive values of surface reflectance.

$$\begin{aligned}
 s &= (1/\rho_1^s)(1 - (F_d T \rho_1^s / (\rho^* - \rho^a))) \\
 &\quad \text{and} \\
 s &= (1/\rho_2^s)(1 - (F_d T \rho_2^s / (\rho^* - \rho^a)))
 \end{aligned}
 \tag{7.1}$$

Here, values of 0.1 and 0.25 were chosen for the surface reflectances ρ_1^s and ρ_2^s . These two equations can be solved for the two unknowns, s and T . These values of F_d , s , and T are included within the LUT, for each indexed value of τ .

7.4: VISvs2.12 surface reflectance

When performing atmospheric retrievals from MODIS or any other passive satellite sensor, the major challenge is separating the total observed reflectance into atmospheric and surface contributions (e.g., Eq. 3.4), and then defining the aerosol contribution. Over the open ocean, the surface reflectance is nearly zero in the 0.66 μm and longer wavelength channels, so that assuming negligible surface reflectance in these channels is a good approximation. Moving from coastline onto land, however, the surface reflectance in 0.66 μm and longer channels can be far from zero and vary over surface type. As the land surface and the atmospheric signals are comparable, errors of 0.01 in assumed surface reflectance can lead to errors on the order of 0.1 in τ retrieval [Kaufman *et al.*, 1997b]. Errors in multiple wavelengths can lead to poor retrievals of spectral τ , which in turn are useless for estimating size parameters.

As discussed in Chapter 5, a single set of VISvs2.12 ratios is not globally applicable. Some surfaces exhibit strong bi-directional reflectance functions (BRF). *Gatebe et al.*, [2001] flew the Cloud Absorption Radiometer at low altitudes over different vegetated surfaces and found not only did VISvs2.12 vary by surface type, but also as a function of angle. In fact VISvs2.12 ratios often greatly differed from the one-to-four and one-to-two values assumed by the c004 algorithm. Also, *Remer et al.*, [2001] noted that VISvs2.12 varied as a function of scattering geometry. Thus, an improved global aerosol retrieval algorithm requires estimates of surface reflectance that include surface type and angular variability.

Application of modeled surface type and global maps of measured spectral albedo (like those described by [*Moody et al.*, 2004]) were explored, but they are not necessarily representative of the directional surface reflectance. Yet, the combined MODIS/AERONET data sets, developed since 2000, contain information that can be used for developing empirical surface reflectance relationships. Before *Terra* launch such data were unavailable.

7.4.1 Atmospheric correction of c004 MODIS/AERONET co-located products

Atmospheric correction [*Kaufman and Sendra*, 1988] attempts to calculate the optical properties of the surface, by theoretically subtracting the effects of the atmosphere from the satellite-observed radiation field. One needs to assume the optical properties of the intervening atmosphere, including all aerosol and non-aerosol components. In addition to knowing or assuming all atmospheric

components, accurate radiative transfer (RT) is also required. The atmospherically corrected surface reflectance ρ_{λ}^s is calculated by re-arranging Eq. 3.5.

In order to minimize errors arising from multiple scattering by the aerosol, the atmospheric corrections should be limited to conditions of low τ (e.g., $\tau < 0.2$). Out of the original 15,000 co-located MODIS/AERONET points (described in section 2), there were over 10,000 collocations with low τ ($\tau_{0.55} < 0.2$). The archive included the ‘gas absorption corrected’ MODIS-Level 2 observed reflectance (average over 50 x 50 km as well as the 10km box nearest the AERONET site), as well as AERONET-observed (L2A) spectral τ_{λ} and column water vapor depth (both averages over 1 hour, and observation nearest in time to MODIS overpass). The closest 10 km MODIS box and nearest AERONET observation were used for atmospheric correction. The molecular properties of the atmosphere were assumed those of the U.S. standard atmosphere [1976], with the Rayleigh optical depth (ROD) values scaled from sea level values, according to the elevation/air pressure of the sunphotometer.

The relationship between the satellite-measured reflectance and the surface reflectance is a complicated function of the atmospheric effects of scattering and absorption by the aerosol. Previous atmospheric correction exercises assumed some form of the Continental aerosol model (e.g., *Vermote et al.* [1997]) to describe both the scattering and absorption properties. While this model may provide reasonable simulations in channels near to 0.55 μm (such as 0.47 and 0.66 μm), it cannot be expected to provide accurate simulations at 2.12 μm , even for low τ . For example, for $\tau_{0.55} = 0.2$, $\tau_{2.12}$ ranges from 0.03 to 0.16, depending on whether fine or coarse

dominated aerosol is assumed. Thus, assuming the wrong aerosol size in the correction procedure will lead to errors in estimating 2.12 μm surface reflectance.

Therefore, the AERONET-derived Ångström exponent (α) was used to decide which aerosol type to assume. In the 4200 cases where $\alpha > 1.6$, the atmospheric correction assumed a fine-dominated model, specifically the ‘moderately absorbing’ model ($\omega_0 \sim 0.9$). When $\alpha < 0.6$ (400 cases), the correction procedure assumed the coarse-dominated model. Co-locations where $0.6 < \alpha < 1.6$ (about 6000 cases) were not used due to uncertainties of aerosol mixing.

The atmospheric correction resulted in two datasets: surface reflectance at three wavelengths (0.47, 0.66, 2.12 μm) for each of the two regimes (fine and coarse-dominated). Separate comparison of 0.66 μm versus 2.12 μm and 0.47 μm versus 2.12 μm , for each regime indicated that their regressions differed by less than 10% (both slope and y-offset values), suggesting to combine the two surface reflectance datasets into one.

7.4.2 Mean values of VISvs2.12 surface reflectance relationships

Atmospheric correction was performed on the 4600 MODIS/AERONET co-locations having AERONET-observed $\tau_{0.55} < 0.2$ and either $\alpha < 0.6$ or $\alpha > 1.6$. Fig. 7.1a plots the regressions of corrected 0.47 μm and 0.66 μm surface reflectance, each versus the corrected 2.12 μm surface reflectance. Note both slope and y-offset. The presence of the y-offset is important, because even in the darkest, most water-laden

vegetation, zero reflectance at 2.12 μm does not imply zero surface reflectance in the visible channels (e.g., *Kaufman et al.*, [2002]).

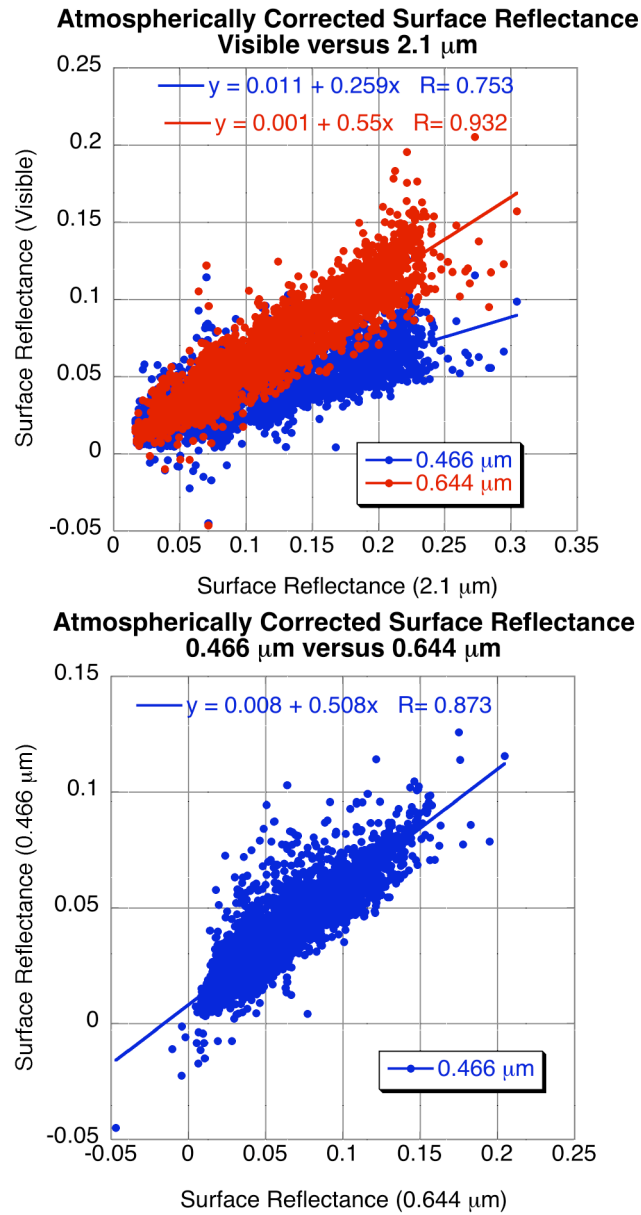


Figure 7.1: Atmospherically corrected surface reflectance in the visible (0.47 and 0.66 μm channels) compared with that in the 2.12 μm SWIR channel (top), and the 0.47 μm compared with that in the 0.66 μm channel (bottom). (Figure adapted from *Levy et al.*, [2007b])

Correlation (R) values are 0.93 for the 0.66vs2.12 μm channel regression, but only about 0.75 for 0.47vs2.12. For 0.47vs2.12, including the offset (about +0.011) yields a slope close to one-quarter (0.258). For 0.66vs2.12, the offset is near zero, but the slope is greater than one-half (0.55). Thus in a mean sense, atmospheric correction of MODIS data yields VISvs2.12 surface reflectance relationships that differ from the assumed c004 VISvs2.12 ratios.

The relationship of 0.47 to 0.66 μm ('0.47vs0.66') may be stronger than 0.47vs2.12 because it has higher correlation ($R = 0.87$) and less scatter (Fig. 7.1b). This suggests that the 0.47 μm surface reflectance should be estimated indirectly via 0.66 μm , rather than directly from 2.12 μm . In other words, the algorithm should first estimate 0.66 μm from 2.12 μm , then estimate 0.47 μm from 0.66 μm , i.e.

$$\begin{aligned} \rho_{0.66}^s &= f(\rho_{2.12}^s) \\ \rho_{0.47}^s &= g(\rho_{0.66}^s) \end{aligned}, \quad (7.2)$$

where $f()$ and $g()$ are different relationships. To test whether the relationships shown in Fig. 7.1 are dependent on the formulation data set, similar regressions were performed on a subset of the data where AERONET-measured $\tau < 0.1$ (2508 cases). The results show differences in both slope and y-offset of less than 1%, suggesting that the average VISvs2.12 relationship (displayed in Fig. 7.1) is robust.

7.4.3 Variability of VISvs2.12 surface reflectance relationships: Angle

However, Fig. 7.1 shows that the VISvs2.12 surface reflectance relationship displays large scatter. For example, if surface reflectance is 0.15 at 2.12 μm ,

applying the regressed relationships of 0.66vs2.12 and 0.47vs0.66 results in estimates of surface reflectance of 0.083 ± 0.03 at $0.66 \mu\text{m}$ and 0.050 ± 0.03 at $0.47 \mu\text{m}$.

Obviously, this could result in very large errors in retrieved τ , on the order of 0.3 or more. Therefore, to reduce the scatter we look for dependencies on other parameters to refine the relationships.

The VISvs2.12 surface reflectance relationships are angle dependent [Remer *et al.*, 2001]; Gatebe *et al.*, 2001; Lypustin *et al.*, 2001]. Out of different possible angle parameters (solar zenith angle, sensor zenith angle, glint angle or scattering angle), the scattering angle has the largest individual influence on the VISvs2.12 relationship.

The Fig. 7.1 data were sorted according to scattering angle and put into 20 groups of equal size (about 230 points for each scattering angle bin). Fig. 7.2a displays the median values of surface reflectance in each bin as a function of scattering angle, and shows a definite relationship at $2.12 \mu\text{m}$, less at $0.66 \mu\text{m}$, and nearly none at $0.47 \mu\text{m}$. Since Fig. 7.1 noted a slope and y-offset for both VISvs2.12 relationships, I suspected that slope and offset might depend on scattering angle. Fig. 7.2 (b-d) plots the slope, y-offset and correlation of the surface reflectance relationships calculated in each scattering angle bin and plotted as a function of scattering angle. The 0.66vs2.12 regression slope (r_{0660} in the Figure) shows dependence on scattering angle, whereas the 0.47vs0.66 regression slope (r_{VIS} in the Figure) shows nearly none. Both y-intercepts show strong dependence on scattering angle.

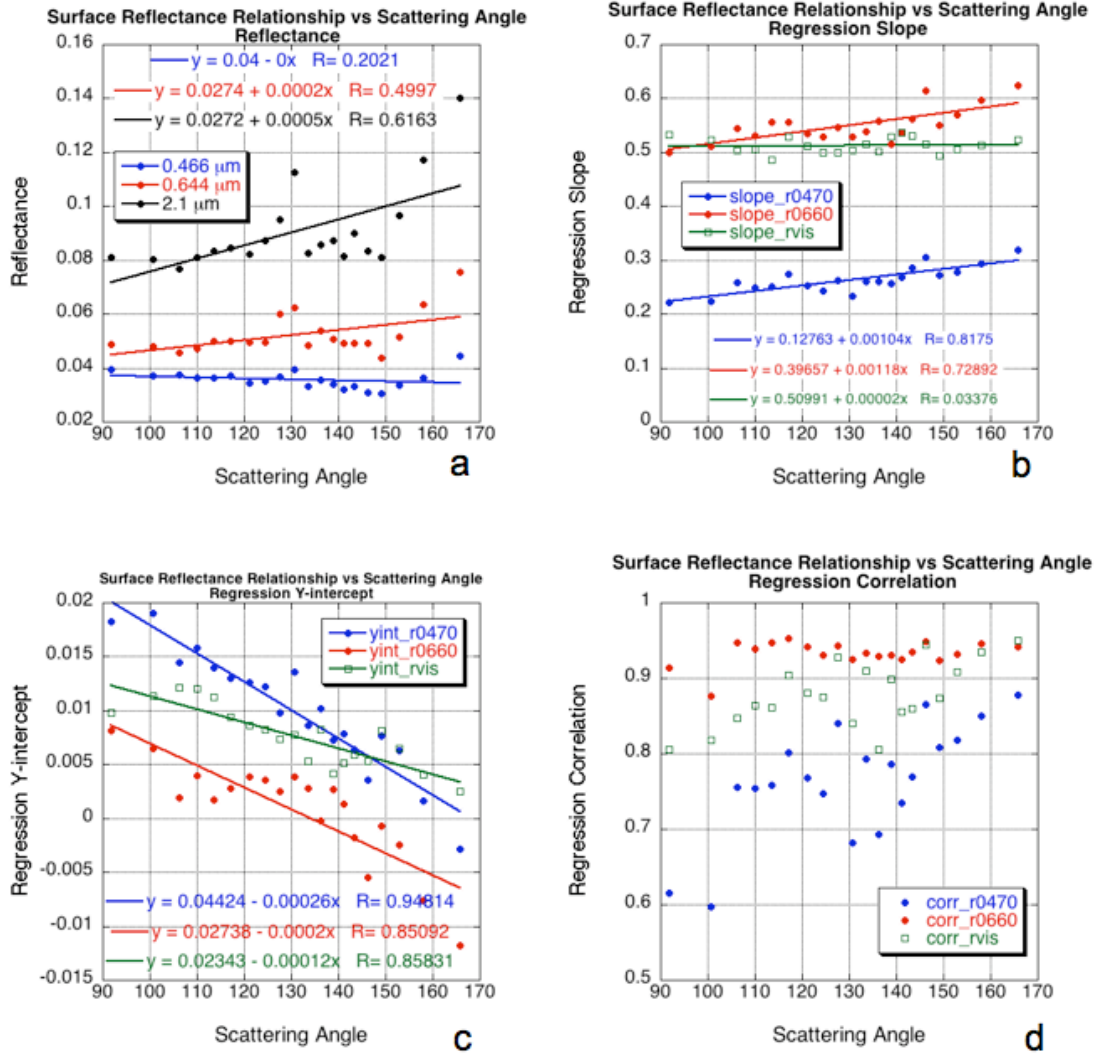


Figure 7.2: VISvs2.12 surface reflectance relationships as a function of scattering angle. The data were sorted according to scattering angle and put into 20 groups of equal size (about 230 points for each scattering angle bin). On all subplots, each point is plotted for the median value of scattering angle in the bin. Part (a) plots median values of reflectance at each channel as a function of the scattering angle. Linear regression was calculated for the 230 points in each group. The slope of the regression (for each angle bin) is plotted in (b), the y-intercept is plotted in (c) and the regression correlation is plotted in (d). Note for (b), (c) and (d) that 0.47 μm vs 2.12 μm (r0470) is plotted in blue, 0.66 μm vs 2.12 μm (r0660) is plotted in red and 0.47 vs 0.66 μm (rvis) is plotted in green. Figure adapted from *Levy et al.*, [2007].

7.4.4 Variability of VISvs2.12 surface reflectance relationships: Surface type and NDVI_{SWIR}

Because AERONET sites are located in different surface type regimes, it could be expected that the VISvs2.12 surface relationships will vary based on surface type and/or season. Using the International Geosphere/Biosphere Programme's (IGBP) scene map of USGS surface types and formatted for MODIS validation (<http://edcdaac.usgs.gov/modis/mod12c1v4.asp>), scene type of the MODIS/AERONET validation box was determined. Urban and non-urban retrievals were separated and grouped into season (winter or summer) and into general location (mid-latitude or tropical). Different surface types display different VISvs2.12 relationships. Generally, more vegetated surfaces (midlatitude summer sites both urban and nonurban) have higher 0.66vs2.12 surface reflectance ratios (ratio > 0.55) than winter sites or tropical savannas and grasslands (ratio < 0.55). Except for the urban sites during summer (ratio ~ 0.766), the 0.47vs0.66 surface reflectance ratio is relatively consistent (ratio ~ 0.52). The relationship of the surface reflectance ratios to known surface condition suggests a relationship to its vegetation amount/condition or 'greenness.'

Except for urban areas, most surfaces seem to have VISvs2.12 surface reflectance relationships that may be related to a vegetation index (VI). The well-known Normalized Difference Vegetation Index (NDVI), defined as a function of the red (0.66 μm – channel 1) and near-IR (0.86 μm – channel 2), are influenced by aerosol, negating its usefulness for determining surface type. We attempted to work with other VIs (such as described by *Karnieli et al.*, [2000]) that have different

sensitivity to atmospheric (aerosol) conditions, and found the most promising to be the $NDVI_{SWIR}$, defined as:

$$NDVI_{SWIR} = (\rho_{1.24}^m - \rho_{2.12}^m) / (\rho_{1.24}^m + \rho_{2.12}^m) \quad (7.3)$$

where $\rho_{1.24}$ and $\rho_{2.12}$ are the MODIS-measured reflectances of the 1.24 μm channel (MODIS channel 5) and the 2.12 μm channel (channel 7). These longer wavelengths are much less influenced by aerosol (except for heavy aerosol or dusts), and thus are potentially most useful for estimating surface condition. This VI is also known as $NDVI_{MIR}$ (Mid-InfraRed) (e.g., Karnieli *et al.*, [2000]). In aerosol free conditions $NDVI_{SWIR}$ is highly correlated with regular $NDVI$. A value of $NDVI_{SWIR} > 0.6$ is relative to more active vegetation, whereas $NDVI_{SWIR} < 0.2$ is representative of dormant or sparse vegetation. Fig. 7.3 plots the relationship of the 0.66 μm channel and 2.12 μm channel (atmospherically corrected) surface reflectance relationship for non-urban sites, as a function of low, medium and high values of $NDVI_{SWIR}$. As the $NDVI_{SWIR}$ increases, the ratio between 0.66 μm and 2.12 μm surface reflectance increases.

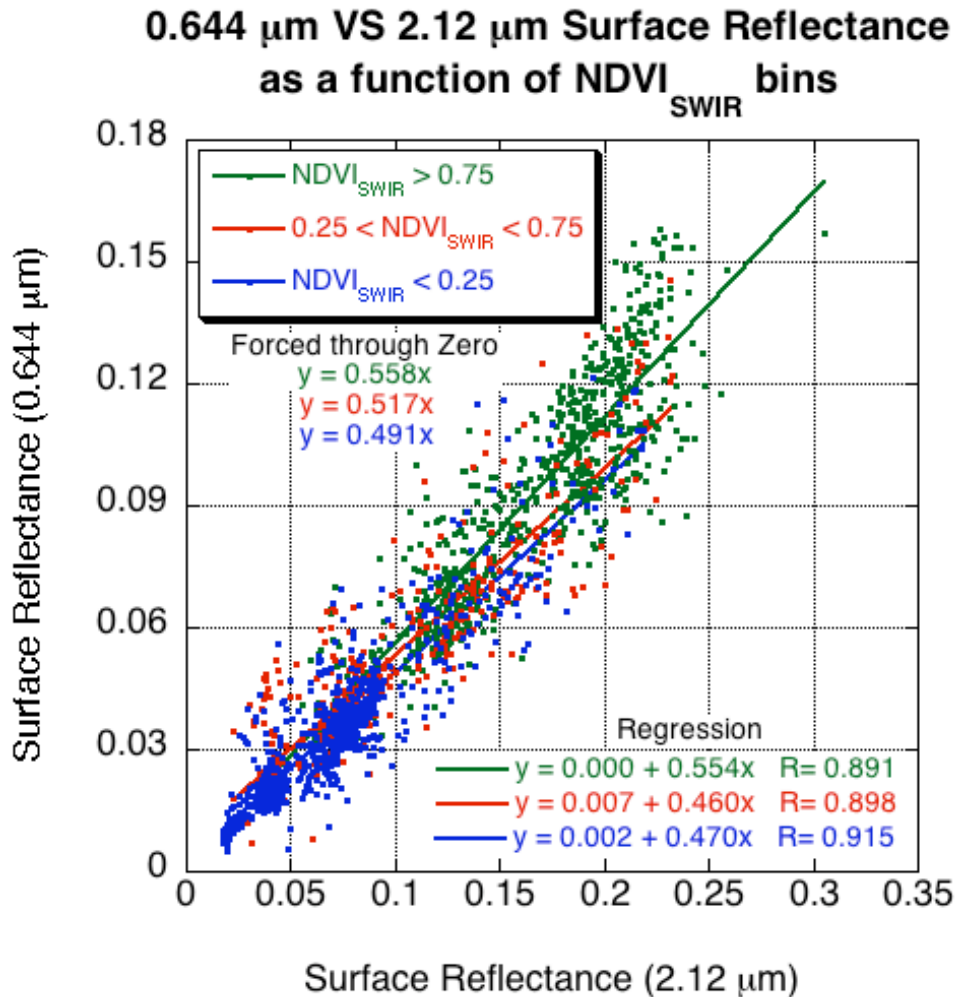


Figure 7.3: 0.66 μm versus 2.12 μm surface reflectance as a function of bins of $\text{NDVI}_{\text{SWIR}}$ values. The standard regression is plotted, with regression Eq.s given in the lower right hand corner. The ratios (if forced through zero) are given beneath the legend. Blue refers to low $\text{NDVI}_{\text{SWIR}}$, red to medium and green to high values. Figure from *Levy et al.*, [2007b]

7.4.5 Final parameterization of VISvs2.12 surface reflectance relationships

Results of the global atmospheric correction exercise imply that not only do the VISvs2.12 surface relationships differ from the ratios assumed by the c004 algorithm, they also have a strong dependence on both geometry and surface type.

Therefore, the VISvs2.12 surface reflectance relationship is parameterized as a function of both $NDVI_{SWIR}$ and scattering angle Θ , such that Eq. (7.2) can be expanded into:

$$\begin{aligned}\rho_{0.66}^s &= f(\rho_{2.12}^s) = \rho_{2.12}^s * slope_{0.66/2.12} + yint_{0.66/2.12} \\ &\text{and} \\ \rho_{0.47}^s &= g(\rho_{0.66}^s) = \rho_{0.66}^s * slope_{0.47/0.66} + yint_{0.47/0.66}\end{aligned}\tag{7.4}$$

where

$$\begin{aligned}slope_{0.66/2.12} &= slope_{0.66/2.12}^{NDVI_{SWIR}} + 0.002\Theta - 0.27, \\ yint_{0.66/2.12} &= -0.00025\Theta + 0.033, \\ slope_{0.47/0.66} &= 0.49, \text{ and} \\ yint_{0.47/0.66} &= 0.005\end{aligned}\tag{7.5}$$

where in turn

$$\begin{aligned}slope_{0.66/2.12}^{NDVI_{SWIR}} &= 0.48; NDVI_{SWIR} < 0.25, \\ slope_{0.66/2.12}^{NDVI_{SWIR}} &= 0.58; NDVI_{SWIR} > 0.75 \\ slope_{0.66/2.12}^{NDVI_{SWIR}} &= 0.48 + 0.2(NDVI_{SWIR} - 0.25); 0.25 \leq NDVI_{SWIR} \leq 0.75\end{aligned}\tag{7.6}$$

If the relationships described by Fig. 7.1 are considered global average relationships, then the above parameterization describes perturbations for angle and land type. Note that while the parameterization is based on the results of Figs. 7.1, 7.2 and 7.3, the coefficients are not identical to those shown in the Figures. Even though the atmospheric corrected data set is the broadest and most comprehensive representation of global surface reflectance relationships, it is limited to AERONET

site locations, which in turn are mostly concentrated in certain geographical regions (<http://aeronet.gsfc.nasa.gov>). Trial and error was used to modify the basic results from the AERONET-based atmospheric correction, to give the best statistics of MODIS retrievals globally, (especially in places where few or no AERONET sites are located). The parameterization derives more accurate estimates of surface reflectance on average, than those estimated using fixed ratios.

7.4.6 Notes on VISvs2.12 surface reflectance relationship errors

Note that even with the surface reflectance parameterization, there still will be errors in estimating surface reflectance. According to the MODIS Land Surface Reflectance Homepage (<http://modis-sr.ltdri.org/html/prodacc.htm>), improper aerosol model assumptions can lead to errors in atmospherically corrected reflectance on the order of 0.002 in the 0.47 and 0.66 μm channels, and 0.006 at 2.12 μm . The errors are especially large at 2.12 μm due to potentially choosing a fine-dominated model instead of a coarse-dominated model (or vice-versa). However, since this study pre-determined the choice of fine or coarse-dominated aerosol models via the AERONET-observed Ångström exponent, errors at 2.12 μm should be much less, dependent on the choice of fine-dominated aerosol model. For $\tau_{0.55}=0.5$, the difference in spectral optical thickness between the moderately absorbing model ($\omega_0\sim 0.90$) and absorbing model ($\omega_0\sim 0.85$) is about 0.02, 0.02 and 0.002, respectively in the 0.47, 0.66 and 2.12 μm channels (e.g., Fig. 6.5b). On average, this would be equivalent to errors of about 0.002, 0.002 and 0.0002, respectively in surface reflectance, but would vary according to the differences in phase function. Regardless, the error at 2.12 μm is small enough so that the derived surface

reflectance relationship should be reasonably robust, even when a model with wrong ω_0 was assumed.

Of course, other errors may creep into the surface reflectance parameterization. These include, but are not limited to additional surface BRF effects lost during averaging over scattering angle and errors due to MODIS instrument calibration. These errors can cause reflectance errors that are similar in magnitude to those caused by improper aerosol model assumptions.

7.5: Inversion of spectral reflectance, including 2.12 μm

A major limitation of the c004 algorithms was that aerosol is assumed transparent in the 2.12 μm channel. Under a dust aerosol regime, aerosol transparency is an extremely poor assumption. Even in a fine aerosol dominated regime, τ is not zero. For the moderately absorbing aerosol model ($\omega_0 \sim 0.90$), $\tau_{0.55} = 0.5$ corresponds to $\tau_{2.12} \sim 0.05$, corresponding to an error in 2.12 μm path reflectance of about 0.005. Via the VISvs2.12 reflectance relationship, the path reflectance error at 0.66 μm is on the order of 0.003, leading to ~ 0.03 error in retrieved τ . As a percentage of the actual τ , the error is not very large. However, combined with errors at 0.47 μm , the resulting error in spectral dependence leads to error in estimating η .

In the spirit of the MODIS aerosol over ocean algorithm [Tanré *et al.*, 1997], an over-land multi-channel reflectance inversion is developed. Analogous to the ocean algorithm's combination of fine and coarse aerosol *modes*, the new land algorithm attempts to combine fine-dominated and coarse-dominated aerosol *models* (each bi-modal) to match with the observed spectral reflectance. The 2.12 μm channel is assumed to contain both surface and aerosol information, and the visible

surface reflectance is a function of the VISvs2.12 surface reflectance relationships derived in section 7.4. Simultaneously inverting the aerosol and surface information in the three channels (0.47 μm , 0.66 μm and 2.12 μm) yields something greater than 2 pieces of information. With some assumptions, three parameters can be derived: $\tau_{0.55}$, $\eta_{0.55}$ and the surface reflectance ($\rho_{2.12}^s$).

Retrieval: The Inversion

Calculate amount τ and weighting η of fine-dominated model (to total τ), combined with the surface reflectance ρ_s , that best matches the observed spectral reflectance (0.47, 0.66 and 2.1 μm)

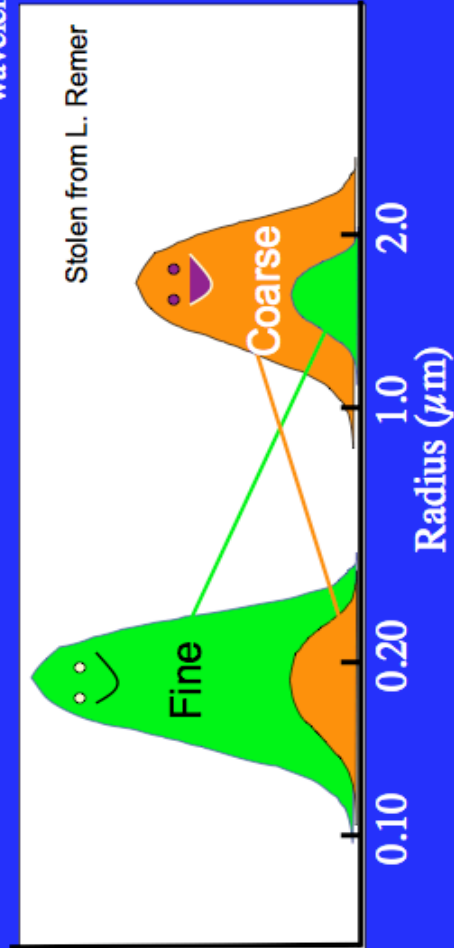
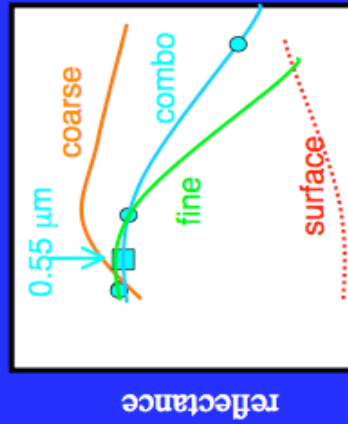


Fig 7.4: Cartoon of inversion technique. Observed reflectance in three channels is represented by turquoise dots in the small sub-figure. Green represents fine-dominated model (and its induced path reflectance), whereas orange represents coarse-dominated model (and its induced path reflectance). Red denotes surface reflectance. The combination of fine, coarse and surface (combo) is the turquoise square and spectral dependence curve that most closely matches the observations (dots). The ‘ghostlike’ modal creatures were adapted from those imagined by Lorraine Remer.

Eq. 3.5 can be rewritten, noting that the calculated spectral total reflectance ρ_{λ}^* at the top of the atmosphere is the weighted sum of the spectral reflectance from a combination of fine and coarse –dominated aerosol models, i.e.,

$$\rho_{\lambda}^* = \eta \rho_{\lambda}^{*f} + (1 - \eta) \rho_{\lambda}^{*c} \quad (7.7)$$

where ρ_{λ}^{*f} and ρ_{λ}^{*c} are each composites of surface reflectance ρ_{λ}^s and atmospheric path reflectance of the separate aerosol models. That is:

$$\begin{aligned} \rho_{\lambda}^{*f} &= \rho_{\lambda}^{af} + F_{d\lambda}^f T_{\lambda}^f \rho_{\lambda}^s / (1 - s_{\lambda}^f \rho_{\lambda}^s) \\ &\text{and} \\ \rho_{\lambda}^{*c} &= \rho_{\lambda}^{ac} + F_{d\lambda}^c T_{\lambda}^c \rho_{\lambda}^s / (1 - s_{\lambda}^c \rho_{\lambda}^s) \end{aligned} \quad (7.8)$$

where ρ_{λ}^{af} and ρ_{λ}^{ac} are the fine and coarse model atmospheric path reflectance, $F_{d\lambda}^f$ and $F_{d\lambda}^c$ are normalized downward fluxes for zero surface reflectance, T_{λ}^f and T_{λ}^c represent upward total transmission into the satellite field of view, and s_{λ}^f and s_{λ}^c are atmospheric backscattering ratios. The weighting parameter, η of Eq. 7.7 is defined for $\lambda = 0.55 \mu\text{m}$. *Remer et al.* [2005] explains how this parameter also represents the fraction of the total optical thickness at $0.55 \mu\text{m}$ contributed by fine (non-dust) aerosol. Note the angular and τ dependence of some of the terms: $\rho^a = \rho^a(\tau, \theta_0, \theta, \phi)$, $F = F(\tau, \theta_0)$, $T = T(\tau, \theta)$, $s = s(\tau)$ and $\rho^s = \rho^s(\theta_0, \theta, \phi)$. Whereas the other terms are a function of the aerosol properties (not aerosol amount or geometry) and are contained within the LUT. The surface reflectance is independent of the aerosol, but dependent on the geometry. In practical terms, we parameterize the surface reflectance using the VISvs2.12 surface reflectance relationships, which assumes it is a function of scattering angle and vegetation index.

Although the second-generation algorithm is intended to be a package that includes many modifications from the c004 algorithm (inversion + models + surface reflectance assumptions), a sanity check can be performed by running the new inversion with old models + surface reflectance assumptions. Fig. 7.5 evaluates only the new inversion technique by assuming c004 aerosol models and c004 VISvs2.12 ratios. The MODIS and AERONET observations were taken from Terra over South America, between 2000 and 2003. Differences between the new 3-channel inversion and old two-channel technique for deriving τ are negligible, whereas the new inversion tends to show some additional sensitivity to η (at least when τ is large > 0.5). Since previous sections of this dissertation explained improvements in the other algorithm updates, from here on, the second-generation algorithm includes all changes.

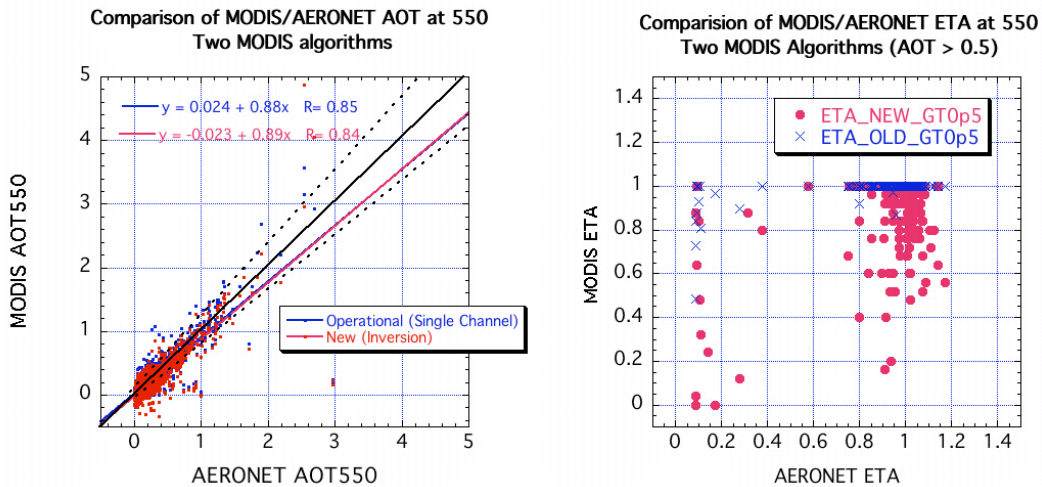


Fig 7.5: Evaluation of 3-channel inversion (red) versus 2-channel technique (blue) for deriving τ (AOT - left) and η (ETA - right) at $0.55 \mu\text{m}$. Both are compared to AERONET (preliminary O'Neill method for η) Regression curves for τ show little difference between the two algorithms, however there may be some extra sensitivity to η . Note the use of c004 assumptions for aerosol model properties and surface reflectance relationships.

Due to the limited set of aerosol optical properties in the lookup table, the equations may not have exact solutions, and solutions may not be unique. In order to reduce the possibility of non-unique retrievals the algorithm attempts to fit with discrete values of η . Upon completion, the retrieval is assigned a Quality Assurance ‘confidence’ (QAC) value that ranges from 0 (bad quality) to 3 (good quality). This QAC flag is used for creation of Level 3 (gridded) products and for combining land retrievals with concurrent over-ocean aerosol retrievals into ‘joint products’ (see [MAST, 2006] and [Hubanks *et al.*, 2005] for more details).

7.5.1 Selection of “dark pixels”

Fig. 7.6 illustrates the main steps of the second-generation land algorithm. The procedure collects Level 1 B (L1B) spectral reflectance in eight wavelength bands (Table 3.1, plus 1.37 μm) at their finest spatial resolutions, as well as associated geo-location information. These L1B reflectance values are corrected for water vapor, ozone, and carbon dioxide obtained from ancillary NCEP analysis data files. Details of this gas correction and cloud masking are found online [MAST, 2006]. Basically, the high resolution (20 x 20 at 500 m resolution) pixels in the 10 km x 10 km box are evaluated pixel by pixel to identify whether the pixel is suitable for aerosol retrieval. Clouds [Martins *et al.*, 2002], snow/ice [Li *et al.*, 2004] and inland water bodies (via NDVI tests) are considered not suitable and are discarded.

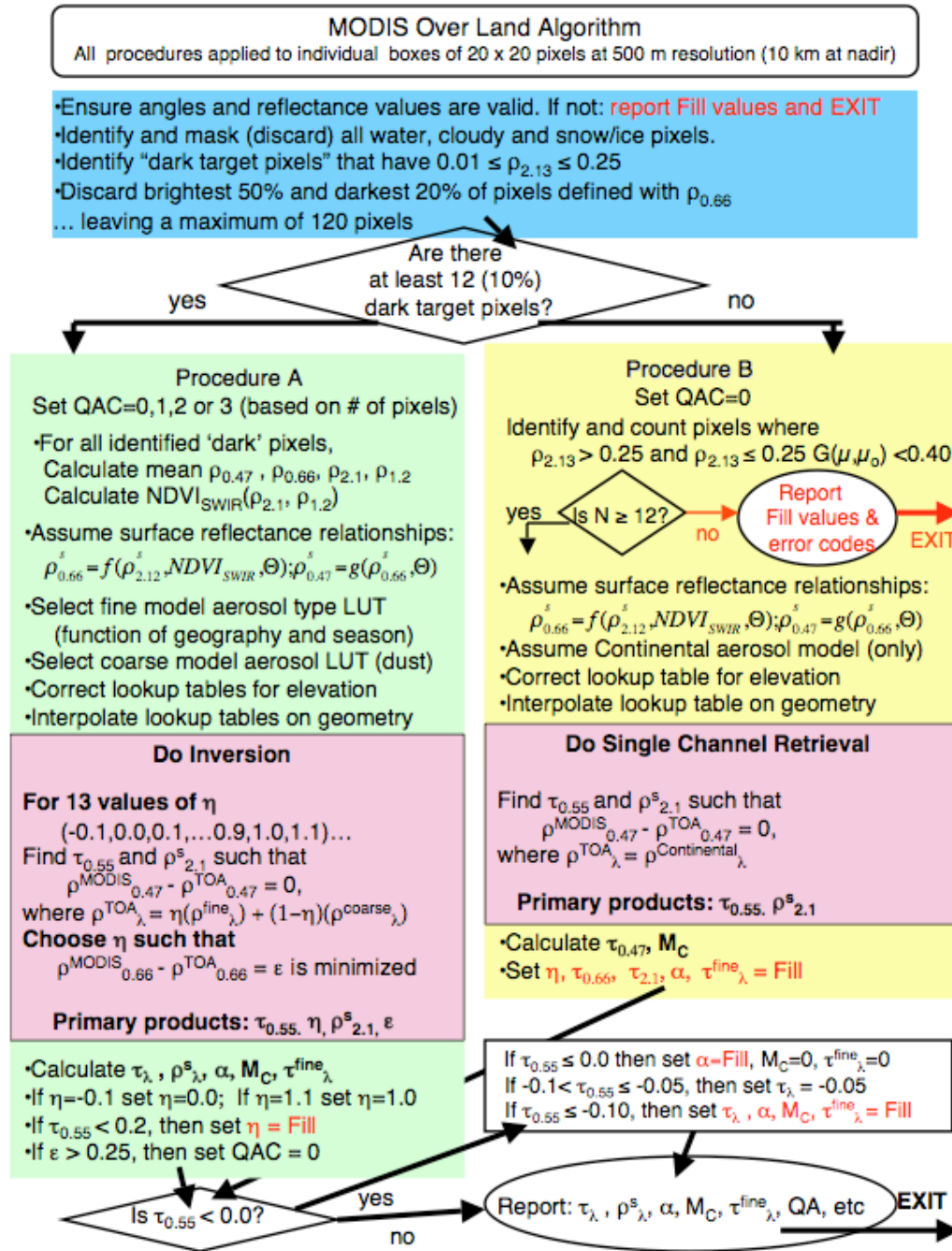


Fig. 7.6: Flowchart illustrating the derivation of aerosol over land for the new algorithm. Figure adapted from Levy et al., [2007].

The non-masked pixels are checked for their brightness. Pixels having measured 2.12 μm reflectance between 0.01 and 0.25 are grouped and sorted by their 0.66 μm reflectance. The brightest (at 0.66 μm) 50% and darkest 20% are discarded, in order to reduce cloud and surface contamination and scale towards darker targets. If there are at least 12 pixels remaining (10% of 30% of the original 400), then the reflectance in each channel is averaged, yielding the “MODIS-measured” spectral reflectance $\rho^m_{0.47}$, $\rho^m_{0.66}$, $\rho^m_{2.12}$, and $\rho^m_{1.24}$. These reflectance values are used for Procedure A. If less than 12 pixels remain, then Procedure B (described later) is followed.

7.5.2 Correcting the LUT for elevation

A major change from the c004 algorithm concerns how the algorithm corrects for elevated surface targets. The sea-level Rayleigh optical depth (ROD , $\tau_{R,\lambda}$) at a wavelength λ (in μm) can be approximated over the visible range [Dutton *et al.*, 1994]; Bodhaine *et al.*, 1999] by

$$\tau_{R,\lambda} = 0.00877\lambda^{-4.05} \quad (7.9)$$

When not at sea level (pressure = 1013 mb), the ROD is a function of pressure (or height, z) so that it can be approximated by:

$$\tau_{R,\lambda}(z = Z) = \tau_{R,\lambda}(z = 0)\exp\left(\frac{-Z}{8.5}\right) \quad (7.10)$$

where Z is the height (in kilometers) of the surface target and 8.5 km is the exponential scale height of the atmosphere. The difference between ROD at $z=0$ and $z=Z$ is $\Delta\tau_{R,\lambda}$.

In c004, the algorithm (too) simply corrected the retrieved τ product by adding the optical depth that was neglected by assuming sea level for the retrieval, (i.e. $\tau_\lambda(z = Z) = \tau_\lambda(z = 0) + \Delta\tau_{R,\lambda}$). However, this correction can give poor results because of the large differences between molecular and aerosol phase functions. Instead, the new algorithm makes use of the procedure described in *Fraser et al.*, [1989], adjusting the lookup table to simulate different ROD by adjusting the wavelength. Substitution of Eq. 7.10 into Eq. 7.9 yields

$$\lambda(z = Z) = \lambda(z = 0) \exp\left(\frac{Z}{34}\right). \quad (7.11)$$

For example, at $Z = 0.4$ km, λ increases by about 1.2%. For the blue 0.47 μm channel, (centered at 0.466 μm) this means that $\tau_{R,\lambda}(z = 0) = 0.194$, $\tau_{R,\lambda}(z = 0.4) = 0.185$ and $\lambda(z = 0.4) = 0.471$ μm . In other words, the algorithm simulates a 0.4 km elevated surface by adjusting the blue channel's wavelength to 0.471 μm . Assuming that gases and aerosols are optically well mixed in altitude, the parameter values of a 0.471 μm LUT can be acquired by interpolating (linearly as functions of log wavelength and log parameter) between the 0.47 μm (0.466 μm) and the 0.55 μm (0.553 μm) entries. Similar interpolations are performed for the other channels (for example, 0.55 μm would be adjusted to 0.559 μm). For the 0.4 km case, this means that lower values of TOA atmospheric path reflectance and higher values of transmission are chosen to represent a given aerosol model's optical contribution. However, also note that since the 0.55 μm channel has also been adjusted, the associated values of the τ indices have been adjusted accordingly. In other words, the algorithm retrieves aerosol optical depth at the adjusted wavelength,

which is equivalent to retrieving τ down to the surface elevation height. For highly elevated terrain (e.g., $Z = 4$ km), ROD decreases by 40%, resulting in a channel equivalent wavelength increase of 10%.

Whereas most global land surfaces are at sea level or above, a few locations are below sea level ($Z < 0$). In these cases, the algorithm is allowed to extrapolate below $0.466 \mu\text{m}$. Since the extrapolation is at most for a hundred meters or so, this is not expected to introduce large errors, and these cases can still be retrieved. Note also that due to the extremely low ROD in the $2.12 \mu\text{m}$ channel, little is gained by adjusting this channel.

7.5.3 Procedure A: Inversion for dark surfaces

If following Procedure A (for dark surfaces), the QAC is initially set to a value between 0 (bad quality) and 3 (good quality), depending on the number of dark pixels remaining. In Procedure A, the algorithm assigns the fine aerosol model, based on the location and season. From the lookup table, ρ^a , F , T and s (for the fine model and coarse model separately) are interpolated for angles (θ_0 , θ and ϕ), resulting in six values for each parameter, each one corresponding to a different aerosol loading (indexed by τ at $0.55 \mu\text{m}$).

The $2.12 \mu\text{m}$ path reflectance is a non-negligible function of the τ , so that the surface reflectance is therefore also a function of the τ . For discrete values of η between -0.1 and 1.1 (intervals of 0.1), the algorithm attempts to find the τ at $0.55 \mu\text{m}$ and the surface reflectance at $2.12 \mu\text{m}$ that exactly matches the MODIS measured

reflectance at 0.47 μm . There will be some error, ε , at 0.66 μm . The solution is the one where the error at 0.66 μm is minimized. In other words,

$$\begin{aligned}\rho_{0.47}^m - \rho_{0.47}^* &= 0 \\ ABS(\rho_{0.66}^m - \rho_{0.66}^*) &= \varepsilon\end{aligned}\quad (7.12abc)$$

$$\rho_{2.12}^m - \rho_{2.12}^* = 0$$

where

$$\begin{aligned}\rho_{2.12}^* &= \eta(\rho_{2.12}^{fa} + F_{d,2.12}^f T_{2.12}^f \rho_{2.12}^f / (1 - s_{2.12}^f \rho_{2.12}^s)) + (1 - \eta)(\rho_{2.12}^{ca} + F_{d,2.12}^c T_{2.12}^c \rho_{2.12}^c / (1 - s_{2.12}^c \rho_{2.12}^s)) \\ \rho_{0.66}^* &= \eta(\rho_{0.66}^{fa} + F_{d,0.66}^f T_{0.66}^f f(\rho_{2.12}^s) / (1 - s_{0.66}^f f(\rho_{2.12}^s))) + (1 - \eta)(\rho_{0.66}^{ca} + F_{d,0.66}^c T_{0.66}^c f(\rho_{2.12}^s) / (1 - s_{0.66}^c f(\rho_{2.12}^s))) \\ &\quad \text{and} \\ \rho_{0.47}^* &= \eta(\rho_{0.47}^{fa} + F_{d,0.47}^f T_{0.47}^f g(\rho_{0.66}^s) / (1 - s_{0.47}^f g(\rho_{0.66}^s))) + (1 - \eta)(\rho_{0.47}^{ca} + F_{d,0.47}^c T_{0.47}^c g(\rho_{0.66}^s) / (1 - s_{0.47}^c g(\rho_{0.66}^s))),\end{aligned}\quad (7.13abc)$$

where in turn, $\rho^a = \rho^a(\tau)$, $F = F(\tau)$, $T = T(\tau)$, $s = s(\tau)$ are each functions of τ indexed within the lookup table, calculated for separate fine and coarse models. The surface reflectance relationships, $f(\rho_{2.12}^s)$ and $g(\rho_{0.66}^s)$ are described by Eqs. 7.4-7.6. The algorithm actually tries non-physical values of η (-0.1 and 1.1) to allow for the possibility of imperfect assumptions in either aerosol models or surface reflectance. Again, the primary products are $\tau_{0.55}$, $\eta_{0.55}$, and the surface reflectance ($\rho_{2.12}^s$). The fitting error ε is also noted.

Once the solution is found, a number of secondary products can also be calculated. These include the fine and coarse mode optical depths $\tau_{0.55}^f$ and $\tau_{0.55}^c$:

$$\tau_{0.55}^f = \tau_{0.55} \eta_{0.55} \quad \text{and} \quad \tau_{0.55}^c = \tau_{0.55} (1 - \eta_{0.55}) \quad (7.14)$$

the columnar mass concentration, M :

$$M = M_c^f \tau_{0.55}^f + M_c^c \tau_{0.55}^c \quad (7.15)$$

the spectral total and model optical thicknesses τ_λ , τ_λ^f and τ_λ^c :

$$\tau_\lambda = \tau_\lambda^f + \tau_\lambda^c \quad (7.16)$$

where

$$\tau_\lambda^f = \tau_{0.55}^f (Q_\lambda^f / Q_{0.55}^f) \quad \text{and} \quad \tau_\lambda^c = \tau_{0.55}^c (Q_\lambda^c / Q_{0.55}^c), \quad (7.17)$$

The Ångstrom Exponent α :

$$\alpha = \ln(\tau_{0.47} / \tau_{0.66}) / \ln(0.466 / 0.644) \quad (7.18)$$

and the spectral surface reflectance $\rho_{\lambda, s}^s$. M_c^f and M_c^c are mass concentration coefficients for the fine and coarse mode, whereas Q_λ^f and Q_λ^c represent model extinction efficiencies at wavelength, λ . If the resulting products are inconsistent, then the QAC value initially assigned to the pixel is changed to 0 ('bad quality').

7.5.4 Procedure B: Alternative Retrieval for Brighter surfaces

The derivation of aerosol properties is still possible when the 2.12 μm reflectance is brighter than 0.25, but is expected to be less accurate [Remer *et al.*, 2005], due to increasing errors in the VISvs2.12 relationship. However, if Procedure A is not possible, but there are at least 12 cloud-screened, non-water pixels that satisfy

$$0.25 < \rho_{2.12}^m < 0.25G < 0.40 \quad (7.19)$$

where

$$G = 0.5((1/\mu) + (1/\sqrt{\mu_0})) , \quad (7.20)$$

then Procedure B is attempted. In this relationship μ_0 is the cosine of the solar zenith angle, $\cos(\theta_0)$, and μ is cosine of the satellite view angle, $\cos(\theta)$. Eq. 7.20 represents the combination of up and down slant paths of the radiation. The concept is that at oblique angles, as the photon path increases, the atmospheric signal dominates over that from the land surface. The contribution from the surface reflectance becomes less important, and the retrieval can tolerate higher surface reflectance [Remer *et al.*, 2005]. In procedure B, the QAC is automatically set to 0 (“bad quality”).

Procedure B is analogous to “Path B” of the c004 algorithm described in Remer *et al.*, [2005]. Like in c004, the Continental aerosol model is assumed. Unlike c004, the VISvs2.12 surface reflectance assumptions are those described by Eqs. 7.4-7.6, and the Continental aerosol properties are indexed to 0.55 μm . In other words, $\eta=1.0$). The primary products for Procedure B are τ ($\tau_{0.55}$) and the surface reflectance ($\rho_{2.12}^s$). The error ε is also saved. Since Procedure B was followed, the only secondary products calculated are M and $\tau_{0.475}$, and the QAC is set to 0. The other products in are left undefined.

7.5.5 Low and negative optical depth retrievals

A major philosophical for the second-generation algorithm is that negative τ retrievals are allowed. Given that there is both positive and negative noise in the MODIS observations, and that surface reflectance and aerosol properties may be under or over-estimated depending on the retrieval conditions, it is statistically imperative to allow retrieval of negative τ . In fact it is necessary for creating an unbiased dataset from any instrument. Without negative retrievals the τ dataset is

biased by definition. However, a large negative retrieval indicates a situation outside the algorithm's solution space and should not be reported. The trick is to determine the cutoff between a retrieved τ that is essentially the same as zero, and a retrieved τ that is truly wrong. MODIS should retrieve with the expected error defined by Eq. 1.1, then values down to -0.05 are essentially the same as a zero retrieval and are reported as retrieved. Allowing for slightly higher uncertainty, the algorithm include τ retrievals down to -0.10 (twice the expected error in pristine aerosol conditions), but report these values as -0.05 and lower the QAC value. Note that all retrievals with $-0.05 < \tau < 0$ are reported with high QAC value = 3, unless identified as poor quality for some other reason. Some of the products that are retrieved or derived (such as η or Ångstrom Exponent) are set to zero or reported as not defined for negative retrievals. In cases of low τ ($\tau < 0.2$), η is too unstable to be retrieved with any accuracy. Therefore, η is reported as un-defined even though other parameters (such as Ångstrom exponent and Fine τ) may be reported.

7.5.6 Sensitivity study

Because it uses MODIS channels with wide spectral range, and assigns expected aerosol type, the algorithm (Procedure A) should be able to retrieve τ with robustness, and have some sensitivity to the size parameter η . I tested the sensitivity of Procedure A by applying the following exercises: (1) simulation of aerosol loadings and angles included within the LUT, with specific combinations of fine and coarse modes (distinct values of η , that are not necessarily integral multiples of 0.1), (2) simulation of aerosol loadings not contained within the lookup table (e.g., extra

values of τ) and (3) simulations for LUT conditions, but including one or more prescribed errors.

Exercise 1: Whereas the study of Tanré *et al.* [1997] tested the algorithm on a single geometrical combination, this experiment simulated the 720 reasonable geometrical combinations in the LUT ($0^\circ \leq \phi \leq 180^\circ$, $\theta \leq 60^\circ$, $\theta_0 \leq 48^\circ$). The fine-dominated aerosol model was set as the moderately absorbing ($\omega_0 \sim 0.9$) aerosol model, with the coarse-dominated model set as the spheroid (dust) model (Chapter 6). For each combination of geometry, and for each MODIS channel, I extracted the fine and coarse mode values of atmospheric path reflectance ρ^a_λ , backscattering ratio s_λ , downward flux F_d and transmission T_λ . I assumed that the 2.12 μm surface reflectance $\rho^s_{2.12} = 0.15$, and the c004 VISvs2.12 surface reflectance ratios (i.e., $\rho^s_{0.66} = 0.5 \rho^s_{2.12}$ and $\rho^s_{0.47} = 0.5 \rho^s_{0.66}$). TOA reflectance ρ^*_λ was simulated for 5 distinct values of η ($\eta = 0.0, 0.25, 0.5, 0.75$ and 1.0). Therefore, for each value of τ in the LUT, there are $720 \times 5 = 3600$ attempts to retrieve that τ . Since the algorithm is designed to only choose between η values that are multiples of 0.1, it should be possible to retrieve values of 0.0, 0.5 and 1.0, but not 0.25 or 0.75.

For smaller τ ($\tau \leq 1$), the τ was retrieved within $\Delta\tau < 0.01$ for all 3600 combinations. As τ increases, however, computational instabilities lead to a less exact solution. Still, though, the retrieved τ is certainly within 10% and in most cases to within $\Delta\tau < 0.1$. When we input LUT parameters for the combination of $\tau=0.5$ with η either 0.0 or 1.0, both τ and η are retrieved exactly.

As might be expected, attempts to retrieve combinations of fine and coarse aerosol (e.g., $\eta \neq 0$ and $\eta \neq 1$) lead to errors in the retrieval. Figs. 7.7 and 7.8 provide a way of assessing the retrieved MODIS products. Fig. 7.7 plots retrieved τ , surface reflectance and fitting error as a function of either air mass (top) or scattering angle (bottom), given that the input conditions are $\tau_{0.55}=0.5$, $\eta=0.5$ and $\rho_{2.12}^s=0.15$. In this case, all of the 720 geometrical combinations in the LUT were plotted. The retrieved values never exactly matches the intended input, although the errors are very small (less than 0.1%). Note that the retrieval uses an under-estimated surface reflectance to balance the over-estimated optical depth. Most errors are small, and are well within any expected error bars. Fig. 7.8 is similar, but for $\eta=0.25$, and plotted only for the air mass dependence. The errors are much larger (up to 1%), but τ is still well within expected error.

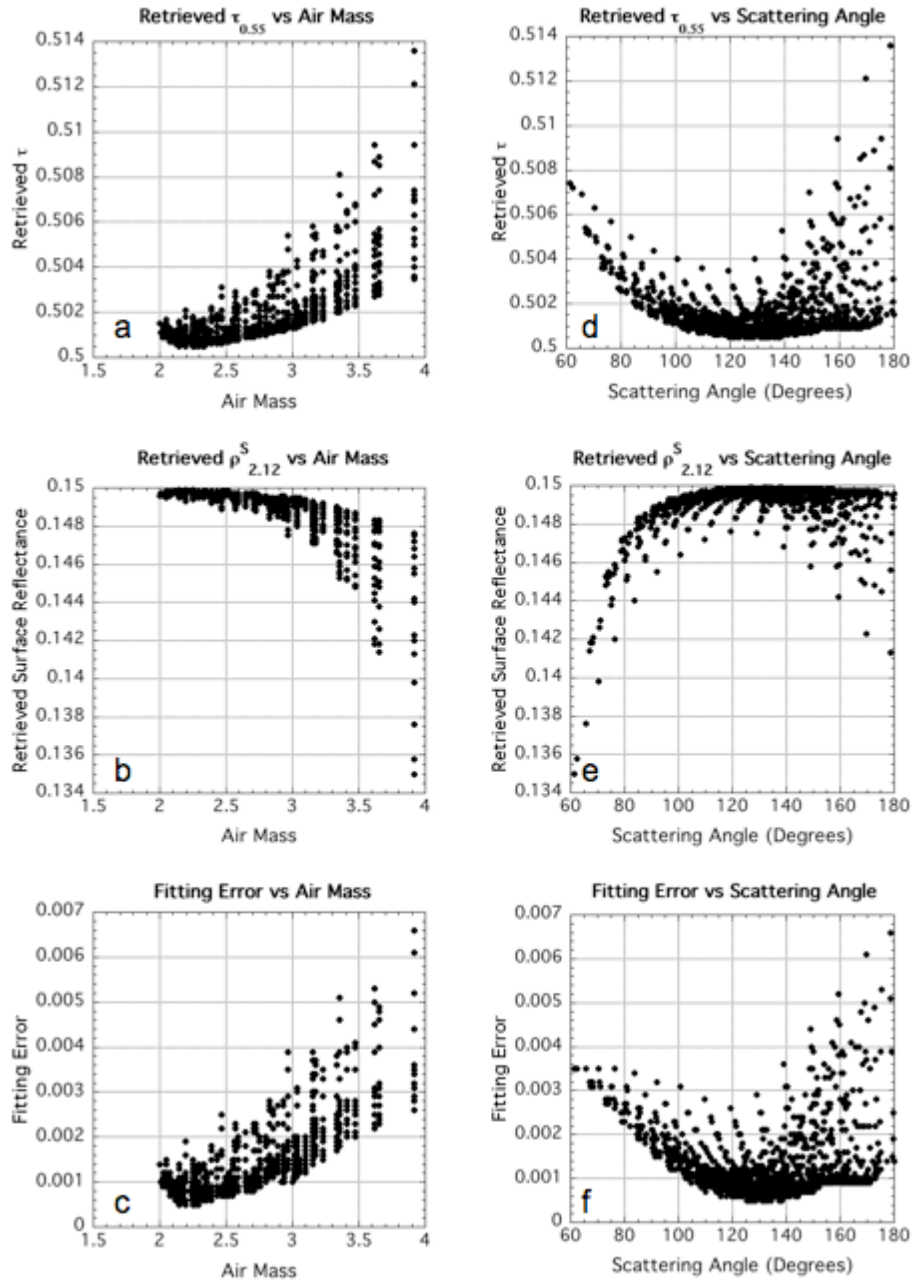


Fig. 7.7: Retrieved MODIS products as a function of Air Mass (a-c) and Scattering Angle (d-f) for inputted atmospheric conditions ($\tau=0.5$, $\eta=0.5$ and $\rho_{2.12}^s=0.15$) and 720 LUT geometrical combinations. The retrieved τ is plotted in (a) and (d), the $2.12 \mu\text{m}$ surface reflectance in (b) and (e) and the fitting error is plotted in (c) and (f). Note that in all cases, the η value of 0.5 was retrieved exactly. Figure from *Levy et al.*, [2007b].

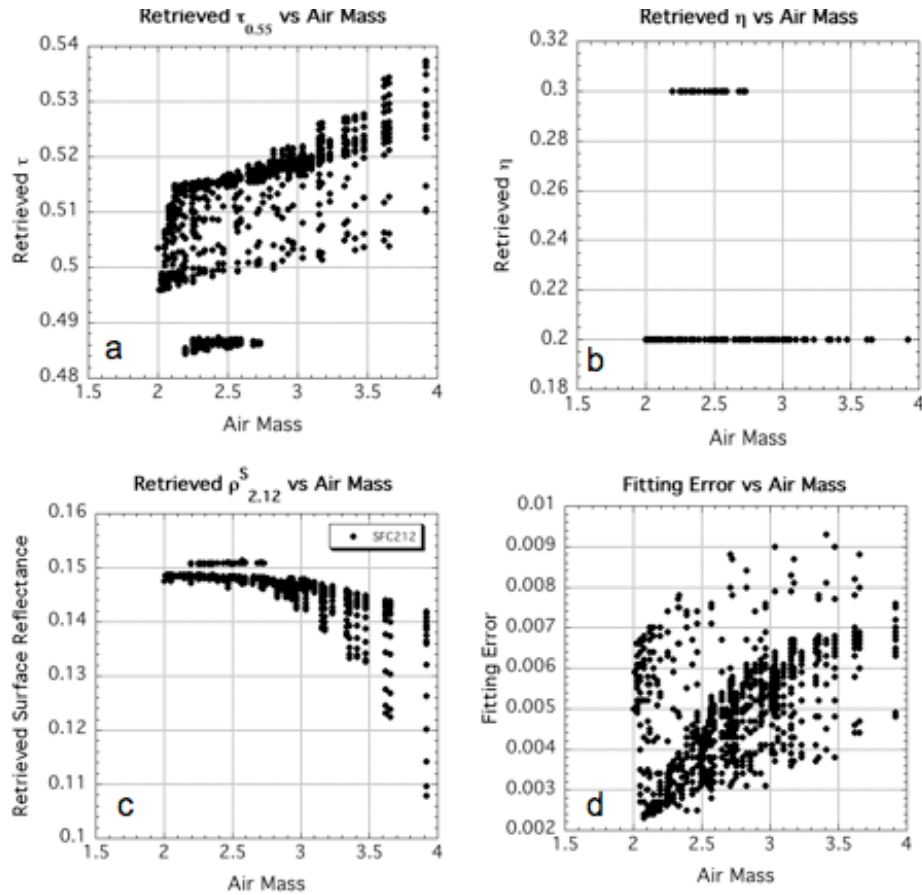


Fig. 7.8: Retrieved MODIS products as a function of Air Mass for inputted atmospheric conditions ($\tau=0.5$, $\eta=0.25$ and $\rho_{2.12}^s=0.15$) and 720 LUT geometrical combinations. The retrieved τ is plotted in (a), retrieved η in (c), the $2.12 \mu\text{m}$ surface reflectance in (c) and the fitting error is plotted in (d). Figure in *Levy et al.*, [2007b].

Exercise 2. The same combination of radiative transfer codes used to create the operational LUT (MIEV + RT3) was used to simulate additional values of aerosol loading ($\tau_{0.55} = 0.35, 1.5$ and 6.0). This “extended” LUT simulates the same 720 geometrical combinations and same set of η values (as in exercise 1). On average the retrieval is very close to the expected value, however, the standard deviation over all geometry is larger than for τ in the normal LUT. A notable exception is the attempt

at retrieving $\tau_{0.55} = 6.0$, where the algorithm does a poor job of extrapolating. In the operational algorithm, we constrain the maximum possible τ to be 5.0.

Another aspect of this exercise is the attempt to retrieve the specific combinations of fine and coarse mode, e.g., η . Attempts to retrieve $\eta=0.5$ are usually successful. All attempts at retrieving either $\eta=0.25$ or $\eta=0.75$ led to retrieving $\eta=0.20$ and $\eta=0.70$. Although it is impossible for an exact retrieval, due to allowing the algorithm to choose η between 0.1 intervals, it is interesting that no retrievals of $\eta=0.30$ or $\eta=0.80$ are produced.

Exercise 3. This exercise studied the impact of different types of errors that could creep into the retrieval process. Potential errors include (but are not limited to) random, systematic or spectrally dependent errors that arise from issues like sensor calibration, assuming the wrong aerosol model at a given location, coarse input topography mapping, or wrong estimates of the VISvs2.12 surface reflectance relationships. These errors are expressed by adding random or systematic errors in the spectral reflectance measurements, geometrical conditions or other input boundary conditions. Table 7.1 lists some prescribed errors, for the same set of eight geometries listed in Table 5.1. Table 7.2 shows the results when attempting to retrieve conditions of $\tau_{0.55}=0.5$, $\eta=0.5$ and $\rho_{2.12}^s=0.15$, for the eight sample geometries. Table 7.2a displays the retrieved values of $\tau_{0.55}$ for each case. Table 7.2b shows the Mean Squared Error (MSE) for each retrieved product, computed over all eight geometries. For any case of prescribed errors/geometry, one or more products may be over- or underestimated. If all geometry leads to either one direction or the other, the MSE value is designated by (+) or (-). For example, when retrieving with

no additional errors ('LUTinput'), τ is never retrieved exactly, but is overestimated by an average MSE of 0.0011 (+). In balance, $\rho_{2.12}^s$ is consistently underestimated (MSE of 0.0004 (-)), with a nonzero fitting error, ϵ . This is simply a result of computer round off error.

TABLE 7.1: LIST OF PRESCRIBED ERRORS FOR V5.2 SENSITIVITY STUDY

Ref.	Error Type	Description
1	LUTinput	LUT input: Use the LUT with no prescribed errors
2	ModError	Aerosol model error: Attempt retrieval with Weakly-absorbing fine model LUT
3	RndError	Random Error: All channels have random reflectance error of up to ± 0.002
4	SfcError	Surface Error: 10% error in assumed 0.66/2.12 surface reflectance relationship
5	CalError	Calibration Error: All channels have random error of up to $\pm 1\%$
6	ElvError	Elevation Error: Elevation is 1km instead of assumed sea level
7	GeoError	Geometry Error: All angles have random error of up to ± 5 degrees
8	AllError	Combination of 2,3,4,5,6 and 7.

TABLE 7.2: RESULTS OF SENSITIVITY STUDY USING PRESCRIBED ERRORS

Geometry								
Error Type	LUTinput	RndError	CalError	GeoError	ModError	ElvError	SfcError	AllError
A	0.501	0.4786	0.5242	0.5143	0.5015	0.6068	0.5402	0.6963
B	0.501	0.4887	0.5242	0.4977	0.4993	0.6035	0.5422	0.6677
C	0.501	0.5227	0.5227	0.4657	0.4835	0.5104	0.4955	0.4809
D	0.5011	0.5104	0.4995	0.4761	0.5014	0.5228	0.498	0.4892
E	0.5008	0.4754	0.502	0.4893	0.4866	0.5211	0.4877	0.5737
F	0.501	0.5135	0.5029	0.4922	0.5035	0.531	0.488	0.5536
G	0.5014	0.4973	0.5199	0.4698	0.4811	0.5097	0.488	0.427
H	0.5016	0.4961	0.5001	0.4744	0.5198	0.5299	0.4939	0.5106

A: Retrieved τ at 0.55 μm (expected $\tau=0.5$)

Product								
Error Type	LUTinput	RndError	CalError	GeoError	ModError	ElvError	SfcError	AllError
τ	0.0011(+)	0.0159	0.0162	0.0215	0.0123	0.0561(+)	0.0221	0.1006
η	0.0000	0.0000	0.0707	0.1000	0.0707	0.4243 (+)	0.1323 (+)	0.4912 (+)
ρ	0.0004 (-)	0.0008	0.0022	0.0025	0.0031 (-)	0.0067	0.0020 (+)	0.0074 (+)
ϵ	0.0010	0.0021	0.0037	0.0028	0.0020	0.0025	0.0035	0.0052

B: MSE of retrieved τ, η, ρ^σ and ϵ (expected $\tau=0.5, \eta=0.5, \rho^\sigma=0.15$ and $\epsilon=0.0$). Entries designated with (+) mean that the product was over-estimated for all 8 geometries, whereas those with a (-) means it was under-estimated for all geometries.

Under most conditions, introducing minor calibration or random errors does not destroy the retrieval of τ . For most individual errors, the retrieved τ is accurate to within 0.02. However, even when errors are combined (model error, random error, surface error, calibration error and geometrical error), the algorithm still retrieves $\tau=0.5$ with $MSE = 0.10$, thus retrieving within the expected error of $\Delta\tau=0.125$. Retrieval of surface reflectance seems to be robust. Retrieval of η is much more unstable. For simple calibration and geometrical errors, the MSE for η is < 0.1 . Combinations of errors lead to large MSE (>0.2) for η retrieval, meaning that η is not a stable product. Yet, even though the η parameter is sensitive to errors, it should give qualitative indication of particle size.

7.6: Preliminary validation

Examples of the three primary aerosol products ($\tau_{0.55}$, η and $\rho_{2.12}^s$) are shown in Fig. 7.9, along with a color composite of the L1B reflectances (RGB image; 0.47, 0.55 and 0.66 μm channels). This image was taken on May 4, 2001 over the U.S. East Coast, and is the same granule used by *King et al.*, [2003]. There is continuity of τ from land to ocean, and that the retrieval of η and surface reflectance seem reasonable. Note that η is not plotted over land when $\tau < 0.2$.

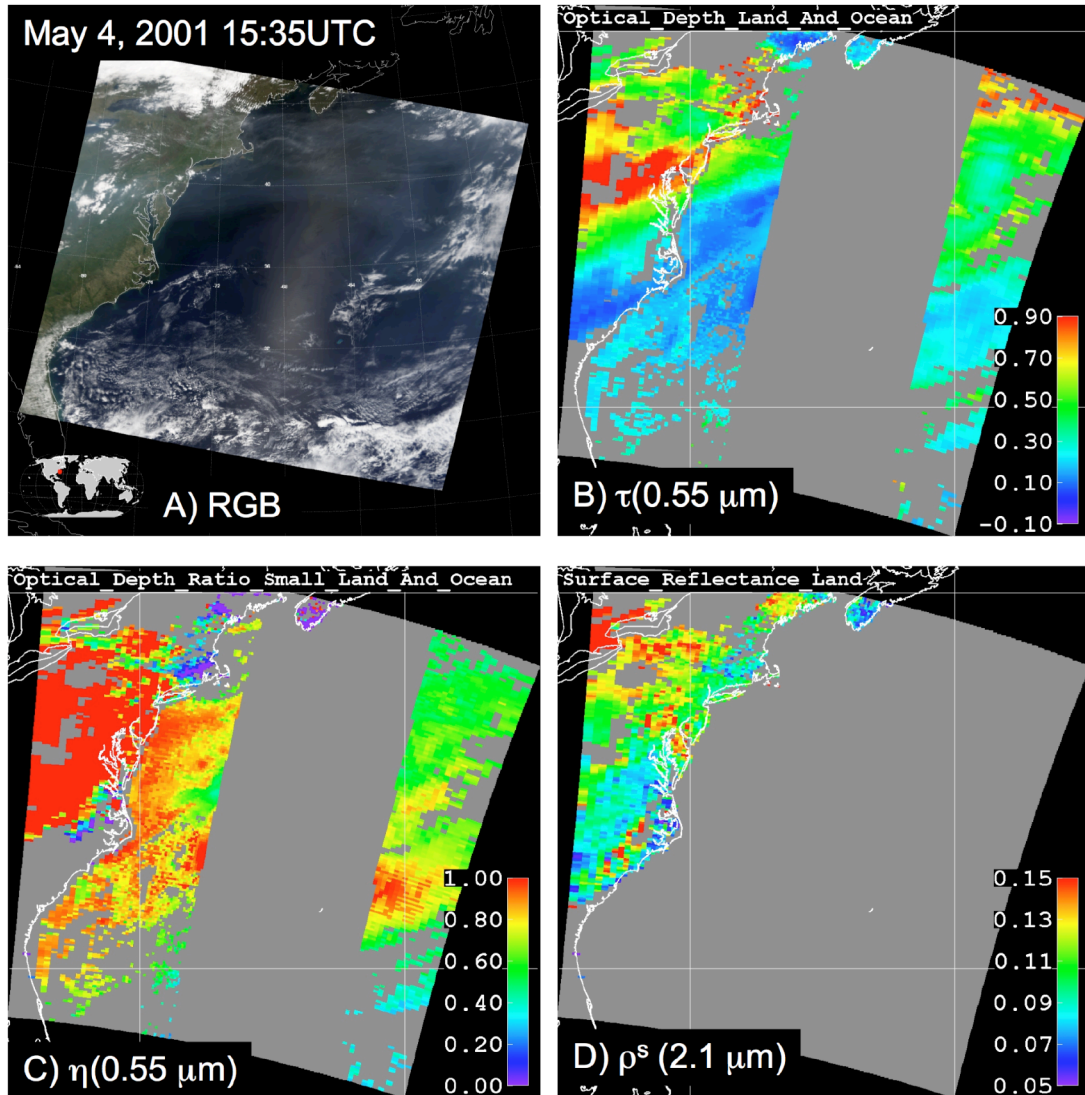


Fig. 7.9: Retrieved aerosol and surface properties over the Eastern U.S. on May 4, 2001 (same granule as in King *et al.*, [2003]). Panel A) is a ‘true-color’ composite image of three visible channels, showing haze over the mid-Atlantic. Panels B) and C) show retrieved τ and η , showing that the heavy aerosol ($\tau \sim 1.0$) is dominated by fine particles. The transport of the aerosol into the Atlantic is well represented with good agreement between land and ocean. Note that over-land η is not reported when $\tau < 0.2$. Panel D) shows the retrieved surface reflectance.

The primary means of MODIS validation is by comparing the products with equivalent measurements from AERONET or other aerosol measurements. In this way, the standard products of c004 were *validated* (e.g., Remer *et al.*, [2005]),

meaning that their uncertainties are quantified. In the case of the land products (through V4.2), this meant that ~60% (slightly less than one standard deviation) of the AERONET-measured τ values were retrieved by MODIS to the expected error described by Eq. 1.1. The other land parameters were either not yet validated, or are diagnostic parameters that cannot be validated. In addition to validation by AERONET, it is important to perform qualitative analyses based on visual inspection and global statistics.

Since the algorithm was described by *Remer et al.*, [2005], it has continued through minor updates. The last update to the c004 family was known as Version 5.1 ('V5.1'). V5.1 updated the snow mask [*Li et al.*, 2005] and cleaned up confusing information in the output files. However, V5.1 never became operational, as there was the opportunity to replace it with the algorithm described in this Chapter. In this work [*Levy et al.*, 2007b] V5.1 is used to bridge from c004 algorithms to the second-generation algorithm, known in operation as V5.2.

7.6.1 Direct comparison of V5.2 and V5.1

Fig. 7.10 plots retrieved τ at $0.55 \mu\text{m}$ from both V5.1 and V5.2, over small areas of a MODIS granule over the Western U.S. on Sep 30, 2003. V5.1 (OLD) is presented in (a), whereas V5.2 (NEW) is shown in (b). The V5.2 aerosol retrieval adds more valid retrievals over very low τ areas (coastal Oregon and northern California). V5.2 reports these areas as having near zero or slightly negative τ , where V5.1 would have reported fill values (no retrieval). In areas farther from the coastline, V5.2 tends to clean up contamination presumably caused by clouds,

(histogram) of the values. For the set of MODIS granules listed in Table 7.3 (about 6300 granules of both Terra and Aqua), the mean $0.55 \mu\text{m } \tau$ is reduced from 0.28 to 0.21. This is a significant reduction that should be evaluated with GOCART [Chin *et al.*, 2002], or other models that estimate aerosol climate effects.

TABLE 7.3: Description of Data used in Provisional Validation (adapted from Levy *et al.*, [2007b])

Date of MODIS Observations	Terra/Aqua	Why interesting?
August 2001 (full month: 4138 granules)	Terra & Aqua	
7 July 2002 (full day: 132 granules)	Aqua	Quebec Smoke in NE US
8 July 2002 (full day: 136 granules)	Aqua	Quebec Smoke in NE US
6 Mar 2004 (full day: 132 granules)	Aqua	Asian Dust
7 Mar 2004 (full day: 138 granules)	Aqua	Asian Dust
Eight days in 2003 (full days: 1070 granules)	Aqua	Yearly Cycle
14 Nov 2005 (full day: 138 granules)	Terra	Low AOD globally
22 Apr 2001 (full day: 136 granules)	Terra	ACE-Asia
26 Jun 2002 (full day: 138 granules)	Terra	Summer time haze
Test_bed_Aqua: (39 granules)	Aqua	interesting Aqua data
Test_bed_Terra: (102 granules)	Terra	interesting Terra data
Total granules = 6299		

Fig. 7.11 plots the histograms of retrieved τ at $0.55 \mu\text{m}$ from both V5.1 and V5.2. These histograms include 141 individual Terra and Aqua granules that are known as the MODIS “test_bed”, and twelve days of global data – all listed in Table 7.3. The use of global data is especially important for determining how the retrieval behaves in regions not selected for algorithm development. Of course, the obvious change in the V5.2 product is that small magnitude negative τ retrievals are valid. About 10-11% of the total τ retrievals are now retrieved as below zero, of which only about 3% are below -0.05. This promising result indicates that V5.2 has reasonable ability to detect very clean conditions within the expected error of ± 0.05 . Also Fig.

7.9 shows that the fraction of retrieved medium to medium high τ ($0.2 < \tau < 0.75$) is reduced, while the fraction of high τ ($\tau > 0.75$) remains about the same.

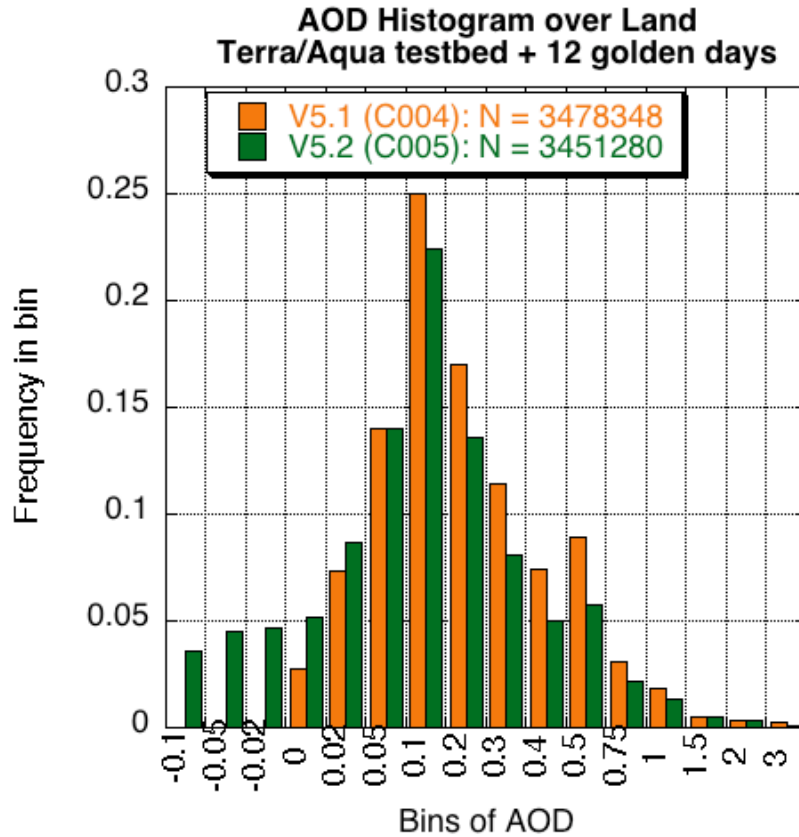


Fig. 7.9: Histogram of retrieved τ (AOD) over land, from V5.2 (c005) in green, compared to V5.1 (c004) in orange. The data include the 141 granules of the Terra and Aqua “test_bed” as well as twelve complete days. The value of each bin refers to the minimum value of the bin (the max value would be the value of the next bin). Note that the general lognormal nature of the retrievals is preserved, except now there are some negative values. (Figure in Levy *et al.*, [2007b])

7.6.3 Comparison of V5.2 to V5.1 and with AERONET

As of 1 April 2006, the V5.2 algorithm was run on nearly 6300 granules, including one full month (August 2001), fifteen entire days (listed in Table 7.3) and about 141 individual granules that are known as the MODIS “test_bed.” These granules include observations from both Terra and Aqua, and are seasonally and yearly representative of the MODIS time series. For comparison, both V5.1 and V5.2 were run on the same set of granules. Note that the database used to derive the land surface relationships (350,000 Aqua and Terra data from 2000-2004) has a small overlap with our 6300 granule-testbed. In that way, the comparison to AERONET shown in this section is not entirely independent of the formulation database. However, the data used in this section includes all values of τ and α , while the formulation database was limited to specific ranges of these variables. Also, the data used here represent a comparison of spatio-temporal statistics, while in the formulation data base only the individual match between sunphotometer location and satellite overpass were used. Thus, the plots shown here, while not entirely independent, offer a test of the new retrieval in more general conditions than in the specific formulation data. Figs. 7.12 and 7.13 plot the comparisons of both V5.1 and V5.2 with the AERONET data, via the spatio-temporal co-location method of *Ichoku et al.*, [2002a].

Fig. 7.12 plots the retrieved MODIS τ against AERONET τ , both at 0.55 μm . The data have been sorted by AERONET τ and averaged into bins with equal numbers of observations in each bin. The mean and standard deviation of each bin are calculated and plotted in Fig. 7.12 as a solid dot and error bars. The correlation is

calculated from the freely plotted points before binning, although the cloud of points is not shown in the plot. The regression equation has improved tremendously compared to V5.1, from “ $y=0.097+0.91x$ ” to “ $y=0.029+1.01x$.” Correlation R is also improved, from $R=0.847$ to $R=0.894$. It should be noted that slight differences in the number of points arise due to different selection of valid dark pixels and allowance of below zero τ retrievals.

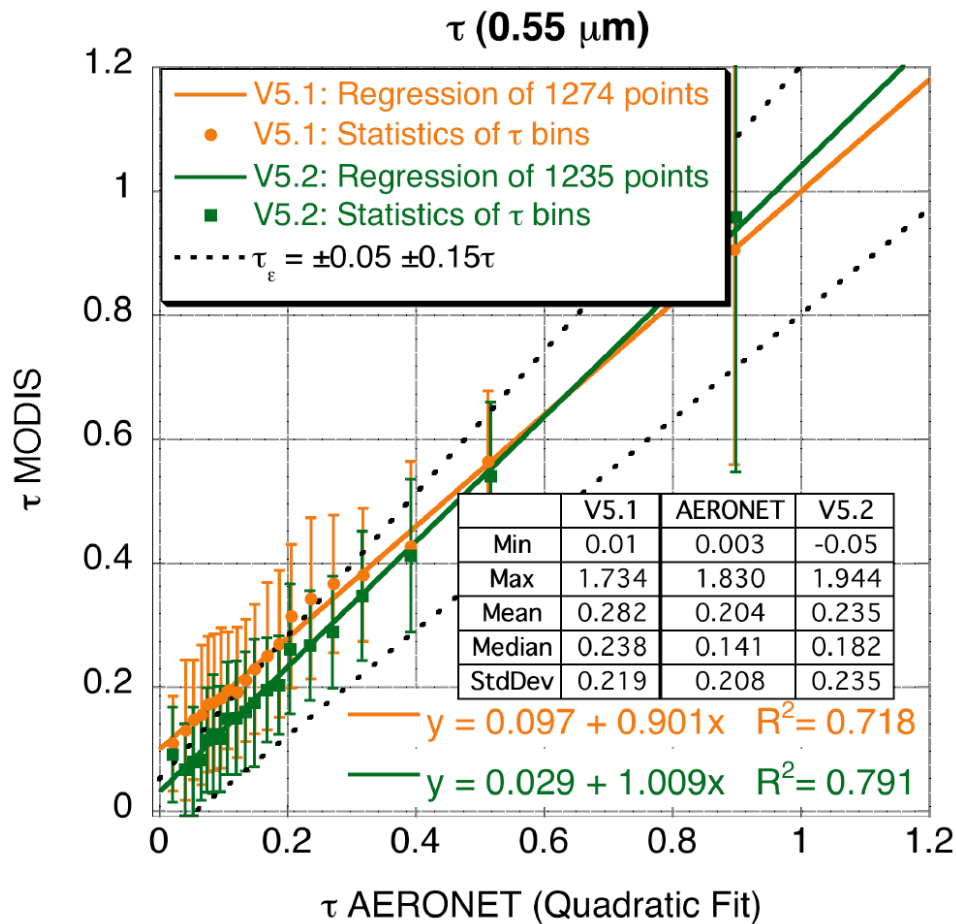


Fig. 7.12: Preliminary validation of c005 products. MODIS τ over land retrieved at 0.55 μm , compared with AERONET τ interpolated to 0.55 μm . The solid shapes and error bars represent the mean and standard deviation of the MODIS retrievals, in 20 bins of AERONET-derived τ . Both the retrievals from V5.1 (orange) and V5.2 (green) are shown. The regressions (solid lines) are for the cloud of all points before binning (not shown). The expected errors for MODIS ($\pm 0.05 \pm 0.15\tau$) are also shown (dashed lines). (Figure in Levy *et al.*, [2007b]).

Fig. 7.13a plots MODIS η against AERONET η , where I calculated AERONET η from sun observations of spectral τ , using the 4th version of the *O'Neill et al.*, [2003] spectral de-convolution algorithm. Keep in mind that unlike MODIS/AERONET comparisons of τ , MODIS and AERONET do not retrieve the same quantity labeled as η . The AERONET retrieval assumes one fine mode and one coarse mode. Thus, AERONET η is the weighting between *modes*. The MODIS land η is a weighting between bi-modal *models*, where fine-dominated models also contain a coarse mode and vice-versa. The improvement to the MODIS η product is mainly its correlation to AERONET. Note that η is defined only when $\tau > 0.2$. Figs 7.13b and c show comparisons for derived products, including the Ångstrom Exponent (defined by 0.47 and 0.66 μm), and Fine optical depth (i.e., $\tau^f = \tau \times \eta$), respectively. For τ^f , the correlation and slopes are nearly unchanged between V5.1 and V5.2; however, the offset decreases from +0.051 to -0.031. The result is that nearly two-thirds of all V5.2 MODIS retrievals of τ^f compare to AERONET within expected uncertainty defined by Eq. 1.1. Note again that the difference in the number of points is due to different selection of dark pixels and treatment of negative τ retrievals. The Ångstrom exponent has little improvement from V5.1 to V5.2, except for slightly better but still poor correlation with the AERONET measured quantities. In general, the changes to the MODIS aerosol retrieval algorithm described here have resulted in a much less biased τ and τ^f products than the previous algorithm. MODIS η and other size parameters correlate better with AERONET, although it still leaves room for improvement.

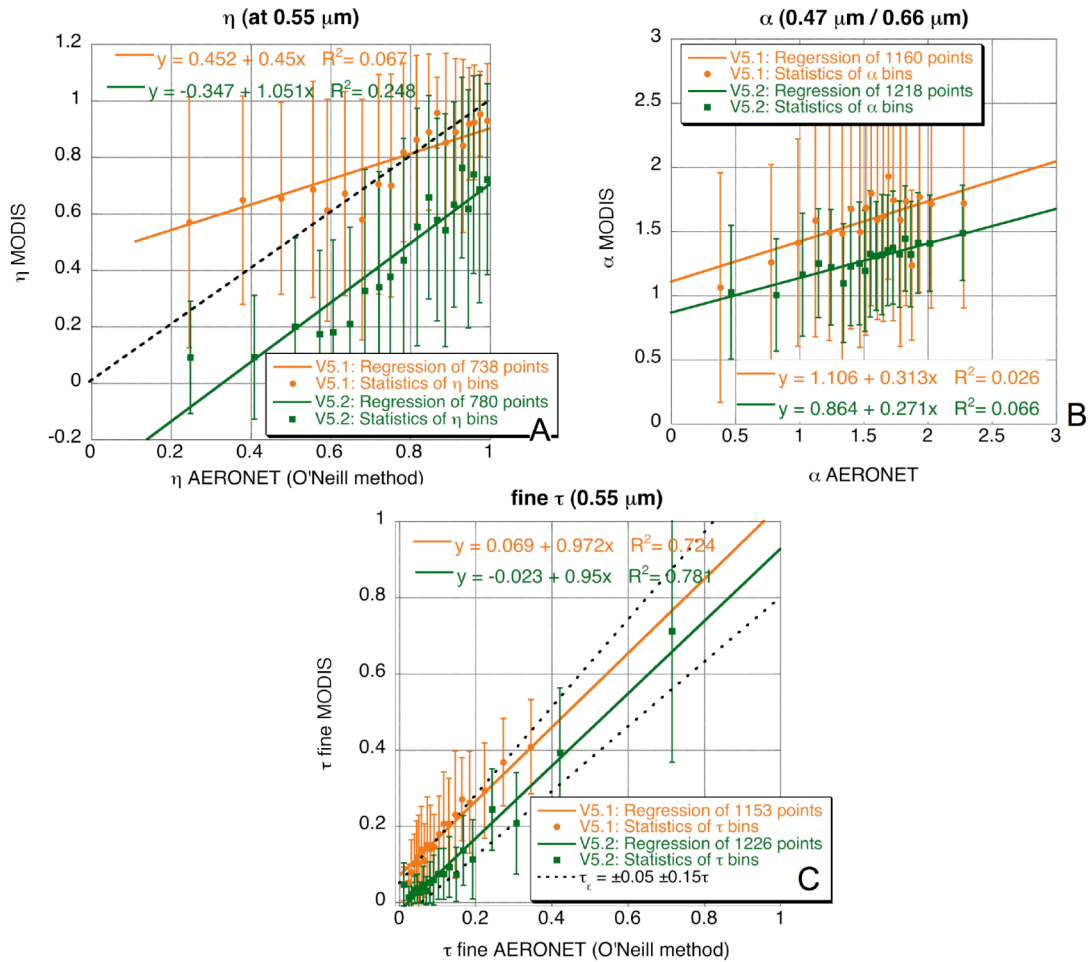


Fig. 7.13: MODIS aerosol size retrievals compared with AERONET derived products. The solid shapes and error bars represent the mean and standard deviation of the MODIS retrievals, in 20 bins of AERONET-derived product. Both the retrievals from V5.1 (orange) and V5.2 (green) are shown. The regressions (solid lines) are for the cloud of all points (not shown). A) η over land retrieved at $0.55 \mu\text{m}$, compared with AERONET η retrieved by the O'Neill (2003) method. Note that η is defined differently for MODIS and AERONET and that we only show results for $\tau > 0.20$. B) MODIS-derived α ($0.466/0.644 \mu\text{m}$) over land with AERONET α interpolated to the same wavelengths. C) MODIS Fine τ over land retrieved at $0.55 \mu\text{m}$, compared with AERONET Fine τ interpolated to $0.55 \mu\text{m}$ by quadratic fitting and the O'Neill method. The expected errors for MODIS ($\pm 0.05 \pm 0.15\tau$) are also shown (dashed lines). (Figure adapted from Levy *et al.*, [2007b]).

7.7: Summary and future c005 evaluation

Over the past three years, I developed the second-generation aerosol retrieval algorithm, that updates or overhauls many assumptions contained the previous algorithm. Preliminary validation of the products indicated that they were accurate to within expected uncertainties. However, the final global algorithm is biased towards fitting AERONET data, so that it is not necessarily representative of everywhere in the world.

In April 2006, the second-generation algorithm went into operational production. By 2007, the entire MODIS mission had been reprocessed, using the second-generation algorithm. Since the products are easily accessible to any investigator, independent researches have evaluated the new products. These evaluations include those for regions not originally studied for c005 development, such as those with lack of independent data. In most cases, the c005 results look good, however, in certain regions under certain conditions, the products are not as accurate as would be hoped.

For example, *Mi et al.*, [submitted, 2007] present a validation of MODIS retrieved aerosol τ over two AERONET sites in Northern and Southern China, and compare the results of c005 with c004. The uncertainties of surface estimation have been singled out from other error sources by replacing the c004 reflectance ratios with atmospherically corrected reflectance. The difference between the aerosol models used in c004 and c005 algorithm is also investigated, in terms of the effects on the quality of τ retrieval at the two sites. As might have been expected, the performance of MODIS τ retrievals differs in Northern and Southern China, where

the surface ecosystem and climate are quite different. Like previous validation studies, *Mi et al.*, [submitted, 2007] showed generally overestimation of τ at both sites by MODIS c004, attributing to the assumptions of VISvs2.12 surface reflectance ratio and single scattering albedo of the aerosol fine model. Although the second-generation algorithm tackled both issues, resulting in generally improved retrieval of τ , uncertainties in aerosol models still dominate retrieval errors. Some of the largest retrieval errors occur at the northern site, primarily due to the presence of complex aerosol compositions, including mixtures of dust with sulfate aerosol, organic and black carbon.

Chapter 8: Using MODIS for evaluating modeled relationship between τ and surface $\{PM_{2.5}\}$ over the U.S. mid-Atlantic

Chapters 6 and 7 introduced the principles of the second-generation algorithm, which was validated (preliminarily) by comparing to global AERONET data. Once the performance of the new MODIS algorithm is evaluated, the products can be applied to answer scientific questions. While the primary goal of the MODIS retrieval is to characterize the global and regional aerosol properties and their effects on climate, investigators have used the MODIS products for various other applications. One interesting and useful application is using MODIS -derived column-averaged aerosol properties to infer properties of aerosol near the Earth's surface that impact air quality and human health.

This Chapter concentrates on MODIS retrievals over the U.S. mid-Atlantic, and how they can be used to further the understanding of aerosols in the region. Since the University of Maryland has been tasked with evaluating the CMAQ model results in the region for 2002, this Chapter attempts to characterize the 3-dimensional aerosol properties during this time period (specifically July and August, 2002).

The primary goal is to understand the relationship between of columnar ambient optical depth and surface dry aerosol concentration in the region. The previous Chapters developed the new MODIS algorithm that retrieves integrated ambient aerosol optical properties (c005) that are more realistic and accurate on a global scale. Here I first evaluate the c005 MODIS products over the mid-Atlantic during the summer of 2002, by comparing to sunphotometer observations. Then I compare the

products against surface-based measurements of $PM_{2.5}$ concentration ($\{PM_{2.5}\}$, where $\{\}$ represents concentration) in the mid-Atlantic region.

Chapter 2 (e.g., Eq. 2.20) suggested that when the conditions are appropriate (aerosol column concentrated in the boundary layer), the two quantities (MODIS aerosol products and $\{PM_{2.5}\}$) should be related. Wind analyses, lidar, and aircraft measurements performed during the summer 2002 period can all help to evaluate the validity of this assumption in specific cases. This dissertation, however, concentrates on UMD (RAMMPP) aircraft profiles to evaluate the apportionment of aerosol within the boundary layer. Since the EPA requires use of the CMAQ model to regulate air quality and develop strategies for pollution reduction, I will evaluate the internal consistency of the $\tau / PM_{2.5}$ relationship within CMAQ over the region.

8.1: Summary of previous satellite / surface $\{PM_{2.5}\}$ studies

In order to capture the variability of aerosols within their short lifetime, it is necessary to measure aerosols with high spatial and temporal coverage. Daily and global measurements (from satellite) may be sufficient for climate applications, but are insufficient for assessing air quality and human exposure to aerosol pollution. Air quality monitoring requires high frequency (e.g., hourly) measurements in local (e.g., urban) scales. Even within the densely populated U.S. mid-Atlantic region, surface $\{PM_{2.5}\}$ is measured at approximately 1 site per 1000 km², ensuring gaps in coverage. Considering that global PM measurements are even sparser, it is imperative to evaluate aerosol data where we can. Rigorous surface to column aerosol characterization, using the relative density of sites in the mid-Atlantic, may

eventually lead to better use of satellite products for monitoring air pollution on a global scale.

Satellites have the vantage point to observe the whole picture, and the operational MODIS algorithm provides data on 10 km x 10 km resolution. While not ideal for urban scale aerosol monitoring, they should improve the existing surface PM_{2.5} observing networks. Since satellites can observe plumes, they can help to determine whether the plumes are a result of local emissions or long-range transport. Thus, they can help determine source-receptor relationships in cases of NAAQS violations in the mid-Atlantic region (e.g., *Engel-Cox et al.*, [2005]). However, passive sensors (such as MODIS) are only sensitive to the column-integrated properties of the aerosol (τ and possibly size information). For a useful relationship between τ and {PM_{2.5}}, either the aerosol profile must be known, or the bulk of the aerosol loading must be near the surface. In addition, surface aerosol properties (size, shape, composition) must be representative of the column.

Given these caveats, *Chu et al.*, [2003] demonstrated that satellite –derived τ (from MODIS) can be applied to global, regional, metropolitan, and even local/urban air pollution events. They designed three case studies around the world, representing regional (~24000 km² over northern Italy), metropolitan (~5000 km² over greater Los Angeles) and urban scales (~900 km² over urban Beijing) and found that MODIS derived τ was comparable to sunphotometer measurements (AERONET and non-AERONET) on all of these spatial scales. They also found that AERONET retrievals of τ were correlated with surface {PM}.

A number of studies have characterized the relationship of τ and $\{PM\}$ and how it varies around the world (e.g., [Gupta *et al.*, 2006; Wang *et al.*, 2004]). Engel-Cox *et al.*, [2004] compared MODIS to hourly $\{PM_{2.5}\}$ measurements from USEPA surface sites. They found correlations on the order of $R \sim 0.5-0.6$ over much of the Eastern half of the U.S., with much lower (including negative) correlations over the Western half. These and other results encouraged Al-Saadi *et al.*, [2005] to elaborate on this concept, describing a joint EPA/NOAA/NASA effort that uses MODIS and other satellite products to monitor and help forecast surface $\{PM\}$ on a national scale. For August and September 2003, they found correlations of $R \sim 0.6$ over the Eastern half of the U.S., but $R < 0.4$ over most of the west. Over the eastern U.S., surface $\{PM_{2.5}\}$ (in $[\mu g \cdot m^{-3}]$) could be approximated by

$$\{PM_{2.5}\} \approx 60[\mu g \cdot m^{-3}] \times \tau_{0.55} \quad (8.1)$$

Engel-Cox *et al.*, [2006] focused on the relationship of MODIS- τ and $\{PM_{2.5}\}$ over Baltimore during the summer of 2004. They found that

$$\{PM_{2.5}\} \approx 30[\mu g \cdot m^{-3}] \times \tau_{0.55} + 5[\mu g \cdot m^{-3}], \quad (8.2)$$

regardless of whether $\{PM_{2.5}\}$ represented hourly ($\{PM_{2.5}\}_{\text{hourly}}$) measurements from non-reference continuous aerosol mass monitors or daily ($\{PM_{2.5}\}_{\text{daily}}$) measurements from Federal Reference Monitors (FRM). Under both surface measurement time scales, correlation coefficients were $R \sim 0.6$, but they had different values of slope and offset. Then they used ~ 100 cases of lidar (at any time during the day) measurements of total τ and τ in the PBL (τ_{PBL}), also comparing with both $\{PM_{2.5}\}_{\text{hourly}}$ and $\{PM_{2.5}\}_{\text{daily}}$. For hourly $\{PM_{2.5}\}$, correlation coefficients were higher when regressing to τ_{PBL} ($R=0.64$) than to total τ ($R=0.56$), but there were significant differences in the

regression equations. Like that reported for MODIS τ , slopes using total τ were 25-30 $\mu\text{g}\cdot\text{m}^{-3}\cdot\tau^{-1}$ (τ is unitless). When regressing to τ_{PBL} , however, the slope was 48 $\mu\text{g}\cdot\text{m}^{-3}\cdot\tau^{-1}$. For estimating daily $\{\text{PM}_{2.5}\}$, both correlation coefficients were $R\sim 0.75$, and slopes rose to 40 and 65 $\mu\text{g}\cdot\text{m}^{-3}\cdot\tau^{-1}$ for τ and τ_{PBL} , respectively. This suggested that knowing the vertical apportionment of aerosol depth (that can be measured from lidar) can determine (case by case) whether a $\tau/\{\text{PM}\}$ correlation should exist [Engel-Cox *et al.*, 2006; Chaw *et al.*, 2006]. When there is significant high altitude aerosol (for example high altitude smoke transport), there will be little or no correlation between the two properties.

Statistical analysis of the vertical apportionments will lead to better quantification of the correlation. Understanding the meteorological conditions that precede specific 3-D aerosol configurations would lead towards improved ability to monitor and even forecast aerosol events at the surface. Van Donkelaar *et al.* [2006] evaluated the relationship by simulating meteorology and vertical profiles using a global chemical transport model, and concluded that temporal variation of τ in the vertical is the dominant variable for determining the $\tau/\{\text{PM}\}$ relationship.

8.2: Observed aerosol properties over the mid-Atlantic during July-August 2002

The Mid-Atlantic Regional Air Management Association, Inc. (MARAMA; <http://www.marama.org>) is a voluntary, non-profit association of ten state and local air pollution control agencies, including those in Delaware, the District of Columbia, Maryland, New Jersey, North Carolina, Pennsylvania, Virginia and West Virginia.

For the purpose of this dissertation, the mid-Atlantic region is defined by the MARAMA domain. MARAMA recognizes pollution as a regional problem, thus encompassing the work of the MDE.

8.2.1 Datasets

A number of aerosol datasets were collected during July and August of 2002 over the mid-Atlantic. MODIS observations from Aqua began in early July, thus this was the first two months of both Terra and Aqua observations. AERONET data were collected at nine sites (AERONET naming conventions) in the mid-Atlantic region: CCNY (40N, 73W), Columbia_SC (34N, 81W), COVE (36N, 75W), GISS (40N, 73W), GSFC (38N, 76W), MD_Science_Center (39N, 76W), Norfolk_State_Univ (36N, 76W), SERC (38N, 76W), and Wallops (37N, 75W). Backtrajectories at multiple levels, from NASA Global Modeling and Assimilation Office (GMAO) assimilated gridded data, are available for most of the AERONET sites. The EPA collected speciated, daily and/or hourly average aerosol concentrations at several sites in the region. The UMD aircraft measured 22 profiles of aerosol extinction and scattering, and there were intensive measurements of PM at Fort Meade, Maryland (FME) [*Hains et al.*, submitted 2007]. Finally observations from the Micropulse LIDAR (MPL: <http://mplnet.gsfc.nasa.gov>) were available during the period. In this chapter, I utilize retrievals of τ from MODIS and AERONET, hourly surface $\{PM_{2.5}\}$ from the EPA's continuous monitors, and scattering and absorption coefficients measured by the three-wavelength nephelometer and the PSAP onboard the UMD Piper-Aztec aircraft. Each of these products are inter-compared and compared with that simulated by the CMAQ model during the period.

8.2.2 Summary of events

Fig. 8.1 shows a plot of daily averaged τ and surface $\{PM_{2.5}\}$ measured in Baltimore, during July-August 2002. The period was marked by episodes of heavy aerosol loadings evident in both the column and at the surface. In most cases, the events tracked together, with a $\tau = 1.0$ representing approximately $40 \mu\text{g}\cdot\text{m}^{-3}\cdot\tau^{-1}$ (matching that found by Engel-Cox *et al.*, [2006]. Days 187-189 (July 6-8) are marked by extreme loadings, both in the column and at the surface, resulting from the transport of heavy smoke from fires in Quebec [Taubman *et al.*, 2004; Vant-Hull *et al.*, 2005; Colarco *et al.*, 2004]. The correlation of the aerosol at Baltimore is high, demonstrating that while the elevated smoke was not brought to the surface everywhere, it was brought to the surface in Baltimore. Other interesting events are days 198-204 (July 16-22), which was a typical episode of summer pollution, marked by stagnant conditions and buildup of local and regional sulfate-based aerosols. This event was observed by both the satellite and at the surface instruments at all sites in the region. Days 225-226 (August 13-14) are likely another episode of smoke transport from Canada, but includes some regional pollution as well.

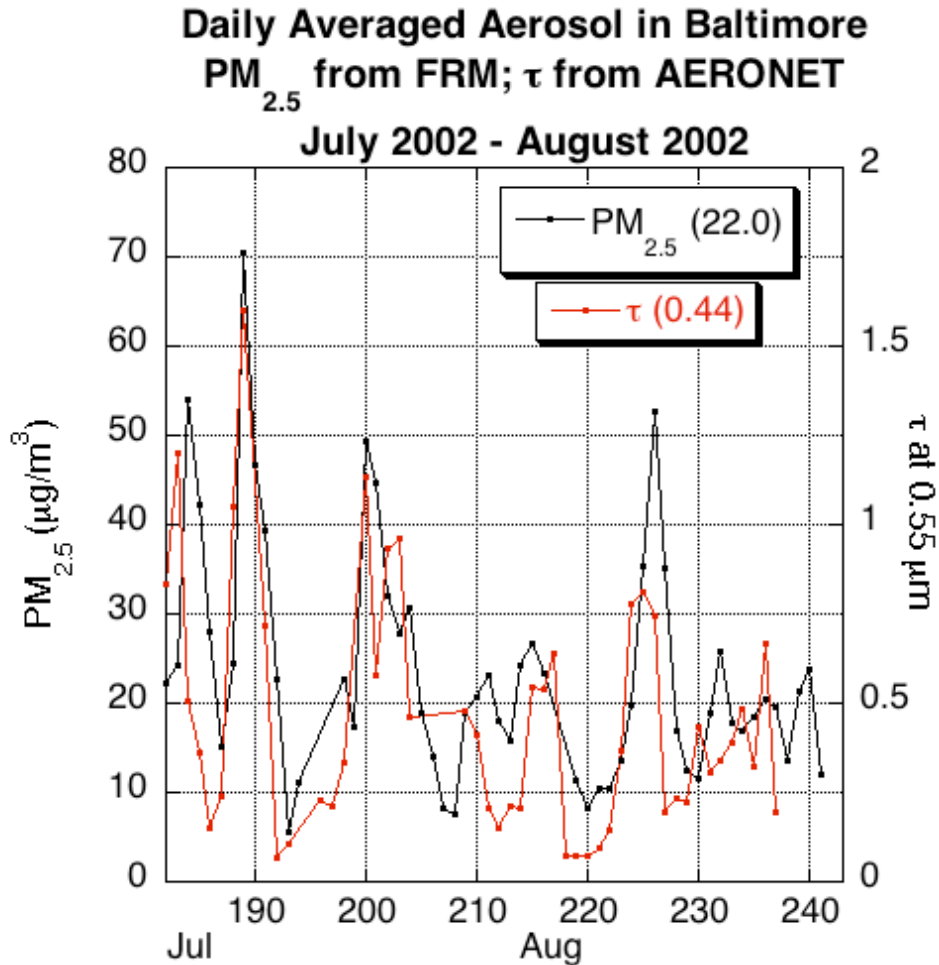


Fig. 8.1: Daily average τ (at 0.55 μm) observed by AERONET sunphotometer (red), compared with daily $\{\text{PM}_{2.5}\}$ from the EPA-FRM monitor (black), in Baltimore, between July and August 2002. The mean of each dataset are given in parentheses in the legend. The AERONET data are Level 2 (quality controlled).

During the entire period, average $\{\text{PM}_{2.5}\}$ was $22.0 \mu\text{g}\cdot\text{m}^{-3}$, with average τ of 0.44 (also displayed in Fig. 8.1). Given a 2km PBL (e.g., [Taubman, 2004]), and a hygroscopic growth factor of 2.0 (e.g., [Gassó *et al.*, 2003]), this converts to a dry mass extinction coefficient of $5 \text{ m}^2\cdot\text{g}^{-1}$ for aerosol in Baltimore. This value is reasonable, and comparable with that given in prior literature.

8.2.3 Comparisons of datasets

This section provides scatterplots of comparison between datasets. They provide some understanding of the variability in measurement techniques and vertical distribution within the mid-Atlantic region.

Fig. 8.2a is a comparison of MODIS with AERONET –derived τ in the region, providing a validation of the MODIS over land product. The correlation is high ($R^2 = 0.86$) with nearly a one-to-one fit. There are some outliers, which should be explained individually. However, this plot indicates that the MODIS τ retrieval can be trusted. Plotted in (Fig. 8.2b) is the comparison of η retrieved by MODIS and AERONET (O’Neill method). There is some correlation ($R^2=0.29$), but it is obvious that the MODIS η product is far from validated.

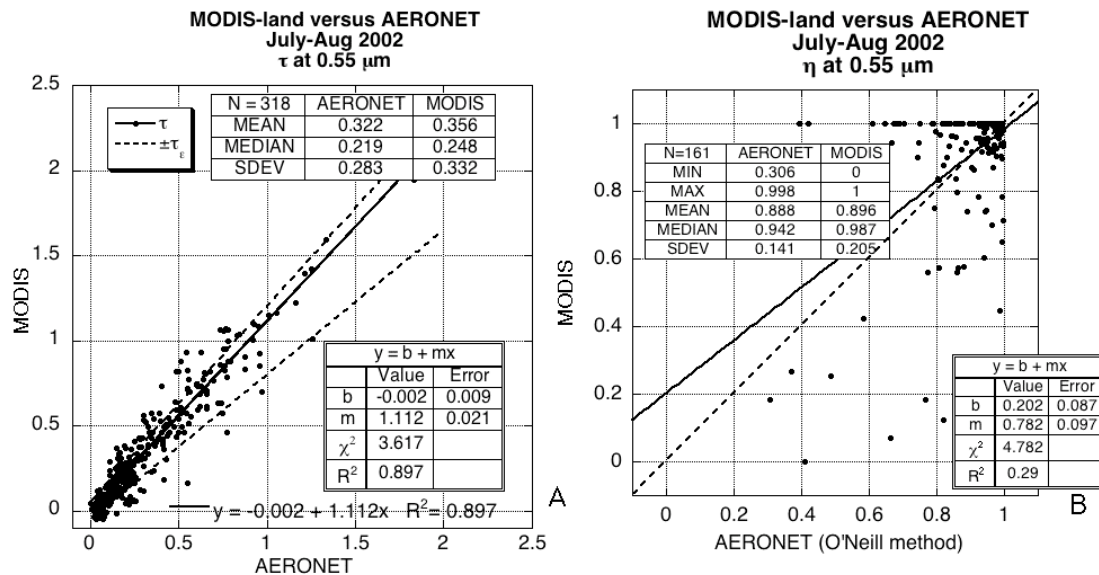


Fig. 8.2: Comparison of MODIS-land and AERONET derived τ (A) and η (B) over the mid-Atlantic region during July-August 2002. The τ expected error is represented by the dashed lines in (A). For AERONET, η is derived using the O’Neill method.

Fig. 8.3 plots the hourly-averaged surface $\{PM_{2.5}\}$ against the MODIS – derived τ in a 5×5 (~50 x 50 km) box. Plotted in red are all co-locations during July-August 2002. Since (except for at Baltimore site), it is known that the July 6-8 smoke did not make it to the surface in all locations, overplotted in black are the same points but without those dates. It is interesting that the red points are widely scattered outliers and not only for high τ , low $\{PM\}$. Aerosol spatial variability and sampling issues within the 50 km x 50 km MODIS may very important (e.g., [Kovacs *et al.*, 2006]), especially for this smoke episode. Without the smoke data, the correlation is larger ($R^2=0.52$). In fact, this correlation is larger than that found by *Engel-Cox et al.*, [2006] for c004, suggesting that c005 retrievals may be better suited for estimating $\{PM_{2.5}\}$ in the U.S. mid-Atlantic region.

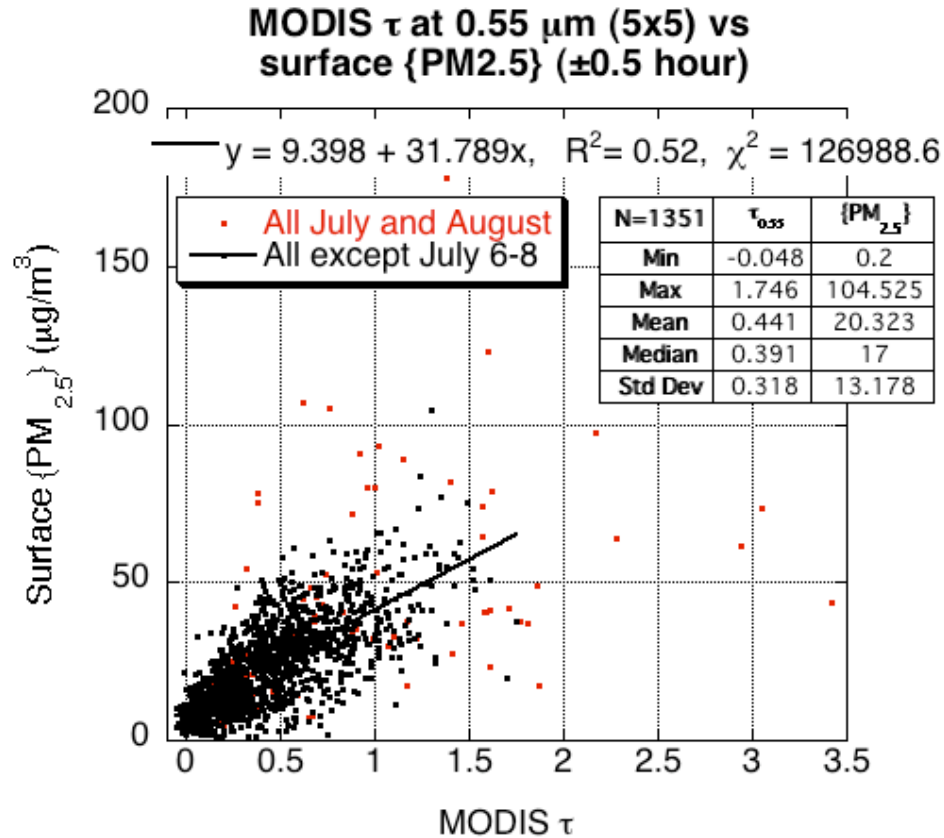


Fig. 8.3: Comparison of two-hourly averaged measured surface {PM_{2.5}} with 5x5 box averaged MODIS over land –derived τ for July and August 2002 in the mid-Atlantic (red). The three days of the heavy smoke episode (July 6-8) are removed (black), and the correlation is displayed.

In support of the MDE, the UMD Piper Aztec aircraft measured 22 profiles of scattering coefficient during the period [Taubman, 2004], concentrating on the interesting events described in section 8.2.2. Jennifer Hains analyzed each flight and calculated τ (from the scattering) at 0.55 μm . Fig. 8.4 compares the values, derived from these profiles, to the averaged MODIS τ in a 5x5 (25 values) box centered at the profiled location. Data are plotted if either Terra or Aqua passed over the site within 2 hours of the profile, and there were sufficient MODIS statistics (5 within the 25 possible); thus, only 10 matches were made. The means are within 6%, but the

regression shows low correlation coefficient ($R^2 = 0.26$). Part of the low correlation may be due the limited sampling height of the aircraft (profiles made below 3km, neglecting elevated aerosol for calculating τ). However, since some of the situations show higher τ from aircraft, the issues are assumptions used to derive scattering/extinction coefficients (and integrating to τ), and sampling variability.

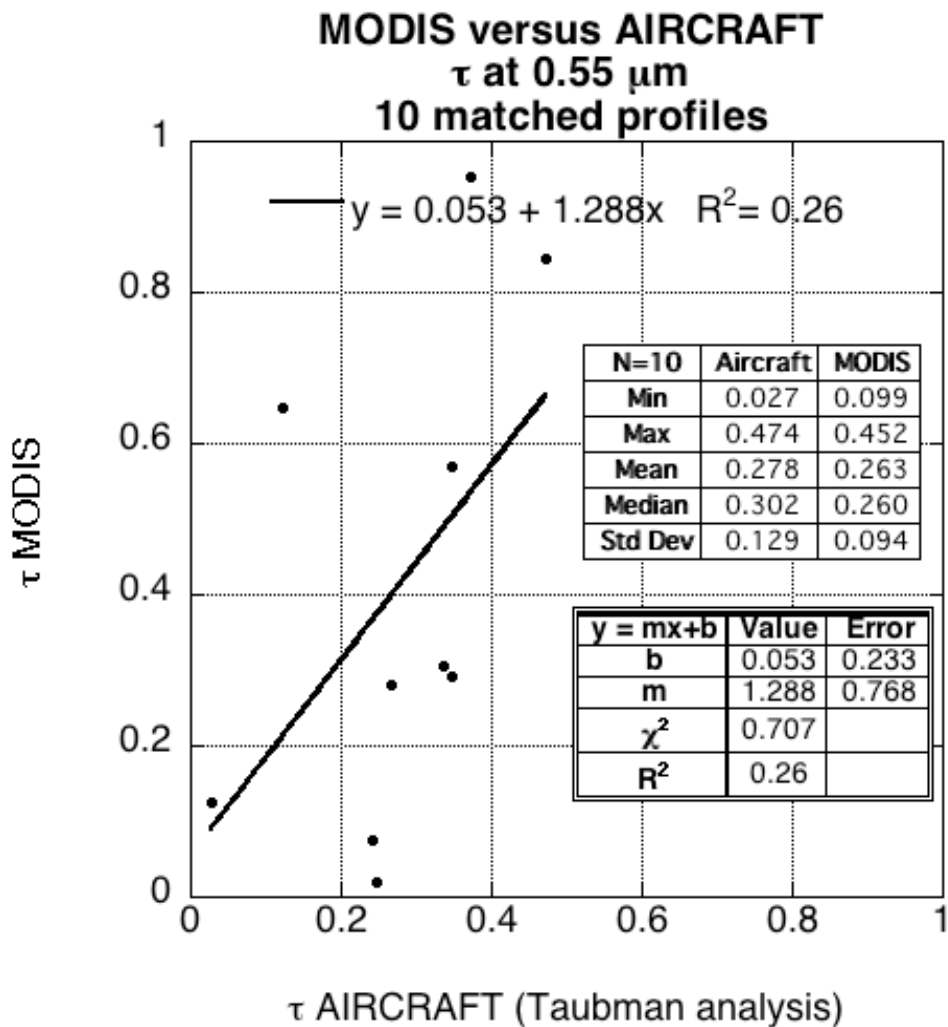


Fig. 8.4: Comparison (and regression) of MODIS derived τ (either Terra or Aqua) if observed within two hours of aircraft measured profile. Aircraft τ values were calculated by *Jennifer Hains*, following *Taubman*, [2004].

8.3: Introduction to CMAQ

For aerosol characterization and air quality forecasting, it is necessary to evaluate the models used for these purposes. They should be realistic in their treatment of aerosol processes, and provide results that can be validated by observations. *Kinne et al.*, [2006] describes a project (known as AeroCom) that is assessing aerosols within global chemical transport models (CTM) and general circulation models (GCM). In general, large-scale models demonstrate agreement in total aerosol optical depth (compared to remote sensing from AERONET and satellite), but completely disagree in deriving component masses and component optical depths. Since each model assumes different aerosol physical and optical properties, different meteorology, different size binning, and different physical and chemical aerosol processing, differences in model outputs are not surprising. While there are coordinated efforts to evaluate aerosol in global models, there is not much in the literature evaluating aerosol properties in regional chemical models, such as are used in air quality forecasting. As the CMAQ model was developed for the EPA, MDE is using the CMAQ model to evaluate scenarios for meeting NAAQS compliance in Maryland. This section evaluates results provided by the CMAQ air quality model to study aerosol in the region during July-August 2002.

The Models-3 Emission Projection and Processing System (MEPPS) is a flexible software framework that encompasses the Community Multi-scale Air Quality Model (CMAQ: *Byun and Ching*, [1999]). Designed and used by the USEPA to model the chemistry and physical processes leading to poor air quality, Models-3/CMAQ addresses applications ranging from regulatory issues to scientific studies.

The CMAQ system can simulate tropospheric ozone, acid deposition, visibility, surface PM_{2.5} and other constituents of air pollution. The Models-3 framework consists of the Fifth generation Penn State University/National Center for Atmospheric Research Mesoscale Model (MM5), the MEPSS emission system, and the CMAQ chemical transport model (CCTM). The Models-3/CMAQ system is an open source collection of computer modules that can be accessed and modified for a user's specific purpose.

One of the major advantages of CMAQ is its high resolution. The 'baseline' version of CMAQ run for the University of Maryland produces hourly output for 22 vertical levels (p-sigma coordinates), at 12 km x 12 km horizontal resolution within a 172 x 172 grid box (~2000 km²). This high resolution is comparable to MODIS 10 km x 10 km resolution and is adequate for studying aerosol variability on a regional scale. *Chandrasekar et al.*, [2002] evaluated the MM5 model for a pollution event over Philadelphia, and concluded that the model was generally successful at predicting the meteorology. Cloud cover, especially fair weather cumulus, is not well simulated by CMAQ (e.g., [Mueller et al., 2006]), in part due to averaging processes from MM5 to CMAQ.

The aerosol component of the CMAQ system is described in general by *Byun and Ching*, [1999], with the most version described by *Binkowski and Roselle*, [2003]. It is designed to be an efficient and economical depiction of aerosol dynamics that includes processes of direct emission, new (from gas) particle formation, coagulation, deposition and activation into cloud droplets. The model includes the primary emissions of elemental (black) carbon, organic carbon, dust, sea

salt and other species (from the 1995 USEPA emission inventory, plus assumed size distributions), as well as secondary (produced) species like sulfate, ammonium, nitrate and organics. CMAQ uses a ‘modal approach’, such that it considers the particle size distribution as a superposition of three lognormal modes (Aitken, accumulation and coarse) that are allowed to grow in size (diameter) and in concentration (loading) at every time step. Hygroscopic growth is also considered. Aerosol is allowed to jump from one mode to another. The properties of the size distribution for each mode and each species are calculated at each time step: the total particle number, surface area and mass concentrations. *Binkowski and Roselle* [2003] describe the components of each aerosol species modeled in CMAQ, as well as a number of diagnostic parameters that represent other properties of the aerosol.

Mebust et al. [2003] evaluated the speciation of the CMAQ air quality model against IMPROVE observations, finding that CMAQ consistently under-predicts the aerosol concentrations of each species (except for sulfate) by ~30-40%. *Smyth et al.* [2006] found similar behavior (under-prediction of mass) of CMAQ over a domain in Western Canada. However, there was excellent temporal agreement between the model and observations, suggesting that some of the aerosol processes simulated within the model are appropriate.

The following sections compare CMAQ output with surface and satellite measurements in the U.S. mid-Atlantic region. The spatial/temporal behavior of the aerosol properties is presumed to relate as described by *Ichoku et al.*, [2002a]. Thus, statistics of products are calculated for 5x5 grid boxes (60 km x 60 km for CMAQ), and compared to data within ± 1 hour.

8.4: CMAQ estimates of surface $\{PM_{2.5}\}$

Hourly CMAQ estimates of total surface $\{PM_{2.5}\}$ were compared to that observed by the continuous $\{PM_{2.5}\}$ monitors in the mid-Atlantic region within ± 1 hour. Fig. 8.5 shows that CMAQ consistently under-predicts total surface $\{PM_{2.5}\}$. Even when the heavy smoke event (July 6-8) is removed, the slope is only 0.349. However, the correlation coefficient is $R^2=0.325$, suggesting that while CMAQ may not be appropriate for quantitative surface $\{PM_{2.5}\}$ forecasting, it has some skill representing the relative magnitude. It is noted that in most cases where CMAQ predicts high $\{PM_{2.5}\}$ ($> 65 \mu\text{g}\cdot\text{m}^{-3}$), that observed concentrations are also high.

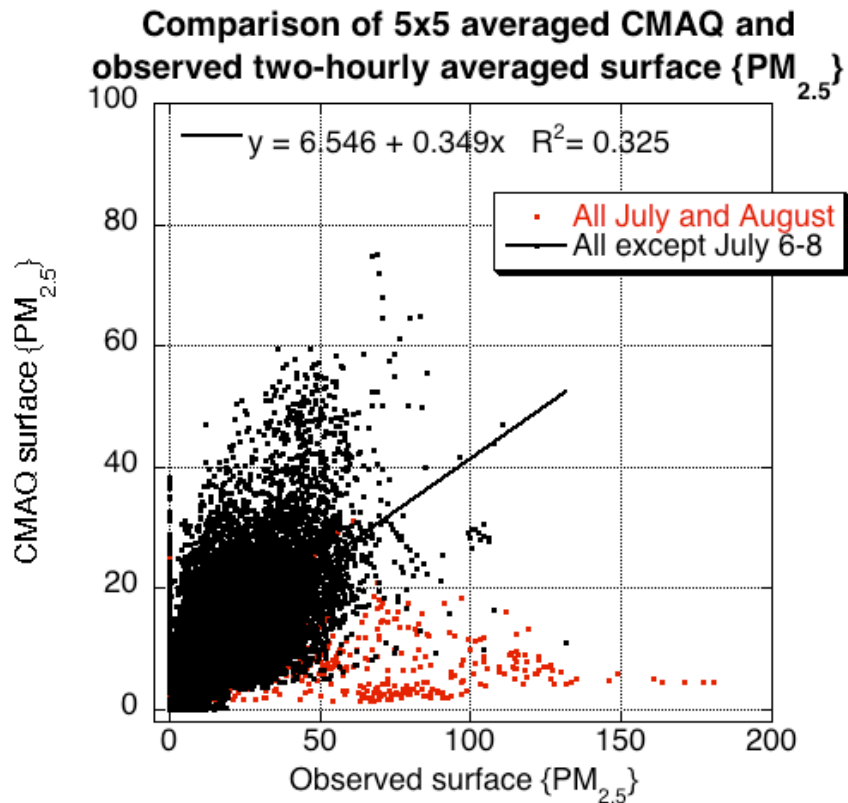


Fig. 8.5: Comparison of CMAQ 5x5 box averages (60 km) of surface $\{PM_{2.5}\}$ with observed two-hourly averaged $\{PM_{2.5}\}$ from continuous monitors. The red points are all collocations during July and August 2002, whereas the black points (and regression) exclude the smoke episode (July 6-8).

8.5: Evaluation of τ /PM relationship in CMAQ

8.5.1 Computation of τ from CMAQ output

The ‘modal’ approach used in CMAQ calculates the properties of the size distribution for each mode at each time step [Binkowski and Roselle, 2003]. Along with the surface PM concentration, another parameter monitored by the USEPA is the visibility, defined as a function of the extinction coefficient, β_{ext} (in units of km^{-1}). CMAQ calculates the extinction coefficient in two different ways.

A theoretical method for computing extinction is to perform full Mie calculations at each time step, integrating over the size distributions and refractive indices of each individual species and mode. This is computationally expensive, and is not necessarily representative of extinction coefficients measured *in situ*. In his Ph.D. dissertation, Park [2001] described a method for calculating aerosol optical properties, by interpolating to a LUT of previously simulated aerosol models. Unfortunately, while this method is now used within CMAQ for computing photolysis rates at each level, the individual calculations at each layer are not saved into output files.

The alternative method is introduced in Malm *et al.*, [1994] and is known as the ‘reconstructed mass extinction.’ This a fit to observations from the IMPROVE network, and is calculated empirically:

$$\beta_{ext} = 3.0 * f_{RH} * (\{\text{ammonium}\} + \{\text{nitrate}\} + \{\text{sulfate}\}) + 4.0 * \{\text{OC}\} + 10.0 * \{\text{BC}\} + 1.0 * \{\text{fine soil}\} + 0.6 * \{\text{coarse}\} \quad (8.3)$$

where the units of the mass extinction coefficients (the constants) are [$\text{m}^2 \cdot \text{g}^{-1}$], the curly braces represent aerosol species dry mass concentrations (sum of all modes) in [$\mu\text{g} \cdot \text{m}^{-3}$], and the f_{RH} is from a lookup table [*Malm et al.*, 1994] (plotted in Fig. 3.3). *Mebust et al.*, [2003] evaluated the visibility component of the CMAQ and found that in general, CMAQ over-predicts visibility by 25-35%, consistent with the under-prediction of aerosol mass at the surface.

While the above equation is intended for computing surface extinction, it can be applied at any level within the CMAQ atmosphere. The optical depth is the integral of the extinction coefficient at the center of each layer, multiplied by the layer thickness (in km).

Due to constraints of computer space, a CMAQ model end-user has access only to the information contained in the {} of Eq. 8.3 (total concentration of each species), and not the size distribution and the extinction properties of each modal component. This means that a reconstructed mass equation, such as Eq. 8.3, is the only way to calculate τ from CMAQ output. It is necessary that the assumed species mass extinction coefficients are appropriate for using a reconstructed mass equation for characterizing aerosol in the mid-Atlantic region.

The CMAQ ‘baseline’ version outputs from July-August 2002 are available on the University of Maryland’s computer network. The ‘concentration’ files contain total speciated PM concentrations (sums of all three modes), as well as pollutant gas concentrations, at 12 km x 12 km horizontal resolution, in 16 p-sigma (p_σ) layers, at every hour during the two month period. Additional files are outputted by CMAQ to

include latitude, longitude, elevation and urban surface percentage in each horizontal box, as well as information about thickness, pressure, temperature, water vapor, liquid water, ice and snow mixing ratios at each level in the atmosphere.

In p-sigma coordinates, (pressure normalized to surface level pressure; $p_\sigma = p_{\text{layer}}/p_{\text{sfc}}$, where p_{layer} is the pressure and p_{sfc} is the pressure at the land surface), the values for each layer (bottom of layer) are $p_\sigma = 1.0, 0.9974, 0.9940, 0.9890, 0.9820, 0.9720, 0.9590, 0.9430, 0.9230, 0.8990, 0.8719, 0.8390, 0.8030, 0.7630, 0.7180, 0.6680$ and 0.5680 . These values correspond to layer middle heights (km above the surface) of approximately $0.010, 0.024, 0.068, 0.116, 0.185, 0.282, 0.398, 0.544, 0.727, 0.949, 1.212, 1.523, 1.886, 2.312, 2.820$ and 3.393 km, depending on the elevation of the surface, pressure and temperature. The 16 layers are a subset of the 22 layers modeled by CMAQ, truncated on assumption that little tropospheric air pollution is contained above about 3.6 km (and that comparable Piper Aztec measurements are limited in the vertical by aircraft design).

In each layer, and at each grid box, the relative humidity is calculated from the CMAQ outputs of vapor mixing ratio [w in kg vapor per kg dry air], using the parameterization from *Rogers and Yau*, [1989], e.g.,

$$RH = \frac{w}{w_s} \quad (8.4)$$

where the saturation mixing ratio (w_s) is

$$w_s = 0.622 \left(\frac{6.112 \exp[17.67T/(T + 243.5)]}{p} \right), \quad (8.5)$$

a function of the temperature (T) in deg C and pressure (p) in millibars. Note that the numerator in the parentheses is the saturation vapor pressure (e_s), and that 0.622 is the

ratio of water vapor and dry air specific heats. This relative humidity is in turn, used to calculate f_{RH} for specific aerosol species.

8.5.2 Calculating τ with the Malm reconstructed mass extinction

As shown by Fig. 8.5, CMAQ tends to under-estimate surface aerosol concentration. The aerosol may exist in the model's column, but not at the correct level. Therefore, it is instructive to compare the CMAQ integrated aerosol loading with observations. A reconstructed extinction coefficient equation like Eq. 8.3 is appropriate.

The extinction coefficients as written in Eq. 8.3 [Malm *et al.*, 1994] were used to compute the aerosol optical depth at each of the 172x172 points in the CMAQ domain, for each daylight hour (9:00 to 23:00 UTC, 5:00 AM to 9:00 PM Eastern Daylight Time). Relative humidity dependence of the optical properties was computed from relative humidity, which was calculated from model temperature, pressure and water vapor mixing ratio at each layer (e.g., Eqs. 8.4-8.5).

Fig. 8.6a compares CMAQ derived τ with MODIS -observed τ , centered at and closest in hour with MODIS overpass. Both datasets are averaged over a 5 x 5 boxes (~50 x 50 km for MODIS; 60 x 60 km for CMAQ). No comparison is made when either MODIS detects a cloud, or there is RH>98% or liquid water present within any layer of the CMAQ output. When the known smoke days are taken out, there is a surprisingly robust correlation ($R^2 = 0.439$), however the slope is 0.235. CMAQ mean τ is only ~31% of observed mean τ . It is interesting that the τ correlation coefficient is somewhat higher than for surface $\{PM_{2.5}\}$ ($R^2 = 0.325$).

Although CMAQ severely underestimates the (reconstructed) optical depth as well the surface $\{PM_{2.5}\}$, it is possible that the relative apportionment of the optical depth to the surface is correct. If the model's internal aerosol apportionment is appropriate, it might indicate that aerosol processes in the atmosphere are well simulated by the model, but that the model is only deficient in its source inventory.

Fig. 8.6b correlates the CMAQ surface $\{PM_{2.5}\}$ with CMAQ -derived τ . Compared to MODIS/monitor observations, CMAQ has larger internal correlation ($R=0.8$), which indicates that CMAQ does not include elevated aerosol information in its domain. The internal CMAQ slope is nearly $58 \mu\text{g}\cdot\text{m}^{-3}\cdot\tau^{-1}$, which is much higher than observed slope ($\sim 30 \mu\text{g}\cdot\text{m}^{-3}\cdot\tau^{-1}$).

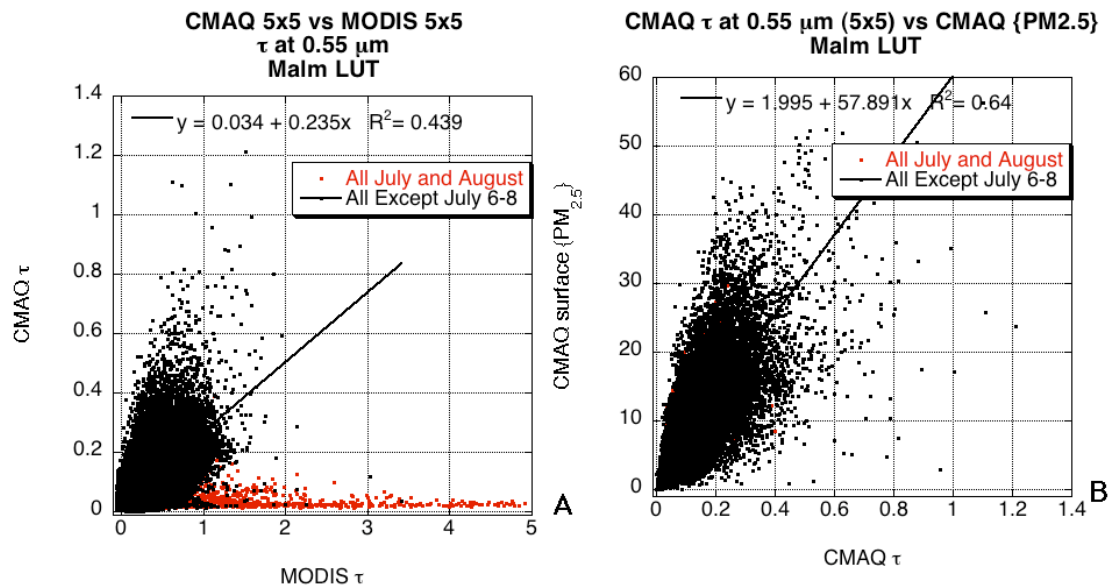


Fig. 8.6: A) CMAQ 5x5 (60 x 60 km) box averaged τ derived with the Malm (IMPROVE) LUT compared with MODIS 5x5 box averages (between 50-80 km depending on view angle). B) CMAQ 5x5 box averages (60 km) of surface $\{PM_{2.5}\}$ compared with CMAQ-derived τ (Malm LUT). The red points are all co-locations during July and August 2002, whereas the black points (and equations) denote exclusion of the three days of heavy smoke episode (July 6-8).

One can suggest that the internal vertical apportionment of CMAQ should match observed surface to column apportionment. One solution is to revise the reconstructed mass extinction equation with updated assumptions for the f_{RH} dependency and/or assumed mass extinction coefficients of the dry aerosol.

8.5.3 Calculating τ using GOCART models for reconstructed mass extinction

Chin et al., [2002] describes the size and optical characteristics of the aerosol assumed within the GOCART model. While they are not identical to the aerosol types modeled by CMAQ, Chin suggested [personal communication] using their properties to represent the CMAQ aerosol types. GOCART's sulfate model was assumed for the union of sulfate, nitrate and ammonium, the OC model for organic carbon, the BC model for elemental carbon, and dust modes B and E for fine mode and coarse mode dusts, respectively. I also used the GOCART formulations for f_{RH} , different for sulfate, organic and black carbon aerosol types (e.g., [Köpke et al., 1997]). Since the optical properties for the GOCART models [Chin et al., 2002] are presented for a wavelength of 0.50 μm , and that fine mode aerosol is assumed to be smaller than $r < 0.5 \mu\text{m}$, I re-calculated the Mie optical properties (using MIEV; Wiscombe, [1980]), for 0.55 μm wavelength and assumed $r < 1.25 \mu\text{m}$ for $\text{PM}_{2.5}$. I used the listed values [Chin et al., 2002] for aerosol density, except for BC, which I updated (as per Bond and Bergstrom, [2006]) to $1.8 \text{ g}\cdot\text{cm}^{-3}$.

Figs. 8.7a and 8.7b are analogous to Figs. 8.6a and 8.6b, using the GOCART properties instead of the IMPROVE [Malm et al., 1994] mass coefficients for reconstructing the extinction. The correlations are nearly the same as those using the

IMRPROVE coefficients, but the slope is raised to 0.374 for τ (mean CMAQ is 56% of mean MODIS). The slope of the CMAQ internal $\tau/\{\text{PM}\}$ equation is lowered to $39 \mu\text{g}\cdot\text{m}^{-3}\cdot\tau^{-1}$, suggesting that GOCART properties provides better representation of the aerosols over the mid-Atlantic.

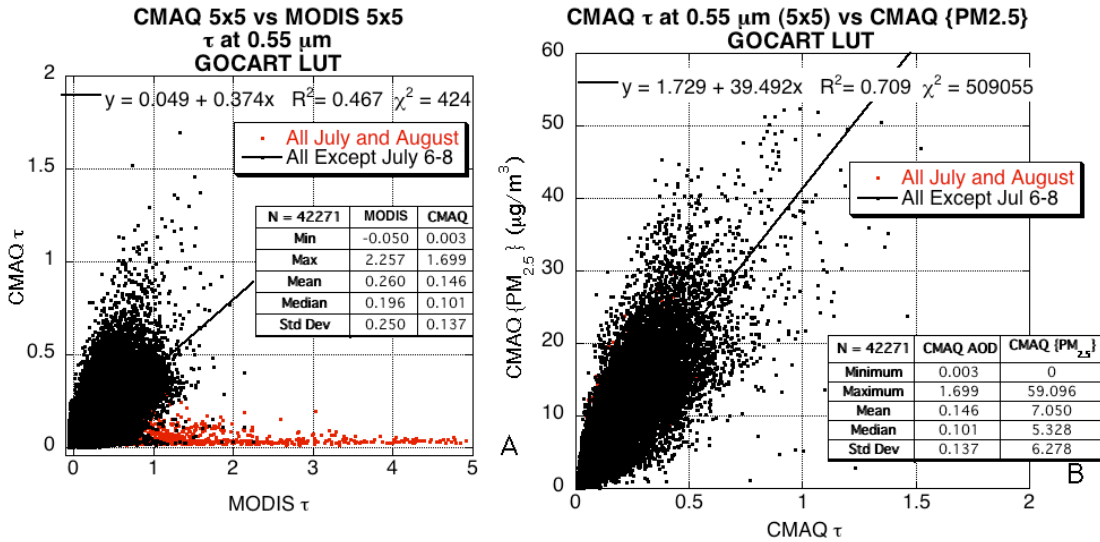


Fig. 8.7: A) CMAQ 5x5 (60 x 60 km) box averaged τ derived with the GOCART LUT compared with MODIS 5x5 box averages (between 50-80 km depending on view angle). B) CMAQ 5x5 box averages (60 km) of surface $\{\text{PM}_{2.5}\}$ compared with CMAQ-derived τ (GOCART LUT). The red points are all co-locations during July and August 2002, whereas the black points (and regressions) denote exclusion of the three days of the heavy smoke episode (July 6-8).

Fig. 8.8 shows CMAQ compared with AERONET, whereas all points during the day (not just near noon-time MODIS over pass time) are available. The regression equation and correlation coefficient is very similar to that of Fig 8.7, indicating consistency. Separating CMAQ and AERONET comparisons by hour shows no significant difference based on time of day, but future study is desirable.

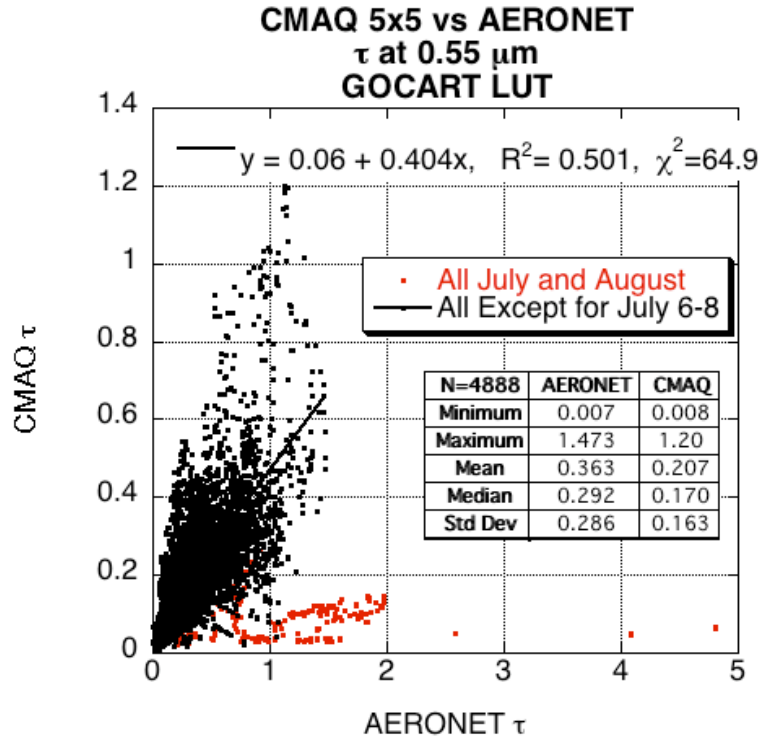


Fig. 8.8: Comparison of CMAQ 5x5 box averages (60 km) of computed τ (GOCART LUT) with observed hourly averaged AERONET observations. The red points are all collocations during July and August 2002, whereas the black points (and regression) exclude the smoke episode (July 6-8).

8.5.4 Calculating τ using c005 LUT models for reconstructed mass extinction

As a final exercise in CMAQ τ calculation, I evaluated CMAQ, but using instead the extinction properties calculated via the new MODIS (c005) LUT, appropriate for the region. However, instead of using values retrieved from Table 6.2, I re-calculated the properties of the weakly absorbing model (Chapter 6) for a truncated size distribution ($r < 1.25 \mu\text{m}$) and appropriate values of dry density (sulfate; $1.8 \text{ g}\cdot\text{m}^{-3}$). The resulting model mass extinction ($\sim 4.1 \text{ m}^2\cdot\text{g}^{-1}$) was applied to the sum of all $\text{PM}_{2.5}$ components (e.g., sulfate + ammonium + nitrate + organic

carbon + elemental carbon + fine soil), while the dust model mass extinction ($0.5 \text{ m}^2 \cdot \text{g}^{-1}$) and density ($2.6 \text{ g} \cdot \text{m}^{-3}$) was assumed to apply to coarse aerosol mass.

Because the aerosol optical models derived in Chapter 6 are intended to represent ‘ambient’ aerosol properties, the weakly absorbing model mass extinction does not necessarily represent ‘dry’ mass as does the GOCART [*Chin et al.*, 2002] and the IMPROVE [*IMPROVE*, 2006] modeled values. Therefore, for f_{RH} , I assumed the formula suggested by *Kotchenruther et al.*, [1999] with values of the exponent ($\gamma=0.35$) suggested by *Taubman*, [2004] in his dissertation. The results turned out to be similar to those using the IMPROVE mass extinction assumptions (simulated mean $\tau \sim 35\%$ of observed and simulated $\tau/\{\text{PM}\}$ slope $\sim 61 \text{ } \mu\text{g} \cdot \text{m}^{-3} \cdot \tau^{-1}$), so they are not plotted here.

8.6: Spatial comparison between MODIS and CMAQ derived τ .

The best simulations of τ itself, as well as internal vertical apportionment of τ and $\{\text{PM}_{2.5}\}$, were realized when using the GOCART assumed aerosol optical properties within CMAQ. Thus, the GOCART model assumptions were selected to provide detailed comparison of CMAQ versus MODIS -derived τ . Figs. 8.9a and 8.9b provide examples for cases when the spatial match was good (July 16) and poor (July 7). As noted before, July 16 is a case of typical summer buildup of regional, sulfate dominated haze, whereas July 7 is an atypical case of dense smoke transported into the region.

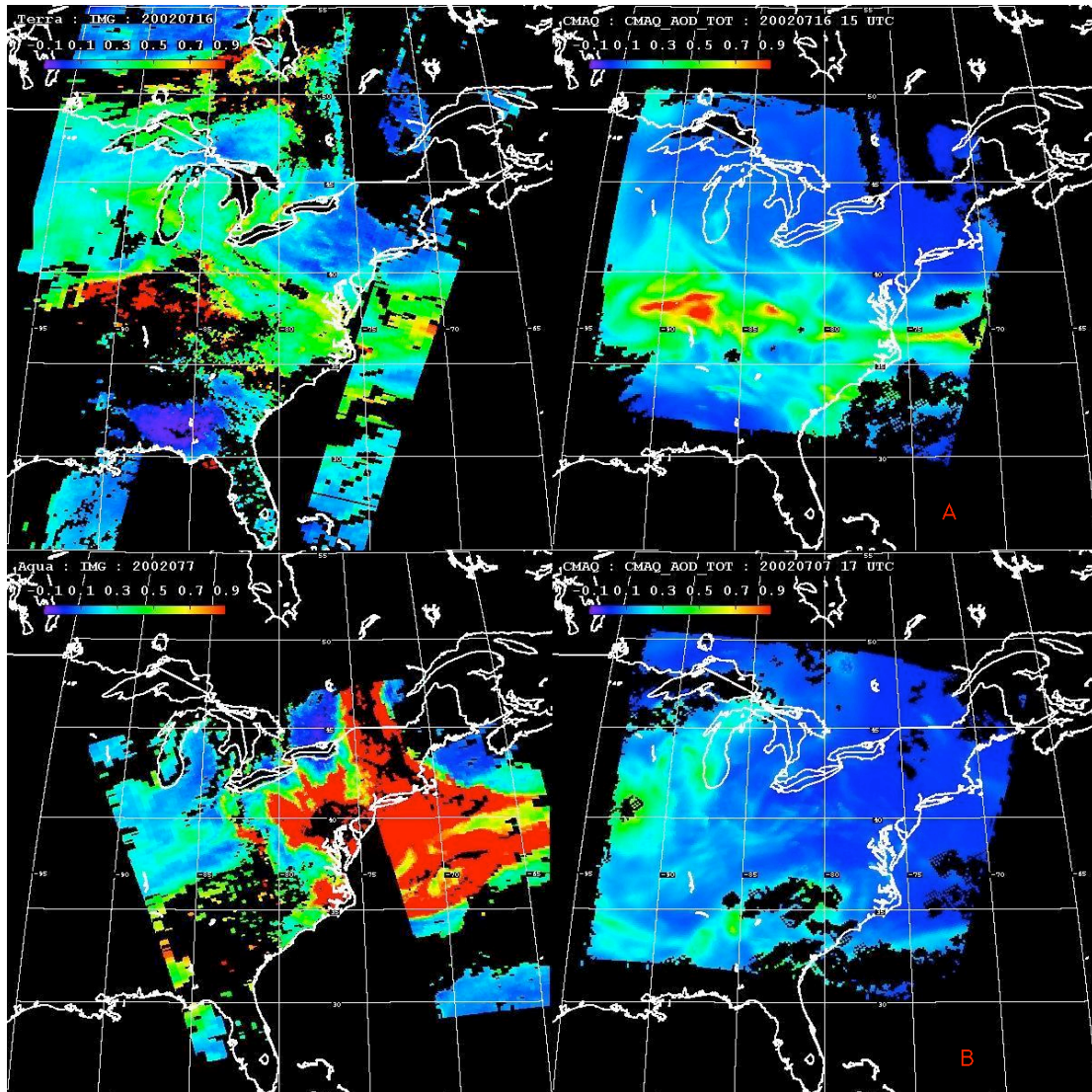


Fig. 8.9: Comparison of CMAQ (GOCART LUT) to MODIS retrievals of τ at $0.55 \mu\text{m}$. The top panel (A) is for a day of typical sulfate pollution (July 16, 2001) where the model matches the satellite. The bottom panel (B) is from an unusually heavy infusion of Canadian smoke at high altitudes (July 7, 2001), where the model fails to capture satellite-measured τ .

For the July 7 case, the spatial distribution and the relative magnitude of the aerosol plume is captured very well by CMAQ. In general CMAQ underestimates MODIS by about 20%, but the location of maximum τ in Kentucky area is confirmed by MODIS. CMAQ is less cloudy than MODIS, but this is at least partially due to

having CMAQ data only to 3.6 km. High (cirrus) clouds that are observed by MODIS cannot be determined from the truncated CMAQ vertical profiles.

The July 16 case shows no similarity between the two datasets. This is the case of heavy smoke transport; CMAQ is not privy to information outside of its domain. Therefore, CMAQ cannot be expected to simulate this smoke.

8.7: CMAQ τ and vertical profiles compared to UMD Aircraft.

As might be expected, the slope of CMAQ –derived τ and aircraft –derived τ is similar to CMAQ compared to either MODIS or AERONET. Figure 8.10a is a scatter plot of this comparison, for all matches during July-August, as well as when excluding the smoke episode of July 6-8 (which is regressed). Although mean CMAQ $\tau = 98\%$ of aircraft -derived τ , this is misleading because the slope is ~ 0.365 , offset = 0.15, and the correlation is low ($R^2=0.26$). Thus, while the model may capture the magnitude of τ in the mean sense, it cannot characterize the spatial distribution of the aerosol.

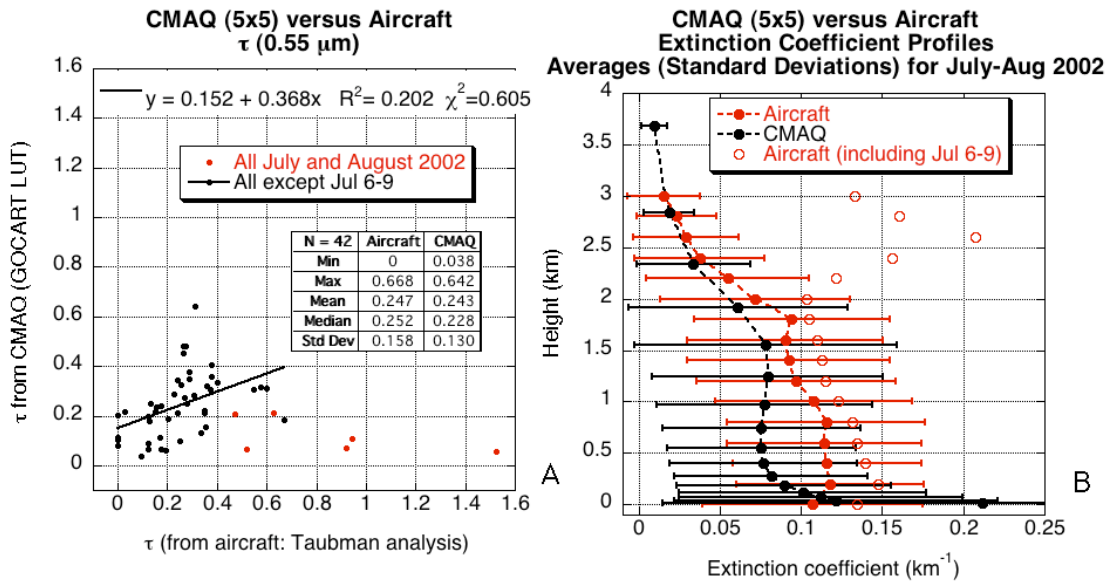


Fig. 8.10: A) Comparison of CMAQ derived τ (GOCART LUT) to derived τ from aircraft profiles. The red points are for all profiles during the July-August 2002, whereas the black points (regressed) exclude the smoke event of July 6-9, 2002. B) Comparison of average CMAQ derived extinction profiles (GOCART LUT) and averaged aircraft extinction profiles (red dots) for the July-August 2002 period, except for the heavy smoke event. The error bars are the standard deviations for each data set. The CMAQ data are 5x5 boxes centered at and hours closest to aircraft profiles. The red circles are the two-month averages if the smoke profiles were included. Aircraft profiles were provided by *Jennifer Hains*, using data and formulas of *Taubman*, [2004].

Finally, both CMAQ and the aircraft profiles provide estimates about the vertical structure of extinction. Figure 8.10b displays averaged (throughout the entire period except for Jul 6-9) of CMAQ and aircraft –derived extinction coefficients. The aircraft extinction profiles are the sum of scattering and absorption at 0.1 km altitude increments, provided by Jennifer Hains. The smoke days (July 6-9) are characterized by greatly increased high altitude values. Without the smoke, there is some similarity between the two profiles, especially when considering the standard deviations during the period (displayed by the error bars). In the middle of the PBL, however, the CMAQ B_{ext} is only about 60% of that measured by aircraft. Detailed

analysis of the modeled vertical profile is beyond the scope of this work, but one hypothesis is that because CMAQ underestimates clouds (especially fair weather cumulus clouds, [Mueller *et al.*, 2006]), CMAQ is not converting enough SO₂ into sulfate aerosol.

Representing the two specific aerosol events compared by the MODIS/CMAQ imagery of Fig. 8.9, I compare extinction profiles from the same two dates in Fig. 8.11. While CMAQ shows some minimal skill at simulating the vertical profile of typical pollution on July 16, it fails at capturing any of the smoke observed on July 8 over Easton, Maryland (also analyzed by [Colarco *et al.*, 2004]).

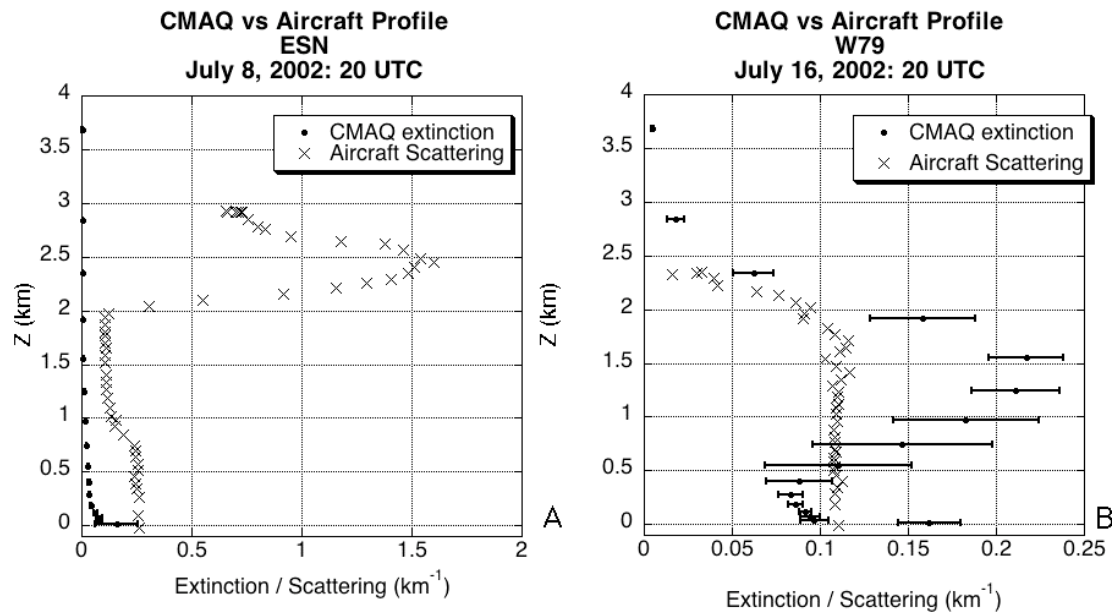


Fig. 8.11: Comparison of CMAQ extinction (GOCART LUT) to specific UMD aircraft profiles of scattering over airports (both at 0.55 μm). The left panel is for a day of typical sulfate pollution (July 16, 2001) where the model reasonably matches the profile. The bottom panel is from an unusually heavy infusion of Canadian smoke at high altitudes (July 7, 2001), where the model does captures very little of the aircraft measured extinction. The error bars for the model represent the standard deviation within a 5x5 box (60 x 60 km) around the airport.

8.8: Summary

Efforts have been made to apply MODIS -derived τ products to help to monitor and forecast surface $\text{PM}_{2.5}$ concentrations and air quality. However, if MODIS is to be used to address policy issues related to poor air quality (for example, withdrawal of federal funds to states or counties in non-attainment of NAAQS), it should be well understood and its products be of high accuracy. In the mid-Atlantic region, the second-generation of MODIS τ products display high enough accuracy (compared to AERONET over a 50 km x 50 km box) with enough spatial resolution to be considered to help characterize aerosol in the region.

The next step tested whether (column integrated) τ would be related to surface $\{\text{PM}_{2.5}\}$. Scatterplots of the two parameters (noting different units) showed that there is a general correlation between the two, but that in some cases (e.g., elevated aerosol layers resulting from long range transport), columnar aerosol properties would be unrelated to what would be measured at the surface.

I evaluated the relationship of τ and surface aerosol concentrates as simulated by the baseline run of the CMAQ air quality model. Three different lookup tables and f_{RH} corrections were used to calculate τ from the model, showing that the use of the GOCART assumed aerosol parameters and relative humidity corrections [Chin *et al.*, 2002] provided the best fit to observed τ from AERONET, MODIS and integration of aircraft measured extinction profiles. The GOCART LUT also provided the best simulation of the τ to $\{\text{PM}_{2.5}\}$ relationship observed by the combination of remote sensing and surface monitors. However, while the τ to $\{\text{PM}_{2.5}\}$ apportionment could be represented internally, both modeled quantities were

only ~40% of the magnitudes of those observed. As for vertical profiles, CMAQ underestimated extinction at all levels, except for overestimation at Earth's surface. Therefore even if MODIS -derived τ could be used to estimate surface $\{PM_{2.5}\}$, CMAQ is not yet realistic and requires substantial improvement before use in air quality application.

Chapter 9: Conclusion: Summary and Further Study

9.1: Summary

Aerosols are recognized as major components of the Earth's atmosphere/surface climate system, influencing the radiative budget, clouds and precipitation processes and the health of organisms on the planet (including humans). A significant fraction of emitted aerosol is anthropogenic, so that they are monitored by the USEPA, the IPCC and other international agencies that regulate pollution and climate. However, unlike long-lived spatially homogenous gaseous pollutants (such as carbon dioxide), aerosols' short lifetimes (~ 1 week), complicated chemical compositions, and tendency to interact with clouds and precipitation processes, make them impossible to monitor on all scales from only one instrument. Thus, aerosol characterization must be performed from multiple sensors, both *in situ* and remotely, from surface, aircraft, and satellite. It is imperative to understand each measurement technique and how it relates to others. Otherwise, aerosol properties gleaned from one instrument may seem contradictory to another set of measurements.

In this dissertation, I concentrated on remote sensing of aerosols from space, specifically from the MODIS sensors aboard NASA's polar-orbiting Terra and Aqua satellites. Although the MODIS operational aerosol retrievals had been validated in the past, it was becoming apparent that the MODIS products were suffering biases and other inaccuracies that could be fixed. By comparing with other remote sensing techniques (e.g both sun and sky sunphotometry, I developed a new algorithm that reduced the bias and uncertainty in retrievals of global τ , over dark land surfaces.

This second-generation operational algorithm was put into operation in early 2006 and provided a complete mission ‘Collection 5’ product dataset by the end of 2006.

During algorithm development, I derived a set of optical and physical properties (aerosol ‘models’) that characterized the range of globally observed aerosol (as observed by AERONET). Using the technique of atmospheric correction, I parameterized surface reflectance in two visible wavelengths (0.47 and 0.66 μm) as a function of 2.12 μm , scattering angle and surface type ($\text{NDVI}_{\text{SWIR}}$). I tapped the 2.12 μm channel to provide coarse aerosol optical information as part of a simultaneous inversion, where previous MODIS algorithms over land presumed no information. Finally, I implemented a better correction for elevated surfaces with sophisticated radiative transfer that includes atmospheric polarization.

I applied the new algorithm to a subset (the testbed) of MODIS observations, retrieving τ with higher accuracy than the previous MODIS algorithm, regressing nearly one to one with global sunphotometer measurements, with correlation coefficient $R=0.9$. Globally, histograms and statistics indicate that the new MODIS algorithm retrieves average global over-land τ of ~ 0.21 (at 0.55 μm), as compared to the previous version’s estimate of 0.28.

Although the new global aerosol retrieval algorithm was intended to help answer global climate questions, the derived products are applicable to problems of poor air quality and surface $\{\text{PM}_{2.5}\}$ non-attainment in the U.S. mid-Atlantic region. As the University of Maryland was funded to evaluate the year 2002 in support of the state of Maryland’s mission to put together an ‘attainment’ plan, I concentrated on the most characterizing aerosol during the most active two months of the year (July and

August 2002), where both surface {PM} and column τ reached high levels (as seen by EPA's continuous monitors and AERONET sites). In addition to typical sulfate-dominated pollution episodes (e.g., July 16-22), the period included infusions of transported smoke (July 6-8) from Canada [Taubman *et al.*, 2004; Vant-Hull *et al.*, 2005; Colarco *et al.*, 2004], when AERONET observed $\tau > 2.0$.

I evaluated MODIS products during the period and demonstrated that the τ product was within expected error bars, as compared to (ground-truth) AERONET sites in the region (regression: $\tau_{\text{MODIS}} = 0.04 + 1.04\tau_{\text{true}}$, with correlation $R^2=0.88$). The η product was somewhat correlated ($R^2=0.18$), but could not be considered validated. We conclude that one is justified to use the MODIS -derived τ for comparison with other datasets.

MODIS derived τ in 5 x 5 boxes (~ 50 x 50 km) centered at surface PM_{2.5} continuous monitors was compared with the measured surface {PM_{2.5}} within ± 1 hour of overpass, in Maryland and the surrounding MARAMA region. Similar to previous studies (e.g., [Engel-Cox *et al.*, 2006]), τ was correlated with {PM_{2.5}}. For typical summertime conditions (not including the smoke episode of July 6-8), the regression equation was ($\{\text{PM}_{2.5}\} = 9.0 + 31.8 \tau_{\text{MODIS}}$; $R^2 = 0.52$), indicating that MODIS products can be used for monitoring surface aerosol.

As part of EPA's Maryland regulatory plan, the CMAQ model is being used to evaluate the processes that lead up to surface PM non-attainment. I analyzed the products from the 'baseline' CMAQ model runs for the period. The major task was calculating ambient optical depth from dry aerosol mass concentrations. This required assumptions about the mass extinction coefficients and dependence on

relative humidity for each species, such that I could integrate the extinction as a function of relative humidity and layer thickness over the entire column. Because the CMAQ model outputs do not include such extinction information, I was forced to make assumptions. I tried three different sets of extinction/humidity assumptions, including those assumed by IMPROVE [Malm *et al.*, 1994], by the GOCART model [Chin *et al.*, 2002], and by modifying my previously derived dust and weakly absorbing aerosol models used in the new MODIS algorithm. The GOCART aerosol optical properties provided the best match to observed τ (from either AERONET or MODIS), as well as the most similar $\tau/\{PM_{2.5}\}$ to that observed by MODIS and surface monitors. However, CMAQ means of each property were only about 50% of the means of those observed, indicating that CMAQ is under-predicting aerosol consistently throughout the column.

For cases of ‘typical’ summertime pollution (e.g., July 16), CMAQ produced a regional picture of τ that visually compared to that observed by MODIS. For cases of atypical pollution (e.g., July 7) marked by transported smoke, CMAQ has no knowledge of emissions outside the regional domain, resulting in no similarities between the two images.

Finally, I compared both MODIS and CMAQ with the total τ and extinction profiles derived from the UMD aircraft flights during July and August 2002. MODIS and aircraft τ were reasonably correlated, especially when considering appropriate single scattering albedo and that the aircraft profiles did not reach above 3.5 km. Similar to the performance at estimating surface aerosol, CMAQ values of extinction

and total aerosol optical depth (in typical conditions, not including the smoke event) were on average only about 50% of those observed aboard the Piper-Aztec.

9.2: Aerosol Direct Radiative Effect

Globally, the new algorithm tends to reduce the average τ over land, from $\tau=0.28$ (c004) to $\tau=0.21$ (c005). This result is important in deriving estimates of aerosol effects on the global radiative budget. *Yu et al.* [2006] estimate the (observationally based) aerosol *direct radiative effect (DRE)* to be -5.5 ± 0.2 and $-4.9\pm 0.7 \text{ W}\cdot\text{m}^{-2}$ over ocean and land, respectively. *Anderson et al.*, [2005] follows *Charlson et al.*, [1991] and linearly relates the *DRE* to τ (when $\tau \ll 1.0$) by a factor known as the aerosol *climate radiative efficiency (E)*. *E* is defined as

$$E = -\frac{1}{\mu_0} F_0 T^2 (1 - A_c) \omega_0 \beta_{\uparrow} \left[(1 - R_s)^2 - \left(\frac{2R_s}{\beta_{\uparrow}} \right) \left(\frac{1}{\omega_0} - 1 \right) \right].$$

Here, F_0 is the globally averaged TOA solar irradiance ($\sim 342 \text{ W}\cdot\text{m}^{-2}$), μ_0 is about 0.5 in the global average, A_c is the fractional cloudiness of the globe (~ 0.6), T is the spectrally integrated atmospheric transmittance above the aerosol (~ 0.8), ω_0 is ~ 0.9 , R_s is the globally spectrally integrated land surface albedo (~ 0.10) and β_{\uparrow} is the aerosol upscattering ratio (~ 0.3 , note β_{\uparrow} is related to g). Plugging these values into the equation results in $E \sim -30 \text{ W}\cdot\text{m}^{-2}\cdot\tau^{-1}$ over land. For $\tau = 0.28$, this translates to $DRE = -8.4 \text{ W}\cdot\text{m}^{-2}$, where for $\tau = 0.21$ (assuming the same values for ω_0 and β_{\uparrow}), $DRE = -6.3 \text{ W}\cdot\text{m}^{-2}$. In other words, a climate model, using MODIS derived τ as input, would reduce the magnitude of over-land aerosol *DRE* by 25% or $2.1 \text{ W}\cdot\text{m}^{-2}$.

Assuming that this estimate is not representative of aerosol over deserts and other

bright surfaces (about 20% of the land area), these before and after DRE estimates are -6.7 and $-5.0 \text{ W}\cdot\text{m}^{-2}$. Regardless, there is significant impact to DRE estimates simply due to a new MODIS algorithm. When this DRE is spread out over the globe (assuming 30% of the Earth's surface is land), the change of global DRE is $\sim +0.5 \text{ W}\cdot\text{m}^{-2}$.

If one estimates that $\sim 30\%$ of global aerosol is anthropogenic (e.g., *Yu et al.* [2006]), then implementing the new algorithm leads to a change of estimated DRF of $\sim +0.15 \text{ W}\cdot\text{m}^{-2}$. In its latest summary for policy makers, the IPCC [*IPCC*, 2007] estimates global aerosol DRF as $\pm 0.5 \pm 0.4 \text{ W}\cdot\text{m}^{-2}$, meaning that the change of $+0.15 \text{ W}\cdot\text{m}^{-2}$ is both a significant change, yet well within the stated uncertainty. More work is needed to further pin down MODIS based estimates of DRE and DRF.

9.3: Further study

As a researcher, I realize that there is still incredible amount of work that should be performed, both in creating algorithms for satellite sensors, as well as in characterizing aerosols globally and within the mid-Atlantic region. Here, I consider possibilities only for the immediate future.

The MODIS instruments do not provide the only observations of aerosol properties. Previous and current lower resolution satellite sensors (such as TOMS, AVHRR and GOES) have value in evaluating decadal aerosol trends [*Mischenko et al.*, 2007], especially when calibrated with MODIS (e.g., *Ignatov et al.*, [2005]). Newer and future passive instruments (such as MISR, POLDER and OMI) provide quality information in different wavelengths as well as directional and polarization information, which can be fused with information from MODIS to determine more of

the climatic and distributional characteristics of aerosol. In fact, numerous proposals have been submitted through NASA agencies (including GSFC and the MAST) for providing such fusion. Yet, this does not mean that *in situ* measurements of aerosols will become obsolete. They are representative of discrete locations and times, and provide direct measurements of the aerosol properties most important in our daily lives.

The next significant step forward in global and regional aerosol research is from active sensors such as those from the Calipso satellite-borne and various surface borne lidar instruments. These instruments, while focused only on narrow swaths or in discrete locations, provide information about the vertical distribution that represents the same physics (light extinction by aerosols) as measurements from passive sensors. Thus, they should be used in combination, each measurement constraining the others. For example, *Anderson et al.*, [2005] presents a strategy for combining the instruments from the “A-Train” of satellite instruments. The REALM group at University of Maryland-Baltimore County (<http://alg.umbc.edu/usaq/>) is using lidar data in national and regional applications (e.g., [*Engel-Cox et al.*, 2006]). These applications are becoming more quantitative, and are the link for applying satellite products to both climate and air quality problems.

Glossary (of symbols and acronyms)

$\{PM_{2.5}\}$ – concentration of Particulate Matter less than 2.5 μm in diameter

AATS – Ames Airborne Tracking Sunphotometer

AERONET – AErosol RObotic NETwork

ATBD – Algorithm Theoretical Basis Document

$B_{\text{ext}}, B_{\text{sca}}$ – Mass extinction/scattering coefficients

CLAMS – Chesapeake Lighthouse and Aircraft Measurements for Satellites (experiment)

CMAQ – Community Mesoscale Air Quality model

EC/BC/OC – Elemental/Black/Organic Carbon

FRM – Federal Reference Monitor

LUT – LookUp Table

MARAMA – Mid-Atlantic Regional Air Management Association

MAST – MODIS Aerosol Team

MDE – Maryland Department of Environment

MODAPS – MODIS Adaptive Processing System

MODIS – MODerate resolution Imaging Spectro-radiometer

$N(r), V(r)$ - Number, Volume size distribution as a function of radius (r).

NAAQS – National Ambient Air Quality Standards

NASA-GSFC: National Aeronautical and Space Administration – Goddard Space Flight Center (in Greenbelt, MD)

$P(\Theta)$ – Phase function (as a function of scattering angle)

RAMMPP - Regional Atmospheric Measurement Modeling and Prediction Program

r_{eff} – effective radius of size distribution

r_g, r_v – median (geometric) radius of number size distribution, median radius of volume (mass) size distribution

subscripts: s = surface, λ = wavelength, a = atmospheric

superscripts: * = top of atmosphere.

TARFOX – Tropospheric Aerosol Radiation FORcing eXperiment

TOA – Top Of Atmosphere

UMCP – University of Maryland, College Park (sometimes also written as UMD)

UMD-Piper Aztec – Aircraft used by the University of Maryland.

USEPA – United States Environmental Protection Agency

VISvs2.12, 0.47vs0.66, 0.47vs2.12, 0.66vs2.12 – Visible versus 2.12 μm surface reflectance relationship, 0.47 μm versus 0.66 μm , etc

w_s , w – saturated, ambient water vapor mixing ratio

X – Mie size parameter

α – Ångstrom exponent

β_{ext} , B_{sca} – extinction/scattering coefficients

η – fine (aerosol) weighting (exact definition in context)

Θ , θ , θ_0 , ϕ - Scattering, view zenith, solar zenith, relative azimuth angles

λ – wavelength

ρ – reflectance (normalized radiance). May have subscripts or superscripts

ρ – particle density

σ – width of size distribution

σ_{ext} σ_{sca} , σ_{abs} – extinction, scattering, absorbing cross section

τ – optical depth (usually taken to mean ‘aerosol’ optical depth, AOD or optical thickness, AOT). May have subscripts to symbolize wavelength or measured by which instrument (e.g., $\tau_{0.55}$ or τ_{MODIS})

ω_0 – single scattering albedo (SSA)

Bibliography

- Ahmad, Z., and R.S. Fraser, (1982), An Iterative Radiative Transfer Code For Ocean-Atmosphere Systems, *J. Atmos. Sci.*, **39**, 656-665.
- Al-Saadi, J., J. Szykman, R. B. Pierce, C. Kittaka, D. Neil, D. A. Chu, L. Remer, L. Gumley, E. Prins, L. Weinstock, C. MacDonald, R. Wayland, F. Dimmick, and J. Fishman, (2005), Improving National Air Quality Forecasts with Satellite Aerosol Observations. *Bull. Am. Met. Soc.*, **86**(9), 1249-1261.
- Ames R.B. and W.C. Malm, (2001), Comparison of sulfate and nitrate particle mass concentrations measured by IMPROVE and the CDN. *Atmos. Environ.* **35**, 905-916.
- Anderson, T.L., *et al.*, (2005), An “A-Train” strategy for quantifying direct climate forcing by anthropogenic aerosols, *Bull. Am. Met. Soc.*, **86**(12), 1795-1809, doi: 10.1175/BAMS-86-12-1795.
- Anderson, T.L., D.S. Covert, S.F. Marshall, M.L. Laucks, R.J. Charlson, A.P. Waggoner, J.A. Ogren, R. Caldow, R.L. Holm, F.R. Quant, G.J. Sem, A. Wiedensohler, N.A. Ahlquist, and T.S. Bates (1996), Performance characteristics of a high-sensitivity, three-wavelength, total scatter/backscatter nephelometer, *J. Atmos. Oceanic Technol.*, **13**, 967-986.
- Anderson, T.L., Y. Wu, D.A. Chu, B.Schmid, J. Redemann and O. Dubovik (2006), Testing the MODIS satellite retrieval of aerosol fine-mode fraction, *J. Geophys. Res.*, **110**(D18204), doi: 10.1029/2005JD005978.
- Andreae, M.O., The dark side of aerosols, (2001), *Nature*, **409** (6821), 671-672.
- Andrews, E., Sheridan, P J., Fiebig, M., McComiskey, A., Ogren, J.A., Arnott, P., Covert, D., Elleman, R., Gasparini, R., Collins, D., Jonsson, H., Schmid, B., and Wang, J. (2006): Comparison of methods for deriving aerosol asymmetry parameter. *J. Geophys. Res.*, **111** (D05S04), DOI 10.1029/2004JD005734.

- Ångström, A., 1929; On the atmospheric transmission of sun radiation and on dust in the air. *Geograf. Ann. Deut.*, **11**, 156 - 166.
- Asrar, G., (1989) Theory and applications of optical remote sensing, Wiley, New York, 734 pp.
- Binkowski, F.S., Roselle, S.J., (2003), Models-3 Community Multiscale Air Quality (CMAQ) model aerosol component 1. Model description. *J. Geophys. Res.*, **108**(D6), 4183, doi:10.1029/2001JD001409.
- Bodhaine, B. A., N. B. Wood, *et al.* (1999), On Rayleigh optical depth calculations, *J. Atmos. Ocean. Tech.* **16**(11), 1854-1861.
- Bond, T.C. and R. W. Bergstrom (2006), Light Absorption by Carbonaceous Particles: An Investigative Review, *Aerosol Sci Tech.*, **40**(1), 27-47.
- Brown, O.B., R.H. Evans, J.W. Brown, H.R. Gordon, R.C. Smith, and K.S. Baker, (1985), Phytoplankton Blooming Off the United-States East Coast - a Satellite Description, *Science*, **229** (4709), 163-167.
- Byun, D. W., and J. K. S. Ching (Eds.), (1999), Science algorithms of the EPA Models-3 Community Multiscale Air Quality (CMAQ) Modeling System. EPA-600/R-99/030, Office of Research and Development, U.S. Environmental Protection Agency, Washington, D.C. (Available from U.S. EPA, ORD, Washington, D.C. 20460)
- Castanho, A. D. A., J. V. Martins, P. V. Hobbs, P. Artaxo, L. Remer, and M. Yamasoe, (2005), Chemical characterization of aerosols on the East Coast of the United States using aircraft and ground-based stations during the CLAMS experiment. *J. Atmos. Sci.*, **62**, 934–946.
- Chandrasekhar, S, (1950), Radiative Transfer, Clarendon Press, London.
- Chandrasekar, A., B.G. Doddridge, C.R. Philbrick, R.D. Clark, and P.G. Georgopoulous, (2003), A Comparative Study of Prognostic MM5 Meteorological Model With Aircraft, Wind Profiler, Lidar, Tethered Balloon and RASS Data Over Philadelphia During a 1999 Summer Episode, *Journal of Environmental Fluid Mechanics*,

- Chaudry, Z., J.V. Martins, Z. Li, S-C. Tsay, C. Li, T. Wen, H. Chen, P. Wang, and R.R. Dickerson (2007), *In situ* measurements of aerosol mass concentration and radiative properties in Xianghe, SE of Beijing, submitted to *J. Geophys. Res.*, (EAST-AIRE special issue).
- Chen, L. W. A., B. G. Doddridge, R. R. Dickerson, J. C. Chow and R. C. Henry, 2002: Origins of fine aerosol mass in the Baltimore-Washington corridor: Implications from observation, factor analysis, and ensemble air parcel back trajectories. *Atmos. Environ.*, **36**(28) 4541-4554.
- Chen, L.-W. A., Chow, J.C., Doddridge, B. G., Dickerson, R. R., Ryan, W. F., Mueller, P. K., (2003), Analysis of a summertime PM_{2.5} and Haze Episode in the Mid-Atlantic Region. *J. Air and Waste Management* **53**, 946-956.
- Chen, L.-W.A., (2002). Urban fine particulate matter: Chemical composition and possible origins. Doctoral dissertation, Chemical Physics, University of Maryland, College Park.
- Chen, L.-W.A., Doddridge, B.G., Dickerson, R.R., Chow, J.C., Henry, R.C., (2002), Origins of fine aerosol mass in the Baltimore-Washington corridor: implications from observation, factor analysis, and ensemble air parcel back trajectories. *Atmos. Environ.* **36**, 4541-4554.
- Chin, M., D. A. Chu, R. Levy, L. Remer, Y. Kaufman, B. Holben, T. Eck, P. Ginoux, and Q. Gao (2004): Aerosol distribution in the Northern Hemisphere during ACE-Asia: Results from global model, satellite observations, and Sun photometer measurements. *J. Geophys. Res.*, **109** (D23), doi: 10.1029/2004GL02014.
- Chin, M., P. Ginoux, *et al.* (2002), Tropospheric aerosol optical thickness from the GOCART model and comparisons with satellite and Sun photometer measurements, *J. Atmos. Sci.*, **59**(3), 461-483.
- Chow, J.C., J.D. Bachmann, S.S.G. Wierman, C.V. Mathai, W.C. Malm, W.H. White, P.K. Mueller, N. Kumar, and J.G. Watson, Visibility (2002), Science and regulation - Discussion, *J. Air & Waste Management Assoc.*, **52** (9), 973-999.
- Chu, D. A., L. A. Remer, Y. J. Kaufman, B. Schmid, J. Redemann, K. Knobelspiesse, J. D. Chern, J. Livingston, P. B. Russell, X. Xiong, and W. Ridgway (2005),

- Evaluation of aerosol properties over ocean from Moderate Resolution Imaging Spectroradiometer (MODIS) during ACE-Asia. *J. Geophys. Res.*, **110** (D07308), doi: 10.1029/2004/JD005208.
- Chu, D. A., Y. J. Kaufman, *et al.* (2002), Validation of MODIS aerosol optical depth retrieval over land, *Geophys. Res. Lett.* **29**(12): art. no.-1617.
- Chu, D. A., Y. J. Kaufman, G. Zibordi, J. D. Chern, J. Mao, C. Li, and B. N. Holben, (2003), Global monitoring of air pollution over land from EOS- Terra MODIS, *J. Geophys. Res.*, **108** (D21), 4661, doi: 10.1029/2002JD003179.
- Code of Federal Regulations (CFR), 18 July 1997, National Primary and Secondary Ambient Air Quality Standards, Final Rules, Title 40, Parts 50-53 and 58.
- Colarco, P.R., M.R. Schoeberl, B.G. Doddridge, L.T. Marafu, O.Torres and E.J. Welton, (2004), Transport of smoke from Canadian forest fires to the surface near Washington, D.C.: Injection height, entrainment and optical properties, *J. Geophys. Res.*, **109**(D06203), doi: 10.1029/2003JD004248.
- Colarco, P.R., O. B. Toon, O. Torres, and P. J. Rasch, (2002), Determining the UV imaginary index of refraction of Saharan dust particles from Total Ozone Mapping Spectrometer data using a three-dimensional model of dust transport, *J. Geophys. Res.*, **107**(D16), , doi: 10.1029/2001JD000903.
- Dave, J. V. (1970), Intensity and Polarization of Radiation Emerging from a Plane-Parallel Atmosphere Containing Monodispersed Aerosols, *App. Optics*, **9**(12): 2673-2687.
- Day, D.E., and W.C. Malm, (2001), Aerosol light scattering measurements as a function of relative humidity: a comparison between measurements made at three different sites, *Atmos Environ.*, **35** (30), 5169-5176.
- Deuze, J.L., F.M. Breon, C. Devaux, P. Goloub, M. Herman, B. Lafrance, F. Maignan, A. Marchand, F. Nadal, G. Perry, and D. Tanre, (2001), Remote sensing of aerosols over land surfaces from POLDER- ADEOS-1 polarized measurements, *J. Geophys. Res.*, **106** (D5), 4913-4926.
- Dickerson, R. R., S. Kondragunta, G. Stenchikov, K. L. Civerolo, B. G. Doddridge and B. N. Holben, (1997). The impact of aerosols on solar ultraviolet radiation and photochemical smog. *Science*, **278**, 5339, 827-830.

- Dickerson, R.R., B.G. Doddridge, P.K. Kelley, and K.P. Rhoads (1995), Large-scale pollution of the atmosphere over the Atlantic, *J. Geophys. Res.* **100**(5), 8945-8952.
- Diner, D.J., J.C. Beckert, T.H. Reilly, C.J. Bruegge, J.E. Conel, R. Kahn, J.V. Martonchik, T.P. Ackerman, R. Davies, S.A.W. Gerstl, H.R. Gordon, J-P. Muller, R. Myneni, R.J. Sellers, B. Pinty, and M.M. Verstraete (1998). Multi-angle Imaging SpectroRadiometer (MISR) description and experiment overview. *IEEE Trans. Geosci. Rem. Sens.*, **36** (4). 1072-1087.
- Draxler, R.R., and G.D. Rolph (2003), HYSPLIT (HYbrid Single-Particle Lagrangian Integrated Trajectory): Model access via NOAA ARL READY website (<http://www.arl.noaa.gov/ready/hysplit4.html>), NOAA Air Resources Laboratory, Silver Spring, MD.
- Dubovik, O. and M. D. King (2000), A flexible inversion algorithm for retrieval of aerosol optical properties from Sun and sky radiance measurements, *J. Geophys. Res.*, **105**(D16), 20673-20696.
- Dubovik, O., A. Sinyuk, T. Lapyonok, B. N. Holben, M. Mishchenko, P. Yang, T. F. Eck, H. Volten, O. Munoz, B. Veihelmann, van der Zander, M Sorokin, and I. Slutsker, (2006) Application of light scattering by spheroids for accounting for particle non-sphericity in remote sensing of desert dust, *J. Geophys. Res.*, **111**(D11208), doi: 10.1029/2005JD006619.
- Dubovik, O., A. Smirnov, B. N. Holben, *et al.* (2000), Accuracy assessments of aerosol optical properties retrieved from AERONET sun and sky radiance measurements, *J. Geophys. Res.*, **105**, 9791-9806.
- Dubovik, O., B. N. Holben, *et al.* (2002a), Variability of absorption and optical properties of key aerosol types observed in worldwide locations, *J. Atmos. Sci.* **59**(3), 590-608.
- Dubovik, O., B. N. Holben, *et al.* (2002b), Non-spherical aerosol retrieval method employing light scattering by spheroids, *Geophys. Res. Lett.* **29**(10): art. no.-1415.
- Durkee, P.A., K.E. Nielsen, P.J. Smith, P.B. Russell, B. Schmid, J.M. Livingston, B.N. Holben, C. Tomasi, V. Vitale, D. Collins, R.C. Flagan, J.H. Seinfeld,

- K.J. Noone, E. Ostrom, S. Gasso, D. Hegg, and L.M. Russell (2000), Regional aerosol optical depth characteristics from satellite observations: ACE-1, TARFOX and ACE-2 results, *Tellus*, **52** (2), 484-497.
- Eck, T. F., B. N. Holben, *et al.* (1999), Wavelength dependence of the optical depth of biomass burning, urban, and desert dust aerosols, *J. Geophys. Res.*, **104**(D24), 31333-31349.
- Eck, T. F., B. N. Holben, *et al.* (2005), Columnar aerosol optical properties at AERONET sites in central eastern Asia and aerosol transport to the tropical mid-Pacific, *J. Geophys. Res.*, **110**(D6).
- Ehsani, A.R., J.A. Reagan, and W.H. Erxleben, 1998: Design and performance analysis of an automated 10-channel solar radiometer instrument, *J. Atmos. Oceanic Tech.*, **15**, 697-707.
- Engel-Cox, J., C. Holloman, B. Coutant, and R. Hoff, (2004), Qualitative and quantitative evaluation of MODIS satellite sensor data for regional and urban scale air quality, *Atmos. Environ.*, **38** (16), pp. 2495-2509.
- Engel-Cox, J., G. Young, and R. Hoff, (2005), Application of satellite remote sensing data for source analysis of fine particulate matter transport events, *J. Air Waste Management*, **55**(9), pp. 1389-1397.
- Engel-Cox, J., R. Hoff, R. Rogers, F. Dimmick, A. Rush, J. Szykman, J. Al-Saadi, D. Chu, and E. Zell (2006), Using particulate matter concentration and lidar and satellite optical depth to build a 3-dimensional integrated air quality monitoring capability, *Atmos. Environ.* **40**, 8056-8067.
- Evans, K.F., and G.L. Stephens, A New Polarized Atmospheric Radiative-Transfer Model, (1991), *Quant. Spect. . Rad. Trans.*, **46**(5), pp. 413-423.
- Ferrare, R., S. Ismail, E. Browell, V. Brackett, S. Kooi, M. Clayton, P.V. Hobbs, S. Hartley, J.P. Veefkind, P. Russell, J. Livingston, D. Tanre, and P. Hignett (2000), Comparisons of LASE, aircraft, and satellite measurements of aerosol

- optical properties and water vapor during TARFOX, *J. Geophys. Res.*, **105** (D8), 9935-9947.
- Frank, Neil, H., 2006. Retained nitrate, hydrated sulfates, and carbonaceous mass in Federal Reference Method fine particulate matter for six Eastern U.S. cities. *Journal of Air and Waste Management Association* **56**, 500-511.
- Fraser, R.S., (1975), Degree of Inter-dependence among Atmospheric Optical Thicknesses in Spectral Bands between 0.36-2.4 microns, *J. Applied Meteorology*, **14** (6), 1187-1196.
- Fraser, R.S., Ferrare, R.A., Kaufman, Y.J., and Mattoo, S. (1989). Algorithm for Atmospheric Corrections of Aircraft and Satellite Imagery. NASA Technical Memorandum 100751. Greenbelt, MD USA, NASA Goddard Space Flight Center.
- Fraser, R.S., Y.J. Kaufman and R.L. Mahoney (1984), Satellite measurements of aerosol mass and transport, *Atmos. Env.*, **18**(12), 2577-2584.
- Gao, B.-C., Y.J. Kaufman, D. Tanré and R.-R. Li, (2002), Distinguishing tropospheric aerosols from thin cirrus clouds for improved aerosol retrievals using the ratio of 1.38- μm and 1.24- μm channels. *Geophys. Res. Lett.*, **29**, 1890, doi:10.1029/2002GL015475.
- Gao, B.C., Y.J. Kaufman, D. Tanre, and R.R. Li, (2002), Distinguishing tropospheric aerosols from thin cirrus clouds for improved aerosol retrievals using the ratio of 1.38- μm and 1.24- μm channels, *Geophys. Res. Lett.*, **29** (18), art. 1890.
- Gasso, S., and D. A. Hegg, (2003), On the retrieval of columnar aerosol mass and CCN concentration by MODIS. *J. Geophys. Res.*, **108** (D1), 4010, doi: 10.1029/2002JD002382.
- Gasso, S., (2001), Retrieval of Aerosol Properties from Space: Studies from an *In situ* Perspective, PhD thesis, University of Washington, Seattle.
- Gatebe, C. K., M. D. King, *et al.* (2001). Sensitivity of off-nadir zenith angles to correlation between visible and near-infrared reflectance for use in remote sensing of aerosol over land, *IEEE Trans. Geosci. Remote Sens.* **39**(4), 805-819.

- Ghan, S.J., R.C. Easter, E.G., Chapman, H. Abdul-Razzak, Y. Zhang, L.R. Leung, N.S. Laulainen, R.D. Saylor, and R.A. Zaveri, (2001), A physically based estimate of radiative forcing by anthropogenic sulfate aerosol, *J. Geophys. Res.*, **106** (D6), 5279-5293.
- Guenther, B., X. Xiong, V.V. Salomonson, W.L. Barnes and J. Young, (2002), On orbit performance of the Earth Observing System Moderate Resolution Imaging Spectroradiometer: First year of data. *Rem. Sens. Environ.*, **83**, pp. 16-30.
- Gupta, P. S.A. Christopher, J. Wang, R. Gehrig, Y. Lee and N. Kumar, (2006). Satellite remote sensing of particulate matter and air quality assessment over global cities, *Atmos Env.*, **40**, 5880-5892.
- Hains, J.C., L-W. A. Chen, B.F. Taubman, B.G. Doddridge and R.R. Dickerson (2007), A side by side comparison of filter-based PM_{2.5} measurements at a suburban site: a closure study, in preparation.
- Hand, J.L., R.B. Ames, S.M. Kreidenweis, D.E. Day, and W.C. Malm, Estimates of particle hygroscopicity during the Southeastern Aerosol and Visibility Study, *Journal of the Air & Waste Management Association*, 50 (5), 677-685, 2000.
- Hansen, E. H., and L. D. Travis, 1974: Light scattering in planetary atmospheres. *Space. Sci. Rev.*, **16**, 527–610.
- Haywood, J., and O. Boucher, (2000), Estimates of the direct and indirect radiative forcing due to tropospheric aerosols: A review, *Revs. Geophys*, **38** (4), 513-543.
- Heald, C.L., D.J. Jacob, R.J. Park, B. Alexander, T.D. Fairlie, D.A. Chu, R.M. Yantosca, (2006), Transpacific transport of Asian anthropogenic aerosols and its impact on surface air quality in the United States, *J. Geophys. Res.*, **111**, D14310, doi:10.1029/2005JD006847.
- Hegg, D.A., and Y.J. Kaufman, (1998), Measurements of the relationship between submicron aerosol number and volume concentration, *J. Geophys. Res.* **103** (D5), 5671-5678.

- Heintzenberg, J., F. Raes, and S. Schwartz (Lead Authors) *et al.*, (2000), Chapter 4: Tropospheric Aerosols (Draft, Oct, 2000). The IGAC (International Global Atmospheric Chemistry) Integration and Synthesis Report, 2001, available online from: <http://www-nacip.ucsd.edu/NACIPreferencelibrary.html>.
- Hess, M., P. Koepke, and I. Schult (1998): Optical Properties of Aerosols and clouds: The software package OPAC, *Bull. Am. Met. Soc.*, **79**, 831-844.
- Hignett, P., J.P. Taylor, P.N. Francis, and M.D. Glew, (1999), Comparison of observed and modeled direct aerosol forcing during TARFOX, *J. Geophys. Res.* **104** (D2), 2279-2287.
- Higurashi, A., T. Nakajima, B.N. Holben, A. Smirnov, R. Frouin, and B. Chatenet, (2000), A study of global aerosol optical climatology with two-channel AVHRR remote sensing, *Journal of Climate*, 13 (12), 2011-2027.
- Holben, B. N., D. Tanre, A. Smirnov, T. F. Eck, I. Slutsker, N. Abuhassan, W. W. Newcomb, J. S. Schafer, B. Chatenet, F. Lavenue, Y. J. Kaufman, J. V. Castle, A. Setzer, B. Markham, D. Clark, R. Frouin, R. Halthore, A. Karnieli, N. T. O'Neill, C. Pietras, R. T. Pinker, K. Voss, and G. Zibordi (2001): An emerging ground based aerosol climatology: Aerosol optical depth from AERONET. *Geophys. Res. Lett.*, **106**, 12067-12097.
- Holben, B. N., T. F. Eck, *et al.* (1998), AERONET - A federated instrument network and data archive for aerosol characterization, *Remote Sens. Environ.* **66**(1), 1-16.
- Hubanks, P. A. (2005), MODIS Atmosphere QA Plan for Collection 005. Greenbelt, MD USA, NASA Goddard Space Flight Center, 57 pages.
- Husar, R.B, J.M. Holloway and D.E. Patterson (1981), Spatial and temporal pattern of Eastern U.S. haziness; a summary, *Atmos. Environ.*, **15**, 1919-1928.
- Ichoku, C., D. A. Chu, *et al.* (2002a), A spatio-temporal approach for global validation and analysis of MODIS aerosol products, *Geophys. Res. Lett.*, **29**(12): art. no.-1616.
- Ichoku, C., R. Levy, Y. J. Kaufman, L. A. Remer, R. R. Li, V. J. Martins, B. N. Holben, N. Abuhassan, I. Slutsker, T. F. Eck and C. Pietras, (2002b). Analysis

- of the performance characteristics of the five-channel Microtops II Sun photometer for measuring aerosol optical thickness and precipitable water vapor. *J. Geophys. Res.-Atmos.*, **107**, D13, art. no.-4179.
- Ichoku, C., L. A. Remer, *et al.* (2003), MODIS observation of aerosols and estimation of aerosol radiative forcing over southern Africa during SAFARI 2000, *J. Geophys. Res.*, **108**(D13): art. no.-8499.
- Ignatov A., L. Stowe, S. Sakerin, G. Korotaev, (1995), Validation of the NOAA/NESDIS satellite aerosol product over the North Atlantic in 1989. ” *J. Geophys. Res.*, **100**(D3), pp. 5123-5132,
- Ignatov, A., and N.R. Nalli, (2002), Aerosol retrievals from the multiyear multisatellite AVHRR Pathfinder Atmosphere (PATMOS) dataset for correcting remotely sensed sea surface temperatures, *J. of Atmos. Ocean. Tech.* **19** (12), 1986-2008,
- Ignatov, A., P. Minnis, N. Loeb, B. Wielicki, W. Miller, S. Sun-Mack, D. Tanré, L. Remer, I. Laszlo, and E. Geier (2005), Two MODIS Aerosol Products over Ocean on the Terra and Aqua CERES SSF Datasets, *J. Atm. Sci.*, **62**, 1008-1031.
- Intergovernmental Panel on Climate Change - IPCC, (2001), Climate Change 2001: The Scientific Basis, J. T. Houghton, Y. Ding, D.J. Griggs, M. Noguer, P. J. van der Linden and D. Xiaosu (Eds.), Cambridge University Press, UK. pp 944.
- Jacobson, M.Z., (2001), Global direct radiative forcing due to multicomponent anthropogenic and natural aerosols, *J. Geophys. Res.* **106** (D2), 1551-1568.
- Jiang, W., S. Smyth, E. Giroux, H. Roth and D. Yin (2006), Differences between CMAQ fine mode particle and PM2.5 concentrations and their impact on model performance evaluation in the lower Fraser valley, *Atmos Environ.* **40**, 4973-4985, doi: 10.1016/j.atmosenv.2005.10.069.
- Karnieli, A., Y. J. Kaufman, L. A. Remer, and A. Wald, (2001) AFRI-aerosol free vegetation index. *Remote Sens. Environ.*, **77**(1), 1-21.
- Kaufman, Y. J. and L. A. Remer, (1994), Detection of Forests Using Mid-Ir Reflectance - an Application for Aerosol Studies. *IEEE Trans. Geosci. Remote*

- Sensing*, **32**, 3, 672-683.
- Kaufman, Y. J. and R. S. Fraser, (1983). Light Extinction by Aerosols during Summer Air Pollution. *Journal of Climate and Applied Meteorology*, **22**, 10, 1694-1706.
- Kaufman, Y. J., A. E. Wald, L. A. Remer, B. C. Gao, R. R. Li and L. Flynn, (1997c): The MODIS 2.1- μ m channel - Correlation with visible reflectance for use in remote sensing of aerosol. *IEEE Trans. Geosci. Remote Sensing*, **35**, 5, 1286-1298.
- Kaufman, Y. J., A. Gitelson, A. Karnieli, E. Ganor, R. S. Fraser, T. Nakajima, S. Mattoo, and B. N. Holben, (1994), Size distribution and scattering phase function of aerosol particles retrieved from sky brightness measurements. *J. Geophys. Res.*, **99**, 10341-10356.
- Kaufman, Y. J., and C. Sendra, (1988), Algorithm for atmospheric corrections of visible and Near IR satellite imagery, *Int. J. Rem. Sens.*, **9**, 1357-1381.
- Kaufman, Y. J., D. Tanré, *et al.* (1997a), Operational remote sensing of tropospheric aerosol over land from EOS moderate resolution imaging spectroradiometer. *J. Geophys. Res.*, **102**(D14), 17051-17067.
- Kaufman, Y. J., D. Tanre, H. R. Gordon, T. Nakajima, J. Lenoble, R. Frouin, H. Grassl, B. M. Herman, M. D. King, and P. M. Teillet, (1997b), Passive remote sensing of tropospheric aerosol and atmospheric correction for the aerosol effect. *J. Geophys. Res.* **102**(D14), 16815-16830.
- Kaufman, Y. J., N. Gobron, B. Pinty, J. L. Widlowski and M. M. Verstraete, (2002), Relationship between surface reflectance in the visible and mid-IR used in MODIS aerosol algorithm – theory, *Geophys. Res. Lett.* **29**(23), art. no.-2116.
- Kaufman, Y. J., O. Boucher, *et al.* (2005), Aerosol anthropogenic component estimated from satellite data, *Geophys. Res. Lett.* **32**(17).
- Kaufman, Y.J., (1989). The atmospheric effect on remote sensing and its correction. In Theory and Applications of Optical Remote Sensing, John Wiley & Sons, New York, G. Asrar, editor, 336-428.
- Kaufman, Y.J., and M.D. Chou, (1993), Model Simulations of the Competing Climatic Effects of SO₂ and CO₂, *J. Climate*, **6** (7), 1241-1252.

- Kaufman, Y.J., and R.S. Fraser, (1983), Light Extinction by Aerosols during Summer Air Pollution, *J. Climate Appl. Met.*, **22** (10), 1694-1706.
- Kaufman, Y.J., D. Tanre, and O. Boucher, (2002), A satellite view of aerosols in the climate system, *Nature*, **419**(6903) , pp. 215-223.
- Kaufman, Y.J., D.D. Herring, K.J. Ranson, and G.J. Collatz, Earth Observing System AM1 mission to earth, (1998), *IEEE Trans. Geosci. Remote Sens.*, **36** (4), 1045-1055.
- Kim, S-W., S.-C. Yoon, J. Kim and S-Y. Kim, (2006), Seasonal and monthly variations of columnar aerosol optical properties over east Asia determined from multi-year MODIS, LIDAR and AERONET sun/sky radiometer measurements, *Atmos. Environ.*, doi: 10.1016/j.atmosenv.2006.10.044.
- King, M. D., W. P. Menzel, Y. J. Kaufman, D. Tanre, B.-C. Gao, S. Platnick, S. A. Ackerman, L. A. Remer, R. Pincus, and P. A. Hubanks (2003), Cloud and aerosol properties, precipitable water, and profiles of temperature and humidity from MODIS. *IEEE Trans. Geosci. Remote Sens.*, **41**, 442-458.
- King, M. D., Y. J. Kaufman, W. P. Menzel and D. Tanre (1992). Remote-Sensing of Cloud, Aerosol, and Water-Vapor Properties From the Moderate Resolution Imaging Spectrometer (MODIS). *IEEE Trans. Geosci. Remote Sensing*, **30**, 1, 2-27.
- King, M.D., Y.J. Kaufman, D. Tanre, and T. Nakajima, (1999), Remote sensing of tropospheric aerosols from space: Past, present, and future, *Bull. Am. Met. Soc.*, **80**(11), pp. 2229-2259.
- Kinne, S., M. Shulz, C. Textor, *et al.*, (2006), An AeroCom initial assessment – optical properties in aerosol component modules of global models, *Atmos. Chem. Phys.*, **6**, 1–20.
- Kleidman, R. G., N. T. O'Neill, *et al.* (2005), Comparison of moderate resolution Imaging spectroradiometer (MODIS) and aerosol robotic network (AERONET) remote-sensing retrievals of aerosol fine mode fraction over ocean, *J. Geophys. Res.*, **110**(D22), Art. No. D22205.

- Knapp, K., R. Fourin, S. Kondragunta, A. Prados, (2005), Toward aerosol optical depth retrievals over land from GOES visible radiances: Determining surface reflectance, *Int. J. of Remote Sensing*,
- Köpke, P., M. Hess, I. Schult, and E.P. Shettle (1997), Global Aerosol Data Set, Report No. 243, Max-Planck-Institut für Meteorologie, Hamburg, ISSN 0937-1060.
- Kotchenruther, R.A., P. V. Hobbs, and D. A. Hegg, (1999), Humidification factors for aerosols off the mid-Atlantic coast of the United States, *J. Geophys. Res.* **104**(D2).
- Kovacs, Thomas (2006), Comparing MODIS and AERONET aerosol optical depth at varying separation distances to assess ground-based validation strategies for spaceborne lidar, *J. Geophys. Res.*, Vol. **III**, D24203 doi. 10.1029/2006JD007349.
- Lacis, A.A., J. Chowdhary, M.I. Mishchenko, and B. Cairns, (1998), Modeling errors in diffuse-sky radiation: Vector vs. scalar treatment, *Geophys. Res. Lett.*, **25**(2) pp. 135-138.
- Lake D.A., Tolocka M.P., Johnston M.V., Wexler, A.S., 2003. Mass spectrometry of individual particles between 50 and 750 nm in diameter at the Baltimore supersite. *Environmental Science and Technology* **37**, 3268-3274.
- Lenoble, J. and C. Brogniez, (1984), A comparative review of radiation aerosol models, *Beitr. Phys. Atmos.*, **57**(1), 1-20.
- Levy, R. C., L. A. Remer, *et al.* (2004), Effects of neglecting polarization on the MODIS aerosol retrieval over land, *IEEE Trans. Geosci. Remote Sens* **42**(11), 2576-2583.
- Levy, R. C., L. A. Remer, *et al.* (2005), Evaluation of the MODIS aerosol retrievals over ocean and land during CLAMS, *J. Atmos. Sci.*, **62**(4), 974-992.
- Levy, R.C., L.A. Remer and O. Dubovik *et al.* (2007a), Global aerosol optical properties and application to MODIS aerosol retrieval over land, accepted to *J. Geophys. Res.*
- Levy, R.C., L.A. Remer, D. Tanré, Y.J. Kaufman, C. Ichoku, B.N. Holben, J.M. Livingston, P.B. Russell and H. Maring, 2003: Evaluation of the MODIS

- retrievals of dust aerosol over the ocean during PRIDE. *J. Geophys. Res.*, **108**(D14), 10.1029/2002JD002460.
- Levy, R.C., L.A. Remer, S. Mattoo, E. Vermote and Y.J. Kaufman, (2007b), The second generation operational algorithm for retrieving aerosol properties over land from MODIS spectral reflectance, accepted to *J. Geophys. Res.*
- Li, R. R., L. Remer, *et al.* (2005). Snow and ice mask for the MODIS aerosol products." *IEEE Geo. and Rem. Sens. Lett.*, **2**(3), 306-310.
- Li, R. R., Y. J. Kaufman, B. C. Gao and C. O. Davis, (2003), Remote sensing of suspended sediments and shallow coastal waters. *IEEE Trans. Geosci. Remote Sens.*, **41**(3), 559-566.
- Liou, K.-N., (2002), *An Introduction to Atmospheric Radiation 2nd Edition*, Academic Press, San Diego, 577 pps.
- Lyapustin, A.I., and Y.J. Kaufman, (2001), Role of adjacency effect in the remote sensing of aerosol, *J. Geophys. Res.* **106**(D11), 11909-11916.
- Malm, W. C., (1992) Characteristics and Origins of Haze in the Continental United-States. *Earth-Sci. Rev.*, **33**(1), 1-36.
- Malm, W.C., B.A. Schichtel, R.B. Ames, and K.A. Gebhart, (2002), A 10-year spatial and temporal trend of sulfate across the United States *J. Geophys. Res.* **107**(D22), art. no.-4627.
- Malm, W.C., J.F. Sisler, D. Huffman, R.A. Eldred, and T.A. Cahill (1994), Spatial and Seasonal Trends in Particle Concentration and Optical Extinction in the United-States, *J. Geophys. Res.* **99** (D1), 1347-1370.
- Martins, J.V., D. Tanré, L.A. Remer, Y.J. Kaufman, S. Mattoo and R. Levy (2002), MODIS Cloud screening for remote sensing of aerosol over oceans using spatial variability. *Geophys. Res. Lett.*, **29**(12), 10.1029/2001GL013252.
- Marufu, L.T., B.F. Taubman, B. Bloomer, C.A. Piety, B.G. Doddridge, and R.R. Dickerson (2004), The 2003 North American electrical blackout: An accidental experiment in atmospheric chemistry, *Geophys. Res. Lett.*, **31**, L13106, doi:10.1029/2004GL019771.

- Mebust, M.R., B.K. Eder, F.S. Binkowski and S.J. Roselle, (2003), Models-3 Community Air Quality (CMAQ) model aerosol component: 2. Model evaluation, , *J. Geophys. Res.*, **108**(D6), 4184, doi: 1029/2001JD001410.
- Mi, W., Z. Li, X. Xia, B.N. Holben, R.C. Levy and H. Chen, (submitted 2007) Evaluation of the MODIS Aerosol Retrievals at Two AERONET Stations in China, submitted to the EAST-AIRE special issue in *J. Geophys. Res.*
- Mims, F.M., B.N. Holben, T.F. Eck, B.C. Montgomery, and W.B. Grant, Smoky skies, mosquitoes, and disease, *Science*, **276** (5320), 1774-1775, 1997.
- Mishchenko, M. I., A. A. Lacis, and L. D. Travis, (1994), Errors induced by the neglect of polarization in radiance calculations for Rayleigh-scattering atmospheres, *J. Quant. Spectrosc. Radiat. Transfer*, **51**, pp.491-510.
- Mishchenko, M. I., and L. D. Travis (1994), *T*-matrix computations of light scattering by large spheroidal particles, *Opt. Commun.*, **109**, 16-21.
- Mishchenko, M. I., L. D. Travis, R. A. Kahn, *et al.* (1997), Modeling phase functions for dustlike tropospheric aerosols using a shape mixture of randomly oriented polydisperse spheroids, *J. Geophys. Res.*, **102**, 16831-16847.
- Mie, G. (1908) A contribution to the optics of turbid media: Special colloidal metal solutions (in German: Beitrage zur Optik trüber Medien speziell kolloidaler Metallösungen). *Ann. Phys.* **25**: 377-445.
- MAST-MODIS Aerosol Science Team (2006), Algorithm Theoretical Basis Document (ATBD): Algorithm for Remote Sensing of Tropospheric Aerosol from MODIS, available from http://modis-atmos.gsfc.nasa.gov/MOD04_L2.
- Moody, E. G., M. D. King, S. Platnick, C. B. Schaaf, and F. Gao (2005), Spatially complete global spectral surface albedos: Value-Added datasets derived from Terra MODIS land products. *IEEE Trans. Geosci. Remote Sens.*, **43**, 144-158.
- Morys, M., F.M Mims III, S. Hagerup, S.E. Anderson, A. Baker, J. Kia, T. Walkup, (2001), Design, calibration and performance of Microtops II handheld ozone monitor and Sun photometer, *J. Geophys. Res.*, **106** (D13), 14573-14582.
- Myhre, G., F. Stordal, M. Johnsrud, D. J. Diner, I. V. Geogdzhayev, J. M. Haywood, B. Holben, T. Holzer-Popp, A. Ignatov, R. Kahn, Y. J. Kaufman, N. Loeb, J. Martonchik, M. I. Mishchenko, N. R. Nalli, L. A. Remer and M. Schroedter-

- Homscheidt (2005): Intercomparison of satellite retrieved aerosol optical depth over ocean during the period September 1997 to December 2000. *Atm. Chem. Physics* **5**, 1697-1719.
- Nakajima, T., and M. D. King, (1990). Determination of the optical thickness and effective particle radius of clouds from reflected solar radiation measurements. Part I: Theory. *J. Atmos. Sci.*, **47**, 1878-1893.
- Nakajima, T., G. Tonna, R. Z. Rao, P. Boi, Y. Kaufman and B. Holben, 1996: Use of sky brightness measurements from ground for remote sensing of particulate polydispersions. *Appl. Optics*, **35**, 15, 2672-2686.
- Novakov, T., D. A. Hegg, and P. V. Hobbs, 1997: Airborne measurements of carbonaceous aerosols on the East Coast of the United States. *J. Geophys. Res.*, **102** (D25), 30 023–30 030.
- Omar, A. H., J. G. Won, D.M. Winker, S-C. Yoon, O. Dubovik and S. Fan (2005), Development of global aerosol models using cluster analysis of Aerosol Robotic Network (AERONET) measurements, *J Geophys. Res.*, **110**(D10S14), 14 pp.
- Ondov, J.M., Buckley, T.J., Hopke, P.K., Ogulei, D., Parlange, M.B., Rogge, W.F., Squibb, K.S., Johnston, M.V. and Wexler, A.S. (2006), Baltimore Supersite Highly time- and size-resolved concentrations of urban PM_{2.5} and its constituents for resolution of sources and immune responses. *Atmos. Environ.*, **40**, S224-A237.
- O'Neill, N. T., Eck, T. F., Smirnov, A., Holben, B. N. and Thulasiraman, S. (2003), Spectral discrimination of coarse and fine mode optical depth, *J Geophys. Res.*, **108**, doi:10.1029/2002JD002975.
- O'Neill, N. T., Smirnov, A., Holben, B., and Thulasiraman, S. (2005), Spectral Deconvolution algorithm: Technical memo.
- O'Neill, N.T., A. Ignatov, B.N. Holben, and T.F. Eck, (2000), The lognormal distribution as a reference for reporting aerosol optical depth statistics; Empirical tests using multi-year, multi-site AERONET sunphotometer data, *Geophys Res. Lett.*, **27** (20), 3333-3336.

- O'Neill, N.T., O. Dubovik, and T.F. Eck, (2001), Modified angstrom exponent for the characterization of submicrometer aerosols, *Applied Optics*, **40** (15), 2368-2375.
- Park, R.J., (2001), The interaction of regional- and global-scale atmospheric chemistry, transport and climate processes, PhD Thesis, University of Maryland, College Park, 232 pages.
- Park, R.J., G.L. Stenchikov, K.E. Pickering, R.R. Dickerson, D.J. Allen, and S. Kondragunta, (2001), Regional air pollution and its radiative forcing: Studies with a single-column chemical and radiation transport model, *J. Geophys. Res.*, **106** (D22), 28751-28770.
- Parkinson, C. L., (2003) Aqua: An earth-observing satellite mission to examine water and other climate variables. *IEEE Trans. Geosci. Remote Sensing*, **41** (2), 173-183.
- Platnick, S., M.D. King, S.A. Ackerman, W.P. Menzel, B.A. Baum, J.C. Riedi, and R.A. Frey, (2003), The MODIS cloud products: Algorithms and examples from Terra, *IEEE Trans. Geosc. Remote Sens*, **41** (2), 459-473.
- Prospero, J.M., (1996), Saharan dust transport over the North Atlantic Ocean and Mediterranean: An overview, in *The Impact of Desert Dust Across the Mediterranean*, edited by S. Guerzoni and R. Chester, pp. 133-151, Kluwer Acad., Dordrecht, The Netherlands.
- Prospero, J.M., (1999) Assessing the impact of advected African dust on air quality and health in the eastern United States, *Human and Ecological Risk Assessment*, **5** (3), 471-479.
- Prospero, J.M., (1999), Long-term measurements of the transport of African mineral dust to the southeastern United States: Implications for regional air quality, *J. Geophys. Res.*, **104** (D13), 15917-15927.
- Ramanathan, V., P.J. Crutzen, J.T. Kiehl, and D. Rosenfeld, (2001), Atmosphere - Aerosols, climate, and the hydrological cycle, *Science*, **294** (5549), 2119-2124.

- Ramanathan, V. and P. J. Crutzen, (2003), New Directions: Atmospheric Brown "Clouds". *Atmos. Env.*, **37**, 4033-4035.
- Redemann, J., B. Schmid, J. A. Eilers, R. Kahn, R. C. Levy, P. B. Russell, J. M. Livingston, P. V. Hobbs, W. L. Smith Jr., B. N. Holben, 2004: Suborbital measurements of spectral aerosol optical depth and its variability at sub-satellite grid scales in support of CLAMS, 2001, *J. Atmos. Sci.*, (**CLAMS special issue**).
- Redemann, J., R.P. Turco, K.N. Liou, P.B. Russell, R.W. Bergstrom, B. Schmid, J.M. Livingston, P.V. Hobbs, W.S. Hartley, S. Ismail, R.A. Ferrare, and E.V. Browell, (2000), Retrieving the vertical structure of the effective aerosol complex index of refraction from a combination of aerosol *in situ* and remote sensing measurements during TARFOX, *J. Geophys. Res.*, **105** (D8), 9949-9970.
- Remer, L. A. and Y. J. Kaufman (1998), Dynamic aerosol model: Urban/industrial aerosol, *J Geophys. Res.*, **103**(D12): 13859-13871.
- Remer, L. A., A. E. Wald, *et al.* (2001), Angular and seasonal variation of spectral surface reflectance ratios: Implications for the remote sensing of aerosol over land, *IEEE Trans. Geosci. Remote Sens.*, **39**(2), 275-283.
- Remer, L. A., S. Gasso, D. A. Hegg, Y. J. Kaufman, and B. N. Holben, (1997), Urban/industrial aerosol: Ground-based sun/sky radiometer and airborne *in situ* measurements. *J. Geophys. Res.*, **102**, 16849-16859.
- Remer, L. A., Y. J. Kaufman, and B. N. Holben, (1999), Interannual variation of ambient aerosol characteristics on the East Coast of the United States. *J. Geophys. Res.* (TARFOX special issue), **104**, 2223-2231.
- Remer, L. A., Y. J. Kaufman, *et al.* (2005), The MODIS aerosol algorithm, products, and validation, *J. Atmos. Sci.*, **62**(4), 947-973.
- Rogers, R.R., and M.K. Yau, (1989) A short course in cloud physics, xiv, Pergamon Press, Oxford ; New York, 293 pp.
- Rosenfeld, D (2000)., Suppression of rain and snow by urban and industrial air pollution, *Science*, **287** (5459), 1793-1796.

- Russell, P. B., J. M. Livingston, E. G. Dutton, R. F. Pueschel, J. A. Reagan, T. E. Defoor, M. A. Box, D. Allen, P. Pilewskie, B. M. Herman, S. A. Kinne, and D. J. Hofmann (1993), Pinatubo and pre-Pinatubo optical-depth spectra: Mauna Loa measurements, comparisons, inferred particle size distributions, radiative effects, and relationship to lidar data. *J. Geophys. Res.*, **98**, 22,969-22,985.
- Russell, P.B., J.M. Livingston, P. Hignett, S. Kinne, J. Wong, A. Chien, R. Bergstrom, P. Durkee, and P.V. Hobbs, (1999), Aerosol-induced radiative flux changes off the United States mid-Atlantic coast: Comparison of values calculated from sunphotometer and *in situ* data with those measured by airborne pyranometer, *J. Geophys. Res.*, **104** (D2), 2289-2307.
- Russell, P.B., P.V. Hobbs, and L.L. Stowe, (1999), Aerosol properties and radiative effects in the United States East Coast haze plume: An overview of the Tropospheric Aerosol Radiative Forcing Observational Experiment (TARFOX), *J. Geophys. Res.*, **104** (D2), (D2), 2213-2222.
- Ryan, W.F., B.G. Doddridge, R.R. Dickerson, R.M. Morales, K.A. Hallock, P.T. Roberts, D.L. Blumenthal, and J.A. Anderson, (1998), Pollutant transport during a regional O-3 episode in the mid-Atlantic states, *J. Air & Waste Manage. Assoc.*, **48** (9), 786-797.
- Salomonson, V.V., W. L Barnes, P.W. Maymon, H.E. Montgomery, and H. Ostrow, (1989), MODIS, Advanced facility instrument for studies of the Earth as a system, " *IEEE Trans. Geosci, Remote Sens.*, **27**, 145-153.
- Samet, J. M., F. Dominici, F. C. Curriero, I. Coursac and S. L. Zeger, (2000), Fine particulate air pollution and mortality in 20 US Cities, 1987-1994. *N. Engl. J. Med.*, **343**, 24, 1742-1749.
- Seinfeld, J.H., and S.N. Pandis, Atmospheric chemistry and physics: From air pollution to climate change, xxvii, 1326 pp., John Wiley, New York, 1998.
- Shettle, E.P. and Fenn R.W. (1979), Models for the aerosols of the lower atmosphere and the effects of humidity variations on their optical properties, AFCRL-TR-79-0214, *Air Force Research Papers*, L.G. Hanscom Field, Bedford, MA USA.
- Smirnov, A., B. N. Holben, T. F. Eck, O. Dubovik and I. Slutsker, (2000), Cloud-

- screening and quality control algorithms for the AERONET database. *Remote Sens. Environ.*, **73**, 3, 337-349.
- Smirnov, A., B.N. Holben, T.F. Eck, I. Slutsker, B. Chatenet, and R.T. Pinker, (2002), Diurnal variability of aerosol optical depth observed at AERONET (Aerosol Robotic Network) sites, *Geophys. Res. Lett.*, **29** (23), art. no.-2115.
- Smith, Jr.W.L, T.P. Charlock, R. Kahn, J.V. Martins and L. Remer: EOS-TERRA aerosol and radiative flux validation (2005), An overview of the Chesapeake Lighthouse and Aircraft Measurements for Satellites (CLAMS) experiment, *J. Atmos. Sci.*, **CLAMS special issue**.
- Smyth, S.C., W. Jiang, D. Yin, H. Roth and E. Giroux, (2006), Evaluation of CMAQ O₃ and PM₂₅ performance using Pacifac 2001 measurement data, *Atmos Env*, **40**, 2735-2749.
- Stowe, L.L., A.M. Ignatov, and R.R. Singh, (1997), Development, validation, and potential enhancements to the second-generation operational aerosol product at the national environmental satellite, data, and information service of the national oceanic and atmospheric administration, *J. Geophys. Res.*, **102**(D14) pp. 16923-16934.
- Tanré, D., M. Hermon, and Y. J. Kaufman, (1996), Information on aerosol size distribution contained in solar reflectance spectral radiances, *J Geophys. Res.*, **101**(D14), 19043-19060.
- Tanré, D., Y. J. Kaufman, *et al.* (1997), Remote sensing of aerosol properties over oceans using the MODIS/EOS spectral radiances, *J Geophys. Res.*, **102**(D14), 16971-16988.
- Taubman, B., 2004, Airborne Characterization of Regional Aerosol Origins and Optical Properties, PhD thesis, University of Maryland, College Park, MD, 242 pages.
- Taubman, B.F., J.C. Hains, A.M. Thompson, L.T. Marufu, B.G. Doddridge, J.W. Stehr, C.A. Piety, and R.R. Dickerson, (2006), Aircraft Vertical Profiles of Trace Gas and Aerosol Pollution over the Mid-Atlantic U.S.: Statistics and Meteorological Cluster Analysis, *J. Geophys. Res.*, **III**(D10), doi: 2005JD006196.

- Taubman, B.F., L.T. Marufu, B.L. Vant-Hull, C.A. Piety, B.G. Doddridge, R.R. Dickerson, and Z. Li (2004b), Smoke over haze: Aircraft observations of chemical and optical properties and the effects on heating rates and stability, *J. Geophys. Res.*, **109**(D2), D02206, doi:10.1029/2003JD003898.
- Taubman, B.F., L.T. Marufu, C.A. Piety, B.G. Doddridge, J.W. Stehr, and R.R. Dickerson (2004a), Airborne characterization of the chemical, optical, and meteorological properties, and origins of a combined ozone/haze episode over the eastern U.S., *J. Atmos. Sci.*, **61**(14), 1781-1793.
- Thomas, G.E., and K. Stamnes, (1999), Radiative transfer in the atmosphere and ocean, Cambridge University Press, New York, 517 pp.
- Toon, O.B., (2000), Atmospheric science - How pollution suppresses rain, *Science*, **287** (5459), 1763.
- Torres O., P.K. Bhartia, J.R. Herman and Z. Ahmad, (1998), Derivation of aerosol properties from satellite measurements of backscattered ultraviolet radiation. Theoretical Basis, *J. Geophys. Res.*, **103**, 17099-17110.
- Torres, O., P.K. Bhartia, J.R. Herman, A. Sinyuk and B. Holben, (2002), A long term record of aerosol optical thickness from TOMS observations and comparison to AERONET measurements, *J. Atm. Sci.*, **59**, 398-413.
- Tucker, C. J. (1979), Red and photographic infrared linear combinations monitoring vegetation, *Remote Sens. Environ.*, **8**, 127-150.
- Twomey, S., 1977: Atmospheric Aerosols. Elsevier. 251 pp.
- U.S. Environmental Protection Agency (USEPA), (2003), National Air Quality and Emissions Trends Report, EPA 454/R-03-005, Research Triangle Park, NC, (<http://www.epa.gov/airtrends>)
- U.S. Government Printing Office, (1976), U.S. Standard Atmosphere, Washington, D.C.
- Van de Hulst, H.C., (1984), Light Scattering by Small Particles, Dover Publications, New York, 470 pps.

- van Donkelaar, A., R. V. Martin, and R. J. Park (2006), Estimating ground-level PM_{2.5} using aerosol optical depth determined from satellite remote sensing, *J. Geophys. Res.*, **111**, D21201, doi:10.1029/2005JD006996.
- Vant-Hull, B., Z. Li, B. F. Taubman, R. Levy, L. Marufu, F.-L. Chang, B. G. Doddridge, and R. R. Dickerson, (2005), Smoke over haze: Comparative analysis of satellite, surface radiometer, and airborne *in situ* measurements of aerosol optical properties and radiative forcing over the eastern United States. *J. Geophys. Res.*, **110**, D10S21, doi:10.1029/2004JD004518.
- Vermote, E. F., D. Tanré, *et al.* (1997a), Second Simulation of the Satellite Signal in the Solar Spectrum, 6S: An overview, *IEEE Trans. Geosci. Remote Sens.*, **35**(3), 675-686.
- Vermote, E. F., N. ElSaleous, C. O. Justice, Y. J. Kaufman, J. L. Privette, L. Remer, J. C. Roger and D. Tanre (1997b): Atmospheric correction of visible to middle-infrared EOS-MODIS data over land surfaces: Background, operational algorithm and validation. *J. Geophys. Res.-Atmos.*, **102**, D14, 17131-17141.
- Vermote, E.F., N.Z. El Saleous, and C.O. Justice, (2002), Atmospheric correction of MODIS data in the visible to middle infrared: first results, *Rem. Sens. Environ.*, **83** (12), 97-111.
- Volten H., O. Munoz, E. Rol, J. F de Haan., W. Vassen., J. W. Hovenier., K. Muinonen, and T. Nousiainen (2001), Scattering matrices of mineral aerosol particles at 441.6 nm and 632.8 nm, *J. Geophys. Res.*, **106**, 17375-17401.
- Wang, J. and S. Christopher (2003), Intercomparison between satellite-derived aerosol optical thickness and PM_{2.5} mass: Implications for air quality studies, *Geophys Res Lett.*, **30** (21), 2095, doi:10.1029/2003GL018174.
- Watson, J.G., (2002), Visibility: Science and regulation, *J. Air & Waste Management Assoc.*, **52** (6), 628-713.
- Welton, E. J., J. R. Campbell, J. D. Spinhirne, and V. S. Scott, (2001). Global monitoring of clouds and aerosols using a network of micropulse lidar systems, *Proc. Lidar Remote Sensing for Industry and Environmental Monitoring*, Sendai, Japan, SPIE, **4153**, pp151–158.

- Whitby, K. T., (1978): The physical characteristics of sulfur aerosols. *Atmos. Environ.*, **12**, 135–159.
- Wiscombe, W. J. (1981), Improved Mie scattering algorithms, *Appl. Opt.*, **19**, 1505-1509.
- Volz, F.E., (1959), Photometer mit Selen-photoelement zur spektralen Messung der Sonnenstrahlung und zur Bestimmung der Wellenlangenabhängigkeit der Dunsttrübung. *Arch. Meteor. Geophys Bioklim.* **B10**:100-131.
- Volz, F.E., (1974) Economical multispectral sun photometer for measurements of aerosol extinction from 0.44 μm to 1.6 μm and precipitable water. *Appl. Opt.*, **13**, 1732–1733.
- Yang P., and K. N. Liou (1996), Geometric-optics-integral-equation method for light scattering by nonspherical ice crystals, *Appl. Opt.*, **35**, 6568-6584.
- Yu, H., Y. J. Kaufman, M. Chin, G. Feingold, L. Remer, T. Anderson, Y. Balkanski, N. Bellouin, O. Boucher, S. Christopher, P. DeCola, R. Kahn, D. Koch, N. Loeb, M. S. Reddy, M. Schulz, T. Takemura, and M. Zhou (2006), A review of measurement-based assessments of aerosol direct radiative effect and forcing, *Atmos. Chem. Phys.*, **6**, 613-666.
- Xiong X, Sun J, Esposito J, Guenther, and Barnes WL, (2003), MODIS Reflective Solar Bands Calibration Algorithm and On-orbit Performance, *Proceedings of SPIE Optical Remote Sensing of the Atmosphere and Clouds III*, 4891, 95-104.